CONTENTS

MHD flow of a polar fluid through a porous medium of variable permeability bounded by horizontal parallel plates

Pradip Kumar Gaur[1], Abhay Kumar Jha[2,3],
Ram Prakash Sharma[1]

Abstract. This paper examines the problem of MHD unsteady flow of a polar fluid through a porous medium bounded by the horizontal parallel plates. The permeability of the porous medium decreases exponentially, with time about a constant mean. Using a perturbation technique the expression for velocity distribution, angular velocity and skin friction are obtained. The effect of the couple stress parameter β, permeability K and other parameters entering into the problem on velocity distribution are shown graphically.

Key words. MHD, polar fluid, skin friction, porous medium.

1. Introduction

The magnohydrodynamic flows have great importance due to its applications in solar physics, meteorology, geophysics, astrophysics and comic fluid dynamics. On account of their varied importance these flows have been studied by several authors, notable among them being [1–4]. The study of flows through porous medium is important among mathematicians and engineers due to its applications in biochemical, electrochemical and petroleum engineering. The petroleum engineering and hydrology depend on the properties of porous media. Petroleum engineering is mainly related to petroleum and natural gas exploration, well drilling logs and production. Hydrology concerns with sand structure and water movement in earth, such as filter beds for purification of drinking water and sewage, intrusion of sea water in coastal areas, flow to well from water-bearing formation and dams. In the light of such

[1]Department of Mathematics, JECRC University, Jaipur, Rajasthan, 303905, India
[2]Department of Mathematics, J. N. College Madhubani, Bihar, 847211, India
[3]Corresponding author

applications, flows though porous medium studied by many authors.

An MHD natural convective motion bounded by parallel vertical plates through porous media was studied by Rapits et al. [5]. An MHD mixed convective flow over an vertical plate in a porous medium was studied by Aldoss et al. [6]. Makinde and Sibanda [7] have analyzed suction driven motion and heat transfer in a pipe through porous media. An MHD natural convective motion over an vertical plate immersed in a porous medium in the presence of Hall effects has considered by Chamkha [8]. An MHD flow over a channel through porous medium have analyzed by Makinde and Mhone [9]. The MHD convective flow of a micropolar fluid from a constantly moving porous plate with heat absorption/generation have analyzed by Rehman and Sattar [10]. MHD convective motion past a horizontal channel with Joule heating and viscous dissipation through porous media have analyzed by Raju et al. [11]. The theory of polar fluids developed by Stokes [12] represents the viscous fluid that sustains couple stresses and the body couple. The main characteristic of these fluids is that the stress tensor is not symmetric and their exact behavior of flow cannot be predicted by Newton study. The main influence of couple stresses will be presenting a size dependent influence that does not exist in classical viscous studies. The fluids containing of rigid, haphazardly oriented particles suspended in a viscous medium, e.g., synthetic fluids, electro-theological, lubricants containing small amount of polymer additive. Cowin [13] presented an extensive theory of polar fluids. The flow of a polar fluid in a porous medium was analyzed by Raptis [14] and Patil and Hiremath [15]. An oscillatory flow of a polar fluid in a porous medium was presented by Patil and Hiremath [16]. By using the generalized Forchheimer's model Rapits and Takhar [17] analyzed a steady motion of a polar fluid in a porous medium. An MHD flow of a polar fluid heated from below through porous media was presented by Sharma and Thakur [18]. An unsteady convective motion of a polar fluid from a vertical moving plate with MHD through porous medium was presented by Kim [19]. Sharma and Sharma [20] studied the flow of a polar fluid saturated with suspended particles soluted and heated from below through porous media. A study of oscillating flow of a couple stress fluids from a vertical plate with radiation through porous medium is presented by Ogulu [21]. An unsteady MHD natural convective flow of a polar fluid from a vertical moving plate through porous media in the presence of thermal diffusion and heat generation was studied by [22]. An oscillatory flow of a polar fluid with MHD in a vertical moving plate through porous media in the presence of heat generation have analyzed by Veena et al. [23].

2. Formulation of the problem

We consider an unsteady MHD motion of a polar fluid between two flat parallel plates submerged in a porous medium with varying permeability. Let the distance between the plates be d and the coordinate axes x and y are along and normal to the plates, respectively. Along the y-axis a constant magnetic field of magnitude B_0 is applied. We assume that the flow is electrically conductive and the effects of the persuaded magnetic field and electric field are ignored. Since the plate is infinite in length, therefore, the variables of the flow depend only on t and y.

Under these assumptions, governing equations for the flow relevant to the problem are:

$$\frac{\partial v^*}{\partial y^*} = 0\,,\tag{1}$$

$$\frac{\partial u^*}{\partial t^*} + v^* \frac{\partial u^*}{\partial y^*} = -\frac{1}{\rho}\frac{\partial p^*}{\partial x^*} + (v + v_{\mathrm{r}})\frac{\partial^2 u^*}{\partial y^{*2}} + 2v_r\frac{\partial \omega^*}{\partial y^*} - \frac{v}{K^*} - \frac{\sigma B_0^2 u^*}{\rho}\,,\tag{2}$$

$$\frac{\partial \omega^*}{\partial t^*} + v^*\frac{\partial \omega^*}{\partial y^*} = \frac{\gamma}{I}\frac{\partial^2 \omega^*}{\partial y^{*2}}\,.\tag{3}$$

The relevant boundary conditions are:

$$u^* = 0,\ \frac{\partial \omega^*}{\partial y^*} = -\frac{\partial^2 u^*}{\partial y^{*2}}\ \text{at}\ y^* = 0\,,$$

$$u^* = U(t) = U_0(1 + \varepsilon\,\mathrm{e}^{-nt}),\ \omega^* \to 0\ \text{at}\ y^* = d\,.\tag{4}$$

In equations (1)–(4), u^* and v^* denote the dimensional components of velocity along the plate and perpendicular to it, x^* and y^* are the dimensional coordinates along the plate and perpendicular to it, t is the time, ρ stands for the density, p represents the pressure, v denotes the kinematic viscosity, v_{r} is the kinematic rotational viscosity, ω^* denotes the dimensional mean angular velocity, B_0 stands for the magnetic induction, K^* is the dimensional permeability parameter, σ denotes the thermal conductivity, γ represents the spin gradient viscosity, I is the moment of inertia of unit mass, U_0 denotes the scale of free stream velocity and n is a real constant.

Integration of the equation (1) for constant suction gives

$$v^* = -V_0\,,\tag{5}$$

where V_0 is the scale of the suction velocity. The permeability of the porous media is defined as below [24]:

$$K = K_0(1 + A\varepsilon\mathrm{e}^{-nt})\,,\tag{6}$$

where $A,\ n > 0,\ \varepsilon A \ll 1$.

The dimensionless quantities are defined as:

$$p = \frac{p^*}{\rho V_0^2},\ t = \frac{t^* V_0^2}{v},\ \omega = \frac{\omega^* v}{V_0 U_0},\ x = \frac{x^* U_0}{v},\ u = \frac{u^*}{U_0},\ y = \frac{y^* V_0}{v},$$

and further we introduce

$M^2 = \frac{\sigma B_0^2 v}{\rho V_0^2}$ (Hartmann number),

$\beta = \frac{vI}{\gamma}$ (couple stress parameter),

$K = \frac{K^* V_0^2}{v^2}$ (permeability parameter) and

$\varpi = \frac{v_r}{v}$ (kinematic rotational viscosity parameter).

$$(7)$$

In view of equations (5), (6), and (7), the governing equations (2) and (3) reduce in the following dimensionless forms:

$$(1+\varpi)\frac{\partial^2 u}{\partial y^2} + 2\varpi\frac{\partial \omega}{\partial y} + \frac{\partial u}{\partial y} - \left[M^2 + \frac{1}{K_0(1+\varepsilon \mathrm{e}^{-nt})}\right](u-U) - \frac{\partial u}{\partial t} = -\frac{\partial U}{\partial t}, \quad (8)$$

$$\frac{\partial^2 \omega}{\partial y^2} + \beta\frac{\partial \omega}{\partial y} = \beta\frac{\partial \omega}{\partial t} \qquad (9)$$

and the corresponding boundary conditions (4) reduce to the following dimensionless forms:

$$u = 0, \quad \frac{\partial \omega}{\partial y} = -\frac{\partial^2 u}{\partial y^2} \quad \text{at } y = 0,$$

$$u = (1+\varepsilon \mathrm{e}^{-nt}), \quad \omega \to 0 \quad \text{at } y = D, \qquad (10)$$

where $D = \frac{dV_0}{v}$ is a constant.

3. Analysis

To solve the equations (8), and (9), under the boundary condition (10), we assume $\varepsilon \ll 1$ and the solutions of the equations in the following manner:

$$u(y,t) = u_0(y) + \varepsilon \mathrm{e}^{-nt} u_1(y), \qquad (11)$$

$$\omega(y,t) = \omega_0(y) + \varepsilon \mathrm{e}^{-nt}\omega_1(y). \qquad (12)$$

Introducing the above equations (11) and (12) into the equations (8) and (9), and neglecting the terms higher power of ε^2, the following differential equations are obtained:

$$\frac{\partial^2 u_0}{\partial y^2} + N_1\frac{\partial u_0}{\partial y} - N_4 u_0 = -N_2\frac{\partial \omega_0}{\partial y} - N_4, \qquad (13)$$

$$\frac{\partial^2 u_1}{\partial y^2} + N_1\frac{\partial u_1}{\partial y} - N_4 u_1 = N_{10} - N_2\frac{\partial \omega_1}{\partial y}, \qquad (14)$$

$$\frac{\partial^2 \omega_0}{\partial y^2} + \beta\frac{\partial \omega_0}{\partial y} = 0, \qquad (15)$$

$$\frac{\partial^2 \omega_1}{\partial y^2} + \beta\frac{\partial \omega_1}{\partial y} + n\beta\,\omega_1 = 0. \qquad (16)$$

The corresponding boundary conditions (10), reduce to

$$u_0 = 0, \; u_1 = 0, \; \frac{\partial \omega_0}{\partial y} = -\frac{\partial^2 u_0}{\partial y^2}, \; \frac{\partial \omega_1}{\partial y} = -\frac{\partial^2 u_1}{\partial y^2} \; \text{at} \; y = 0 \,,$$

$$u_0 = 1, \; u_1 = 1, \; \omega_0 = 0, \; \omega_1 = 0 \; \text{at} \; y = D \,. \tag{17}$$

The solutions of equations (13)–(16) satisfying the boundary conditions (17) are

$$u_0 = C_5 \mathrm{e}^{N_5 y} + C_6 \mathrm{e}^{N_6 y} + N_9 C_2 \mathrm{e}^{-\beta y} + 1 \,, \tag{18}$$

$$u_1 = C_7 \mathrm{e}^{N_{13} y} + C_8 \mathrm{e}^{N_{14} y} + N_{15} - N_{16} C_3 \mathrm{e}^{N_7 y} - N_{17} C_4 \mathrm{e}^{N_8 y} \,, \tag{19}$$

$$\omega_0 = C_2 \left(\mathrm{e}^{-\beta y} - \mathrm{e}^{-\beta D} \right) \,, \tag{20}$$

$$\omega_1 = C_3 \mathrm{e}^{N_7 y} + C_4 \mathrm{e}^{N_8 y} \,. \tag{21}$$

Substituting the values of u_0, u_1, ω_0 and ω_1 in the equations (11) and (12), we obtain velocity $u(y, t)$ and micro-rotation profile $\omega(y, t)$, respectively.

The skin friction coefficient is defined as

$$\tau = (1 + \varpi) \left(\frac{\partial u}{\partial y} \right)_{y=0} \,. \tag{22}$$

The couple stress coefficient is defined as

$$C_{\mathrm{m}} = (1 + \beta) \left(\frac{\partial \omega}{\partial y} \right)_{y=0} \,. \tag{23}$$

4. Numerical results and discussion

In order to get a physical view of the problem, velocity, angular velocity, skin friction and couple stress coefficients have been discussed by assigning numerical values to ϖ, β, M and K that describe flow characteristics, and the results are demonstrated graphically. In this problem, we have taken $t = 1.0$, $\varepsilon = 0.02$, $A = 0.4$, $D = 3.0$, and $n = 0.2$.

Figures 1 and 2 depict the effects of the Hartmann number on the velocity and angular velocity, respectively, for different values of M. It is clear that the velocity decreases with the improving values of M while the reverse effect is observed for angular velocity. Figures 3 and 4 present the effects of permeability parameter on the velocity and angular velocity, respectively, for various values of K. It is observed that the velocity enhances for enriched values of K while the reverse effect is observed for angular velocity. Figures 5 and 6 illustrate the effects of couple stress parameter on the velocity and angular velocity, respectively, for distinct values of β. It is noted

that the velocity diminishes with growing values of β. In the case of angular velocity, an opposite effect is observed. Figures 7 and 8 depict the effects of the kinematic rotational viscosity parameter on the velocity and angular velocity, respectively, for various values of ϖ. It is obtained that velocity increases with the rising value of ϖ while angular velocity diminishes with the growing value of ϖ.
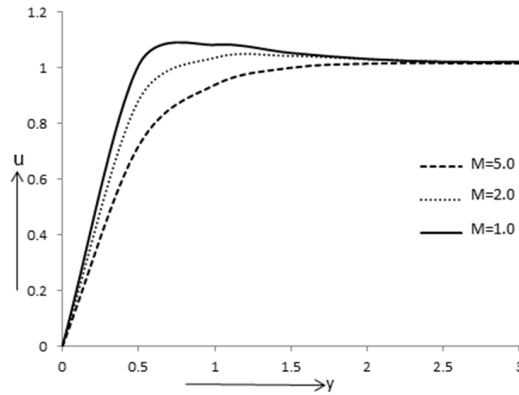
Fig. 1. Velocity profiles for various values of Hartmann parameter
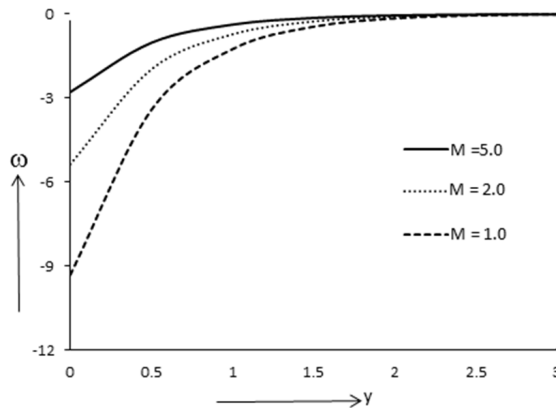
Fig. 2. Angular velocity profiles for various values of magnetic parameter

Figure 9 depicts the effects for the various values of ϖ, β, n, ε and K on the skin friction coefficient against M. It is observed that the skin friction coefficient at the plate falls with growing values of β, n, t and K, while it upsurges with the growing value of ϖ and ε. Figure 10 depicts the effects for the various values of ϖ, β, n, ε, t, and K on the couple stress coefficients against M. It is observed that the couple stress coefficient at the plate diminishes with growing values of ϖ, n, ε and K while it enhances as t and β increases.
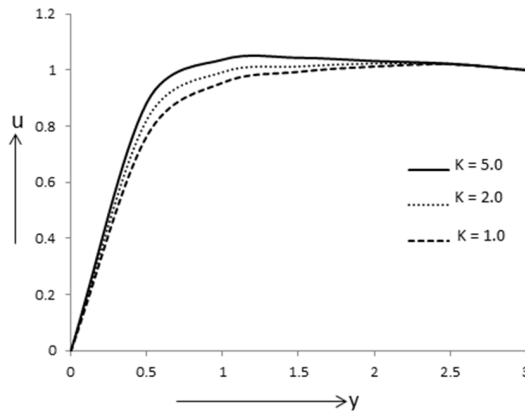
Fig. 3. Velocity profiles for various values of permeability parameter
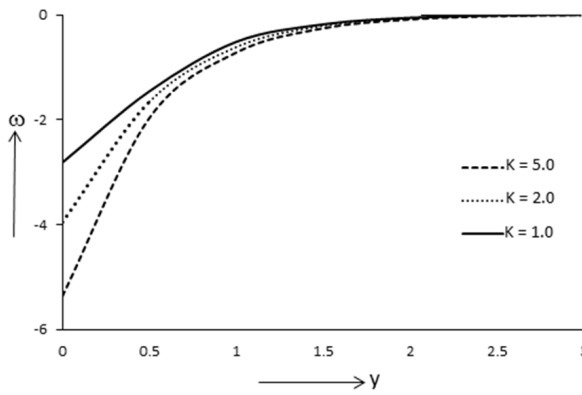
Fig. 4. Angular velocity profiles for various values of permeability parameter
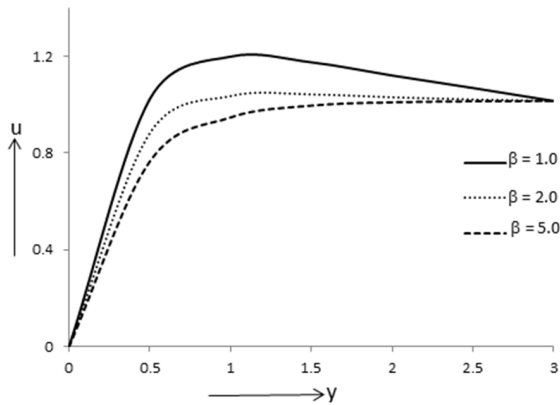
Fig. 5. Velocity profiles for various values of couple stress parameter
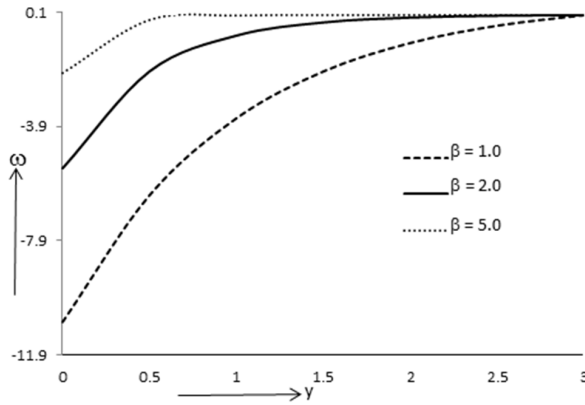
Fig. 6. Angular velocity profiles for various values of couple stress parameter
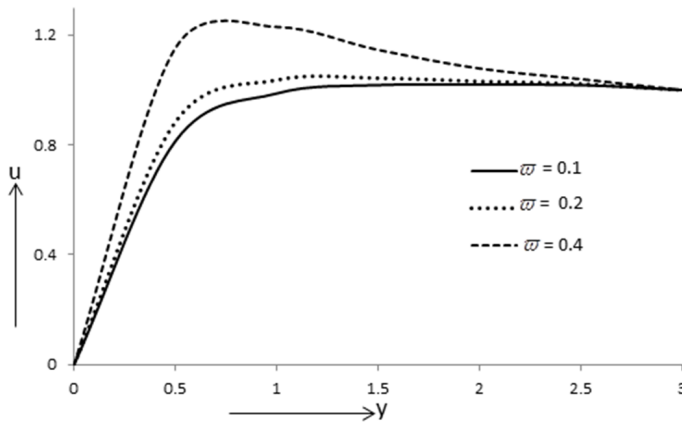
Fig. 7. Velocity profiles for various values of kinematic rotational viscosity
parameter

5. Conclusion

1. As the values of β and M increase, the height of the translation velocity profile decreases while the reverse happens to ϖ and K.

2. The angular velocity reduces with the growing value of ϖ and K, while the reverse trend is noticed for the magnetic parameter β and M.

3. The shearing stress at the wall reduces with the growing value of K and β, while the opposite trend is observed for ϖ.

4. The couple stress coefficient rises with rising values of β while the opposite happens with K and ϖ.
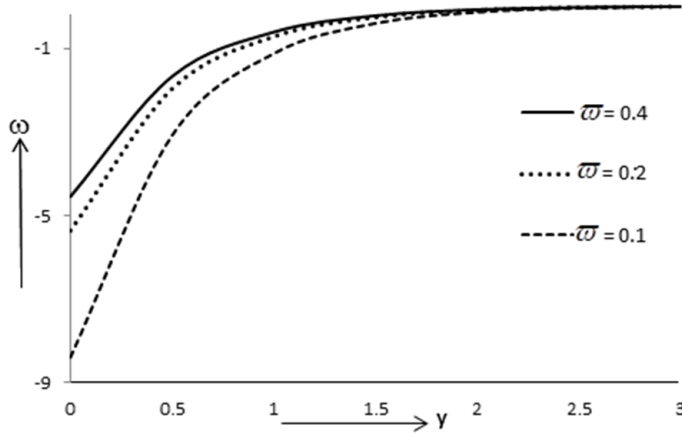
Fig. 8. Angular velocity profiles for various values of kinematic rotational viscosity parameter
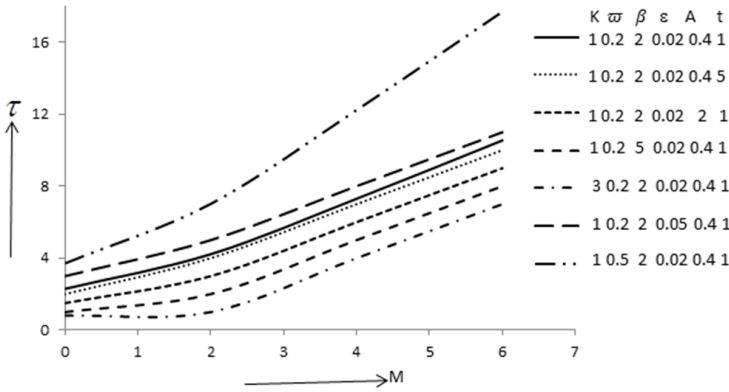
Fig. 9. Skin friction coefficient for various values of ϖ, β, n, ϵ, t and K

6. Appendix

The Appendix contains coefficients occurring in equations (13)–(21)

$$N_1 = \frac{1}{1+\varpi}, \ N_2 = \frac{2\varpi}{1+\varpi}, \ N_3 = \left[M^2 + \frac{1}{K_0\left(1 + A\varepsilon\mathrm{e}^{-nt}\right)}\right], \ N_4 = \frac{N_3}{1+\varpi},$$

$$N_5 = \frac{-N_1 + \sqrt{N_1^2 + 4N_4}}{2}, \ N_6 = \frac{-N_1 - \sqrt{N_1^2 + 4N_4}}{2},$$

$$N_7 = \frac{-\beta + \sqrt{\beta^2 - 4n\beta}}{2}, \ N_8 = \frac{-\beta - \sqrt{\beta^2 - 4n\beta}}{2},$$

$$N_9 = \frac{N_2\beta}{\beta^2 - N_1\beta - N_4}, \ N_{10} = \frac{n - N_4}{1+\varpi}, \ N_{11} = K_2N_7, \ K_{12} = K_2N_8,$$
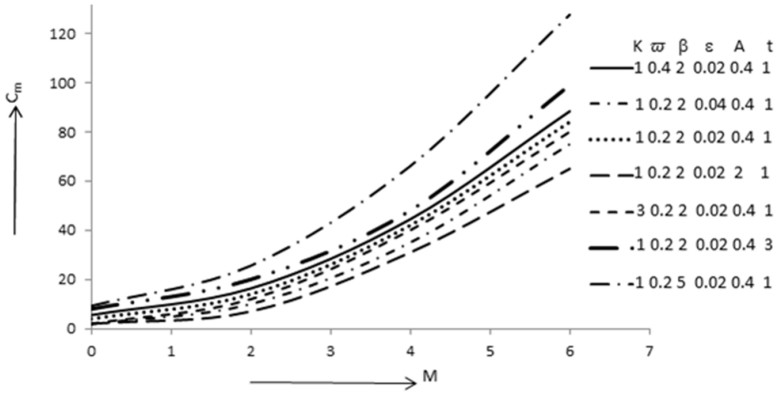
Fig. 10. Couple stress coefficient for various values of ϖ, β, n, ϵ, t and K

$$N_{13} = \frac{-N_1 + \sqrt{N_1^2 + 4N_4}}{2}, \ N_{14} = \frac{-N_1 - \sqrt{N_1^2 + 4N_4}}{2},$$

$$N_{15} = -\frac{N_{10}}{N_4}, \ N_{16} = \frac{N_{11}}{N_7^2 + N_1 N_7 - N_4}, \ N_{17} = \frac{N_{12}}{N_8^2 + N_1 N_8 - N_4},$$

$$N_{18} = \frac{\mathrm{e}^{N_5 D}}{\mathrm{e}^{N_6 D} - \mathrm{e}^{N_5 D}}, \ N_{19} = \frac{\left(\mathrm{e}^{-\beta D} - \mathrm{e}^{N_5 D}\right) N_9}{\mathrm{e}^{N_6 D} - \mathrm{e}^{N_5 D}},$$

$$N_{20} = \frac{\mathrm{e}^{N_6 D}}{\mathrm{e}^{N_5 D} - \mathrm{e}^{N_6 D}}, \ N_{21} = \frac{\left(\mathrm{e}^{-\beta D} - \mathrm{e}^{N_6 D}\right) N_9}{\mathrm{e}^{N_5 D} - \mathrm{e}^{N_6 D}},$$

$$N_{22} = \frac{1}{\mathrm{e}^{N_{14} D} - \mathrm{e}^{N_{13} D}}, \ N_{23} = \frac{N_{15}\left(1 - \mathrm{e}^{N_{13} D}\right)}{\mathrm{e}^{N_{14} D} - \mathrm{e}^{N_{13} D}},$$

$$N_{24} = \frac{N_{16}\left(\mathrm{e}^{N_7 D} - \mathrm{e}^{N_{13} D}\right)}{\mathrm{e}^{N_{14} D} - \mathrm{e}^{N_{13} D}}, \ N_{25} = \frac{N_{17}\left(\mathrm{e}^{N_8 D} - \mathrm{e}^{N_{13} D}\right)}{\mathrm{e}^{N_{14} D} - \mathrm{e}^{N_{13} D}},$$

$$N_{26} = \frac{1}{\mathrm{e}^{N_{13} D} - \mathrm{e}^{N_{14} D}}, \ N_{27} = \frac{N_{15}\left(1 - \mathrm{e}^{N_{14} D}\right)}{\mathrm{e}^{N_{13} D} - \mathrm{e}^{N_{14} D}},$$

$$N_{26} = \frac{1}{\mathrm{e}^{N_{13} D} - \mathrm{e}^{N_{14} D}}, \ N_{27} = \frac{N_{15}\left(1 - \mathrm{e}^{N_{14} D}\right)}{\mathrm{e}^{N_{13} D} - \mathrm{e}^{N_{14} D}},$$

$$N_{28} = \frac{N_{16}\left(\mathrm{e}^{N_7 D} - \mathrm{e}^{N_{14} D}\right)}{\mathrm{e}^{N_{13} D} - \mathrm{e}^{N_{14} D}}, \ N_{29} = \frac{N_{17}\left(\mathrm{e}^{N_8 D} - \mathrm{e}^{N_{14} D}\right)}{\mathrm{e}^{N_{13} D} - \mathrm{e}^{N_{14} D}},$$

$$N_{30} = -\frac{\mathrm{e}^{N_8 D}}{\mathrm{e}^{N_7 d}}, \ N_{31} = N_{13}^2 N_{26} - N_{13}^2 N_{27} + N_{14}^2 N_{22} - N_{14}^2 N_{23},$$

$$N_{32} = N_{13}^2 N_{28} - N_{14}^2 N_{24} + N_{14}^2 N_{22} - N_7^2 N_{16},$$

$$N_{33} = N_{13}^2 N_{29} - N_{14}^2 N_{25} + N_{14}^2 N_{22} - N_8^2 N_{17},$$

$$N_{34} = N_6 N_{30} + N_8 + N_{30} N_{32} + N_{33},$$

$$C_5 = -C_6 e^{\beta D}, \ C_6 = \frac{N_5^2 N_{20} + N_6^2 N_{18}}{\beta - (\beta^2 N_9 - N_5^2 N_{21} - N_6^2 N_{19})},$$

$$C_7 = C_8 N_{30}, \ C_8 = -\frac{N_{31}}{N_{34}}, \ C_9 = N_{20} - N_{21} C_6, \ C_{10} = N_{18} - N_{19} C_6,$$

$$C_{11} = N_{26} - N_{27} + N_{28} C_7 + N_{29} C_8, \ C_{12} = N_{22} - N_{23} + C_7 N_{24} + C_8 N_{25}.$$

References

[1] S. D. Nigam, S. N. Singh: *Heat transfer by laminar flow between parallel plates under the action of transverse magnetic field.* Quarterly Journal of Mechanics and Applied Mathematics *13* (1960), No. 1, 85–97.

[2] H. A. Attia, N. A. Kotb: *MHD flow between two parallel plates with heat transfer.* Acta Mechanica *117* (1996), Nos. 1–4, 215–220.

[3] G. Bodosa, A. K. Borkakti: *Unsteady free convection MHD flow and heat transfer of a visco-elastic fluid past between two heated horizontal plates with heat source or sinks.* Indian Journal of Theoretical Physics *51* (2003), No. 1, 39–46.

[4] R. C. Chaudhary, A. K. Jha, S. S. Dhayal: *Heat transfer to magnetohydrodynamic flow in a horizontal channel with heat source.* Journal Rajasthan Academy of Physical Sciences *5* (2006), No. 2, 233–238.

[5] A. Raptis: *Effects of couple stresses on the flow through a porous medium.* Rheologica Acta *21* (1982), No. 6, 736–737.

[6] T. K. Aldoss, A. Al-Nimr, M. A. Jarrah, B. J. Al-Shaer: *Magnetohydrodynamic mixed convection from a vertical plate embedded in a porous medium.* Numerical Heat Transfer, Part A: Applications *28A* (1995), No. 5, 635–645.

[7] O. D. Makinde, P. Sibanda: *On suction driven flow and heat transfer in a pipe filled with porous media.* Computer Assisted Mechanics and Engineering Sciences *5* (1998), No. 4, 389–398.

[8] A. J. Chamkha: *MHD-free convection from a vertical plate embedded in a thermally stratified porous medium with Hall effects.* Applied Mathematical Modelling *21* (1997), No. 10, 603–609.

[9] O. D. Makinde, P. Y. Mhone: *Heat transfer to MHD oscillatory flow in a channel filled with porous medium.* Romanian Journal of Physics *50* (2005), Nos. 9–10, 931–938.

[10] M. M. Rahman, M. A. Sattar: *Magnetohydrodynamic convective flow of a micropolar fluid past a continuously moving porous plate in the presence of heat generation/absorption.* ASME Journal Heat Transfer *128*, (2005), No. 2, 142–152.

[11] K. V. S. Raju, T. S. Reddy, M. C. Raju, P. V. Satyanarayna, S. Venkataramana: *MHD convective flow through porous medium in a horizontal channel with insulated and impermeable bottom wall in the presence of viscous dissipation and joule heating.* Ain Shams Engineering Journal *5* (2014), No. 2, 543–551.

[12] V. K. Stokes: *Couple stresses in fluids.* AIP Physics of Fluids *9* (1966), No. 9, 1709–1715.

[13] S. C. Cowin: *The theory of polar fluids.* Advances in Applied Mechanics *14* (1974), 279–347.

[14] A. Rapits, C. Masslas, G. Tzivanidis: *Hydromagnetic free convection flow through a porous medium between two parallel plates.* Physics Letters A *90A* (1982), No. 6, 288–289.

[15] P. M. Patil, P. S. Hiremath: *A note on effects of couple stresses on the flow through a porous medium.* Rheologica Acta *31* (1992), No. 2, 206–207.

[16] P. S. Hiremath, P. M. Patil: *Free convection effects on the oscillatory flow of a couple stress fluid through a porous medium.* Acta Mechanica *98* (1993), Nos. 1–4, 143–158.

[17] A. RAPTIS, H. S. TAKHAR: *Polar fluid through a porous medium.* Acta Mechanica *135* (1999), Nos. 1–2, 91–93.

[18] R. C. SHARMA, K. D. THAKUR: *On couple stress fluid heated from below in porous medium in hydromagnetics.* Czechoslovak Journal of Physics *50* (2000), No. 6, 753–758.

[19] Y. J. KIM: *Unsteady MHD convection flow of polar fluids past a vertical moving porous plate in a porous medium.* International Journal of Heat and Mass Transfer *44,* (2001), No. 15, 2791–2799.

[20] R. C. SHARMA, M. SHARMA: *On couple stress fluid permeated with suspended particles heated and soluted from below in porous medium.* Indian Journal of Physics B *78B* (2004), 189–194.

[21] A. OGULU: *On the oscillating plate-temperature flow of a polar fluid past a vertical porous plate in the presence of couple stresses and radiation.* International Communications in Heat and Mass Transfer *32* (2005), No. 9, 1231–1243.

[22] S. S. SAXENA, G. K. DUBEY: *Unsteady MHD heat and mass transfer free convection flow of polar fluids past a vertical moving porous plate in a porous medium withheat generation and thermal diffusion.* Advances in Applied Science Research *2* (2011), No. 4, 259–278.

[23] P. H. VEENA, N. RAVEENDRA, V. K. PRAVIN: *Oscillatory flow of MHD polar fluid with heat and mass transfer past a vertical moving porous plate with internal heat generation.* International Journal of Mechanical Engineering and Technology *7* (2016), No. 2, 212–231.

[24] D. A. NIELD, A. BEJAN: *Convection in Porous Media.* Book Publisher: Springer-Verlag, New York, USA (2013).

Non-linear MHD flow and heat transfer of nanofluid over a moving and static wedge under temperature jump[1]

Shalini Jain[2], Rakesh Choudhary[3]

Abstract. The paper aims to investigate the flow of two types of nanofluids i.e. Al_2O_3 -water nanofluid and Cu-water nanofluid over a moving and static wedge in the presence of non-linear MHD and porous medium. Effects of mixed convection flow, viscous dissipation and temperature jump are also considered. The governing boundary layer equation and boundary conditions are converted into dimensionless differential equations. These converted equations are solved numerically with Runge-Kutta fourth-order method using the shooting technique. A comparative study of Newtonian fluid (pure water), copper-water nanofluid and aluminum oxide water nanofluid under the influence of various physical parameters for both moving and static wedge have been analyzed and discussed. The results obtained are depicted graphically and in tabular form. It is observed that velocity profile is maximum for aluminum oxide and minimum for copper-water nanofluid.

Key words. MHD, nanofluid, moving wedge, porous medium, mixed convection, temperature jump, Runge-Kutta method.

1. Introduction

In recent years, several researchers have been attracted on studying the incompressible nanofluids due to their wide applications in many areas such as chemical engineering, thermal processes, cooling processes etc. These nano- and micro-size particles enhance the efficiency of the considered setup, extend the presence of machine and reduce the processing time. Nanoparticles also enhance the thermal conductivity of the fluid and cause increases in heat transfer efficiency of the fluid. The base fluid such as water or ethylene-glycol have low thermal conductivities compared

[2]Department of Mathematics & Statistics, Manipal University Jaipur, Rajasthan, 303007, India; E-mail: shalini.jain@jaipur.manipal.edu

[3]Department of Mathematics & Statistics, Manipal University Jaipur, Rajasthan, 303007, India; E-mail: raakeshnitharwal@gmail.com

with nano-solid particle such as Cu, Ag, Au, Fe, Hg, CuO, Al, SiC, Al_2O_3 etc. White [1] described the viscous fluid flow earlier in 1991. Buongiorno [2] investigated the nanofluid model with Brownian diffusion and thermophoresis slip. These properties are used to examine the heat transfer efficiency. Suction/injection effects of uniform forced convection past a wedge were studied by Yih [3]. Tiwari and Das [4] examined effects of heat transfer in two-sided lid-driven differentially heated square cavity with nanofluid model.

Falkner and Skan [5] established approximate results concerning the behavior of viscous fluid past a wedge. Yacub et al. [6] studied the problem of Falkner–Skan flow in nanofluids with static or moving wedge. Khan et al. [7–8] also investigated the effects of nanofluids with moving or static wedge. Zheng et al. [9–10] investigated the MHD flow and effects of heat transfer with temperature jump and slip over a porous stretching surface. After that they extended their problem and examined the same model in the presence of nano-particles.

Muhaimin et al. [11] studied thermophoresis and chemical reaction effects on magnetohydrodynamic mixed convection flow with temperature dependent viscosity over a porous wedge. Non-similar solutions for mixed convection along a wedge saturated in a porous medium embedded by a non-Newtonian nanofluid examined by Chamkha et al. [12], Kandasamy et al. [13] and Alam et al. [14] studied the porous medium phenomenon past a wedge in the presence of nanoparticles and viscous fluid, respectively.

Yih [15] presented the force convection flow past a non-isothermal wedge and examined the effects of heat transfer in the presence of magnetic field. Bhargava et al. [16] investigated the non-Newtonian nanofluid flow in the presence of magnetic field over a permeable stretching sheet with velocity slip and heat source. Using finite element method to find out the better results of heat transfer. Several authors such as Abolbashari et al. [17], Hayat et al. 18], Jain and Choudhary [19], Jain and Bohra [20], Chauhan and Jain [21–22], Khan et al. [23], Raju and Sandeep [24] etc., have investigated the magnetohydrodynamics phenomenon for boundary layer flow.

The impact of mixed convection on boundary layer flow with silver and copper water nanofluids is studied by Hayat et al. [25]. They analyzed the comparative study between Ag-water nanofluid and Cu-water nanofluid. Rashidi et al. [26] investigated MHD mixed convection nanofluid flow in a channel. The effects of melting conditions in Falkner–Skan flow past a wedge of second grade nanofluid were investigated by Hayat et al. [27–28]. Recently, Pal and Mandal [29] described the double diffusive effects of MHD nanofluids over a non-linear stretching/shrinking sheet with thermal radiation properties.

In the present paper, a comparative study of Cu-water nanofluid and Al_2O_3-water nanofluid and pure water in the presence of non-linear magnetic field and porous medium over a moving or static wedge with mixed convection effect and the effects of temperature jump has been done. The influence of diverse pertinent parameters on velocity profile and temperature profile are studied through graphically and tabular forms. To our best knowledge, no such work has been done yet.

2. Mathematical formulation

Consider a non-linear MHD boundary layer incompressible nanofluid over a moving and static wedge with porous medium in the presence of viscous dissipation. The temperature jump is also taken into consideration. The coordinates system such as x-axis is parallel to the wedge surface and y-axis is taken normal to it. We have assumed that the free stream velocity is $u_e(x) = U_\infty x^m$ and the moving wedge velocity is $u_w(x) = U_w x^m$, where U_∞, U_w and m are constants. Table 1 shows the thermo-physical properties of the nanofluids.

Table 1. Thermo-physical properties of nanofluids

Fluids	ρ (kg m^{-3})	c_p (J kg^{-1} K^{-1})	k (Wm^{-1}K^{-1})	$\beta \times 10^5$ (K^{-1})
H$_2$O (pure water)	997.1	4179	0.613	21
Cu (copper)	8933	385	401	1.67
Al$_2$O$_3$ (alumina)	3970	765	40	0.85

The Boussinesq boundary layer approximations along with suitable boundary conditions are given as follows (see [6], [7]):

$$\frac{\partial u}{\partial x} + \frac{\partial v}{\partial y} = 0 \,, \tag{1}$$

$$u\frac{\partial u}{\partial x} + v\frac{\partial v}{\partial y} = u_e \frac{\mathrm{d}u_e}{\mathrm{d}x} + v_{nf}\frac{\partial^2 u}{\partial y^2} + \frac{(\beta\rho)_{nf}}{\rho_{nf}} g(T - T_\infty) \sin \Omega -$$

$$- \frac{\sigma_{nf} B(x)^2}{\rho_{nf}}(u - u_e) - \frac{v_{nf}}{k}(u - u_e) \,, \tag{2}$$

$$(\rho c_p)_{nf}\left(u\frac{\partial T}{\partial x} + v\frac{\partial T}{\partial y}\right) = k_{nf}\frac{\partial^2 T}{\partial y^2} + \mu_{nf}\left(\frac{\partial u}{\partial y}\right)^2 \,. \tag{3}$$

The corresponding boundary conditions for above approximations are:
(i) Static wedge:

$$u = 0, \ v = 0, \ T = T_w + l_1\frac{\partial T}{\partial y} \ \text{at} \ y = 0 \,,$$

$$u = u_e(x), \ T = T_w \ \text{as} \ y \to \infty \,.$$

(ii) Moving wedge:

$$u = u_w(x), \ v = 0, \ T = T_w + l_1\frac{\partial T}{\partial y} \ \text{at} \ y = 0 \,,$$

$$u = u_e(x), \ T = T_w \ \text{as} \ y \to \infty \,. \tag{4}$$

In the above equations (1)–(4), u and v are the velocity components along the x and y directions, respectively. T and T_w are the temperature of the fluid and wall temperature, respectively. T_∞ is the temperature far away from the surface of the wedge. Symbols v_{nf}, ρ_{nf}, μ_{nf} and σ_{nf} are the kinematic viscosity, density, dynamic viscosity and electrical conductivity of the nanofluid. Quantity $B(x) = B_0 x^{(m-1)/2}$ is the magnetic field of the fluid, where B_0 is the magnetic flux density, $(\rho c_p)_{nf}$ is the heat capacitance of nanofluid, k_{nf} is the effective thermal conductivity of the nanofluid, $(\beta\rho)_{nf}$ is the volumetric thermal expansion coefficient, g is the gravitational acceleration, Ω is the total angle of moving wedge, l_1 is a constant and k is the permeability of porous medium.

The nanofluid constant are as follows: (see [6], [7])

$$\rho_{nf} = (1 - \phi)\rho_f + \phi\rho_s, \ \ (\rho_{cp})_{nf} = (1 - \phi)(\rho_{cp})_f + \phi(\rho_{cp})_s,$$

$$(\beta\rho)_{nf} = (1 - \phi)(\beta\rho)_f + \phi(\beta\rho)_s,$$

$$\frac{k_{nf}}{k_f} = \left(\frac{k_s + (n-1)k_f - \phi(n-1)(k_f - k_s)}{k_s + (n-1)k_f + (n-1)\phi(k_f - k_s)}\right), \ \mu_{nf} = \frac{\mu_f}{(1-\phi)^{2.5}}, \tag{5}$$

where n denotes the nanoparticle shape and ϕ is the volume fraction of the nanoparticle. The subscripts f and s denote the fluid and solid properties correspondingly.

Introduce the similarity transformation

$$\psi(x,y) = \sqrt{\frac{2v_f x u_e(x)}{m+1}} f(\eta), \ \eta(x,y) = \sqrt{\frac{(m+1)u_e(x)}{2v_f x}} y, \ \theta(\eta) = \frac{T - T_\infty}{T_w - T_\infty}. \tag{6}$$

Here, ψ is the stream function, which satisfy (1) identically. It is defined as

$$u = \frac{\partial\psi}{\partial y}, \ v = -\frac{\partial\psi}{\partial x}. \tag{7}$$

Substituting (5), (6) and (7) into (2)–(4), we obtain

$$f''' + ABff'' + AB(1 - f'^2)\lambda - AM^2(f' - 1) - K(f' - 1) + AC\lambda_T \sin\Omega = 0, \tag{8}$$

$$\theta'' + \frac{E\,Pr}{D}f\theta' + \frac{Pr}{AD}Ec f''^2 = 0. \tag{9}$$

The boundary conditions for considered flow are
(i) static wedge:

$$f(0) = 0, \ f'(0) = 0, \ \theta(0) = 1 + \delta\theta'(0),$$

$$f'(\infty) = 1, \ \theta(\infty) = 0. \tag{10}$$

(ii) moving wedge:

$$f(0) = 0, \ f'(0) = \gamma, \ \theta(0) = 1 + \delta\theta'(0),$$

$$f'(\infty) = 1, \ \theta(\infty) = 0. \tag{11}$$

In equations (8)–(11), the prime signifies the differentiation with respect to η, $\lambda = \frac{2m}{m+1}$ is the Hartree pressure gradient parameter, $M^2 = \frac{2\sigma_{\mathrm{nf}}B_0^2}{\rho_{\mathrm{f}}U_\infty(m+1)}$ is the magnetic field parameter, $K = \frac{2v_{\mathrm{f}}x}{ku_{\mathrm{e}}(m+1)}$ is the porous medium parameter, $\gamma = \frac{U_{\mathrm{w}}}{U_\infty}$ is the moving wedge parameter, $\mathrm{Re}_x = \frac{xu_{\mathrm{e}}}{v_{\mathrm{f}}}$ is the local Reynolds number, $\mathrm{Gr}_x = \frac{2g\beta_{\mathrm{f}}(T_{\mathrm{w}}-T_\infty)x^3}{v_{\mathrm{f}}^2(m+1)}$ is the local Grashof number, $\lambda_T = \pm\frac{\mathrm{Gr}_x}{\mathrm{Re}_x^2}$ is the thermal buoyancy parameter ($\lambda_T > 0$ for assisting flow and $\lambda_T < 0$ for opposing flow), $\mathrm{Pr} = \frac{u_{\mathrm{f}}c_{\mathrm{pf}}}{k_{\mathrm{f}}}$ is the Prandtl number, $\mathrm{Ec} = \frac{u_{\mathrm{e}}^2}{c_{\mathrm{pf}}(T_{\mathrm{w}}-T_\infty)}$ is the Eckert number and $\delta = l_1\sqrt{\frac{(m+1)u_{\mathrm{e}}}{2v_{\mathrm{f}}x}}$ is the temperature jump parameter. Also we get $A = \frac{1}{(1-\phi)^{2.5}}$, $B = (1-\phi) + \frac{\rho_{\mathrm{s}}}{\rho_{\mathrm{f}}}\phi$, $C = (1-\phi) + \frac{(\rho\beta)_{\mathrm{s}}}{(\rho\beta)_{\mathrm{f}}}\phi$, $D = \frac{k_{\mathrm{nf}}}{k_{\mathrm{f}}}$ and $E = (1-\phi) + \frac{(\rho c_{\mathrm{ps}})_{\mathrm{s}}}{(\rho c_{\mathrm{pf}})_{rmf}}\phi$.

The skin friction coefficient Cf_{x}, local Nusselt number Nu_x and local Sherwood number Sh_x are as follows (see [17], [25]):

$$Cf_x = \frac{\tau_{\mathrm{w}}}{\rho_{\mathrm{f}}u_{\mathrm{e}}^2}, \mathrm{Nu}_x = \frac{xq_{\mathrm{w}}}{k_{\mathrm{f}}(T_{\mathrm{w}}-T_\infty)}. \tag{12}$$

Here τ_{w} and q_{w} are the wall skin friction and wall heat flux, respectively, defined as

$$\tau_{\mathrm{w}} = \mu_{\mathrm{f}}\left(\frac{\partial u}{\partial y}\right)_{y=0}, \ q_{\mathrm{w}} = -k_{\mathrm{nf}}\left(\frac{\partial T}{\partial y}\right)_{y=0},$$

$$(\mathrm{Re}_x)^{1/2}Cf_x\sqrt{\frac{2}{m+1}} = \frac{1}{(1-\phi)^{2.5}}f''(0), \ (\mathrm{Re}_x)^{-1/2}\mathrm{Nu}_x\sqrt{\frac{2}{m+1}} = -\frac{k_{\mathrm{nf}}}{k_{\mathrm{f}}}\theta'(0).$$

3. Method of solution

The system of equations (8)–(9) is solved by the Runge-Kutta fourth order method with shooting technique using MATLAB software. We have converted boundary value problem into initial value problem and then these equations are rewritten into a system of first-order differential equations such as

$$f = f(1), \ f' = f(2), \ f'' = f(3), \theta = f(4), \ \theta' = f(5),$$

$$f'(3) = K\left[f(2) - 1\right] - ABf(1)f(3) - AB\left[1 - f^2(2)\right]\lambda + AM^2\left[f(2) - 1\right] - AC\lambda_T\sin\Omega,$$

$$f'(5) = -\frac{E\,\mathrm{Pr}}{D}f(1)f(5) - \frac{\mathrm{Pr}}{AD}\mathrm{Ec}f^2(3)$$

subject to boundary conditions

$$f(1) = 0, \ f(2) = \gamma, \ f(3) = g_1, \ f(4) = 1 + \delta f(5), \ f(5) = g_2,$$

where g_1 and g_2 are the initial estimations for $f''(0)$ and $\theta'(0)$, respectively. First we considered a finite domain for η. In this study we have taken $\eta_\infty = 8$. And then find some initial guesses using hit and trial method. We have used the Secant method to find better approximations.

4. Results and discussion

The present study is aimed to examine the comparative analysis of Newtonian fluid (water), Cu-water nanofluid and Al_2O_3-water nanofluid in the presence of non-linear magnetic field and porous medium over a moving or static wedge with mixed convection effects. The effects of temperature jump in heat transfer phenomenon has also been considered.

Table 2 shows the comparison between the present results and the existing results. It can be seen that results obtained are excellent in agreement with the existing results given by White [1], Yih [3], Yacub et al. [6], Khan and Pop [7] and Khan et al. [8].

Table 2. Comparison of coefficient of local skin friction $f''(0)$ for different values of m with $\mathrm{Pr} = 0$, $M^2 = K = \lambda_\mathrm{T} = \gamma = \mathrm{Ec} = 0$ and $\phi = 0$ where $\lambda = 2m/(m+1)$

m	White [1]	Yih [3]	Yacob et al. [6]	Khan and Pop [7]	Khan et al. [8]	Present result
0	0.4696	0.4696	0.4696	0.4696	0.4699	0.4696
1/11	0.6550	0.6550	0.6550	0.6550	0.6574	0.6550
1/5	0.8021	0.8021	0.8021	0.8021	0.8045	0.8021
1/3	0.9277	0.9276	0.9276	0.9277	0.9298	0.9277
1/2	1.0389	-	-	1.0389	1.0394	1.0389
1	1.2326	-	1.2326	1.2326	1.2358	1.2326

Figures 1 and 2 demonstrate the effects of moving wedge parameter γ on velocity profile and temperature profile for Al_2O_3-water and Newtonian model (pure water). We know that $\gamma < 0$ displays when the wedge is moving in the direction of the fluid flow. $\gamma = 0$ represents that wedge is stationary and $\gamma > 0$ exhibits when wedge is moving with the fluid. Figure 1 depicts that velocity profile increases when the moving wedge parameter enhances. It is noted that velocity profile of Al_2O_3-water is little bit higher than that of the $Cu - water$ nanofluid for $\gamma > 0$, while exactly opposite result arise for $\gamma < 0$. It is also observed that for Newtonian fluid (pure water) the velocity profile is lower, compared to metal and metal oxide nanofluids. This is due to the fact that nanoparticles increases the efficiency of the fluid. Figure 2 depicts that when we increase moving wedge parameter, the temperature profile

shows reduction for $\gamma < 0$, however for $\gamma > 0$, the temperature profile increases with moving wedge parameter, hence the thermal boundary layer thickness shows enhancement for both the nanofluids and pure water.
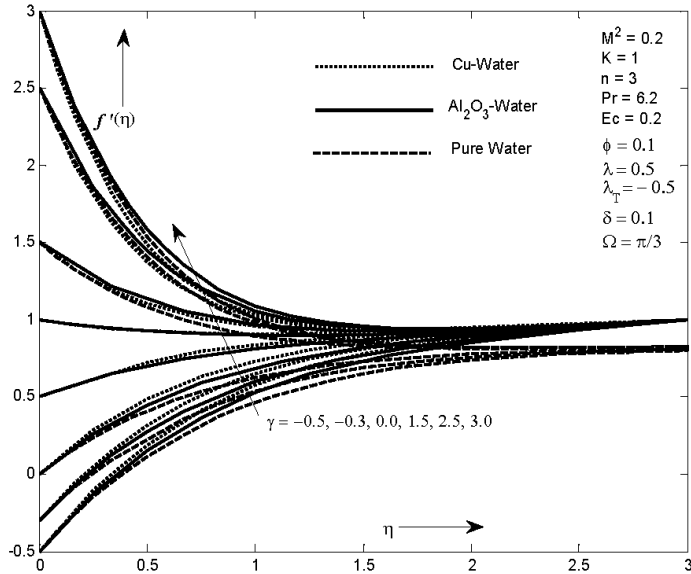
Fig. 1. Velocity profiles for various values of moving wedge parameter γ

Fig. 2. Temperature profiles for various values of moving wedge parameter γ

Figures 3 and 4 show the effects of magnetic field parameter M^2 on velocity profile and temperature profile for Al$_2$O$_3$-water, $Cu - water$ and pure water.
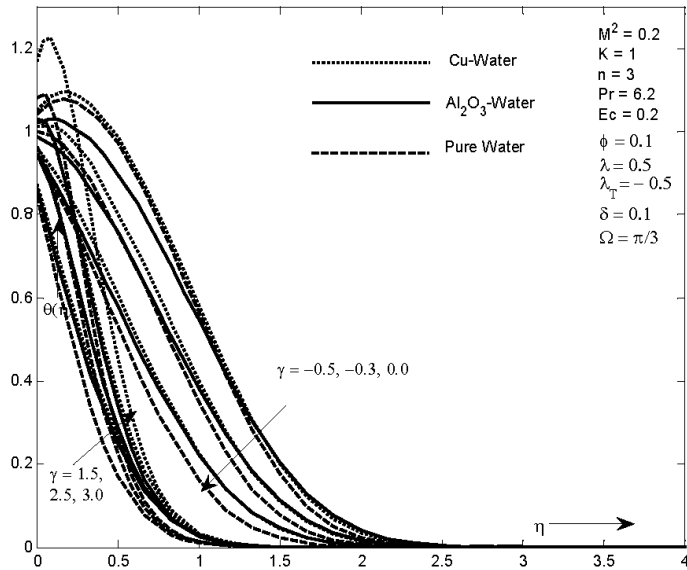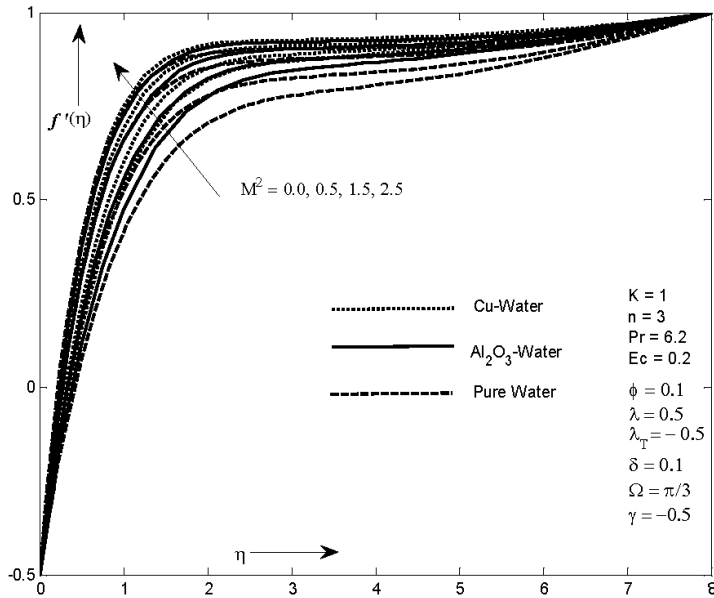

Fig. 3. Velocity profiles for various values of magnetic field parameter M^2
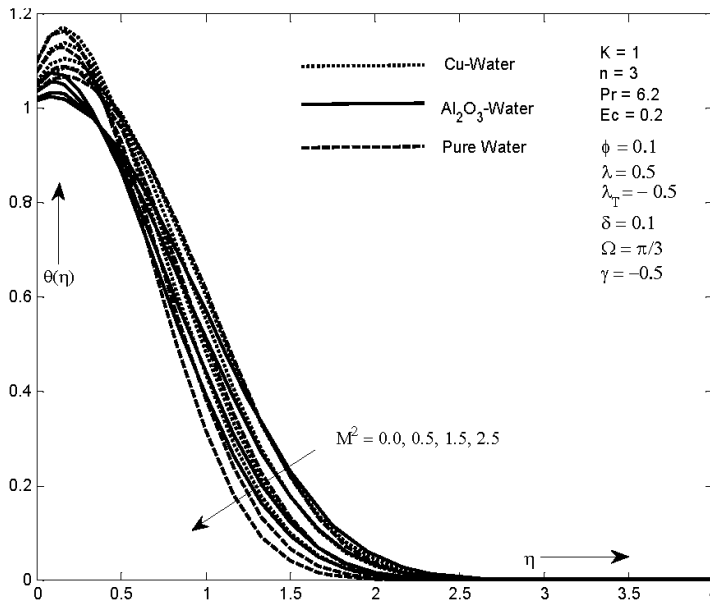
Fig. 4. Temperature profiles for various values of magnetic field parameter M^2

It is clearly seen that magnetic field parameter is responsible for increasing velocity profile, however, it decreases the boundary layer thickness. The velocity of Cu-water nanofluid in higher than Al_2O_3-water nanofluid, hence Cu-water nanofluid is more effective when we increase magnetic parameter. Also it is detected that the efficiency of pure water is lower than both the nanofluids. As we know that reduction in boundary layer thickness is obtained due to the Lorentz force, which works against the fluid flow. In Fig. 4, increasing values of magnetic field parameter causes reduction in temperature profile and thermal boundary layer thickness, too.

Figures 5 and 6 depict the effects of porous medium parameter K on both profiles for pure water, Cu-water nanofluid and Al_2O_3-water nanofluid. For every increasing value of porous medium parameter K the velocity profile increases, while temperature profile shows reduction for both nanofluids and pure water. Porosity is a measure of empty space, so when we increase porosity parameters, it naturally enhanced the velocity of the fluid flow, and reduces the fluid temperature. In both figures the velocity profile and temperature profile are lower for pure water, when we compare it with nanofluids.
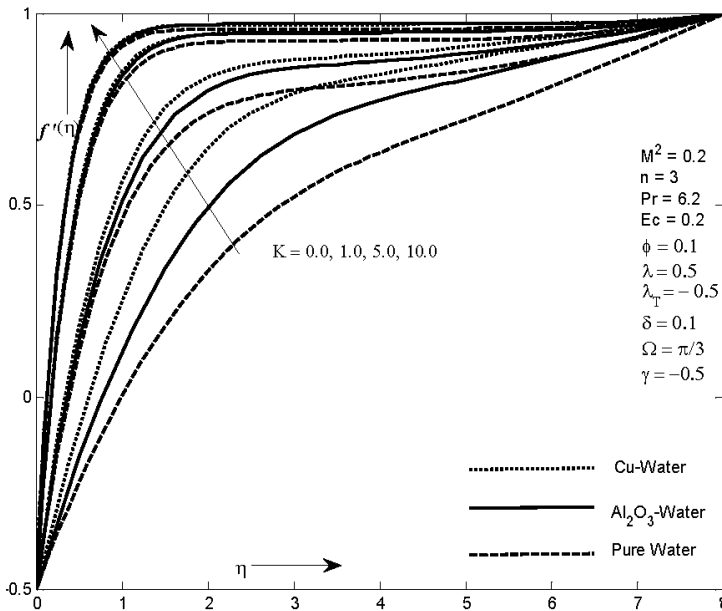
Fig. 5. Velocity profiles for porous parameter K

The influence of wedge angle Ω on velocity profile and temperature profile for pure water, Cu-water nanofluid and Al_2O_3-water nanofluid are shown in Figs. 7 and 8, respectively. It is observed from Fig. 7 that the velocity profile enhances with the wedge angle Ω, however, the boundary layer thickness decreases, while the boost of wedge angle Ω causes increase in temperature profile. It is noted that in temperature profile near the wall the temperature of Cu-water nanofluid is higher than that of Al_2O_3-water nanofluid.
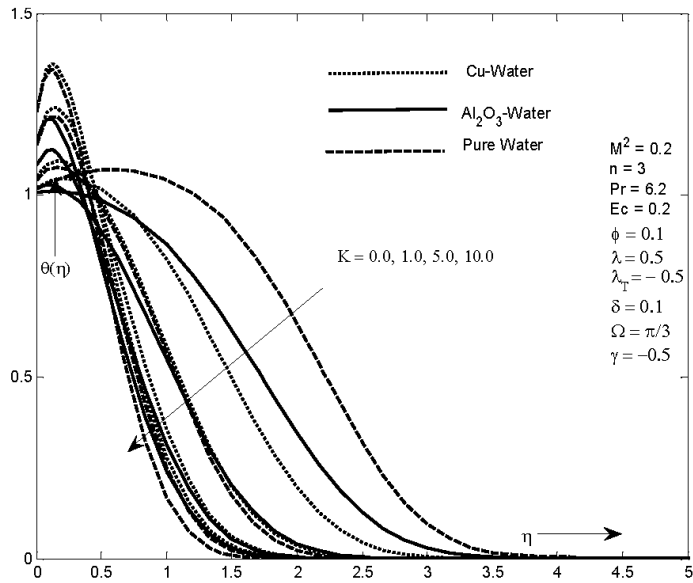
Fig. 6. Temperature profiles for porous parameter K

Figures 9–10 depict the effects of Hartree pressure gradient parameter λ on velocity profile and temperature profile illustrated, respectively.
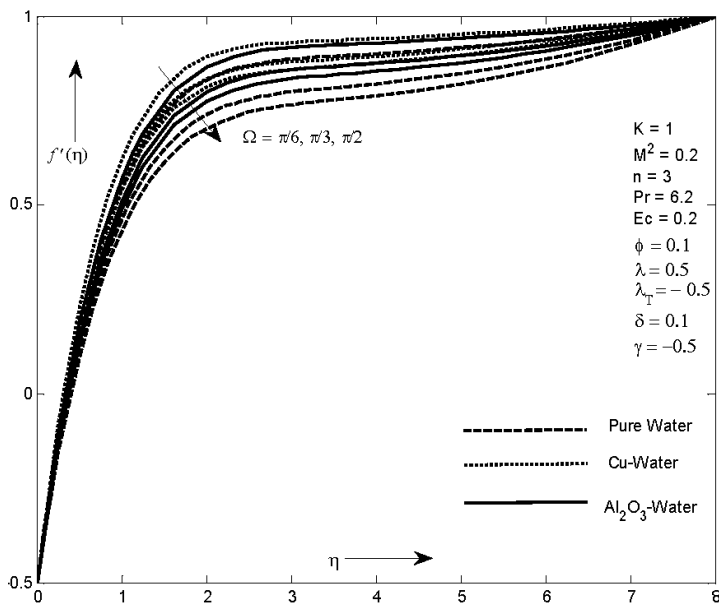
Fig. 7. Velocity profiles for wedge angle Ω
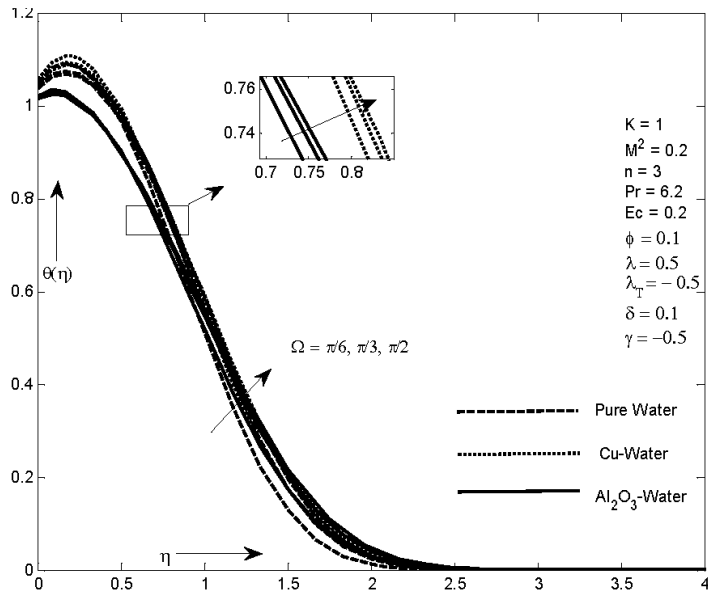
Fig. 8. Temperature profiles for wedge angle Ω
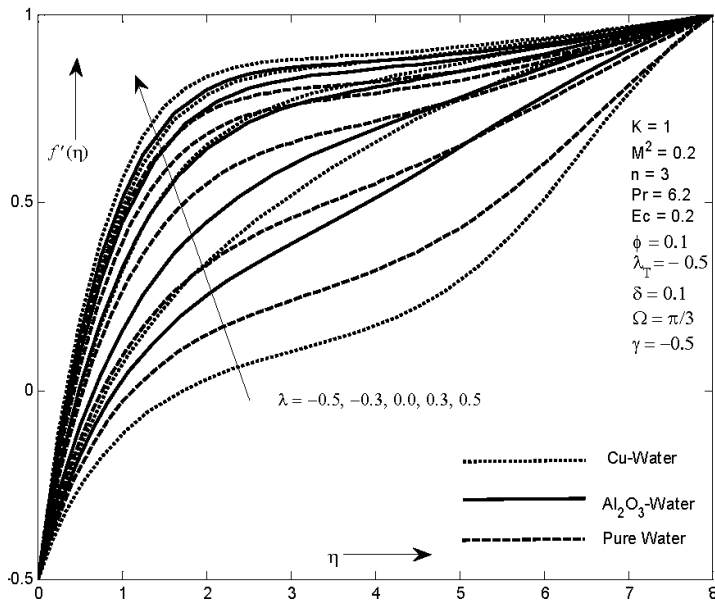
Fig. 9. Velocity profiles for Hartree pressure gradient parameter λ

We know that $\lambda > 0$ demonstrates the decreasing pressure, $\lambda = 0$ signifies flat plate case, while $\lambda < 0$ shows enhancing pressure state. It is observed that the velocity profile increases by the raise of Hartree pressure gradient parameter λ, while

temperature profiles decreases. Again it is found that the temperature and velocity profile is more for Cu-water nanofluid in comparison with Al_2O_3-water nanofluid and pure water.
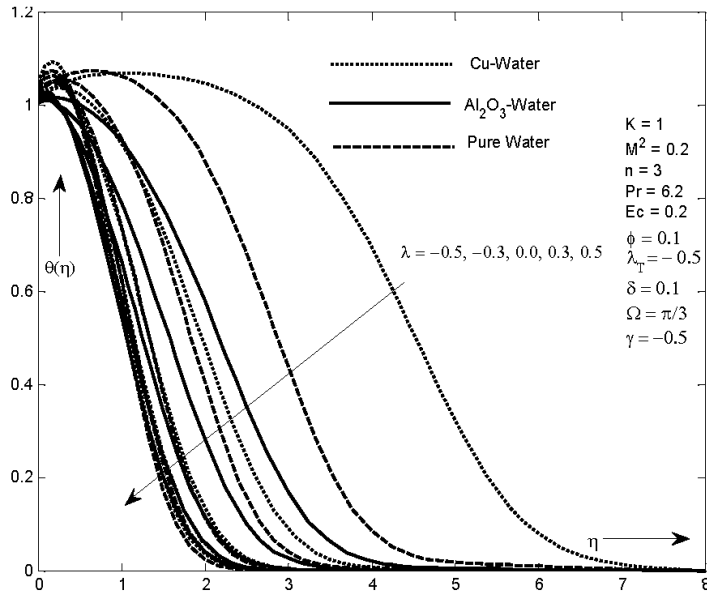
Fig. 10. Temperature profiles for Hartree pressure gradient parameter λ
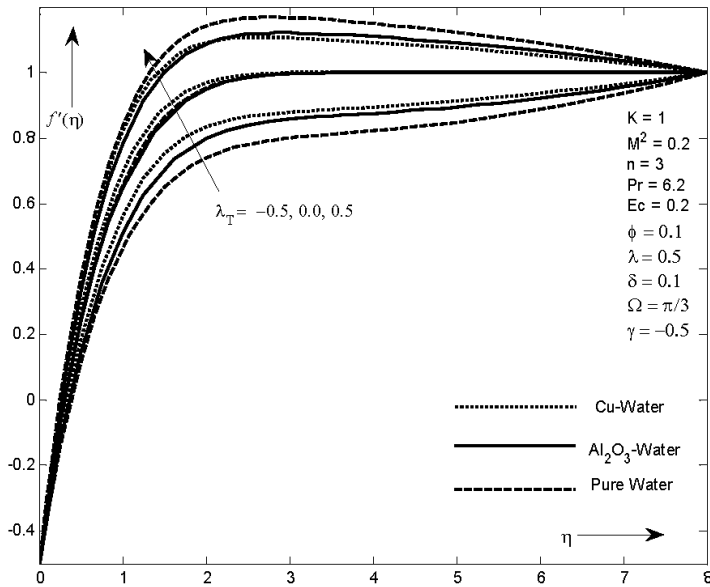
Fig. 11. Velocity profiles for thermal buoyancy parameter λ_T

Figures 11–12 show the effects of thermal buoyancy parameter λ_T on velocity and temperature profiles for both the nanofluids and pure water. We have observed that for assisting flow ($\lambda_T > 0$) the velocity profile enhanced while for opposing flow ($\lambda_T < 0$) it shows reduction in velocity. Physically, it is well known that buoyancy force is stronger for assisting flow, while weaker for opposing flow. In the temperature profile, the thickness of thermal boundary layer decreases with thermal buoyancy parameter. It is due to the fact that buoyancy parameter enhanced the rate of heat transfer, hence this act causes reduction in thermal boundary layer thickness. Also noted that the velocity profile and temperature profile are higher for Cu-water in comparison to Al_2O_3 water and pure water.
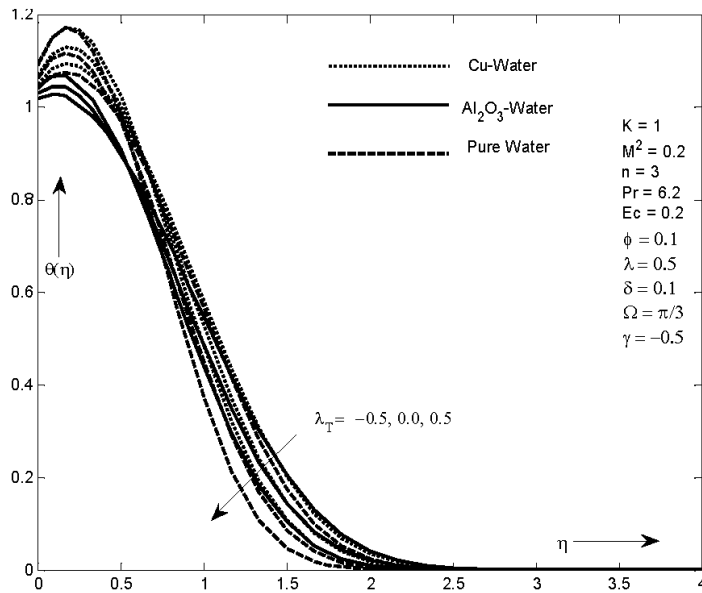
Fig. 12. Temperature profiles for thermal buoyancy parameter λ_T

Figures 13–14 depicts the effects of volume fraction of nanoparticle ϕ on velocity profile and temperature profile in the presence of Al_2O_3-water and Cu-water nanofluids. It is noticed that velocity profile and temperature profile increase as we increase volume fraction of nanoparticles. When the volume fraction of Al_2O_3 water and Cu-water nanofluid enhanced, the thermal conductivity of both the nanofluids are increased and causes enhancement of thermal boundary layer thickness. Figure 15 demonstrates the effects of temperature jump on temperature profile for both the nanofluids and pure water. It can be seen that thermal boundary layer thickness increases as we enhance temperature jump. The presence of nanoparticles enhances the thermal conductivity of the fluid, hence, the temperature profile is higher for nanofluids in comparison to pure water. It is also observed that Cu-water nanofluid's temperature profile is higher than that of Al_2O_3 water.

Figure 16 shows the influence of Eckert number Ec on temperature profile. Because the viscous dissipation produces heat between the fluid particles, the fluid

temperature enhancing also Eckert number generates heat in the fluid due to frictional heating.
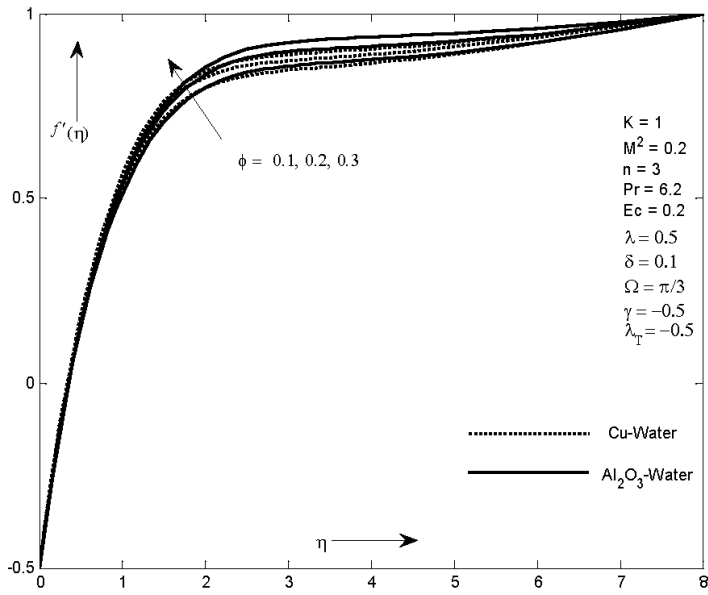
Fig. 13. Velocity profiles for volume fraction of nanoparticles ϕ
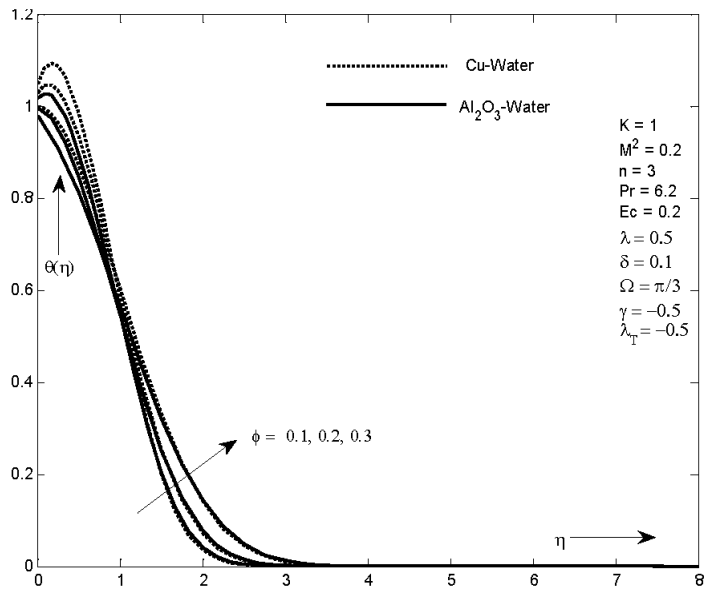
Fig. 14. Temperature profiles for volume fraction of nanoparticles ϕ
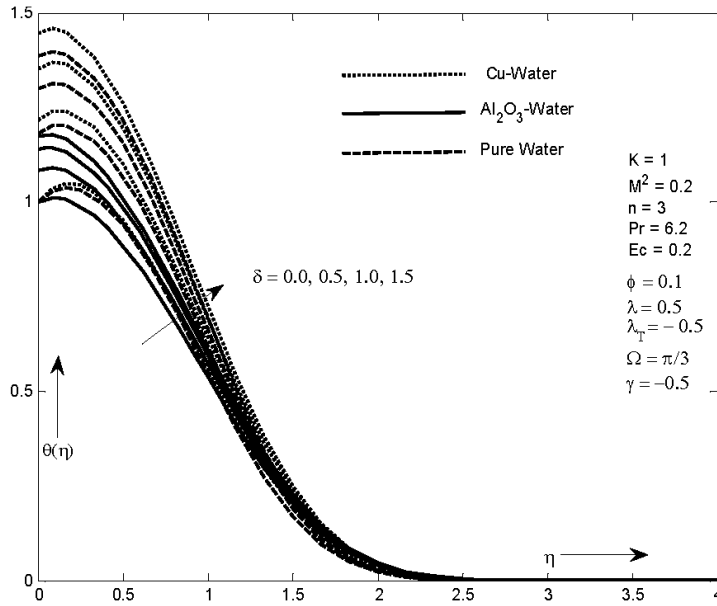
Fig. 15. Temperature profiles for thermal jump parameter δ
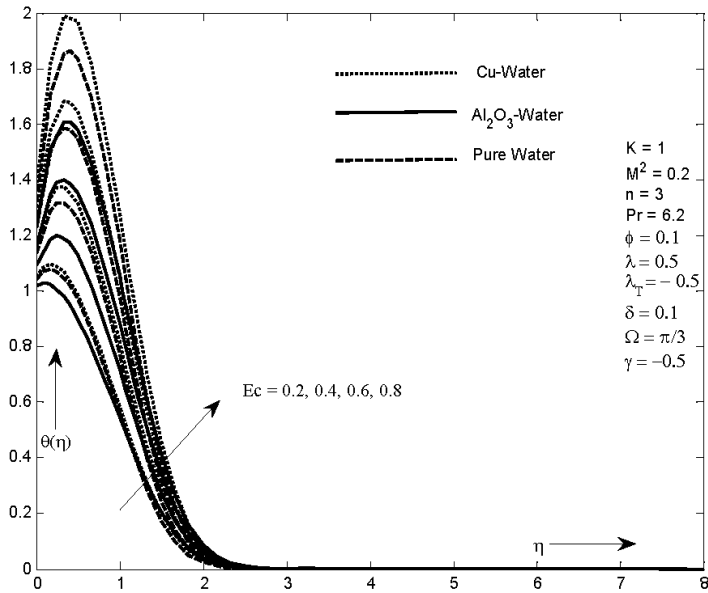
Fig. 16. Temperature profiles for Eckert number Ec

Tables 3 and 4 summarize the numerical results of skin friction coefficient and Nusselt number for various parameters. These tables also show the comparative study of Cu-water nanofluid and Al_2O_3 water nanofluid. After looking at these tables

we can say that Cu-water nanofluid is more effective than Al_2O_3 water nanofluid.

Table 3. Numerical results of skin friction coefficient for various values of ϕ, λ, K, M^2, λ_T, δ, γ, and Ec when $\Omega = 60°$ and Pr $= 6.2$

ϕ	λ	K	M^2	λ_T	δ	γ	Ec	$\frac{f''(0)}{(1-\phi)^{2.5}}$ Cu-water	$\frac{f''(0)}{(1-\phi)^{2.5}}$ Al_2O_3 water
0.1	0.5	1	0.2	–0.5	0.1	–0.5	0.2	2.3138	2.1785
0.2								3.2441	2.9784
0.3								4.5546	4.1540
	–0.3							1.1795	1.3594
	0.0							1.6675	1.7002
		10						6.2984	6.2481
		100						19.5605	19.5442
			0.4					2.4373	2.3087
			0.8					2.6671	2.5496
				–0.3				2.4494	2.3117
				0.3				2.8466	2.7035
					0.2			2.3138	2.1785
					0.3			2.3138	2.1785
						–0.3		2.0862	1.9393
						0.3		1.1618	1.0414
							0.4	2.3138	2.1785
							0.6	2.3138	2.1785

5. Conclusion

In this study we have analyzed heat transfer effects of non-linear MHD boundary layer of incompressible nanofluid over a moving and static wedge with porous medium in the presence of temperature jump and viscous dissipation. Also we performed a comparative study between pure water, Cu-water nanofluid and Al_2O_3 water nanofluid. The significant finding for the current study is given below:

1. Velocity profile rises with magnetic field parameter M^2, porous medium parameter K, Hartree pressure gradient parameter λ ($\lambda > 0$), thermal buoyancy parameter λ_T ($\lambda_T > 0$), wedge angle Ω, moving wedge parameter γ ($\gamma > 0$) and volume fraction parameter ϕ, while it reduces with the negative values of λ, λ_T and γ.

2. The temperature profile shows enhancement for every increasing values of

wedge angle Ω, moving wedge parameter γ ($\gamma > 0$), Eckert number Ec, temperature jump parameter δ and volume fraction parameter ϕ, but on other hand the thermal boundary layer thickness decreases as we increase magnetic field parameter M^2, porous parameter K, Hartree pressure gradient parameter λ and thermal buoyancy parameter λ_T.

3. It is also noted that efficiency of Cu-water nanofluid is higher than Al_2O_3 water nanofluid in each case of velocity profile and temperature profile.

Table 4. Numerical results of Nusselt number for various values of ϕ, λ, K, M^2, λ_T, δ, γ, and Ec when $\Omega = 60°$ and Pr = 6.2

ϕ	λ	K	M^2	λ_T	δ	γ	Ec	$-\frac{k_{nf}}{k_f}\theta'(0)$ Cu-water	$-\frac{k_{nf}}{k_f}\theta'(0)$ Al_2O_3 water
0.1	0.5	1	0.2	−0.5	0.1	−0.5	0.2	−0.7836	−0.2970
0.2								−0.7180	0.0549
0.3								−0.0823	0.7023
	−0.3							−0.2679	−0.1156
	0.0							−0.4122	−0.1537
		10						−3.4903	−2.1359
		100						−14.2094	−9.7939
			0.4					−0.8504	−0.3373
			0.8					−0.9801	−0.41804
				−0.3				−0.8914	−0.35664
				0.3				−1.2518	−0.57124
					0.2			−0.7432	−0.28254
					0.3			−0.7069	−0.2694
						−0.3		−0.1956	0.1758
						0.3		1.2372	1.3166
							0.4	−2.3792	−1.3475
							0.6	−3.9749	−2.3980

References

[1] F. M. WHITE: *Viscous fluid flow.* McGraw-Hill, New York, NY, USA (1991).

[2] J. BUONGIORNO: *Convective transport in nanofluids.* Journal of Heat Transfer *128* (2005), No. 3, 240–250.

[3] K. A. YIH: *Uniform suction/blowing effect on forced convection about a wedge: Uniform heat flux.* Acta Mechanica *128* (1998), Nos. 3–4, 173–181.

[4] R. K. TIWARI, M. K. DAS: *Heat transfer augmentation in two-sided lid-driven differentially heated square cavity utilizing nanofluids.* International Journal of Heat and Mass Transfer *50* (2007), No. 9, 2002–2018.

[5] V. M. FALKNER, S. W. SKAN: *Some approximate solutions of the boundary layer equations.* Philosophical Magazine *12* (1931), No. 7, 865–896.

[6] N. A. YACOB, A. ISHAK, I. POP: *Falkner–Skan problem for a static or moving wedge in nanofluids.* International Journal of Thermal Sciences *50* (2011), No. 2, 133–139.

[7] W. A. KHAN, I. POP: *Boundary layer flow past a wedge moving in a nanofluid.* Mathematical Problems in Engineering (2013), Article ID No. 637285, 1–7.

[8] M. S. KHAN, I. KARIM, M. S. ISLAM, M. WAHIDUZZAMAN: *MHD boundary layer radiative, heat generating and chemical reacting flow past a wedge moving in a nanofluid.* Nano Convergence *1* (2014), No. 1, 1–20.

[9] L. ZHENG, J. NIU, X. ZHANG, Y. GAO: *MHD flow and heat transfer over a porous shrinking surface with velocity slip and temperature jump.* Mathematical and Computer Modelling *56* (2012), Nos. 5–6, 133–144.

[10] L. ZHENG, C. ZHANG, X. ZHANG, J. ZHANG: *Flow and radiation heat transfer of a nanofluid over a stretching sheet with velocity slip and temperature jump in porous medium.* Journal of the Franklin Institute *350*, (2013), No. 5, 990–1007.

[11] I. MUHAIMIN, R. KANDASAMY, A. B. KHAMIS, R. ROSLAN: *Effect of thermophoresis particle deposition and chemical reaction on unsteady MHD mixed convective flow over a porous wedge in the presence of temperature-dependent viscosity.* Nuclear Engineering and Design *261* (2013), 95–106.

[12] A. J. CHAMKHA, M. RASHAD, R. S. R. GORLA: *Non-similar solutions for mixed convection along a wedge embedded in a porous medium saturated by a non-Newtonian nanofluid.* International Journal of Numerical Methods for Heat & Fluid Flow *24* (2014), No. 7, 1471–1486.

[13] R. KANDASAMY, I. MUHAIMIN, A. K. ROSMILA: *The performance evaluation of unsteady MHD non-Darcy nanofluid flow over a porous wedge due to renewable (solar) energy.* Renewable Energy *64* (2014), 1–9.

[14] M. S. ALAM, M. A. KHATUN, M. M. RAHMAN, K. VAJRAVELU: *Effects of variable fluid properties and thermophoresis on unsteady forced convective boundary layer flow along a permeable stretching/shrinking wedge with variable Prandtl and Schmidt numbers.* International Journal of Mechanical Sciences *105* (2016), 191–205.

[15] K. A. JIH: *MHD forced convection flow adjacent to a non-isothermal wedge.* International Communications in Heat and Mass Transfer *26* (1999), No. 6, 819–827.

[16] R. BHARGAVA, M. GOYAL: *MHD non-Newtonian nanofluid flow over a permeable stretching sheet with heat generation and velocity slip.* International Journal of Mathematical, Computational, Physical, Electrical and Computer Engineering *8* (2014), No. 6, 912–918.

[17] M. H. ABOLBASHARI, N. FREIDOONIMEHR, F. NAZARI, M. M. RASHIDI: *Entropy analysis for an unsteady MHD flow past a stretching permeable surface in nano-fluid.* Powder Technology *267* (2014), 256–267.

[18] T. HAYAT, M. IMTIAZ, A. ALSAEDI, M. A. KUTBI: *MHD three-dimensional flow of nanofluid with velocity slip and nonlinear thermal radiation.* Journal of Magnetism and Magnetic Materials *396* (2015), 31–37.

[19] S. JAIN, R. CHOUDHARY: *Effects of MHD on boundary layer flow in porous medium due to exponentially shrinking sheet with slip.* Procedia Engineering *127* (2015), 1203–1210.

[20] S. JAIN, S. BOHRA: *Radiation effects in flow through porous medium over a rotating disk with variable fluid properties.* Advances in Mathematical Physics (2016), Article ID No. 9671513, 1–12.

[21] [D. S. CHAUHAN, S. JAIN: *Steady flow and heat transfer of a viscous fluid through a circular naturally permeable tube surrounded by a porous material.* Journal of Rajasthan Academy of Physical Sciences *2* (2003), No. 1, 35–34.

[22] D. S. CHAUHAN, S. JAIN: *Steady flow between highly permeable rotating disks.* Indian Journal of Theoretical Physics *52* (2004), No. 1, 39–50.

[23] [W. A. KHAN, O. D. MAKINDE, Z. H. KHAN: *Non-aligned MHD stagnation point flow of variable viscosity nanofluids past a stretching sheet with radiative heat.* International Journal of Heat and Mass Transfer *96* (2016), 525–534.

[24] C. S. K. RAJU, N. SANDEEP: *Nonlinear radiative magnetohydrodynamic Falkner-Skan flow of Casson fluid over a wedge.* Alexandria Engineering Journal *55*, (2016), No. 3, 2045–2054.

[25] T. HAYAT, S. QAYYUM, M. IMTIAZ, A. ALSAEDI: *Comparative study of silver and copper water nanofluids with mixed convection and nonlinear thermal radiation.* International Journal of Heat and Mass Transfer *102* (2016), 723–732.

[26] M. M. RASHIDI, M. NASIRI, M. KHEZERLOO, N. LARAQI: *Numerical investigation of magnetic field effect on mixed convection heat transfer of nanofluid in a channel with sinusoidal walls.* Journal of Magnetism and Magnetic Materials *401* (2016), 159–168.

[27] T. HAYAT, A. SHAFIQ, M. IMTIAZ, A. ALSAEDI: *Impact of melting phenomenon in the Falkner–Skan wedge flow of second grade nanofluid: A revised model.* Journal of Molecular Liquids *215* (2016), 664–670.

[28] T. HAYAT, M. IMTIAZ, A. ALSAEDI: *Unsteady flow of nanofluid with double stratification and magnetohydrodynamics.* International Journal of Heat and Mass Transfer *92* (2016), 100–109.

[29] D. PAL, G. MANDAL: *Double diffusive magnetohydrodynamic heat and mass transfer of nanofluids over a nonlinear stretching/shrinking sheet with viscous-Ohmic dissipation and thermal radiation.* Propulsion and Power Research *6* (2017), No. 1, 58–69.

Carreau model for blood flow through a tapered, stenosed artery: Analytical solution[1]

SUBRATA MUKHOPADHYAY[2], SWATI
MUKHOPADHYAY[3, 4]

Abstract. The aim of this article is to present the flow of blood through a narrow tapered axi-symmetric stenosed artery treating blood to be non-Newtonian. The non-Newtonian character of blood in small arteries at low rates of shear has been analyzed mathematically assuming that blood behaves as a Carreau fluid which is a generalized Newtonian fluid. The flow of blood in a stenosed artery has been considered to be steady, laminar, incompressible and axi-symmetric. The effects of tapering and height of the stenosis on various significant characteristics of blood flow viz., axial velocity, wall shear stress and resistance to flow have been investigated in detail. It is shown that the wall shear stress and the resistance to flow increase with the increasing size of stenosis. The results are explained graphically.

Key words. Carreau fluid, tapered artery, stenosis, perturbation technique, wall shear stress, resistance to flow.

1. Introduction

Cardiovascular diseases, such as heart attack and stroke, are the major causes of mortality in the developed nations of the world. The formation of lesions, known as atherosclerosis or stenosis is the underlying cause of these diseases. The word atherosclerosis comes from the Greek words 'athero' means paste and 'sclerosis' means hardness. The common form of arterial stenosis is that caused by atheroma, a deposition of fats and fibrous tissues in the arterial wall. The inner wall of the blood vessels bulges inwards at some places due to deposition of plaques. Due to the formation of stenosis, the arterial lumen becomes typically narrowed and

---

[2]Department of Mathematics, Acharya P. C. Roy Govt. College, Siliguri, W.B., India

[3]Department of Mathematics, the University of Burdwan, Burdwan 0713104, W.B., India

[4]Corresponding author; email: `swati_bumath@yahoo.co.in`

stiff. Sometimes the arterial wall remodels itself by increasing its internal radius to accommodate a plaque without narrowing its lumen. But in most of the cases this is not possible. As a result, the occlusion prevents the supply of blood to the distal area. Plaques with calcium may sometime rupture and help to form blood clots or thrombus. Thus the smaller blood vessels become occluded, resulting interruption of blood supply to the distal bed. Plaques formed in coronary arteries can lead to heart attack and blood clots in the cerebral arteries can result in a stroke [1].

The exact reasons and mechanisms responsible for the initiation of atherosclerosis are not clearly known. But it has been established that the development of the disease is closely related with the locally irregular flow rates, high arterial wall shear stress etc. The flow behavior in a stenosed artery is completely different than that of a normal artery. Such type of disease is localized in the regions of irregular geometry. Moreover, the blood flow characteristics are altered significantly due to the formation of a mild stenosis. It may further influence the development of the disease and can also change the regional blood rheology in due course of time [2]. For early detection and prevention of the disease a major research work is going on through all parts of the world. The flow description through a stenosed vessel can help in early detection of the diseases even before the disease becomes clinically relevant.

For complete understanding of the stenosis build up one needs to know the haemodynamic behavior of the streaming blood from physiological point of view. In most of the investigations the researchers model blood treating it as Newtonian fluid. Blood behaves like a Newtonian fluid when it flows through larger arteries at high shear rates [3], whereas it behaves like a non-Newtonian fluid when it flows through smaller arteries at low shear rates $\dot{\gamma} < 10$ /s [4]. To study the blood flow in stenosed arteries using Newtonian/non-Newtonian fluid models several experimental and theoretical research works have been done during the past few decades [5–8]. Most of the coronary arteries have the diameter less than 0.5 mm [9]. In most of these studies, the flow is considered in cylindrical pipes of uniform cross section. But it is well known fact that the blood vessels bifurcate at frequent intervals and the radius of the vessels varies with the distance [10]. Porenta et al. [11] pointed out that most of the blood vessels can be considered as long and narrow, having slowly tapering cones. Hence the effects of vessel tapering should be considered together with the non-Newtonian behavior of the streaming blood in arteries having small diameters. To the best of the authors knowledge, analytical solutions of blood flow treating blood as Carreau fluid through a tapered, stenosed artery have not yet been addressed in the open literature.

With the above motivation, an attempt is made in the present theoretical investigation in developing a mathematical model in order to study the significant characteristics of the non-Newtonian blood flow through a tapered narrow artery having a mild stenosis. Carreau fluid model has been taken to characterize the non-Newtonian behaviour of the streaming blood. As the existence and uniqueness as well as the stability characteristics of such flow problems have already been established, so the existence of the flow characterized by the Carreau fluid model has not been presented in this article. Analytical solutions of the governing equations have

been calculated using perturbation technique. The expressions for axial velocity, resistance to flow, wall shear stress and shear stress at the throat of the stenosis have been obtained. The behaviour of different types of tapered arteries has been explained graphically for different pertaining parameters involved in this study.

2. Formulation of the problem

2.1. Stenosis model

Let us consider a steady, laminar, incompressible, isothermal and axi-symmetric flow of blood in a narrow tapered artery with a mild axi-symmetric stenosis in its lumen. We assume that the segment of the artery under consideration is axi-symmetric and straight. Let us consider cylindrical polar coordinates (r, θ, z) such that $r = 0$ corresponds to the axis of the artery (for the arrangement see Fig. 1).
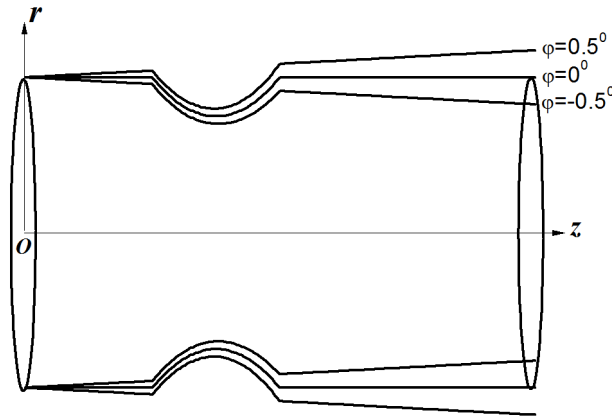
Fig. 1. Schematic diagram of stenosed and tapered artery

The geometry of the stenosed tapered arterial segment may be described as:

$$r_0(z) = \begin{cases} (R_0 + \xi z)\left[1 - \frac{\delta}{2R_0}\left\{1 + \cos\frac{\pi(z-a)}{b}\right\}\right], & a - b \leq z \leq a + b, \\ \\ (R_0 + \xi z), & 0 \leq z \leq a - b \text{ or } a + b \leq z \leq L, \end{cases} \quad (1)$$

where $r_0(z)$ and R_0 are the radii of the tapered artery at a distance z and at $z = 0$ respectively, ξ is the tapering parameter, $2b$ is the length of the stenosis, a and δ indicate the centre and height of the stenosis and L is the length of the arterial segment under consideration.

If φ is the tapering angle then $\xi = \tan\varphi$. For converging tapering $\varphi < 0$, for non-tapered artery $\varphi = 0$ and for diverging tapering $\varphi > 0$.

2.2. Governing equations

The equations governing the steady, laminar, incompressible blood flow are

$$\frac{\partial u}{\partial r} + \frac{u}{r} + \frac{\partial w}{\partial z} = 0 \,, \tag{2}$$

$$\rho \left(u \frac{\partial}{\partial r} + w \frac{\partial}{\partial z} \right) u = -\frac{\partial p}{\partial r} + \frac{1}{r} \frac{\partial}{\partial r} \left(r \tau_{rr} \right) + \frac{\partial}{\partial z} \left(\tau_{rz} \right) - \frac{\tau_{\theta\theta}}{r} \,, \tag{3}$$

$$\rho \left(u \frac{\partial}{\partial r} + w \frac{\partial}{\partial z} \right) w = -\frac{\partial p}{\partial z} + \frac{1}{r} \frac{\partial}{\partial r} \left(r \tau_{rz} \right) + \frac{\partial}{\partial z} \left(\tau_{zz} \right) \,, \tag{4}$$

where u and w are the velocities of the flowing blood along the radial and axial directions, respectively, p is the pressure and ρ is the density of blood, and τ's are the components of the stress tensor.

When the lumen radius is small, the radial velocity is negligibly small and can be neglected for a low Reynolds number flow [12]. In that case, equations (2), (3) and (4) reduce to

$$\frac{\partial w}{\partial z} = 0 \,, \tag{5}$$

$$\frac{\partial p}{\partial r} = 0 \,, \tag{6}$$

$$-\frac{\partial p}{\partial z} + \frac{1}{r} \frac{\partial}{\partial r} \left(r \tau_{rz} \right) = 0 \,. \tag{7}$$

Thus, in one-dimensional motion $w = w\left(r\right)$ and $p = p\left(z\right)$.

2.3. Constitutive equation

In this study, streaming blood has been regarded as a non-Newtonian fluid characterized by the Carreau model. The constitutive equation for such model is given by

$$\eta = \eta_\infty + \left(\eta_0 - \eta_\infty \right) \left(1 + \lambda^2 S \right)^{(m-1)/2} \,, \tag{8}$$

where η_0 and η_∞ are the zero and infinite shear rate viscosities, λ is the relaxation time, S is (–4) times the second invariant of the strain rate tensor and m is the power law index. Thus the shear stress is obtained as

$$\tau = -\eta\left(S\right)\dot{\gamma} = - \left[\eta_\infty + \left(\eta_0 - \eta_\infty \right) \left(1 + \lambda^2 S \right)^{(m-1)/2} \right] \dot{\gamma} \,. \tag{9}$$

For one dimensional flow

$$\dot{\gamma} = -\frac{\mathrm{d}w}{\mathrm{d}r} \,, \quad S = \dot{\gamma}^2 = \left(\frac{\mathrm{d}w}{\mathrm{d}r} \right)^2 \tag{10}$$

so that

$$\tau_{rz} = \left[\eta_\infty + (\eta_0 - \eta_\infty) \left\{ 1 + \left(\lambda \frac{\mathrm{d}w}{\mathrm{d}r} \right)^2 \right\}^{(m-1)/2} \right] \frac{\mathrm{d}w}{\mathrm{d}r}. \tag{11}$$

Assuming λ to be small, then

$$\tau_{rz} \cong \eta_0 \left[1 + \frac{m-1}{2} \left(\lambda \frac{\mathrm{d}w}{\mathrm{d}r} \right)^2 \right] \frac{\mathrm{d}w}{\mathrm{d}r}. \tag{12}$$

3. Boundary conditions

We impose the no-slip boundary condition on the arterial wall as

$$w = 0 \text{ at } r = r_0(z),\ 0 \le z \le L. \tag{13}$$

Also w is maximum along the axis of the tube, i.e.

$$\frac{\mathrm{d}w}{\mathrm{d}r} = 0 \text{ at } r = 0. \tag{14}$$

4. Method of solution

From (7) and (12) we have

$$\frac{\mathrm{d}p}{\mathrm{d}z} = \eta_0 \frac{1}{r} \frac{\mathrm{d}}{\mathrm{d}r} \left[r \left\{ \frac{\mathrm{d}w}{\mathrm{d}r} + \lambda^2 \frac{m-1}{2} \left(\frac{\mathrm{d}w}{\mathrm{d}r} \right)^3 \right\} \right]. \tag{15}$$

This equation is non-linear and its exact solution is very difficult to find. For the analytical solution we apply perturbation technique by considering λ^2 as a small parameter. We expand w, p and Q (flow rate) as follows

$$w = w_0 + \lambda^2 w_1 + \mathrm{o}\left(\lambda^4 \right), \tag{16}$$

$$p = p_0 + \lambda^2 p_1 + \mathrm{o}\left(\lambda^4 \right), \tag{17}$$

$$Q = Q_0 + \lambda^2 Q_1 + \mathrm{o}\left(\lambda^4 \right). \tag{18}$$

By substituting eqns. (16) and (17) in (15), we obtain

$$\frac{\mathrm{d}p_0}{\mathrm{d}z} + \lambda^2 \frac{\mathrm{d}p_1}{\mathrm{d}z} =$$

$$= \eta_0 \frac{1}{r} \frac{\mathrm{d}}{\mathrm{d}r} \left[r \left\{ \left(\frac{\mathrm{d}w_0}{\mathrm{d}r} + \lambda^2 \frac{\mathrm{d}w_1}{\mathrm{d}r} \right) + \lambda^2 \frac{m-1}{2} \left(\frac{\mathrm{d}w_0}{\mathrm{d}r} + \lambda^2 \frac{\mathrm{d}w_1}{\mathrm{d}r} \right)^3 \right\} \right]. \tag{19}$$

4.1. Zeroth order problem and its solution

Zeroth order problem is obtained by equating the terms independent of λ^2 from both sides. Thus we have

$$\frac{\mathrm{d}p_0}{\mathrm{d}z} = \eta_0 \frac{1}{r} \frac{\mathrm{d}}{\mathrm{d}r} \left(r \frac{\mathrm{d}w_0}{\mathrm{d}r} \right) \tag{20}$$

subject to the boundary conditions

$$w_0 = 0 \text{ at } r = r_0(z) \tag{21}$$

and

$$\frac{\mathrm{d}w_0}{\mathrm{d}r} = 0 \text{ at } r = 0. \tag{22}$$

The solution of (20) is obtained as

$$w_0 = \frac{\mathrm{d}p_0}{\mathrm{d}z} \frac{r^2 - r_0^2}{4\eta_0} \tag{23}$$

Now

$$Q_0 = 2\pi \int_0^{r_0} r w_0 \, \mathrm{d}r = \frac{\pi r_0^4}{8\eta_0} \frac{\mathrm{d}p_0}{\mathrm{d}z} \Rightarrow \frac{\mathrm{d}p_0}{\mathrm{d}z} = -\frac{8 Q_0 \eta_0}{\pi r_0^4}. \tag{24}$$

4.2. First order problem and its solution

The first order problem is obtained by comparing the coefficients of λ^2 from both sides. Thus we have

$$\frac{\mathrm{d}p_1}{\mathrm{d}z} = \eta_0 \frac{1}{r} \frac{\mathrm{d}}{\mathrm{d}r} \left[r \left\{ \frac{\mathrm{d}w_1}{\mathrm{d}r} + \frac{m-1}{2} \left(\frac{\mathrm{d}w_0}{\mathrm{d}r} \right)^3 \right\} \right] \tag{25}$$

subject to the boundary conditions

$$w_1 = 0 \text{ at } r = r_0(z) \tag{26}$$

and

$$\frac{\mathrm{d}w_1}{\mathrm{d}r} = 0 \text{ at } r = 0. \tag{27}$$

The solution of (25) is obtained as

$$w_1 = \frac{\mathrm{d}p_1}{\mathrm{d}z} \frac{r^2 - r_0^2}{4\eta_0} + \frac{8(m-1) Q_0^3}{\pi^3 r_0^{12}} \left(r^4 - r_0^4 \right). \tag{28}$$

Now

$$Q_1 = 2\pi \int_0^{r_0} r w_1 \, \mathrm{d}r = -2\pi \left[\frac{\mathrm{d}p_1}{\mathrm{d}z} \frac{r_0^4}{16\eta_0} + \frac{8\,(m-1)\,Q_0^3}{3\pi^3 r_0{}^6} \right]$$

and hence

$$\frac{\mathrm{d}p_1}{\mathrm{d}z} = -\left[\frac{8\eta_0 Q_1}{\pi r_0^4} + \frac{128\eta_0\,(m-1)\,Q_0^3}{3\pi^3 r_0{}^{10}} \right] . \tag{29}$$

Thus,

$$w = w_0 + \lambda^2 w_1 \cong \frac{\mathrm{d}p}{\mathrm{d}z} \frac{r^2 - r_0{}^2}{4\eta_0} + \lambda^2 \frac{8\,(m-1)\,Q^3}{\pi^3 r_0{}^{12}} \left(r^4 - r_0{}^4 \right) , \tag{30}$$

where

$$\frac{\mathrm{d}p}{\mathrm{d}z} = \frac{\mathrm{d}p_0}{\mathrm{d}z} + \lambda^2 \frac{\mathrm{d}p_1}{\mathrm{d}z} \cong -\left[\frac{8\eta_0 Q}{\pi r_0{}^4} + \lambda^2 \frac{128\eta_0\,(m-1)\,Q^3}{3\pi^3 r_0{}^{10}} \right] . \tag{31}$$

Let $p = p_0$ at $z = 0$ and $p = p_1$ at $z = L$. Integrating (31), we get the pressure drop as

$$p_0 - p_1 = \frac{8\eta_0 Q}{\pi} \int_0^L r_0{}^{-4} \, \mathrm{d}z + \lambda^2 \frac{128\eta_0\,(m-1)\,Q^3}{3\pi^3} \int_0^L r_0{}^{-10} \, \mathrm{d}z . \tag{32}$$

Thus the flow resistance is obtained as

$$\lambda = \frac{p_0 - p_1}{Q} = \frac{8\eta_0}{\pi} \int_0^L r_0{}^{-4} \, \mathrm{d}z + \lambda^2 \frac{128\eta_0\,(m-1)\,Q^2}{3\pi^3} \int_0^L r_0{}^{-10} \, \mathrm{d}z . \tag{33}$$

Also, the wall shear stress is given by

$$\tau_w = -\frac{r_0}{2} \frac{\mathrm{d}p}{\mathrm{d}z} = \frac{4\eta_0 Q}{\pi r_0{}^3} + \lambda^2 \frac{64\eta_0\,(m-1)\,Q^3}{3\pi^3 r_0{}^9} . \tag{34}$$

Now putting $m = 1$ in (30), (31) and (34), the corresponding expressions for a Newtonian fluid ($\eta = \eta_0$) can be obtained as

$$w = \frac{\mathrm{d}p}{\mathrm{d}z} \frac{r^2 - r_0{}^2}{4\eta_0}, \quad \frac{\mathrm{d}p}{\mathrm{d}z} = -\frac{8\eta_0 Q}{\pi r_0{}^4}, \quad \tau_w = \frac{4\eta_0 Q}{\pi r_0{}^3} . \tag{35}$$

These results agree completely with those given by Bansal [13].

5. Analysis of the results

For the purpose of numerical computations of the quantities of major physiological significance, the following parameter values have been taken: $R_0 = 0.2\,\mathrm{cm}$, $L = 4\,\mathrm{cm}$, $a = 1.5\,\mathrm{cm}$, $b = 0.5\,\mathrm{cm}$, $\eta_0 = 0.056\,\mathrm{dyne.s/cm^2}$, $\lambda = 0.3313\,\mathrm{s}$, $m = 0.3568$, $Q = 0.5\,\mathrm{cm^3/s}$. To observe the quantitative effects of δ and φ, Figs. 2–8 are prepared where the behavior of pressure gradient, velocity field, wall shear stress, flow resistance can be viewed. Knowledge of these flow parameters can help the biomedical

engineers to develop different aids for treatment.

Pressure distribution plays an important role as the post stenotic dilatation owing to arterial damage is caused by the variation of pressure. Moreover, the acoustic signal due to the fluctuation of pressure can be detected externally which helps in diagnosing the disease in due time [14]. So it deserves a special attention.

In Figs. 2 and 3, the pressure gradient in the artery is plotted. A rapid fall in pressure gradient and hence the in wall pressure (as $\mathrm{d}p/\mathrm{d}z < 0$) is noted as it approaches the constriction. Local minimum is attained by the pressure gradient at the throat of the constriction and the pressure gradient recovers its value downstream of the constriction. The position of lowest pressure gradient indicates the position of maximum mean velocity and the position of highest pressure gradient corresponds to the minimum mean velocity. The region of low pressure around the stenotic region gives rise to a health risk as the arterial wall around the stenosis can collapse due to low pressure [15]. Loss of pressure in the stenotic region can reduce the supply of blood in the artery due to which an additional load on the heart is imposed. It can be seen from the figures that the pressure gradient (in magnitude) is stronger at the stenosis zone and particularly at the throat of the stenosis. The pressure gradient decreases as the height of the stenosis increases or the tapering angle decreases. Also, it is noted that the pressure gradient is weaker in case of Carreau fluid than Newtonian fluid; this is due to the shear thinning property of the Carreau fluid.
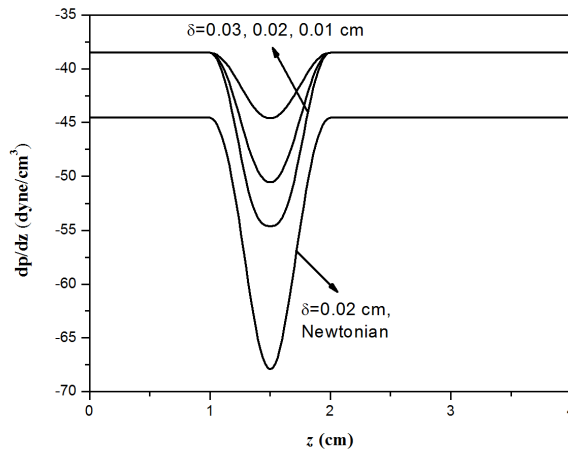
Fig. 2. Pressure gradient along the stenosed artery for $\varphi = 0°$

Figures 4 and 5 present the axial velocity profile at the centre of the stenosis. For non-tapered artery it is found that velocity curve for Newtonian fluid is of sharp parabolic nature whereas for non-Newtonian Carreau fluid, velocity curves are also of parabolic nature but become blunt, to some extent. With the increasing height of the stenosis or decreasing values of the tapering angle, the lumen area gets contracted. As a result, to maintain a constant flow rate the velocity increases.

Wall shear stress plays an important role in the formation of stenosis. Experimental observations report that cholesterol is amalgamated along the inner wall of
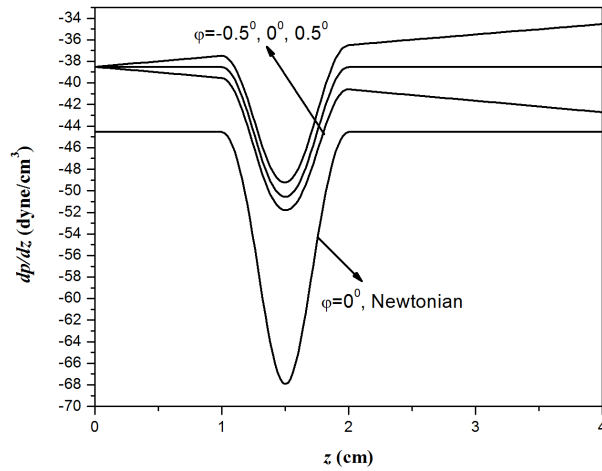
Fig. 3. Pressure gradient along the stenosed artery for $\delta = 0.02\,\mathrm{cm}$
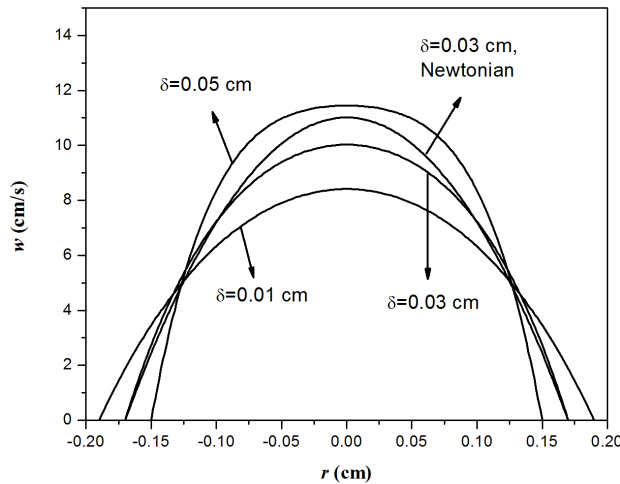
Fig. 4. Axial velocity profile at $z = 1.5\,\mathrm{cm}$ for $\varphi = 0°$

the artery. In the region of high shear stress, cholesterol is washed away by the blood stream. On the other hand excess cholesterol is deposited on the surface of lumen in the region of low wall shear stress. In Figs. 6 and 7, variation of the wall shear stress is exhibited. We notice that with increasing height of the stenosis or decreasing values of the tapering angle, the wall shear stress increases. From the figures it is found that the wall shear stress is significantly higher at the stenosis zone and is highest at the throat of the stenosis. It is noted that the rate of increase of the wall shear stress with respect to the stenosis height increases with the severity of the stenosis, which appears to be reasonable from the medical perspective. Also due to the shear thinning property of Carreau fluid, the wall shear stress in case of Newtonian fluid is stonger than that of Carreau fluid. From these figures it is
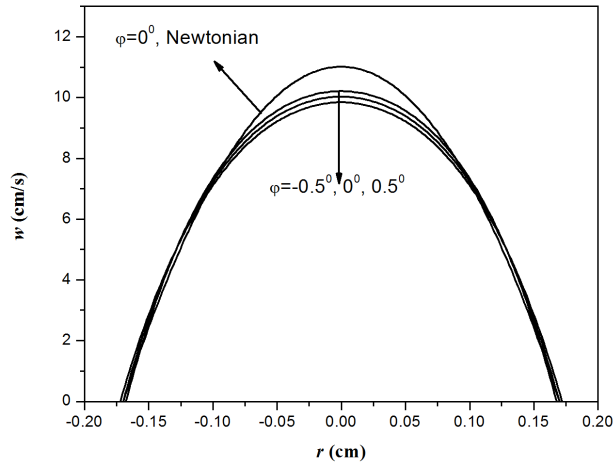
Fig. 5. Axial velocity profile at $z = 1.5\,\text{cm}$ for $\delta = 0.03\,\text{cm}$
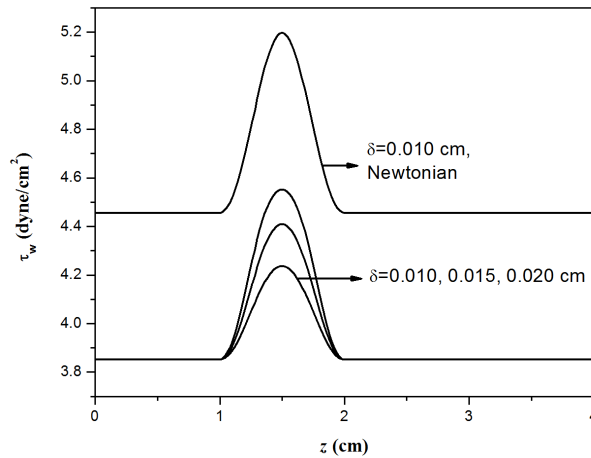
Fig. 6. Wall shear stress distribution for $\varphi = 0°$

found that peaks of the wall shear stress are found in the region where the arterial narrowing is maximum. Peaks of the wall shear stresses are believed to damage the endothelial cells and helps to aggregate the platelets.

Figure 8 reveals the effect of various parameters on the flow resistance. It can be seen from the figure that the flow resistance increases with the height of the stenosis and rate of increase of the flow resistance with the severity of the stenosis is approximately linear. This seems to be reasonable from the clinical point of view. The flow resistance increases from diverging to converging tapering. Due to the shear thinning property of Carreau fluid, the flow resistance in case of Newtonian fluid is higher than that of Carreau fluid.
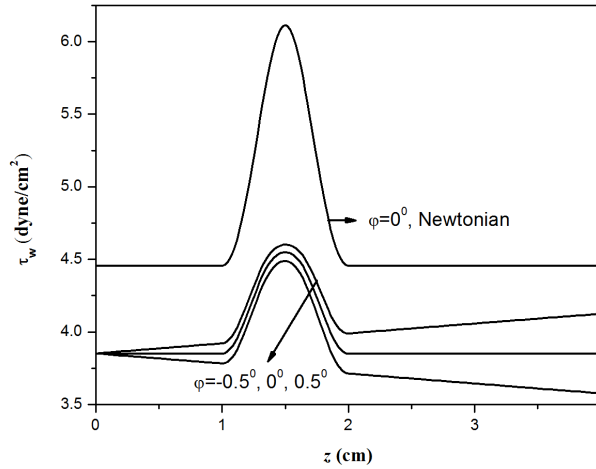
Fig. 7. Wall shear stress distribution for $\delta = 0.02\,\text{cm}$
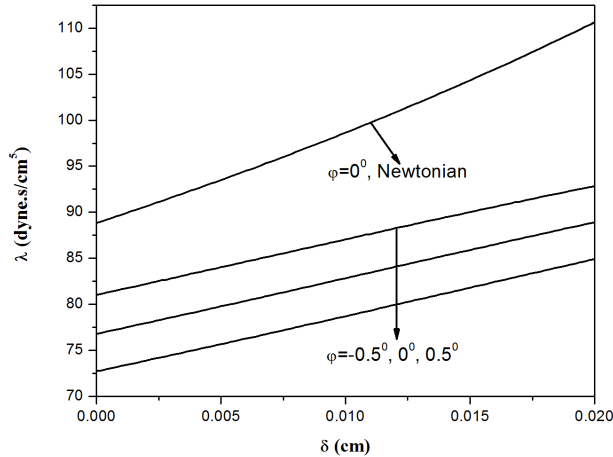
Fig. 8. Variation of flow resistance with height of the stenosis

6. Conclusion

Blood flow is analyzed in a narrow tapered stenosed artery using the Carreau fluid model. The main findings of the performed analysis are as follows:

1. It is noted that for a constant flow rate, the velocity field increases if the tapering angle decreases or the stenosis height increases. Hence narrowing of the arterial lumen causes to increase the velocity field.

2. It is observed that for a constant flow rate, the wall shear stress increases if the tapering angle decreases or the stenosis height increases. Thus due to narrowing of the blood vessel the wall shear stress increases.

3. The wall shear stress is maximum at the throat of the stenosis.

4. For a constant flow rate, the flow resistance increases if the tapering angle decreases or the stenosis height increases. Hence area reduction in the arterial lumen increases the resistance to the flow.

References

[1] M. J. Davies, A. C. Thomas: *Plaque fissuring–the cause of acute myocardial infarction, sudden ischaemic death, and crescendo angina.* British Heart Journal *53* (1985), No. 4, 363–373.

[2] D. Liepsch: *An introduction to biofluid mechanics–basic models and applications.* Journal of Biomechanics *35* (2002), No. 4, 415–435.

[3] C. Tu, M. Deville: *Pulsatile flow of non-Newtonian fluids through arterial stenoses.* Journal of Biomechanics *29* (1996), No. 7, 899–908.

[4] S. Chien: *Hemorheology in clinical medicine.* International Congress of Biorheology, 3 August 1981, Osaka Japan, Proceedings of the Satellite Meeting, Issue title: Hemorheological Approach to Cardiovascular Diseases (1981), 21–26; Clinical Hemorheology and Microcirculation *2* (1982), Nos. 1–2, 137–142.

[5] J. C. Misra, M. K. Patra, S. C. Misra: *A non-Newtonian fluid model for blood flow through arteries under stenotic conditions.* Journal of Biomechanics *26* (1993), No. 9, 1129–1141.

[6] S. Chakravarty, P. K. Mandal: *Two-dimensional blood flow through tapered arteries under stenotic conditions.* International Journal of Non-Linear Mechanics *35* (2000), No. 5, 779–793.

[7] P. K. Mandal: *An unsteady analysis of non-Newtonian blood flow through tapered arteries with a stenosis.* International Journal of Non-Linear Mechanics *40* (2005), No. 1, 151–164.

[8] Sarifuddin, S. Chakravarty, P. K. Mandal: *Numerical simulation of Casson fluid flow through differently shaped arterial stenoses.* Zeitschrift für Angewandte Mathematik und Physik *65* (2014), No. 4, 767–782.

[9] K. L. Moore: *Clinically oriented anatomy.* Williams and Wilkins, Baltimore, MD (1990).

[10] R. L. Whitemore: *Rheology of circulation.* Pergamon Press, Oxford (1968).

[11] G. Porenta, D. F. Young, T. R. Rogge: *A finite-element model of blood flow in arteries including taper, branches, and obstructions.* Journal of Biomechanical Engineering *108* (1986), No. 2, 161–167.

[12] J. Malek, K. R. Rajagopal, M. Ruzicka: *Existence and regularity of solutions and the stability of the rest state for fluids with shear dependent viscosity.* Mathematical Models and Methods in Applied Sciences *5* (1995), No. 6, 789–812.

[13] J. L. Bansal: *Viscous fluid dynamics.* Oxford & IBH Pub. Co. (1992), 74–76.

[14] R. Mittal, S. P. Simmons, H. S. Udaykumar: *Application of large-eddy simulation to the study of pulsatile flow in a modeled arterial stenosiss.* Journal of Biomechanical Engineering *123* (2001), No. 4, 325–332.

[15] D. Tang, C. Yang, S. Kobayashi, D. N. Ku: *Generalized finite difference method for 3-D viscous flow in stenotic tubes with large wall deformation and collapse.* Applied Numerical Mathematics *38* (2001), Nos. 1–2, 49–68.

Entropy analysis for boundary layer flow due to a point sink at the vertex of the cone

Paresh Vyas[1, 2], Swati Soni[1, 3]

Abstract. Entropy analysis of boundary layer flow inside a circular cone due to a point sink at the vertex of the cone is considered. The cone is filled with homogeneously fluid saturated porous medium. The fluid viscosity varies with temperature in an inverse linear fashion. Similarity transformation is performed to convert the governing partial differential equations into ordinary differential equations. Fourth order Runge–Kutta Scheme together with shooting method is employed to solve the governing equations. The velocity and temperature regimes are used to compute entropy generation distribution. The profiles for entropy generation distribution for various values of pertinent parameters are drawn, and discussed.

Key words. Entropy analysis, point sink, cone, porous medium, temperature dependent fluid viscosity.

1. Introduction

Boundary-layer flow in a cone due to a point sink at the vertex simulates conical nozzle or diffusion flow problems [1]. Rosenhead [2] presented similarity solution for heat transfer analysis of the axisymmetric flow inside a cone due to a point sink at the vertex. Ackerberg [3] presented series solution for the converging motion of the viscous fluid inside a cone. Takhar et al. [4] extended the problem for electrically conducting fluid and investigated heat and mass transfer effects. Eswara et al. [5] examined the problem for the transient case. Eswara and Bommaiah [6] considered the same problem for the temperature dependent fluid viscosity. Asatur and Koltan [7] obtained a numerical solution for the momentum boundary layer flow in an axisymmetric convergent duct, treating the convergent axisymmetric potential flow as a point discharge bounded by a cone with a vertex angle. All these studies pertain to transport phenomenon only and no attempt has been made to peep into entropy

[1]Department of Mathematics, University of Rajasthan, Jaipur, India
[2]E-mail: `pvyasmaths@gmail.com`, `pvyasmaths@yahoo.com`
[3]E-mail: `swatisoni19@yahoo.in`

analysis. From the physical considerations we know that all real processes are irreversible. Second law of thermodynamics provides pertinent information about the involved irreversibilities. One may recall that entropy is a measure of irreversibility. Bejan [8]–[10] was the first to bring the idea that thermo-fluidic systems can be optimized by entropy generation analysis [EGA] and entropy generation minimization [EGM]. He shown that parameters responsible for entropy generation can be identified and simulated, and the information can be utilized to minimize the entropy. Since the pioneer works of Bejan, many researchers investigated entropy generation in different fluid flow configurations [11]–[26].

The foregoing problem has been aimed to study entropy generation inside a cone for flow due to a point sink at the vertex of the cone. It is expected that the study would help open new dimension wherein previous similar configurations were restricted to first law of thermodynamics only.

2. Formulation of the problem

Let us consider steady laminar axisymmetric flow of an incompressible fluid inside a circular cone at rest with a hole at the vertex of the cone is considered. The cone is filled with fluid saturated porous medium. The boundary layer flow is due to the presence of the hole which is regarded as a three-dimensional point sink. The cone has been taken as a semi-infinite in length so that it can be regarded as independent of length r. The flow model and physical coordinate system are presented in schematic diagram in Fig. 1.

Fig. 1. Schematic sketch of the problem
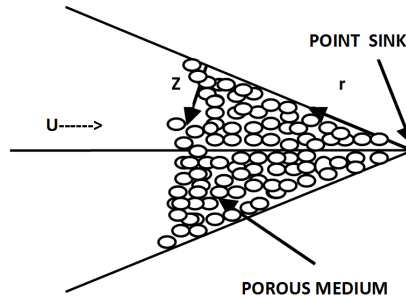
The boundary layer equations for the set up are

$$\frac{\partial (ru)}{\partial r} + \frac{\partial (rw)}{\partial z} = 0, \tag{1}$$

$$u\frac{\partial u}{\partial r} + w\frac{\partial u}{\partial z} = U\frac{\partial U}{\partial r} + \frac{1}{\rho_\infty}\frac{\partial}{\partial z}\left(\mu\frac{\partial u}{\partial z}\right) - \frac{\mu}{\rho_\infty K^*}\left(u - U\right), \tag{2}$$

$$u\frac{\partial T}{\partial r} + w\frac{\partial T}{\partial z} = \frac{\kappa}{\rho_\infty C_p}\frac{\partial^2 T}{\partial z^2} + \frac{1}{\rho_\infty C_p}\left\{\mu\left(\frac{\partial u}{\partial z}\right)^2 + \frac{\mu u^2}{K^*}\right\} \tag{3}$$

together with the following boundary conditions

$$\begin{aligned}
z = 0: \quad & u = 0, \quad w = 0, \quad T = T_w, \\
z \to \infty: \quad & u = U, \quad T = T_\infty.
\end{aligned} \tag{4}$$

Here, u and w are the radial and axial velocities in the directions of r and z, ρ_∞ is the density of free stream, T is the temperature, C_p is the specific heat at a constant pressure, μ is the fluid viscosity, κ is the thermal conductivity, U is the free stream velocity, T_w is the temperature at the wall, T_∞ is the temperature of the free stream, and K^* is the permeability of the porous medium.

The main stream flow is given by

$$U = -\frac{m}{r^2}, \tag{5}$$

where r is the distance measured along the cone from the vertex and m is the strength of point sink $m > 0$.

The fluid viscosity μ is assumed to be inverse linear function of temperature as follows [27]

$$\frac{1}{\mu} = \frac{1}{\mu_\infty}\left[1 + \gamma\left(T - T_\infty\right)\right] \tag{6}$$

or

$$\frac{1}{\mu} = \alpha\left(T - T_r\right)$$

where $\alpha = \gamma/\mu_\infty$ and $T_r = T_\infty - 1/\gamma$, μ_∞ being the viscosity of the fluid at free stream, α and T_r being constants and their values depend on the reference state and γ is a viscosity variation constant based on thermal property of the fluid.

We introduce

$$ru = \frac{\partial\psi}{\partial z} \quad rw = -\frac{\partial\psi}{\partial r} \quad,\psi = -\left(2m\frac{\mu_\infty}{\rho_\infty}r\right)^{1/2} f(\eta), \quad \eta = z\left(\frac{\rho_\infty m}{2\mu_\infty r^3}\right)^{1/2},$$

$$u = Uf'(\eta), \quad w = \left(\frac{m\mu_\infty}{2r^3\rho_\infty}\right)^{1/2}(f - 3\eta f'), \quad \theta(\eta) = \frac{T - T_\infty}{T_w - T_\infty},, \quad U = -\frac{m}{r^2}, \quad m > 0. \tag{7}$$

We see that the equation of continuity (1) is identically satisfied and equations (2) and (3) take the following respective forms

$$f''' + \left(1 - \frac{\theta}{\theta_r}\right)\left\{4\left(1 - f'^2\right) - ff''\right\} + \frac{f''\theta'}{\theta_r - \theta} - K\left(f' - 1\right) = 0, \tag{8}$$

$$\theta'' - \Pr f\theta' + \frac{\text{Br}\theta_r}{\theta_r - \theta}\left(f''^2 + f'^2 K\right) = 0, \tag{9}$$

where

$$K = \frac{2\mu_\infty r^3}{\rho_\infty m K^*}, \quad \mathrm{Pr} = \frac{\mu_\infty C_\mathrm{p}}{\kappa_\infty}, \quad \mathrm{Br} = \frac{\mu_\infty U^2}{\kappa_\infty \left(T_\mathrm{w} - T_\infty\right)},$$

$$\theta_\mathrm{r} = \frac{T_\mathrm{r} - T_\infty}{T_\mathrm{w} - T_\infty} = -\frac{1}{\gamma \left(T_\mathrm{w} - T_\infty\right)} \tag{10}$$

are permeability parameter, Prandtl number, Brinkmann number and viscosity parameter, respectively,

The boundary conditions (4) become

$$\eta = 0: \quad f' = 0, \quad \theta = 1, \quad f = 0,$$
$$\eta \to \infty: \quad f' \to 1, \quad \theta \to 0. \tag{11}$$

3. Solution

The governing equations (8) and (9) together with the boundary conditions (11) have been solved numerically by Runge–Kutta fourth order scheme together with shooting method. The essence of shooting method to solve a boundary value problem (BVP) is to convert it into a system of initial value problems where systematic guesses are made for unknown quantities such that the end conditions are satisfied. For the present case the BVP governed by the equations (8), (9) and (11) is reduced to following system of initial value problems.

$$f_3' = \left(\frac{f_4}{\theta_\mathrm{r}} - 1\right) \left\{4 \left(1 - f_2^2\right) - f_1 f_3\right\} - \frac{f_3 f_5}{\theta_r - f_4} + K \left(f_2 - 1\right), \tag{12}$$

$$f_5' = \mathrm{Pr}\, f_1 f_5 - \frac{\mathrm{Br}\theta_\mathrm{r}}{\theta_\mathrm{r} - f_4} \left(f_3^2 + f_2^2 K\right), \tag{13}$$

with initial conditions

$$f_1\left(0\right) = 0, \quad f_2\left(0\right) = 0, \quad f_3\left(0\right) = ?, \quad f_4\left(0\right) = 1, \quad f_5\left(0\right) = ?, \tag{14}$$

where

$$f = f_1, \quad f' = f_2, \quad f'' = f_3, \quad \theta = f_4, \quad \theta' = f_5. \tag{15}$$

The numerical computation has two challenges. Firstly, $f_3(0)$ and $f_5(0)$ are not available. Secondly η_∞, i.e. maximum value of η for which end conditions $f' \to 1$ and $\theta \to 0$ as $\eta \to \infty$ are satisfied, was not available beforehand. To accomplish the task, systematic guesses for $f_3(0)$ and $f_5(0)$ are made for taking a finite value of η as η_∞ and then integration of IVP (12)–(14) is done by R–K method of order four. If the end conditions are satisfied for prescribed error tolerance of magnitude 10^{-6}, then we finished, otherwise the procedure is repeated for another set of guesses. In fact, these guesses are initially found on the hit and trial basis and their refinement is done by the Newton iteration method. Furthermore, η_max, i.e. η_∞ is also optimized together with the grid independence. It was found that step size $\Delta\eta = 0.0005$ is

satisfactory for desired convergence of magnitude 10^{-6}.

4. Second law analysis

The local volumetric rate of entropy generation S_{G} for a viscous fluid flow is given by

$$S_{\mathrm{G}} = \frac{\kappa}{T_\infty^2} \left(\frac{\partial T}{\partial z}\right)^2 + \frac{\mu}{T_\infty} \left\{ \left(\frac{\partial u}{\partial z}\right)^2 + \frac{u^2}{K^*} \right\}. \tag{16}$$

The equation (16) reveals that three sources contribute to entropy generation. The first term shows the contribution of heat transfer to entropy across boundary layer, the second term is the local entropy generation due to viscous dissipation due to fluid friction and the third term gives the local entropy generation due to the resistance to fluid flow offered by the porous medium.

We introduce the characteristic entropy generation rate S_{G0}, the characteristic temperature ratio ω respectively as follows

$$S_{\mathrm{G}0} = \frac{\kappa(T_{\mathrm{w}} - T_\infty)^2}{T_\infty^2} \left(\frac{\rho_\infty m}{2\mu_\infty r^3}\right), \quad \omega = \frac{T_\infty}{T_{\mathrm{w}} - T_\infty}. \tag{17}$$

Thus, the non-dimensional entropy generation number N_{s} is given as

$$N_{\mathrm{s}} = \frac{S_{\mathrm{G}}}{S_{\mathrm{G}0}} = \theta'^2 + \mathrm{Br}\omega \frac{\theta_{\mathrm{r}}}{(\theta_{\mathrm{r}} - \theta)} \left(f''^2 + f'^2 K\right) = \mathrm{HTI} + \mathrm{FFI}, \tag{18}$$

where
heat transfer irreversibility (HTI) $= \theta'^2$,
and fluid friction irreversibility (FFI) $= \mathrm{Br}\omega \frac{\theta_{\mathrm{r}}}{(\theta_{\mathrm{r}} - \theta)} \left(f''^2 + f'^2 K\right)$.

The Bejan Number Be which is pertinent irreversibility parameter is defined as

$$Be = \frac{\mathrm{HTI}}{\mathrm{HTI} + \mathrm{FFI}}. \tag{19}$$

Here, it should be noted that values 0 and 1 for Be correspond, respectively, to the cases when the irreversibility is dominated by frictional effects and when the irreversibility due to heat transfer is significant.

The global entropy G_{Ns} is computed by integrating the local entropy and is obtained as follows

$$G_{\mathrm{Ns}} = \int_0^{\eta_\infty} N_{\mathrm{s}} d\eta. \tag{20}$$

Tables 1–3 list the values of missing $f''(0)$ and $\theta'(0)$ for selected parameters Br, K, ω and θ_{r}.

Table 1. Missing $f''(0)$ and $\theta'(0)$ when Br $= 4$, $K = 0.1$ and $\omega = 0.6$

θ_{r}	$f''(0)$	$\theta'(0)$
-4	2.550163	2.852006
-6	2.475837	2.974227
-8	2.438761	3.041776
-10	2.416602	3.084712
-13	2.396238	3.126119

Table 2. Missing $f''(0)$ and $\theta'(0)$ when $K = 0.1$, $\omega = 0.6$ and $\theta_{\mathrm{r}} = -13$

Br	$f''(0)$	$\theta'(0)$
2	2.372107	1.671839
3	2.362943	2.728798
4	2.354001	3.775738
5	2.345272	4.813045
6	2.336745	5.841080

Table 3. Missing $f''(0)$ and $\theta'(0)$ when Br $= 4$, $\theta_{\mathrm{r}} = -13$ and $\omega = 0.6$

K	$f''(0)$	$\theta'(0)$
0	2.335877	3.618484
0.1	2.354001	3.775738
0.2	2.371901	3.932822
0.3	2.389584	4.089711
0.4	2.407058	4.246385
0.5	2.424330	4.402824
0.6	2.441406	4.559010

5. Results and discussion

After having determined velocity and temperature regimes, the entropy generation number is computed. Plots for entropy generation number, Bejan number and global entropy have been drawn for various sets of values of parameters. The figures reveal that entropy generation number N_{s} attains minima for some spatial distance η. This "minima" indicates the vanishing velocity and temperature gradients. Further it should be noted that in the regions where Be > 0.5, heat transfer irreversibility is more dominant over irreversibility due to fluid friction. These figures reveal that every parameter has both qualitative and quantitative effect on the entropy generation. Here, we recall that Be=0 represents the case when fluid friction irreverisibility dominates fully over the irreversibility due to heat transfer, i.e., there is no irreversibility due to heat transfer and Be $= 1$ stands for the case when heat transfer irreversibility takes a toll over fluid friction irreversibility. Figures 6–9 displaying Bejan number show that Be is very large (i.e. approximately 0.9) at the edge of the boundary layer. This means that heat transfer irreversibility is more

pronounced than fluid friction irreversibility at far away distances from the wall of the cone. Figure 2 displays that entropy generation number N_s increases with the increasing values of Brinkmann number Br. Here, it is emphasized that the Brinkman number Br accounts for fluid friction. Larger values of Br are indicative of larger dissipative effects. That is why we see larger entropy generation for higher values of Br. Figure 3 shows that N_s increases with the increasing values of the permeability parameter K. Here the permeability parameter K is reciprocal of the permeability K^*. Hence, larger values of K means lesser fluid traversal, i.e., larger resistance by the porous medium walls to fluid flow. Consequently entropy generation number rises with the increasing values of K. Furthermore, this also means rather larger cooling time for larger values of K.
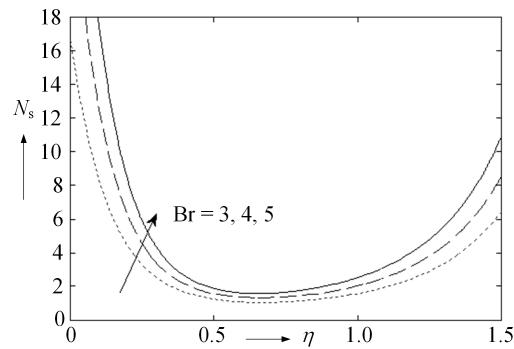
Fig. 2. Entropy variation for varying Brinkman number Br for $\theta_r = -13$, $K = 0.1$ and $\omega = 0.6$
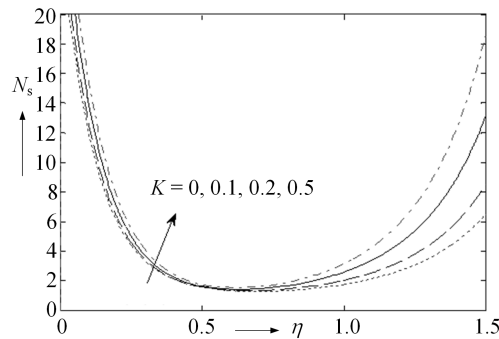
Fig. 3. Entropy variation for varying K for Br $= 4$, $\theta_r = -13$ and $\omega = 0.6$

Figure 4 exibits that N_s increases with the increasing values of characteristics temperature ratio ω. Figure 5 shows that N_s increases with the increasing numerical values of θ_r. Figures 6–9 display variations in Bejan number Be. These figures show that Be has respective minima for different sets of values of the parameters. Furthermore, Fig. 6 shows that near the wall of cone the Bejan number rises with the increasing values of Br and after some spatial distance it vanishes and a reverse

trend is witnessed as we move away from the wall. Further we see that Be > 0.5 at large distance from the wall of the cone. Hence, we conclude that at some distance from the wall heat transfer irreversibility is more pronounced as compared to fluid friction irreversibility.
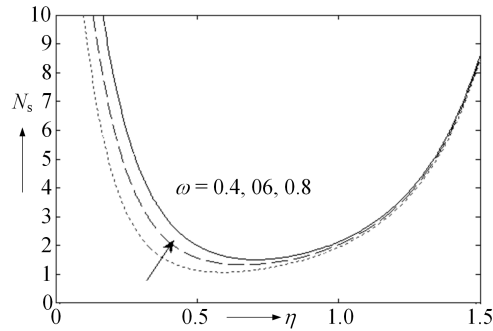
Fig. 4. Entropy variation for varying ω for $Br = 4$, $\theta_r = -13$ and $K = 0.1$
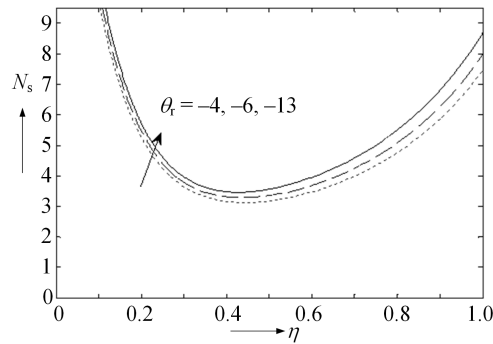
Fig. 5. Entropy variation for varying θ_r for $Br = 4$, $K = 0.1$ and $\omega = 0.6$
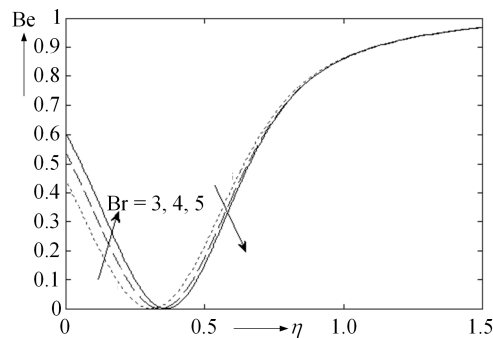
Fig. 6. Bejan number variation for varying Br for $\theta_r = -13$, $K = 0.1$ and $\omega = 0.6$

Figure 7 exibits that Be increases in the region close to wall of the cone for

increasing values of K, however, this trend is reversed at some distance from the wall. Figure 8 shows that Be decreases with the increasing values of ω in the boundary layer while it vanishes, too, at some spatial distances η for respective values of K.
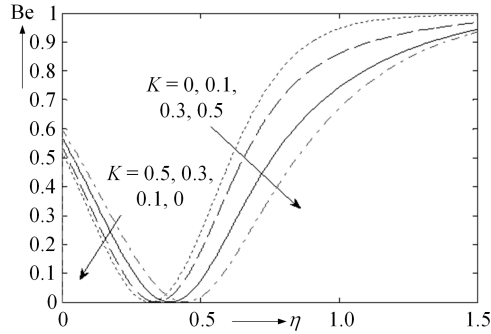
Fig. 7. Bejan number variation for varying K for Br $= 4$, $\theta_r = -13$ and $\omega = 0.6$
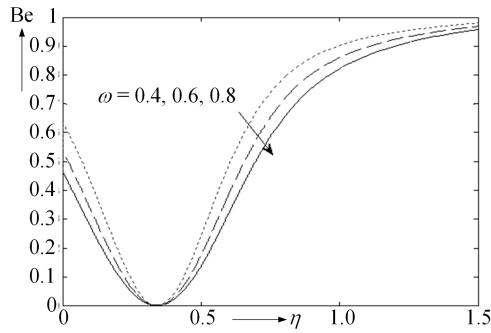
Fig. 8. Bejan number variation for varying ω for Br $= 4$, $\theta_r = -13$ and $K = 0.1$
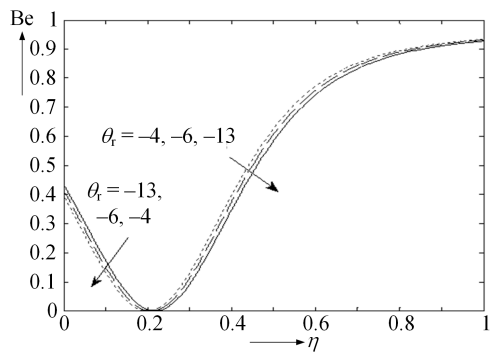
Fig. 9. Bejan number variation for varying θ_r for Br $= 4$, $K = 0.1$ and $\omega = 0.6$
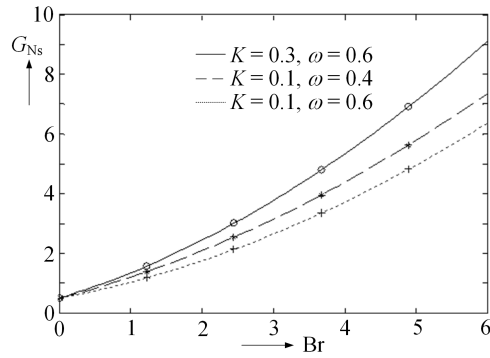
Fig. 10. Global entropy generation rate as a function of Br for different values of
K and $\omega = 0.6$ and for $\theta_\mathrm{r} = -13$ and $K = 0.1$
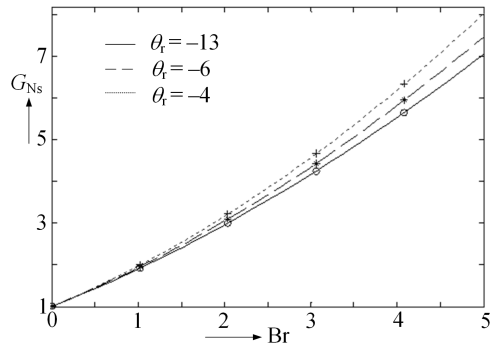
Fig. 11. Global entropy generation rate as a function of Br for different values of
θ_r, $K = 0.1$ and $\omega = 0.6$
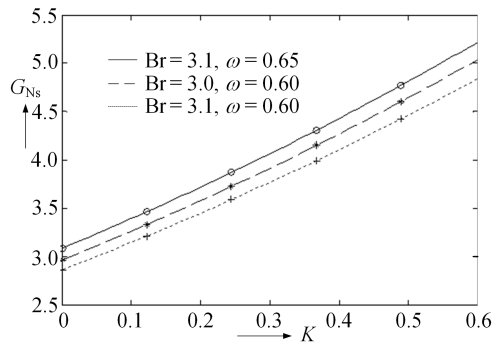
Fig. 12. Global entropy generation rate as a function of K for different values of
Br and ω and for $\theta_\mathrm{r} = 13$

Figure 9 shows that Be increases with numerically increasing values of θ_r near
the wall of the cone and then it attains minima for some η and afterwards the trend
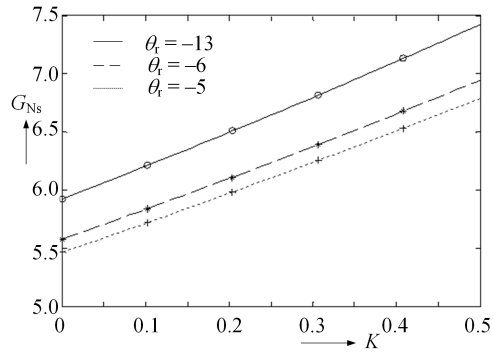
Fig. 13. Global entropy generation rate as a function of K for different values of θ_{r}
and for Br $= 4$ and $\omega = 0.6$

is reversed. Finally Figs. 10–13 exhibit plots for global entropy G_{Ns}. These figures show that G_{Ns} increases with the increasing values of Br, K, ω, and numerically increasing values of θ_{r}.

6. Conclusion

The problem aimed to analyze entropy generation for variable viscosity fluid flow inside a cone with a point sink at the vertex. The mathematical model devised for the problem constituted a coupled nonlinear boundary value problem (BVP) not amenable to closed form solution for the momentum and energy equations. Therefore, a numerical solution strategy of Runga–Kutta scheme together with shooting method was developed for solving the BVP. The velocity and temperature distributions computed numerically were employed to compute local entropy generation number and global entropy. Graphs plotted for the quantities of interest led to following conclusions:

1. Entropy generation number N_{s} and global entropy G_{Ns} increase with the increasing values of Br, K, ω and for numerically increasing values of θ_{r}.

2. The Bejan number attains different minima at spatial distances η for respective cases of set of parameter values. These minima indicate that there is no irreversibility due to heat transfer. However, we see that Be is quite large far away from the wall of cone indicating the region where heat transfer irreversibility contributes significantly to entropy generation.

References

[1] S. H. Choi, H. E. Wilhelm: *Self-similar magnetohydrodynamic diffuser flows with induced magnetic fields*. Physics of Fluids *20* (2008), No. 11, 1821–1826.

[2] L. Ed Rosenhead: *Laminar boundary layers*. Oxford University Press, Oxford (1963), 427–428.

[3] R. C. ACKERBERG: *The viscous incompressible flow inside a cone.* Journal of Fluid Mechanics *21* (1965), No. 1, 47–81.

[4] H. S. TAKHAR, C. D. SURMA DEVI, G. NATH: *MHD flow with heat and mass transfer due to a point sink.* Indian Journal of Pure and Applied Mathematics *17* (1986), No. 10, 1242–1247.

[5] A. T. ESWARA, S. ROY, G. NATH: *Unsteady MHD forced flow due to a point sink.* Acta Mechanica *145* (2000), Nos. 1–4, 159–172.

[6] A. T. ESWARA, B. C. BOMMAIAH: *The effect of variable viscosity on laminar flow due to a point sink.* Indian Journal of Pure and Applied Mathematics *35* (2004), No. 6, 811–815.

[7] K. G. ASATUR, G. A. KOLTON: *Laminar boundary layer in an axisymmetric convergent duct.* Fluid Mechanics (Soviet Research) *20*(1991), 24–27.

[8] A. BEJAN: *Second law analysis in heat transfer.* Energy *5* (1980), Nos. 8–9, 720–732.

[9] A. BEJAN: *Entropy generation through heat and fluid flow.* Wiley, New York (1982).

[10] A. BEJAN: *Entropy generation minimization: The method of thermodynamic optimization of finite-size systems and finite-time processes.* CRC Press, Boca Raton (1986).

[11] L. B. ERBAY, M. S. ERCAN, B. SÜLÜS, M. M. YALÇY̌N: *Entropy generation during fluid flow between two parallel plates with moving bottom plate.* Entropy *5* (2003), No. 5, 506–518.

[12] O. HADDAD, M. ABUZAID, M. AL-NIMR: *Entropy generation due to laminar incompressible forced convection flow through parallel-plates microchannel.* Entropy *6* (2004), No. 5, 413–426.

[13] S. MAHMUD, R. A. FRASER: *Flow, thermal, and entropy generation characteristics inside a porous channel with viscous dissipation.* International Journal of Thermal Sciences *44* (2005),No. 1, 21–32.

[14] K. HOOMAN, A. EJLALI: *Entropy generation for forced convection in a porous saturated circular tube with uniform wall temperature.* International Communications in Heat and Mass Transfer *34* (2007), No. 4, 408–419.

[15] G. IBÁÑEZ, S. CUEVAS: *Entropy generation minimization of a MHD (magnetohydrodynamic) flow in a microchannel.* Energy *35* (2010), No. 10, 4149–4156.

[16] P. VYAS, A. RAI: *Entropy regime for radiative MHD couette flow inside a channel with naturally permeable base.* International Journal of Energy & Technology *5* (2013), No. 19, 1–9.

[17] G. IBÁÑEZ, A. LÓPEZ, J. PANTOJA, J MOREIRA, J. A. REYES: *Optimum slip flow based on the minimization of entropy generation in parallel plate microchannels.* Energy *50* (2013), 143–149.

[18] D. S. CHAUHAN, V. KUMAR: *Entropy analysis for third-grade fluid flow with temperature-dependent viscosity in annulus partially filled with porous medium.* Theoretical and Applied Mechanics *40* (2013), No. 3, 441–464.

[19] M. LÓPEZ DE HARO, S. CUEVAS, A. BELTRÁN: *Heat transfer and entropy generation in the parallel plate flow of a power-law fluid with asymmetric convective cooling.* Energy *66* (2014), 750–756.

[20] G. IBÁÑEZ: *Entropy generation in MHD porous channel with hydrodynamic slip and convective boundary conditions.* International Journal of Heat and Mass Transfer *80* (2015), 274–280.

[21] P. VYAS, N. SRIVASTAVA: *Entropy analysis of generalized MHD Couette flow inside a composite duct with asymmetric convective cooling.* Arabian Journal for Science and Engineering *40* (2015), No. 2, 603–614.

[22] P. VYAS, A. RANJAN: *Entropy analysis of radiative MHD forced convection flow with weakly temperature dependent convection coefficient in porous medium channel.* Acta Technica *60* (2015), No. 1, 1–14.

[23] P. VYAS, A. RANJAN: *Entropy analysis for MHD generalised Couette flow in a composite duct.* Journal of Industrial Mathematics (2015), Article ID 895046.

[24] P. Vyas, S. Soni: *Entropy analysis for MHD Casson fluid flow in a channel subjected to weakly temperature dependent convection coefficient and hydrodynamic slip.* Journal of Rajasthan Academy of Physical Sciences *15* (2016), Nos. 1–2, 1–18.

[25] P. Vyas, S. Khan: *Entropy analysis for MHD dissipative Casson fluid flow in porous medium due to stretching cylinder.* Acta Technica *61* (2016), No. 3, 299–315.

[26] G. Ibáñez, A. López, J. Pantoja, J. Moreira: *Entropy generation analysis of a nanofluid flow in MHD porous microchannel with hydrodynamic slip and thermal radiation.* International Journal of Heat and Mass Transfer *100* (2016), 89–97.

[27] J. X. Lings, A. Dybbs: *The effect of variable viscosity on forced convection over a flat plate submersed in a porous medium.* Journal of Heat Transfer *114* (1992), No. 4, 1063–1065.

Mass diffusion with chemical reaction in boundary layer flow due to an exponentially expanding sheet with variable wall concentration[1]

A. Banerjee[2], S. K. Mahato[3],
K. Bhattacharyya[4, 5]

Abstract. A model investigation is made to study the mass diffusion with chemical reaction in boundary layer flow over an exponentially expanding sheet with variable wall concentration. Here the first order chemical reaction is considered. Also, the reaction rate of species and the wall concentration are taken exponentially variable. The governing equations are transformed into nonlinear self-similar equations by similarity transformations and are then solved numerically using shooting method. From the analysis it is found that for the increase of Schmidt number and reaction rate parameter the concentration at a point and concentration boundary layer thickness decrease. The mass absorption takes place for certain values of parameters, in addition with the usual mass transfer.

Key words. Mass diffusion, chemical reaction; boundary layer flow; exponentially expanding sheet; variable wall concentration.

1. Introduction

The viscous boundary layer flow due to stretching sheet is very significant problem in fluid dynamics due to its huge applications in many manufacturing processes in industry, such as, extraction of polymer sheet, paper production, hot rolling, wire drawing, glass-fiber production and so on. Crane [1] first investigated the steady

boundary layer flow of an incompressible viscous fluid over a linearly stretching plate and gave an exact similarity solution in closed analytical form. The pioneering work of Crane [1] work was extended by many researchers such as Gupta and Gupta [2], Chen and Char [3], Pavlov [4] considering the effects of heat and mass transfer and magnetic field under various physical conditions. Later, Andersson [5] studied the MHD flow of a viscoelastic fluid over a stretching surface. Char [6] explained the heat transfer in a hydromagnetic flow over a stretching sheet. El-Aziz [7] analysed the flow, heat and mass transfer characteristics of a viscous electrically conducting fluid having temperature dependent viscosity and thermal conductivity past a continuously stretching surface with Ohmic heating.

The diffusion of mass with chemical reaction in the boundary layer flow also has many applications in water and air pollutions, fibrous insulation, atmospheric flows and many other chemical engineering problems. Chambre and Young [8] considered the diffusion of a chemically reactive species in a laminar boundary layer flow. Stan [9] discussed the boundary layer flow with chemical surface reaction. Andersson et al. [10] investigated the effect of transfer of chemically reactive species in the laminar flow over a stretching sheet. Afify [11] explained the MHD free convective flow of viscous incompressible fluid and mass transfer over a stretching sheet with chemical reaction. Cortell [12] reported the motion and mass transfer for two classes of viscoelastic fluid over a porous stretching sheet with chemically reactive species. Bhattacharyya and Layek [13] discussed the behaviour of chemically reactive solute distribution in MHD boundary layer flow over a permeable stretching sheet. In addition, the chemical reaction effects on the flow over a flat sheet were also studied in the articles [14–22].

Last few decades in almost all investigations on the flow over a stretching sheet, the flow occurs because of linear stretching velocity of the flat sheet. But, the boundary layer flow induced by an exponentially stretching sheet is not studied much, though it is very important and realistic flow frequently appeared in many engineering processes. Magyari and Keller [23] first considered the boundary layer flow due to an exponentially stretching sheet and they also investigated the heat transfer in the flow taking exponentially varied wall temperature. Elbashbeshy [24] numerically examined the flow and heat transfer over an exponentially stretching surface considering wall mass suction. Khan and Sanjayanand [25] studied the flow of viscoelastic fluid and heat transfer over an exponentially stretching sheet with viscous dissipation effects. Partha et al. [26] obtained a similarity solution for mixed convection flow past an exponentially stretching surface by taking into account the influence of viscous dissipation on the convective transport. Sanjayanand and Khan [27] discussed the effects of heat and mass transfer on the boundary layer flow of viscoelastic fluid. Al-Odat et al. [28] explained the effect magnetic field on thermal boundary layer on an exponentially stretching continuous surface with an exponential temperature distribution. Sajid and Hayat [29] showed the influence of thermal radiation on the boundary layer flow past an exponentially stretching sheet and they reported series solutions for velocity and temperature using homotopy analysis method (HAM). Bhattacharyya [30] investigated the boundary layer flow due to shrinking sheet with wall mass suction. Recently, Bhattacharyya and Layek

[31] discussed the thermal boundary layer in fluid flow over exponentially stretching surface with an exponentially moving free stream.

In the present paper, the mass diffusion with first order chemical reaction in boundary layer flow past an exponentially expanding sheet is investigated. The reaction rate of the species and the wall concentration distribution are also taken variable in exponential form. Using similarity transformation, the self-similar ordinary differential equations are obtained and solved numerically by shooting method. The numerical results are depicted in some figures and the various physical characteristics of flow field and solute diffusion are discussed.

2. Mathematical formulation

Let us consider the steady two-dimensional boundary layer flow and mass transfer over an exponentially expanding sheet with first order chemical reaction. The governing equations of motion and the equation of concentration distribution are written in usual notation as

$$\frac{\partial u}{\partial x} + \frac{\partial v}{\partial y} = 0 \,, \tag{1}$$

$$u\frac{\partial u}{\partial x} + v\frac{\partial u}{\partial y} = \upsilon\frac{\partial^2 u}{\partial y^2} \tag{2}$$

and

$$u\frac{\partial C}{\partial x} + v\frac{\partial C}{\partial y} = D\frac{\partial^2 C}{\partial y^2} - R(C - C_\infty) \,. \tag{3}$$

Here, u and v are the velocity components in the x- and y-directions, respectively, $\upsilon \, (= \mu/\rho)$ is the kinematic fluid viscosity, ρ is the fluid density, μ is the coefficient of fluid viscosity, C is the species concentration, D is the diffusion coefficient and C_∞ is the concentration in the free stream. Symbol $R(x)$ denotes the variable reaction rate of solute and is given by as $R(x) = R_0 \exp(x/L)$, where L is the reference length and R_0 is a constant.

The boundary conditions are given by

$$u = U_{\mathrm{w}}(x), \quad v = 0 \quad \text{at} \quad y = 0, \quad u \to 0 \text{ as } y \to 0 \tag{4}$$

and

$$C = C_{\mathrm{w}} = C_\infty + C_0 \exp(\lambda x/(2L)) \text{ at } y = 0, \quad C \to C_\infty \text{ as } y \to \infty \,, \tag{5}$$

where C_{w} is the variable concentration on the sheet, C_0 is a constant which measures the rate of concentration increase along the sheet and λ is a parameter which is physically very important in controlling the exponential increment of surface concentration and it may have both positive and negative values. The velocity of expansion of the sheet, U_{w} is given by

$$U_{\mathrm{w}}(x) = a \exp(x/L) \,, \tag{6}$$

where $a > 0$ is the expansion constant.

3. Similarity analysis and solution procedure

The stream function $\psi(x, y)$ is implemented as

$$u = \frac{\partial \psi}{\partial y} \;\; \text{and} \;\; v = -\frac{\partial \psi}{\partial x}. \tag{7}$$

For relations in (7), the continuity equation (1) is identically satisfied and the momentum equation (2) and the concentration equation (3) are reduced to the following forms:

$$\frac{\partial \psi}{\partial y}\frac{\partial \psi}{\partial x \partial y} - \frac{\partial \psi}{\partial x}\frac{\partial^2 \psi}{\partial y^2} = \upsilon \frac{\partial^3 \psi}{\partial y^3} \tag{8}$$

and

$$\frac{\partial \psi}{\partial y}\frac{\partial C}{\partial x} + \frac{\partial \psi}{\partial x}\frac{\partial C}{\partial y} = D\frac{\partial^2 C}{\partial y^2} - R(C - C_\infty). \tag{9}$$

The boundary conditions in (4) for the velocity components become

$$\frac{\partial \psi}{\partial y} = U_w(x), \;\; \frac{\partial \psi}{\partial x} = 0 \text{ at } y = 0, \;\; \frac{\partial \psi}{\partial y} \to 0 \text{ as } y \to \infty. \tag{10}$$

Next, let us introduce the dimensionless variables for ψ and T as

$$\psi = \sqrt{2\upsilon La}\, f(\eta) \exp(x/2L) \text{ and } C = C_\infty + (C_{\mathrm{w}} - C_\infty)\phi(\eta), \tag{11}$$

where η is the similarity variable and is defined as [23]

$$\eta = y\sqrt{\tfrac{a}{2\upsilon L}} \,\exp(\tfrac{x}{2L}).$$

Using relations in (11) we finally obtain the following nonlinear self-similar equations

$$f''' + ff'' - 2f'^2 = 0 \tag{12}$$

and

$$\phi'' + \mathrm{Sc}(f\phi' - \lambda f'\phi - \beta\phi) = 0, \tag{13}$$

where $\mathrm{Sc} = \upsilon/D$ is the Schmidt number and $\beta = 2\frac{LR_0}{a}$ is the reaction rate parameter.

The boundary conditions (10) and (5) reduce to the following forms

$$f(\eta) = 0, \;\; f'(\eta) = 1 \text{ at } \eta = 0, \;\; f'(\eta) \to 0 \text{ as } \eta \to \infty \tag{14}$$

and

$$\phi(\eta) = 1, \;\text{ at } \eta = 0, \;\; \phi(\eta) \to 0 \text{ as } \eta \to \infty. \tag{15}$$

The nonlinear coupled differential equations (12) and and (13) along with the boundary conditions (14) and (15) form a two point boundary value problem (BVP)

and is solved using shooting method [32, 33], by converting it into an initial value problem (IVP). In this method we have to choose a suitable finite value of $\eta \to \infty$, say η_∞. We set the following first-order system

$$f' = p, \; p' = q, \; q' = 2p^2 - fq, \tag{16}$$

and

$$\phi' = z, \; z' = -\mathrm{Sc}(fz - \lambda p\phi - \beta\phi) \tag{17}$$

with the boundary conditions

$$f(0) = 0, \; p(0) = 1, \; \phi(0) = 1. \tag{18}$$

To solve (16) and (17) with (18) as an IVP we must need the values for $q(0)$, i.e., $f''(0)$ and $z(0)$, i.e., $\phi'(0)$, but no such values are given. The initial guess values for $f''(0)$ and $\phi'(0)$ are chosen and the fourth order Runge–Kutta method is applied to obtain the solution. We compare the calculated values of $f'(\eta)$ and $\phi(\eta)$ at η_∞ (=30) with the given boundary conditions $f'(\eta_\infty) = 0$ and $\phi(\eta_\infty) = 0$ and adjust values of $f''(0)$ and $\phi'(0)$ using the Secant method to give better approximation for the solution. The step-size is taken as $\Delta\eta = 0.01$. The process is repeated until we get the results corrected up to the desired accuracy of 10^{-6} level.

4. Results and discussion

Numerical computations have been performed for various values of the physical parameters involved in the equations viz., the Schmidt number Sc, the reaction rate parameter β and the parameter λ. To understand the behaviour of diffusion and the effect of chemical reaction, the computed results are plotted in Figs. 1–6.

The skin friction coefficient $f''(0)$ and $f(\infty)$ are physically very important and using the above numerical scheme the obtained values of those are $f''(0) = 1.28180838$ and $f(\infty) = 0.90564328$, which are found in superb agreement with the values obtained by Magyari and Keller [23] ($f''(0) = 1.281808$ and $f(\infty) = 0.905639$).

At first, our focus is concentrated on the effect of Schmidt number Sc on chemically reactive mass diffusion. The reactive concentration profiles $\phi(\eta)$ for various values of Sc are presented in Fig. 1 and 2 for $\lambda = 1$ and $\lambda = -1$, respectively. From the figures, it is observed that for both direct variation and inverse variation of exponential surface concentration the dimensionless concentration at a point and the solute boundary layer thickness rapidly decrease with the increase of Sc. The increase of Schmidt number means the decrease of diffusion coefficient and consequently the rate of mass transfer enhances. As a result, this causes the reduction of species boundary layer thickness.

Next, the changes in concentration profiles for different values of the reaction rate parameter β are discussed. The concentration profiles for different values of β are exhibited in Fig. 3 and 4 for first order chemical reaction for direct and inverse variations of exponential wall concentration distribution. In both situations, the concentration at a point decreases with the reaction rate. Also, the increase in the

Fig. 1. Concentration profiles $\phi(\eta)$ for various values of Sc with $\lambda > 0$
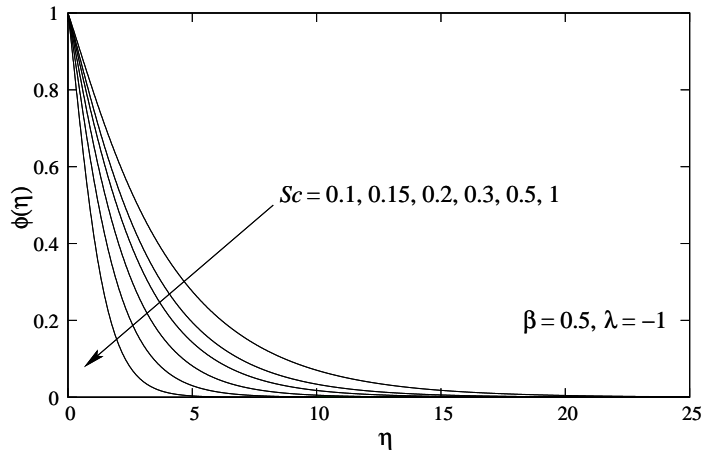
Fig. 2. Concentration profiles $\phi(\eta)$ for various values of Sc with $\lambda < 0$

value of β reduces the species boundary layer thickness.

The effect of the parameter λ which is related to wall concentration distribution plays an important role in controlling the reactive mass diffusion. In Figs. 5 and 6, the reactive species profiles $\phi(\eta)$ are depicted for several values of λ. Out of which, in Fig. 5 all values of λ are non-negative, whereas in Fig. 6 all are non-positive. From Fig. 5, it is noticed that the concentration decreases as λ increases and the species boundary layer thickness slightly reduced with λ. On the other hand, for negative variation of λ, the concentration at fixed point increases and also the overshoot of concentration profiles observed for higher negative values of λ. Importantly, the overshoot pick raises as the magnitude of $\lambda < 0$ increases. Hence, it can be understood that below a certain value of $\lambda < 0$ mass absorption occurs at the sheet and it increases with increasing magnitude of $\lambda < 0$. As a consequence, the species boundary layer thickness increases with increase in magnitude of $\lambda < 0$.
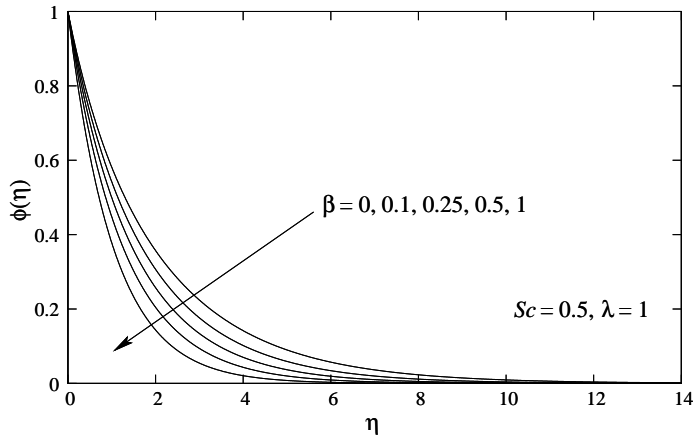
Fig. 3. Concentration profiles $\phi(\eta)$ for various values of β with $\lambda > 0$
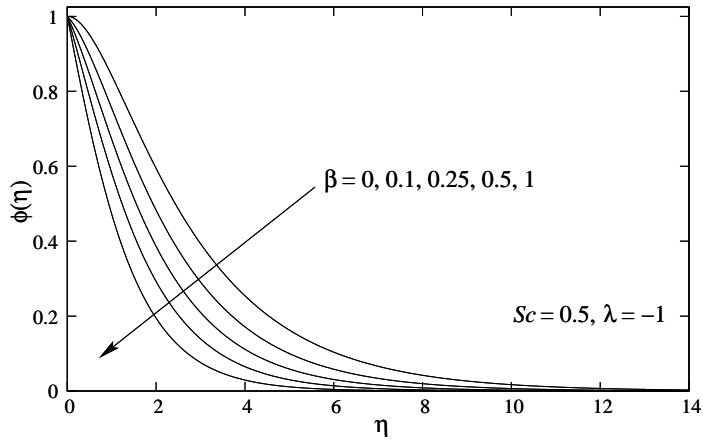
Fig. 4. Concentration profiles $\phi(\eta)$ for various values of β with $\lambda < 0$

Finally, the dimensionless thickness of the species boundary layer $\eta_{\delta C}$ is reported in Table 1 for various values of Schmidt number Sc, reaction rate parameter β and parameter λ. Symbol $\eta_{\delta C}$ is defined as the value of the dimensionless similarity variable η at which the dimensionless concentration $\phi(\eta)$ has been reduced to 0.001. As mentioned above, the thickness of solute boundary layer reduces with Sc, β and $\lambda > 0$, while it increases with increasing magnitude of $\lambda < 0$.

5. Concluding remarks

Mass diffusion with chemical reaction in boundary layer flow induced by an exponentially expanding sheet is investigated. The reaction rate of solute and the wall concentration are taken variable. The governing equations are transformed into
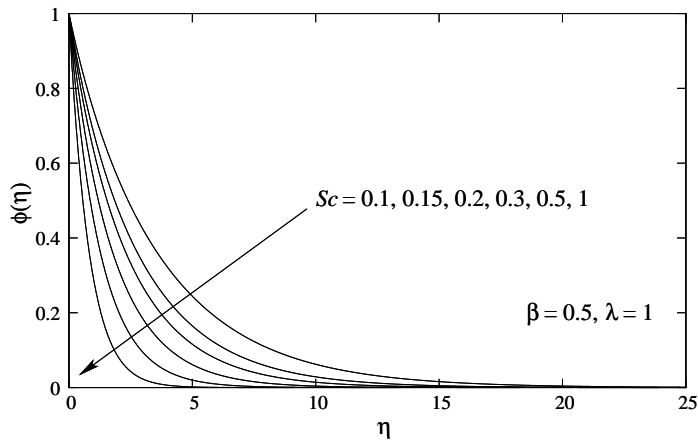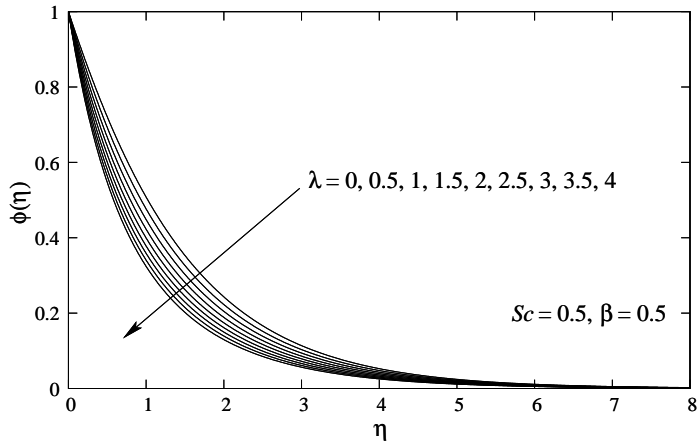
Fig. 5. Concentration profiles $\phi(\eta)$ for various values of $\lambda > 0$
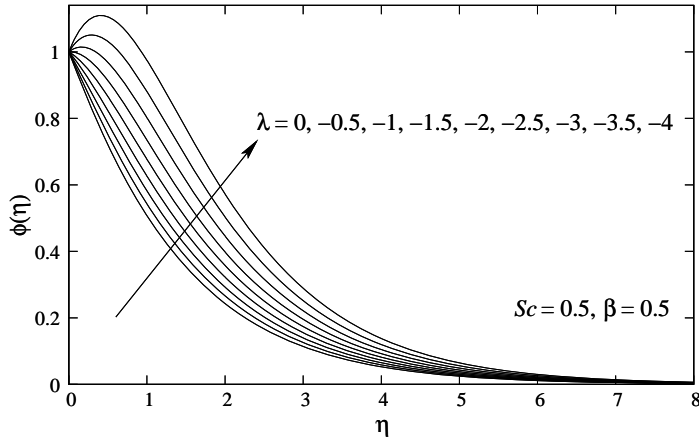
Fig. 6. Concentration profiles $\phi(\eta)$ for various values of $\lambda < 0$

nonlinear self-similar equations by similarity transformations. Then using shooting method, the transformed self-similar equations are solved. The study reveals that due to increase of Schmidt number the concentration and species boundary layer thickness significantly decrease and the effect of reaction rate parameter is similar to that of Schmidt number. The variable wall concentration, characterized by the parameter λ, controls the mass transfer. Most importantly, below a certain value of λ mass absorption occurs at the sheet. It is hoped that this model study will serve a motivation for future experimental work.

Table 1. Values of $\eta_{\delta C}$ for various value of Sc, β and λ

Sc	β	λ	$\eta_{\delta C}$
0.1	0.5	1	25.08
		−1	25.11
0.2	0.5	1	16.33
		−1	16.84
0.3	0.5	1	12.52
		−1	13.06
0.5	0.5	1	8.85
		−1	9.40
1.0	0.5	1	5.42
		−1	5.93
0.5	0.0	1	14.94
		−1	16.26
0.5	0.1	1	12.49
		−1	13.47
0.25	0.5	1	10.57
		−1	11.31
0.5	0.5	−2	9.69
0.5	0.5	0	9.12
0.5	0.5	2	8.62

References

[1] L. J. CRANE: *Flow past a stretching plate.* Zeitschrift für angewandte Mathematik und Physik ZAMP *21* (1970), No. 4, 645–647.

[2] P. S. GUPTA, A. S. GUPTA: *Heat and mass transfer on a stretching sheet with suction and blowing.* Canadian Journal of Chemical Engineering *55* (1977), No. 6, 744–746.

[3] C. K. CHEN, M. I. CHAR: *Heat transfer of a continuous, stretching surface with suction or blowing.* Journal of Mathematical Analysis and Applications *135* (1988), No. 2, 568–580.

[4] K. B. PAVLOV: *Magnetohydrodynamic flow of an incompressible viscous fluid caused by deformation of a surface.* Magnitnaya Gidrodinamika *10* (1974), No. 4, 146–147.

[5] H. I. ANDERSSON: *MHD flow of a viscous fluid past a stretching surface.* Acta Mechanica *95* (1992), Nos. 1–4, 227–230.

[6] M. I. CHAR: *Heat transfer in a hydromagnetic flow over a stretching sheet.* Wärme - und Stoffübertragung *29* (1993), No. 8, 495–500.

[7] M. A. EL-AZIZ: *Temperature dependent viscosity and thermal conductivity effects on combined heat and mass transfer in MHD three-dimensional flow over a stretching surface with Ohmic heating.* Meccanica (2007), No. 42, 375–386.

[8] P. L. CHAMBRE, J. D. YOUNG: *On diffusion of a chemically reactive species in a laminar boundary layer flow.* Physics of Fluids *1* (1958), 48–54.

[9] I. I. STAN: *On boundary layer flow with chemical surface reaction.* Meccanica (1972), No. 7, 72–76.

[10] H. I. ANDERSSON, O. R. HANSEN, B. HOLMEDAL: *Diffusion of a chemically reactive species from a stretching sheet.* International Journal of Heat and Mass Transfer (1994), No. 37, p. 659–664.

[11] A. A. AFIFY: *MHD free convective flow and mass transfer over a stretching sheet with chemical reaction.* Heat and Mass Transfer *40* (2004), Nos. 6–7, 495–500.

[12] R. CORTELL: *Toward an understanding of the motion and mass transfer with chemically reactive species for two classes of viscoelastic fluid over a porous stretching sheet.* Chemical Engineering and Processing: Process Intensification *46* (2007), No. 10, 982–989.

[13] K. BHATTACHARYYA, G. C. LAYEK: *Chemically reactive solute distribution in MHD boundary layer flow over a permeable stretching sheet with suction or blowing.* Chemical Engineering Communications *197* (2010), No. 12, 1527–1540.

[14] A. J. CHAMKHA, A. M. ALY, M. A. MANSOUR: *Similarity solution for unsteady heat and mass transfer from a stretching surface embedded in a porous medium with suction/injection and chemical reaction effects.* Chemical Engineering Communications *197* (2010), No. 6, 846–858.

[15] M. A. EL-AZIZ: *Unsteady fluid and heat flow induced by a stretching sheet with mass transfer and chemical reaction.* Chemical Engineering Communications *197* (2010), No. 10, 1261–1272.

[16] K. BHATTACHARYYA, M S. UDDIN, G. C. LAYEK: *Application of scaling group of transformations to steady boundary layer flow of Newtonian fluid over a stretching sheet in presence of chemically reactive species.* Journal of Bangladesh Academy of Sciences *35* (2011), No. 1, 43–50.

[17] A. J. CHAMKHA, R. A. MOHAMED, S. E. AHMED: *Unsteady MHD natural convection from a heated vertical porous plate in a micropolar fluid with Joule heating, chemical reaction and radiation effects.* Meccanica *46* (2011), No. 2, 399–411.

[18] K. BHATTACHARYYA, G. C. LAYEK: *Slip effect on diffusion of chemically reactive species in boundary layer flow over a vertical stretching sheet with suction or blowing.* Chemical Engineering Communications *198* (2011), No. 11, 1354–1365.

[19] K. BHATTACHARYYA, M. S. UDDIN: *Reactive solute diffusion in boundary layer flow through a porous medium over a permeable flat plate with power-law variation in surface concentration.* Journal of Engineering (2013), Article ID 840596.

[20] K. BHATTACHARYYA, M. S. UDDIN, G. C. LAYEK, P. K. ALI: *Diffusion of chemically reactive species in boundary layer flow over a porous plate in a porous medium.* Chemical Engineering Communications *200* (2013), No. 12, 1701–1710.

[21] E. M. A. ELBASHBESHY, A. M. SEDKI: *Effect of chemical reaction on mass transfer over a stretching surface embedded in a porous medium.* International Journal of Computational Engineering Research *4* (2014), No. 2, 20–28.

[22] K. BHATTACHARYYA: *Reactive solute transfer in stagnation-point flow over a shrinking sheet with diffusive mass flux.* Journal of Applied Mechanics and Technical Physics *56* (2015), No. 3, 464–470.

[23] E. MAGYARI, B. KELLER: *Heat and mass transfer in the boundary layers on an exponentially stretching continuous surface.* Journal Physics D: Applied Physics *32* (1999), No. 5, 577-585.

[24] E. M. A. ELBASHBESHY: *Heat transfer over an exponentially stretching continuous surface with suction.* Archives of Mechanics *53* (2001), No. 6, 643–651.

[25] S. K. KHAN, E. SANJAYANAND: *Viscoelastic boundary layer flow and heat transfer over an exponential stretching sheet.* International Journal of Heat and Mass Transfer *48* (2005), No. 8, 1534–1542.

[26] M. K. PARTHA, P. V. S. N. MURTHY, G. P. RAJASEKHAR: *Effect of viscous dissipation on the mixed convection heat transfer from an exponentially stretching surface.* Heat and Mass Transfer *41* (2005), No. 4, 360–366.

[27] E. SANJAYANAND, S. K. KHAN: *On heat and mass transfer in a viscoelastic boundary layer flow over an exponentially stretching sheet.* International Journal of Thermal Sciences *45* (2006), No. 8, 819–828.

[28] M. Q. AL-ODAT, R. A. DAMSEH, T. A. AL-AZAB: *Thermal boundary layer on an exponentially stretching continuous surface in the presence of magnetic field effect.* International Journal of Applied Mechanics and Engineering *11* (2006), No. 2, 289–299.

[29] M. SAJID, T. HAYAT: *Influence of thermal radiation on the boundary layer flow due to an exponentially stretching sheet.* International Communications in Heat and Mass Transfer *35* (2008), No. 3, 347–356.

[30] K. BHATTACHARYYA: *Boundary layer flow and heat transfer over an exponentially shrinking sheet.* Chinese Physics Letters *28* (2011), No. 7, p.074701.

[31] K. BHATTACHARYYA, G. C. LAYEK: *Thermal boundary layer in flow due to an exponentially stretching surface with an exponentially moving free stream.* Modelling and Simulation in Engineering (2014), Article ID 785049.

[32] K. BHATTACHARYYA, G. C. LAYEK: *Effects of suction/blowing on steady boundary layer stagnation-point flow and heat transfer towards a shrinking sheet with thermal radiation.* International Journal of Heat and Mass Transfer *54* (2011), Nos. 1–3, 302-307.

[33] K. BHATTACHARYYA, S. MUKHOPADHYAY, G. C. LAYEK: *Slip effects on boundary layer stagnation-point flow and heat transfer towards a shrinking sheet.* International Journal of Heat and Mass Transfer *54* (2011), Nos. 1–3, 308–313.

Lightweight design of tractor gearbox based on topology optimization[1]

Jingjing Kang[2], Maohua Xiao[2,3], Xiuqing Fu[2],
Junqing Tang[2], Chengcheng Yan[2], Shanshan
Guo[2], Zhixiong Lu[2]

Abstract. In order to solve the problem of heavy weight and poor manufacturability of the mechanical continuously variable gearbox of high power tractors, the structural design of the gearbox was based on topology optimization. Firstly, the static analysis of the gearbox was carried out, and then the minimum flexibility of the gearbox housing was taken as the objective function. The variable-density method was used to optimize the gearbox topology, remove some excess material and perform rib design. Finally, the results before and after optimization were compared and analyzed. The results show that the weight of the optimized box has been reduced by 21.3 % and the strength and stiffness have been improved to achieve the aim of lightweight.

Key words. Tractor, gearbox, topology optimization, lightweight.

1. Introduction

As the most widely used agricultural vehicle in the development of today's agricultural economy, tractors play an extremely important role. The working environment of the tractors is harsh and the load changes violently. As an important part of the tractor transmission system, the gearbox needs to bear a great deal of load. Therefore, without changing the performance of the gearbox, optimizing the structure of the gearbox housing is an important method to improve the dynamic performance and reliability of the tractor system [1].

ANSYS software is a finite element analysis software developed by ANSYS, USA

---

[2] College of Engineering, Nanjing Agricultural University, Nanjing, 210031, China

[3] Corresponding author; e-mail: `xiaomaohua@njau.edu.cn`

[2]. It uses ANSYS Workbench to optimize the products and the topology optimization is the primary optimization method for structural optimization [3].

At present, lightweight design based on topology optimization is mainly applied to mechanical engineering, aeronautical engineering and material design. It can find a better structure mode on the premise of satisfying the requirement of strength, hardness, etc., however, it is more difficult to solve the problem because it is impossible to describe quantitatively or parameterize the structure, so the practical application is relatively small and it is still in the early stage of development [4]. This paper mainly focuses on the lightweight design of the gearbox housing of the tractor and chooses the topology optimization selectively, based on these, the spatial material distribution of the designated gearbox designed and completed in advance is used as the optimization object, the algorithm further optimized by finite element analysis and then get the best design of the object. Finally, on the premise of ensuring the structure, hardness and rigidity of the gearbox housing, the purpose of reducing the volume, weight and saving the material is realized [5].

2. Structural design and finite element analysis of gearbox housing

The gearbox housing adopted the welding structure, considering the assembly technology of the internal parts of the box body, the input cover plate of the transmission gearbox housing was designed to be detachable ,the plate and the gearbox housing were connected by bolts and the positioning was achieved through the positioning pin; a bearing carrier was designed inside the box to support the output shaft and the input shaft; a hydraulic pump and hydraulic motor are arranged on both sides of the box; and an oil discharge hole was opened at the bottom of the gearbox. The structure of the gearbox housing was designed by "containment of the structure", which simplifies the non-main force receiving parts and ignores overly complex parts such as oil hole. And the gearbox housing structure is shown in Fig. 1.
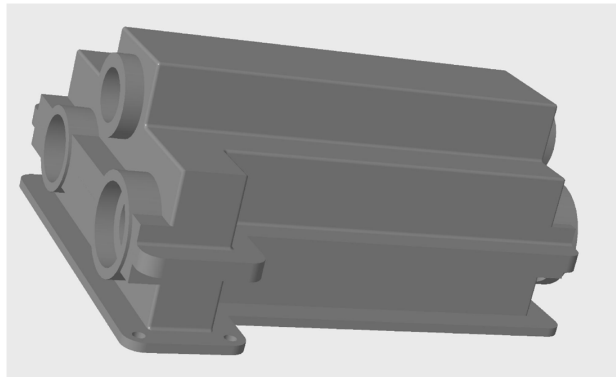
Fig. 1. Box structure

2.1. Previous static analysis of the gearbox

The gearbox housing was made of HT200 gray cast iron with tensile strength of 200 MPa, Poisson's ratio of 0.26, elastic modulus of 100 GPa, density of $7.15\,\mathrm{g/cm^3}$. The total mass of the gearbox housing was 203.06 kg before optimization. The three-dimensional model built in Creo was imported into ANSYS workbench, the model material attribute was added, then the default Solid186 unit type was used to mesh.
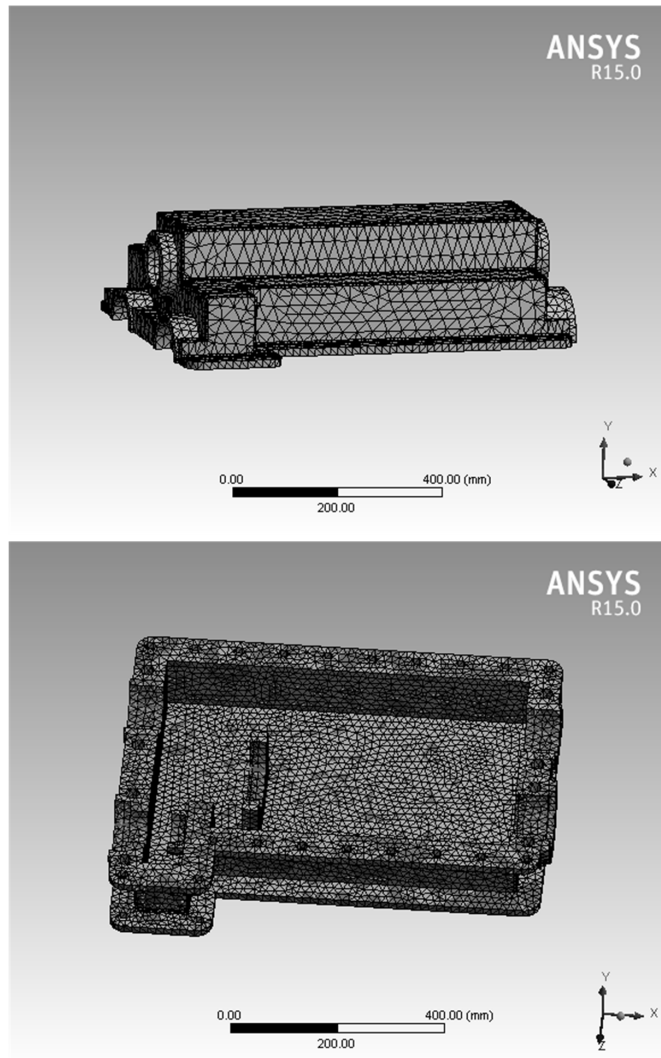
Fig. 2. Grid partition diagram: top–upper case, bottom–lower case

As shown in Fig. 2, the number of upper box nodes is 36025 and the number of units is 18737; the number of lower box nodes is 71244 the number of units is 39133.

Applying load to the gearbox with the maximum power input from the tractor engine, fully considering the weight of the gearbox housing, the gearbox housing mainly bears the bearing force of the moving power transmission shaft system and the cutting table power drive shaft system, etc. The stress-strain cloud diagram of upper and lower box after statics analysis is shown in Figs. 3 and 4.
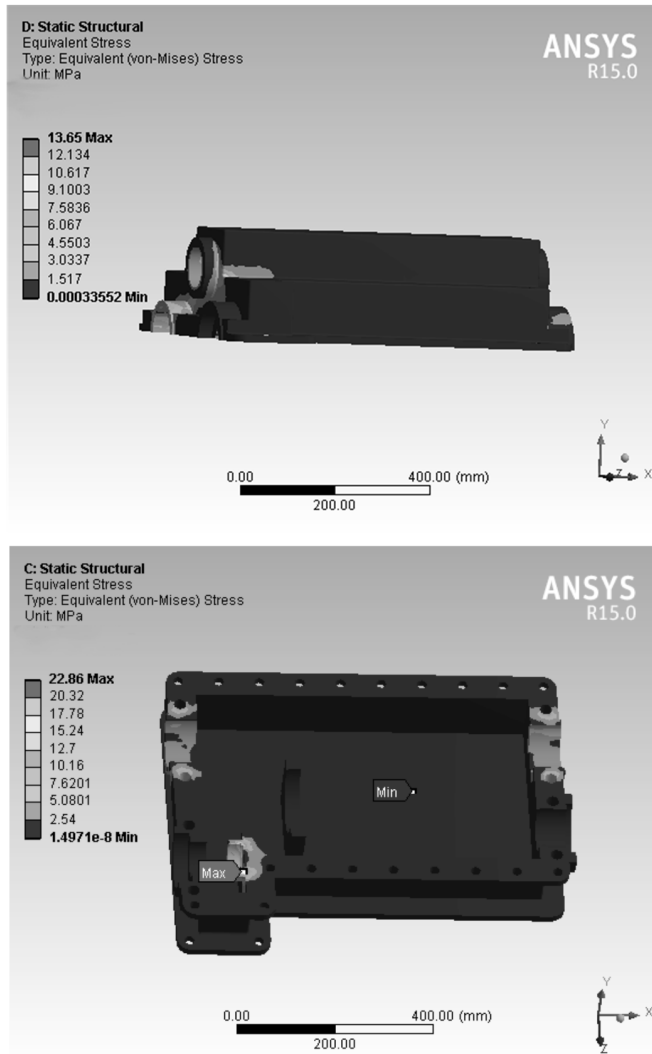
Fig. 3. Optimum stress cloud image: top–upper case, bottom–lower case

The maximum equivalent stress of the gearbox was 22.86 MPa and the maximum deformation was 2.73×10^{-7} mm, both of them were found in the input bearing carrier hole. Other parts of the stress and deformation were small enough to satisfy the overall design requirements. The tensile strength of material is 200 MPa, which meets

the strength requirements nevertheless the weight of the gearbox is comparatively large. Thus, the gearbox housing could be optimized.
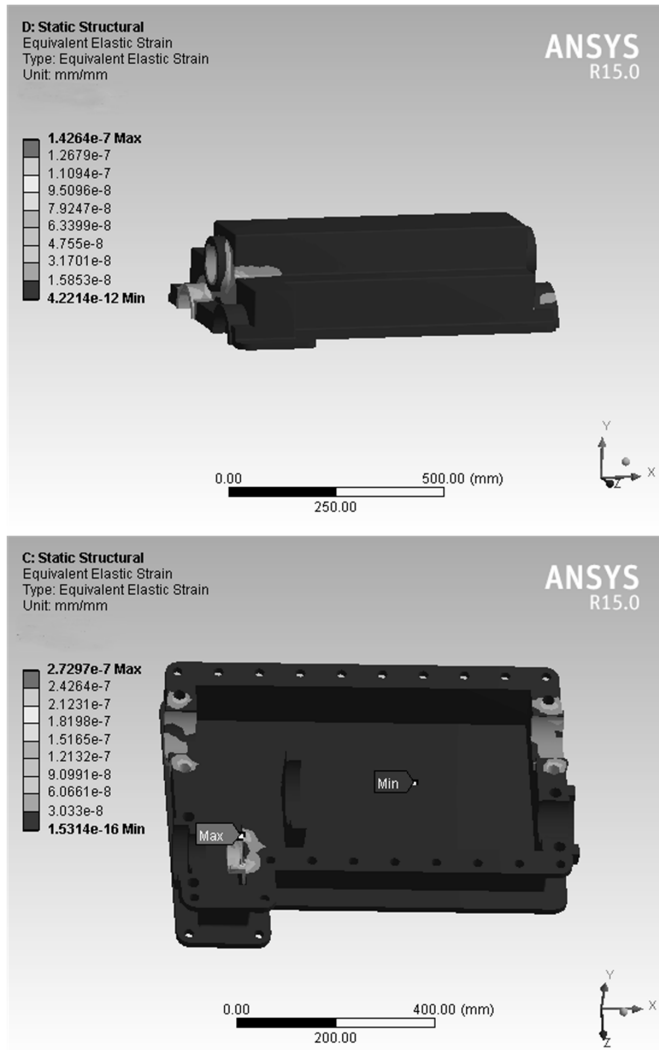
Fig. 4. Optimized strain cloud image: top–upper case, bottom–lower case

3. Topology optimization of the gearbox

3.1. Topological optimization theory

Topology optimization is a kind of mathematical method which optimizes the distribution of materials in a given area according to the given load conditions,

constraint condition and performance criteria. Furthermore, it is also a kind of structural optimization. Structural optimization can be divided into optimization of measurement, optimization of shape, optimization of appearance and topology optimization. At present, the methods of continuum topology optimization mainly include homogenization method, variable density method [5] and gradual structure optimization method, etc. [6].

The type of topological optimization used in this paper is the variable density method with the selected algorithm: Lagrange multiplier method [7]. The minimum flexibility of the gearbox housing is taken as the objective function and the mathematical model is

$$\text{Minimize}: \quad C(X) = F^{\mathrm{T}} D \,, \tag{1}$$

$$X = \{X_1, X_2, \cdots X_N\}^{\mathrm{T}} \,, \tag{2}$$

$$\text{s.t.} \left\{ \begin{array}{c} f = \frac{V - V_1}{V_0} \,, \\[2mm] 0 < X_{\min} < X_\varepsilon < X_{\max} \,, \\[2mm] F = KD \,. \end{array} \right\} \tag{3}$$

Here, C is the degree of structural flexibility, F is the load vector; D is the displacement vector of the structure, f is the percentage of the remaining material, V is the volume of the filled material of the structure and V_0 is the volume of the design range of the housing structure, V_1 is the volume of material with density less than 1, $X_{\min}$ is the lower limit of relative density of the element, $X_{\max}$ is the upper limit of relative density of the element and K is the matrix of global stiffness.

3.2. Topology optimization design of gearbox structure

The three-dimensional model of the box built in Creo 4.0 was imported into ANSYS workbench and the topology optimization of the finite element model was performed based on the shape optimization module in Workbench [8]. The density of element material was taken as the design variable, the percentage of the volume reduction was used as the constraint function and the flexibility minimization of the structure was taken as the objective function. First of all, the model constraint settings were carried out. And those were the same as the static analysis. According to multiple tests, the Target Reduction in Shape Finder was set to 70 to optimize the model. The results are shown in Fig. 5. Remove indicates the part to be removed (see Fig. 6), Keep indicates that the part to be retained is also the most effective part bearing the load, which is mainly distributed near the bearing holes of the dynamic transmission shaft system and the output bearing holes of the gearbox housing. The relevant section needs to be reinforced in the design. Marginal indicates that it can be retained or removed [9].

In this paper, stiffeners were arranged around the bearing holes and the thick-
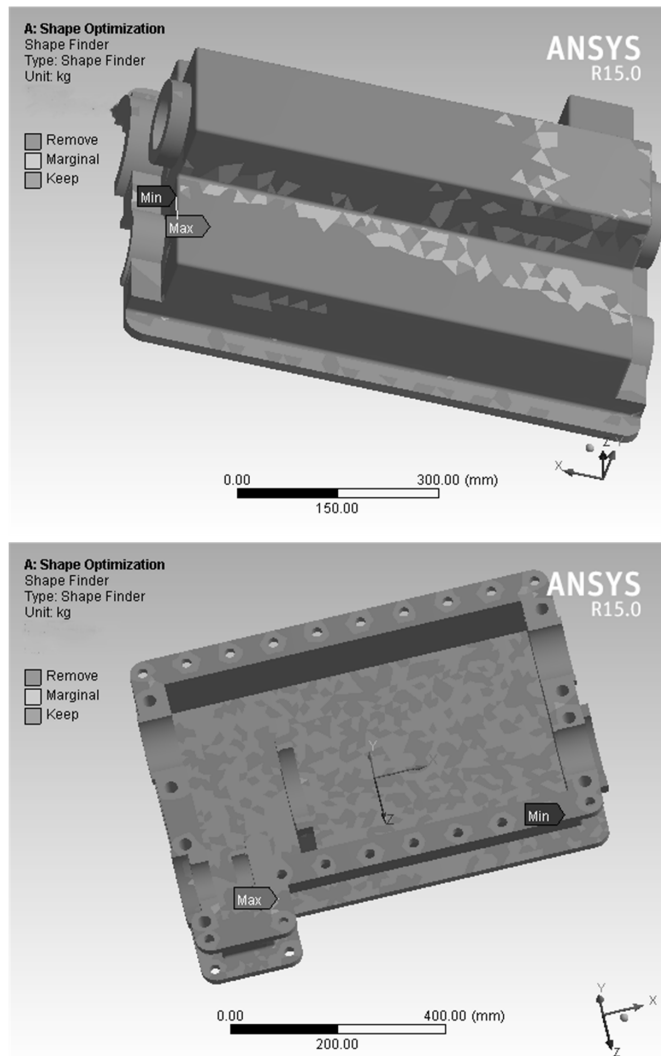
Fig. 5. Case topology optimization results: top–upper case, bottom–lower case

ness of the partial protruding table of the dynamic drive shaft system was reduced appropriately. The fixed bottom surface of the gearbox and the side surface of the bearing hole are more removed. Thereby, its wall thickness can be reduced in the design. The box structure was redesigned based on the optimized results, as shown in Fig. 7.
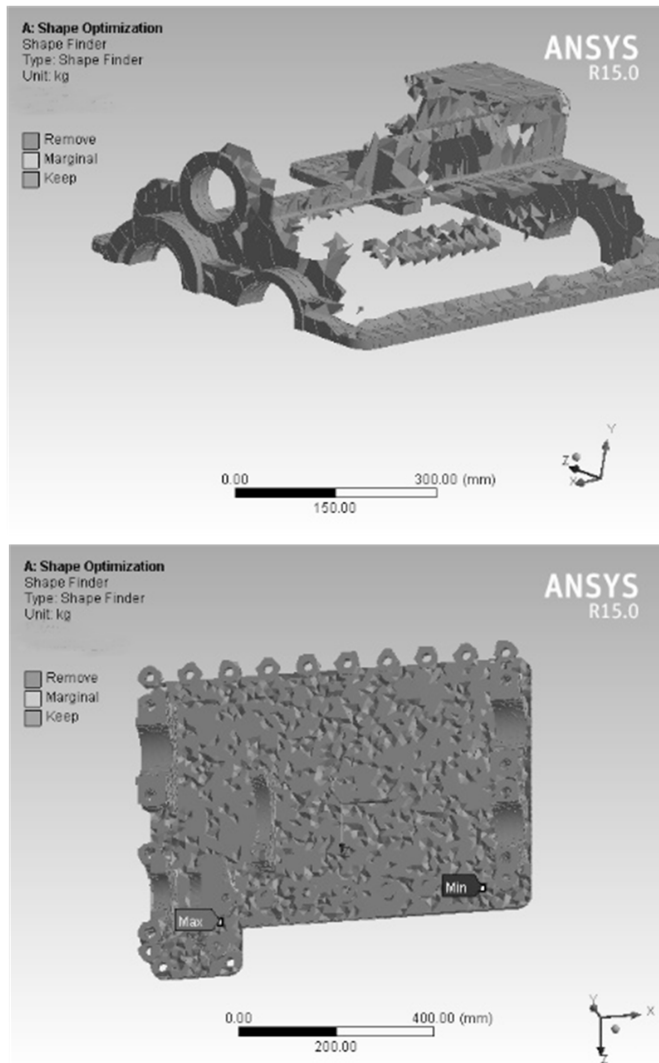
Fig. 6. Case topology optimization results: top–upper case, bottom–lower case

4. Comparison and analysis of statics of gearbox housing after optimization

The optimized three-dimensional model was imported into the ANSYS workbench. The same constraints and loads were applied to the box as in the previous section. The optimized gearbox housing was subjected to static analysis to obtain an optimized rear gearbox. The stress and strain conditions of the optimized gearbox housing are shown in Figs. 8 and 9.

In Fig. 8, the stress distribution of the housing is improved after optimization
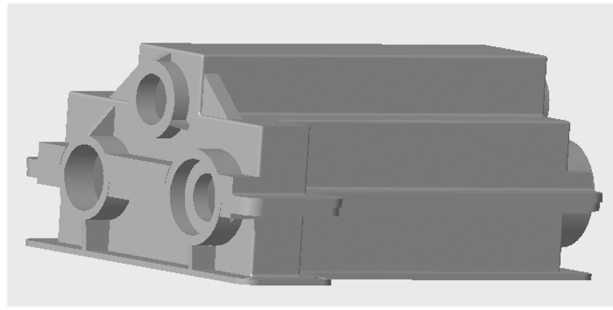
Fig. 7. Optimized tank model

and the maximum stress is 17.964 MPa, which is 21.42 % lower than that before optimization. Also, the allowable stress is smaller than that before optimization, which meets the requirements of box strength. The optimized housing maximum value of the total deformation of the optimized box is 1.943×10^{-7} mm, which is a decrease of 28.83 % compared to the previous data.

Compared with the parameters before and after optimization (such as Table 1), it is found that the deformation of the box has been reduced, the stress distribution has become more reasonable and the strength and stiffness have been obviously improved after the optimization. At the same time, the weight of the gearbox housing after optimization is 159.83 kg, which is 21.3 % lower than the 43.23 kg before optimization. And the reliability has been enhanced and the mass has been reduced.

Table 1. Parameters of the gearbox before and after the model improvement under the same load and constraints

Parameter	Mass (kg)	Maximum stress (MPa)	Maximum displacement (mm)
Before optimization	203.06	22.86	2.73×10^{-7}
Optimized	159.83	17.964	1.943×10^{-7}

5. Conclusion

In this paper, the topology optimization method of variable density method was used to optimize the design of gearbox housing, which could remove some of the surplus materials to obtain the best layout of reinforcement and control the total structural weight magnificently. Through the contrast analysis before and after the optimization of the gearbox housing, it can be seen that under the premise of satisfying the stiffness and strength, the final design mass of the structure was controlled at 159.83 kg which was a decrease of 21.3 %. As a result, the maximum
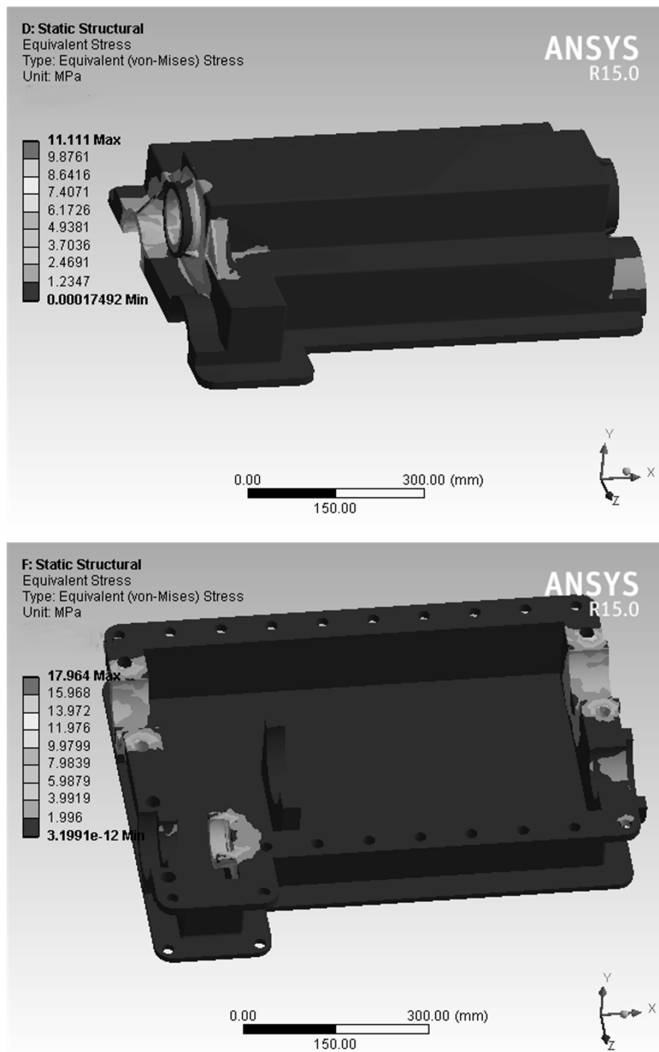
Fig. 8. Optimized stress cloud: top–upper case, bottom–lower case

deformation and stress of the gearbox were diminished and thus the lightweight
design was realized.

References

[1] Fan Zijie, Gui Liangjin, Su Ruiyi: *Research and development of automotive lightweight technology.* Journal of Automotive Safety and Energy 5 (2014), No. 1, 1–16

[2] Cha Taidong, Yang Ping: *Optimization design of fixed support based on ANSYS workbench.* Coal Mine Machinery 33 (2012), No. 2, 28–30.
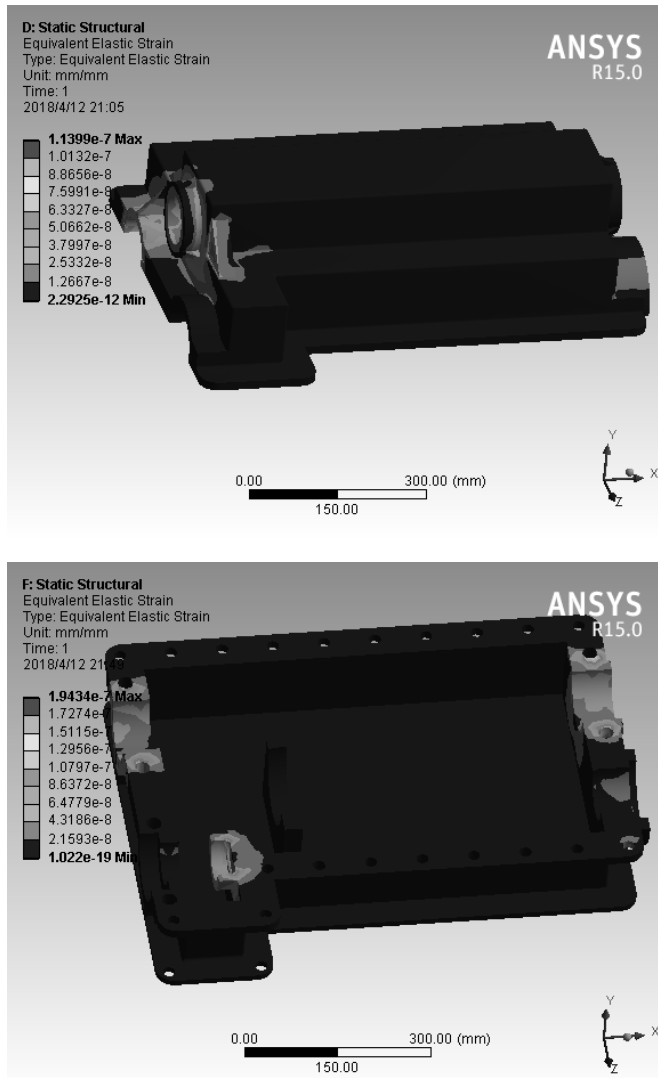
Fig. 9. Optimized stress cloud: top–upper case, bottom–lower case

[3] HE YUSONG, LI YUFENG: *Topological optimization design of the base of position stage based on ANSYS workbench.* Ordnance Industry Automation *35* (2016), No. 8, 94–96.

[4] ZHAO LIHONG, GUO PENGFEI, SUN HONGJUN: *Development actuality and prospect on research of structural topology optimization.* Journal of Liaoning Institute of Technology (2004), No. 1, 46–49.

[5] M. P. BENDSØE: *Optimal shape design as a material distribution problem.* Structural optimization *1* (1989), No. 4, 193–202.

[6] Y. L. LEE, J. PAN, R. HATHAWAY, B. RICHARD: *Fatigue testing and analysis.* New York, Elsevier Inc., 2005.

[7] DU HAIZHEN, RONG JIANHUA: *Topology optimization design of vehicle frame structure.* Machine Design & Research (2007), No. 1, p. 116–119.

[8] XU XIAOMEI, JIANG YIPING, CHEN NING, LEE HEOW PUEH: *Dynamic behavior of a vehicle with rear axle compliance steering.* Journal of Vibroengineering *18* (2007), No. 4, 4483–4497.

[9] XU XIAOMEI, CHEN NING, LEE HEOW PUEH: *A review on the applied research of rear wheel compliance steering.* Automobile Technology (2016), No. 7, 1–6.

Study on torsion fatigue life by steering knuckle arm drive in vehicle parts[1]

Weifeng Cao[2]

Abstract. The steering knuckle arm is the main part steering the front axle as well as the key part connecting the front suspension with the hub and the vehicle. Also, it is an important part of the steering drive mechanism with multiple functions, whose fatigue size directly affects the safety of vehicle driving. Once fracture happens to it, steering failure can be caused, resulting in irreparable damage. In this paper, the simulation analysis of double wishbone cantilever beam and the topological optimization of steering knuckle were carried out. The method of relieving the fatigue life was studied by experiments. The results showed that the mechanical properties and fatigue life of the steering knuckle were greatly improved after topology optimization.

Key words. Knuckle arm, fatigue life, structure optimization.

1. Introduction

The steering knuckle arm is an important safety part in the car steering system [1], which plays a bearing and guiding role in the process of vehicle running. If the steering knuckle arm is suddenly broken, it can cause serious accidents. Therefore, there is a need to impose some measures on the strength, stiffness and fatigue life of the knuckle arm to extend its service life [2]. Many experts in China and abroad have carried out related researches. According to the reason of the breakage of steering knuckle arm of light automobile, Wang et al. [3] proposed to prolong the fatigue life of the steering arm by improving the excessive fillet and the surface quality. Sivananth et al. [4] compared the differences between the conventional materials and metal matrix composites for making knuckle arm and found that the metal matrix composites could reduce joint weight by 60 % compared to nodular cast iron materials and could be widely used in automobiles. In this paper, the bearing of the knuckle arm was analyzed and the fatigue life of the 40Cr knuckle was tested. The results

[2]School of Energy Engineering, Yulin University, Yulin, 719000, Shaanxi, China; E-mail: weifengc@sohu.com

showed that the fatigue life of the knuckle did not meet the requirements. Hence, the 40Cr knuckle was topologically optimized and a test was carried out after the optimization. The test results showed that the mechanical properties of the knuckle were greatly improved and its fatigue life was prolonged, which provided references for the research of the fatigue life of knuckle arm.

2. Steering knuckle arm fatigue analysis

Based on the characteristics of structural fatigue stress, there are two methods for the analysis of finite life fatigue: stress fatigue analysis [5] and strain fatigue analysis [6]. In this study, stress fatigue analysis was selected. In the fatigue analysis, we need to collect the load spectrum, carry out material property experiments and structural stress analysis to make life prediction according to the results.

2.1. Fatigue analysis load spectrum determination

When calculating the fatigue life, we can use the stress-life curve method of the stress material applying structural unit load stress field and material fatigue performance curve, which is a widely applied method [7]. The fatigue load spectrum is usually obtained by field measurement. With the increasing popularity of technology, we can obtain the load spectrum through simulation analysis and verify it with experiments. The specific steps are as follows:
(1) Consider the use of research objects.
(2) Obtain the load time history by test.
Based on the two steps, the working conditions to be tested can be determined and data statistics can be carried out to finally get the target load spectrum.

2.1.1. Static strength analysis. Under the condition of satisfying the principle of meshing, a model of the steering knuckle arm was established. A force was applied along the horizontal direction of the other circular hole in the swing arm. The material of the steering knuckle arm was 40Cr, the lower yield strength was 785 MPa, and the selection of safety coefficient was determined according to the fatigue curve of different materials. By querying "Mechanical Engineering Material Performance Data Manual" [8], it was obtained that the safety factor of 40Cr was 1.57 and the allowable stress of the material was 500 MPa. The maximum stress of the steering knuckle arm was calculated to be 770 MPa using Radioss engineering software and the area was located in the fracture position. Since the model set the boundary conditions and this area was also the area where the stress was concentrated in the model, the maximum stress was greater than the allowable stress. Therefore, it was determined that the fatigue life in this area was not long and fatigue analysis was applied to solve the fracture problem of the knuckle arm. To make the analysis results more reliable, the unit load spectrum to be used in the fatigue analysis was obtained by testing the strain relation of the knuckle arm in the specific situation, which was taken as the standard for the application software to carry out fatigue analysis.

2.1.2. Collection point layout of steering arm stress test. The test value of the steering knuckle stress can be obtained from the strain value and modulus of elasticity calculation while the strain value is obtained by pasting strain rosette on the knuckle arm [9]. On the smooth surface of the steering arm near the fracture, choose a pasted strain rosette, then the strain spectrum of the strain rosette can be extracted by the experiment equipment and converted to the actual stress spectrum.

2.1.3. Working condition test. Keep the vehicle speed at $40\,\mathrm{km/h}$ and drive it around the experimental site (perimeter: $6\,\mathrm{km}$). During the process, the data of the steering knuckle state was recorded and the actual stress load spectrum was obtained through conversion.

2.2. Determination of material fatigue characteristics

The profitability fatigue analysis method was applied in this section and the fatigue characteristics of the steering knuckle could be described with the S-N curve. The power function in describing is as follows:

$$S^m N = C \,, \tag{1}$$

where m and C refer to material and stress ratio. Then, the following equation can be obtained by taking logarithm:

$$\ln S = X + Y \ln N \,, \tag{2}$$

where $X = \ln C/m$ and $Y = -1/m$.

According to the fatigue parameters of 40Cr in the manual of mechanical materials, the S-N curve of 40Cr is as follows:
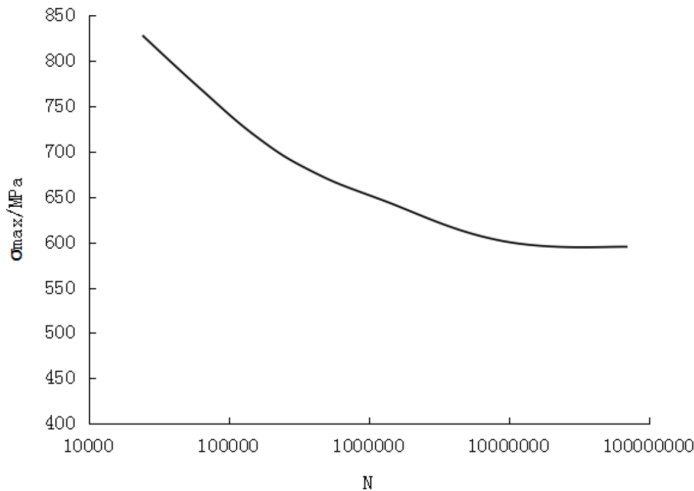
Fig. 1. S-N curve for 40Cr

According to the above S-N curve, the fatigue mileage at the fracture site of the knuckle arm was $6 \times 13224 = 79344$ km under the original state of the knuckle arm, which was obviously low and needed to be optimized.

3. Knuckle topology optimization

Topology optimization is based on the achieved optimization shape and optimal material distribution of the vehicle, which is a mathematical method [10]. When designing, the computer can propose constraints based on the material characteristics of each part, so as to change the distribution of materials to achieve the purpose of optimizing the parts. In OptiStruct, optimal results are obtained when the amount of change in the objective function in any three consecutive iterations is less than the given tolerance. When making knuckle optimization, we need to distinguish the range that we can design. As a vehicle is composed of many parts which are connected to each other, with the position of each and the connecting mode fixed, the parts which are designable should be determined first before optimization is carried out. The designable part of the vehicle knuckle is shown in Fig. 2.
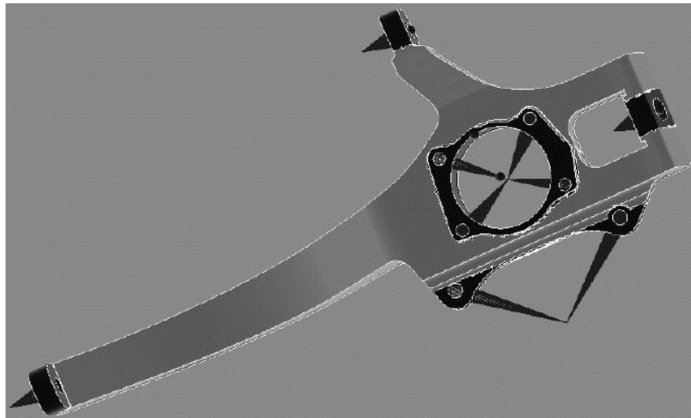
Fig. 2. Part of the knuckle to be designed

3.1. Design variables and response settings

OptiStruct has a good optimization solver procedure that optimizes static, modal, buckling and frequency response processes and can therefore define optimization parameters in the model, which is a design variable [11]. In optimizing, OptiStruct requires multiple structural responses to define optimization goals and constraints. In this design, the structural responses include quality, volume, static displacement and buckling factor.

3.2. *Optimization objective function and constraints*

In this paper, the knuckle optimization goal is to maximize the knuckle weight under the premise that the maximum stress on the steering knuckle under all working conditions is less than the allowable stress. Allowable stress is the most basic data in mechanical design. The working stress of a part cannot exceed the allowable stress. Allowable stress is determined based on the material strength, load, environmental conditions, processing quality, calculation accuracy and the importance of parts. Therefore, allowable stress and the ultimate stress of the part material are related to the safety factor. In addition, the size of allowable stress also has a great relationship with the characteristics of the material. The accuracy of the load, the reliability of the material's performance data, and the importance of the part are all related to the safety factor. Allowable stress is calculated as follows:

(1) The yield limit of plastic material is the ultimate stress. Because plastic materials can mitigate local stresses, they have a safety factor of between 1.2 and 1.5, while a less plastically ductile material has a safety factor of between 1.5 and 2.5.

(2) The strength limit of brittle materials is the ultimate stress, under which circumstance we need to select a larger value as the safety factor of the material. In this study, the knuckle material is 40Cr, which is a plastic material whose permissible stress should be calculated in accordance with the allowable stress of the plastic material above. Because the material's yield strength to strength limit ratio exceeds 0.6, the safety factor for this material is relatively large.

3.3. *Knuckle design*

According to the above design variables and constraints, we optimized the steering knuckle arm. As the steering knuckle is processed using the embryo, it is necessary to use manufacturing process as a reference for design. The embryo of the steering knuckle designed in this paper is a forge piece. As shown in Fig. 3, the B, C and D parts of the steering knuckle underwent major changes. Part B and C are in the form of a truss that can greatly reduce the material amount, but the forging of this structure is very complicated. The D area has a hollow area, which is difficult to design. For part B, a convex shaped groove was designed, which was 15 mm deep, with the wall thickness on both sides of 9 mm. Similarly, a groove with 5 mm depth and 28 mm width was designed for part C and a groove with 5 mm depth was designed for part D. The final designed result is shown in Fig. 3.

4. Optimized knuckle test results and analysis

4.1. *Allowable stress test*

After the optimization design, we tested the steering knuckle under the emergency braking condition, the uneven road condition and the side slipping condition, and recorded the test data. The test results are listed in Table 1.
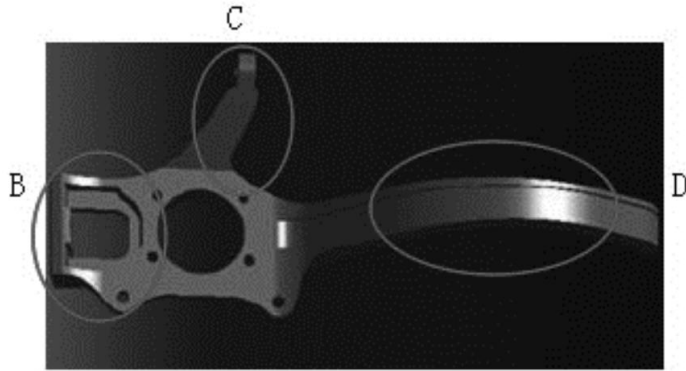
Fig. 3. Knuckle optimized design model

Table 1. Stress data before and after optimization

	Emergency braking (MPa)	Uneven road (MPa)	Side slipping (MPa)
Before optimization	203.6	129.6	125.7
After optimization	309.4	212.3	175.2

As shown in Table 1, the stress of the optimized knuckle increased by 105.8 MPa under emergency braking condition and 82.7 MPa under uneven road condition and again 49.5 MPa under slide slipping condition. The maximum allowable stress after optimization was greatly improved and within the constraint range. Therefore, the knuckle meets the conditions of use of the equipment after optimization.

4.2. Service life test

The results are summarized in Table 2.

Table 2. Fatigue mileage test results

	Fatigue mileage (km)
Before optimization	79344
After optimization	242586

As shown in Table 2, after the optimization, the fatigue mileage of steering knuckle is 40431×6 km/time $= 242586$ km, which is greatly improved compared with 79344 km before optimization, suggesting that the knuckle had longer service life after optimization. The analysis of the fatigue life of the knuckle after optimization found that the optimization could greatly improve the fatigue life of the knuckle arm. In summary, after topology optimization, the mechanical properties of the knuckle were greatly improved, and its allowable stress was greatly improved in

the allowable range of material requirements. The topologically optimized knuckle had a longer service life and met the optimal design requirements of the knuckle.

5. Conclusion

In this paper, the torsional fatigue life of the steering knuckle was studied. Firstly, the bearing of the knuckle arm was analyzed, and then the fatigue life of the knuckle arm was analyzed, the result of which showed that the knuckle had a short fatigue life. Hence, we topologically optimized the material and tested the optimized material. The test results showed that the mechanical properties of the knuckle were greatly improved and its fatigue life was prolonged, which provided a reference for delaying the fatigue life of knuckle arm.

References

[1] G. Yang, X. Tan, Y. R. Zhang: *An intelligent video surveillance system for android smart phone.* Advanced Materials Research *850–851* (2014), 884-888.

[2] Z. Y. Wang, L. Chen: *Design of mobile phone video surveillance system for home security based on embedded system.* Chinese Control and Decision Conference (2015 CCDC), 23–25 May 2015, Qingdao, China, IEEE Conferences (2015), 5856–5859.

[3] B. Cui, J. Cui, Y. Duan: *Intelligent security video surveillance system based on DaVinci technology.* International Conference on Measuring Technology and Mechatronics Automation (ICMTMA), 16–17 Januar 2013, Hong Kong, China, IEEE Conferences (2013), 655–658.

[4] M. Komorkiewicz: *Real-time detection of movement in prohibited direction for video surveillance system.* Image Processing & Communications *17* (2012), No. 4, 251–264.

[5] J. Zhang, Y. Shan, K. Huang: *ISEE Smart Home (ISH): Smart video analysis for home security.* Neurocomputing *149* Part B, (2015), 752–766.

[6] G. Di Caterina, I. Hunter, J. J. Soraghan: *DSP embedded smart surveillance sensor with robust SWAD-based tracker.* International Conference on Advanced Concepts for Intelligent Vision Systems (ACIVS), 4–7 September 2012, Brno, Česká Repulika, Springer Nature (LNCS), *7517* (2012), 48–58.

[7] H. Liu, S. Chen, N. Kubota: *Intelligent video systems and analytics: A survey.* IEEE Transactions on Industrial Informatics *9* (2012), No. 3, 251–264.

[8] G. Garibotto: *Video surveillance and biometric technology applications.* International Conference on Advanced Video and Signal Based Surveillance, 2–4 September 2009, Genova, Italy, IEEE Conferences (2009), 288.

[9] M. Campos, T. Martins, M. Ferreira, C. Santos: *Detection of defects in automotive metal components through computer vision.* International Symposium on Industrial Electronics (ISIE), 30 June–2 July 2008, Cambridge, UK, IEEE Conferences (2008), 860–865.

[10] P. Li, J. Liao, C. Hu, Y. Yin, M. Q. H. Meng: *Design of medical remote monitoring system base on embedded Linux.* International Conference on Information and Automation (ICIA), 6–8 June 2011, Shenzhen, China, IEEE Conferences (2011), 590–594.

[11] S. Yang, W. Shao, H. Song, W. Xu: *Compass: A data center bootloader for software defined infrastructure.* International Conference on Networking and Services (ICNS), 24–29 May 2015, Rome, Italy, IARIA (2015), 98–103.

[12] P. Sagar, N. Naveen, A. Joseph, K. H. Abdul Nazer, M. Likhin: *Implementation of CMNN based industrial controller using VxWorks RTOS Ported to MPC8260.*

International Conference on Advances in Computing and Communications, 29–31 August 2013, Cochin, India, IEEE Conferences (2013), 239–242.

[13] S. C. HUANG: *An advanced motion detection algorithm with video quality analysis for video surveillance systems.* IEEE Transactions on Circuits and Systems for Video Technology *21* (2011), No. 1, 1–14.

[14] J. H. DUNCAN, T. C. CHOU: *Temporal edges: The detection of motion and the computation of optical flow.* International Conference on Computer Vision, 5–8 December 1988, Tampa, FL, USA, IEEE Conferences (1988), 374–382.

[15] Y. LUO, T. D. WU, J. N. HWANG: *Object-based analysis and interpretation of human motion in sports video sequences by dynamic bayesian networks.* Computer Vision and Image Understanding *92* (2003), Nos. 2–3, 196–216.

Analysis of marine diesel engine main bearing lubrication based on thermoelastic hydrodynamic pressure lubrication

Xu Yanming[1], Du Jinyin[1], Wang Xin[1], Wang Ranran[1]

Abstract. Based on the average flow model, Greenwood/Tripp asperity contact theory and generalized Reynolds equation, combination of finite difference method, finite element method (FEM) and multibody dynamics simulation calculation method, considering the influence factors such as the roughness of main crankshaft journal and bush of diesel engine, and the deformation and thermal effect of crankshaft and bearing seat, a crankshaft model of a marine diesel engine is established in this paper. The final results show that the third main bearing lubrication conditions is relatively poor, the methods of enlarging the groove width, reducing the lubricating oil pressure, increasing the bearing clearance and increasing roughness can ensure that the diesel engine main bearing minimal oil film thickness increases, the lard membrane pressure decreases, and good lubrication is achieved.

Key words. Marine diesel engine, asperity contact, main bearing, thermal elastic fluid, hydrodynamic lubrication.

1. Introduction

The crankshaft stress of marine diesel engine is complex, whose running status will directly affect the operation of a ship. As the developing direction of marine diesel engines to super long stroke, high eruption and high power, the lubrication condition of crankshaft-bearing model has been a research focus. In the 1880s, Reynolds put forward the famous idea of Reynolds equation [1], which means the formation of hydrodynamic lubrication theory. In the 1960s, Dawson and Hudson [2] put forward the corresponding theory of thermal hydrodynamic (THD) lubrication analysis. They considered the various thermal effects of the related factors on the lubricating oil viscosity. Since then, with the increase of engine explosion

---

[1]Department of Marine Engineering, Tianjin Maritime College, Tianjin, 300350, China

pressure and increase of the rotational speed, in bearing dynamic lubrication theory, the elastic deformation influence of friction pairs on bearing lubrication under the condition of overloading should be considered, then comes the elastic hydrodynamic lubrication theory (TEHD) [3]. After decades of development, since there is a deviation between the two approaches to theoretical calculation, in order to be more consistent with the actual situation, and considering the friction pairs affected by mechanical deformation and thermal factors, a new thermal elastic hydrodynamic lubrication theory (TEHD) was put forward integrating EHD and THD [4].

2. Mathematical model and control equation

Based on the average flow model, Greenwood/Tripp asperity contact theory, generalized Reynolds equation, thermoelastic hydrodynamic lubrication theory, the finite element theory and the theory of multibody dynamics, the paper establishes an entity model of a marine diesel engine crankshaft, calculating the influence factors such as the surface roughness of diesel engine crankshaft main bearing journal and bush, the deformation and thermal effect of crankshaft and bearing seat and analyzing the bearing lubrication characteristics.

2.1. Extended Reynolds equation based on the average flow model

During the diesel engine operation, with regard to the main bearing lubrication, crank shaft journal rotation, and the upper and lower bearing bushes are fixed under certain constraints, the oil filling ratio γ is introduced, based on the average flow model, the generalized Reynolds equation of the sliding bearing under dynamic load condition is established, and solved using the finite difference method.

$$\frac{\partial}{\partial y}\left(\frac{1}{12\eta}\gamma h^3 \cdot \frac{\partial p}{\partial y}\right) + \frac{\partial}{\partial x}\left(\frac{1}{12\eta}\gamma h^3 \cdot \frac{\partial p}{\partial x}\right) = \gamma\frac{\upsilon}{2} \cdot \frac{\partial h}{\partial y} + h\frac{\upsilon}{2} \cdot \frac{\partial \gamma}{\partial y} + \frac{\partial\left(\gamma h\right)}{\partial t} \qquad (1)$$

In the equation, x and y denote the coordinates, t is time, p stands for the the oil film pressure, h is the oil film thickness, υ represents the linear velocity, γ denotes the oil filling rate and η stands for the lubricating oil dynamic viscosity [5].

1. The axial boundary condition reads

$$p = P_{\mathrm{a}}\left(x = \pm\frac{B}{2}\right). \qquad (2)$$

Here, P_{a} denotes the environmental stress, B is the bearing width and p stands for the oil film pressure.

2. The circumferential boundary conditions:

At the oil film starting, i.e. $\gamma = 0$

$$p = P_{\mathrm{in}} \text{ for } |X| \le \frac{l}{2},$$

$$p = P_{in} \frac{B - 2\,|X|}{B - l} \ \text{for} \ \frac{l}{2}\,|X| \le \frac{B}{2}\,. \tag{3}$$

In this equation, P_{in} means the oil pressure and l denotes the groove width. Moreover,

$$\frac{\partial p}{\partial \gamma} = 0, \quad P = P_{\text{a}}, \quad v = \frac{y}{r}\,, \tag{4}$$

where r denotes the radial coordinate.

3. The oil supply area:

$$p = P_{in}\,. \tag{5}$$

4. The hole boundary conditions:

$$P = P_{\text{c}}, \quad \gamma = 1\,,$$

$$P < P_{\text{c}}, \quad \gamma < 1\,, \tag{6}$$

where P_{c} is the air-pocket pressure.

2.2. The bearing bush heat conduction equation

The main bearing of diesel engine in this paper is simplified, uniform solid density, isotropic, no heat source in the system, the simplified heat transfer equation is

$$\frac{\partial T}{\partial t} = \frac{K_{\text{b}}}{C_{\text{b}} P_{\text{b}}} \left(\frac{\partial^2 T}{\partial r^2} + \frac{1}{r} \cdot \frac{\partial T}{\partial r} + \frac{1}{r^2} \cdot \frac{\partial^2 T}{\partial \theta^2} + \frac{\partial^2 T}{\partial x^2} \right)\,. \tag{7}$$

The boundary conditions are:

$$T\,|_{\theta=0} = T\,|_{\theta=2\pi}\,, \tag{8}$$

$$\frac{\partial T}{\partial x}\,|_{x=0} = 0\,. \tag{9}$$

The interface of bearing bush and oil:

$$\frac{\partial T}{\partial r}\,|_{r=R} = -K\,(\theta)\,\frac{R}{C_{\text{b}} K_{\text{b}} h}\,\frac{\partial T}{\partial y}\,|_y\,, \tag{10}$$

The interface of bearing bush and circumstance:

$$\frac{\partial T}{\partial r}\,|_{r=R_{\text{b}}} = -\frac{h_{\text{b}} R_{\text{b}}}{K_{\text{b}}}\,(T\,|_{r=R_{\text{b}}} - T_{\text{a}})\,. \tag{11}$$

The two end surfaces of the bearing:

$$\frac{\partial T}{\partial x}\Big|_{x=\pm\frac{B}{2}} = -\frac{h_{\mathrm{b}}R_{\mathrm{b}}}{K_{\mathrm{b}}}\left(T\Big|_{x=\pm\frac{B}{2}} - T_{\mathrm{a}}\right), \tag{12}$$

where T_{a} denotes the ambient temperature.

3. Diesel engine model and parameters

A marine diesel engine is considered as the prime mover of marine generator, with four-cylinders, five main bearings together, and rated speed 900 rpm. The main performance parameters are listed in Table 1. The relationship curve between the explosion pressure and the crank angle is shown in Fig. 1.

Table 1. Working parameters of diesel engine

Parameter	Parameter value
Bearing bush width B (mm)	19
Bearing bush oil groove/width	$270°$–$90°/4\,\mathrm{mm}$
Oil supply pressure P (MPa)	0.5
Oil supply tempersture (°C	90
Nominal diameter of the main journal mm	60
Nominal diameter of the bearing bush (mm)	60
Bearing clearance $(C/\mu\mathrm{m})$	25
Bearing bush surface roughness (μm)	0.8
Journal surface roughness (μm)	0.4
Rated rotational speed (rpm)	900

Through the establishment of the three-dimensional finite element model of bearing bush and bearing seat, combined with the above mathematical equations, we obtained for every load cycle the oil film thicknesses, the oil film pressure, the rough contact pressure, etc., and then the analysis research is carried on.
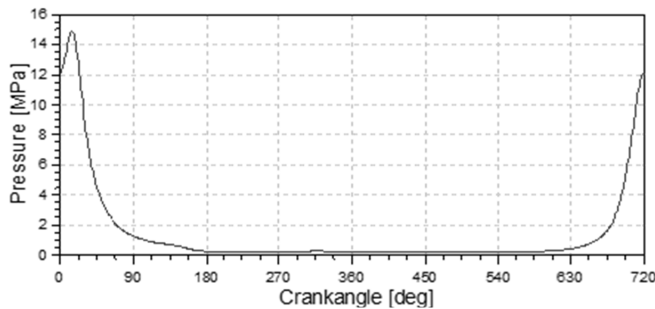
Fig. 1. Curve of diesel engine cylinder pressure and crank angle relationship

4. The calculation results and analysis

The main bearing of diesel engine is hydrodynamic lubricated, we consider using the dynamic pressure oil film formed by the crankshaft-bearing formed wedge structure to support external load, and separating the crankshaft form the bearing, to achieve the goal of reducing friction and wear. Choosing the oil film thickness, the oil film pressure, the rough contact pressure as the research object, the diesel engine crankshaft 1# to 5# main bearing lubrication condition as shown in Figs. 2, 3, and 4. It can be found from Figs. 2 and 3 that the oil film pressure to the crankshaft-bearing generated by the four working processes of the diesel engine is different, among which the closer to the third power stroke, the greater the oil film pressure, and vice versa.

The maximum oil film pressures of each main bearing is: 1# main bearing 52.32 MPa, 2# main bearing 63.34 MPa, 3# main bearing 54.96 MPa, 4# main bearing 66.51 MPa, 5# main bearing 54.91 MPa. Taking 3# main bearing as an example, when its maximum oil film pressure crank angles are 1620 °AC and 1980 °AC, it is just the moment when 2# and 3# cylinders do work and this moment has little effect to the oil film pressure of other main bearings.
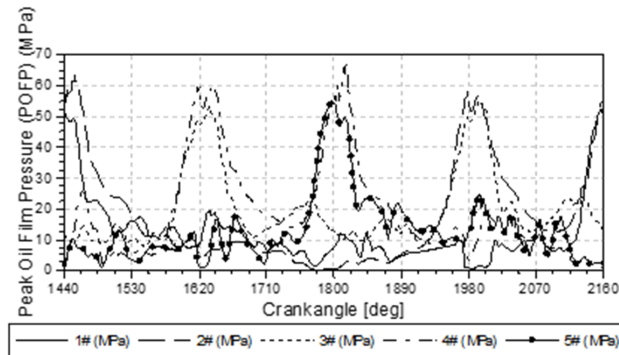
Fig. 2. Maximum oil film pressure contrast of 5 main bearings
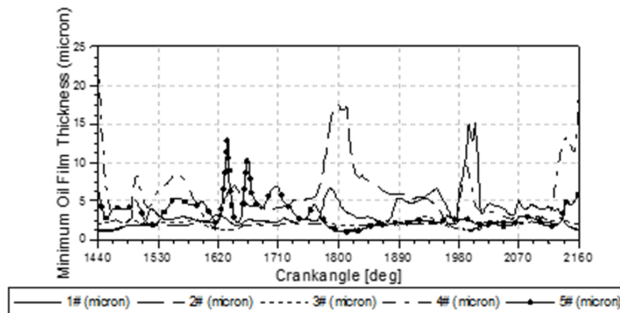
Fig. 3. Minimum oil film rhickness contrast of 5 main bearing

While the minimal oil film thickness of 1# main bearing is 1.04μm, the minimal oil film thickness of 2# main bearing is 1.23μm, that of 3# main bearing is 1.18 μm, that of 4# main bearing is 1.23μm, that of 5# main bearing is 1μm. Austrian List Institute (AVL) requires that the allowable minimum oil film thickness of main bearing is 1.2–1.4 μm, however, 1#, 3# and 5# main bearing of this diesel engine are lower than that value, which is likely to arise bearing bush and journal contact and mixed friction.

Selecting 3# main bearing as the research object, Fig. 4 indicates the average hydrodynamic pressure and average rough contact pressure cloud atlas of 3# main bearing in one work cycle. It can be seen that the friction and wear occur mainly on the lower bearing bush 135 °–240 ° (bearing bush angle), where bad lubrication, easy to contact to arise friction and wear.
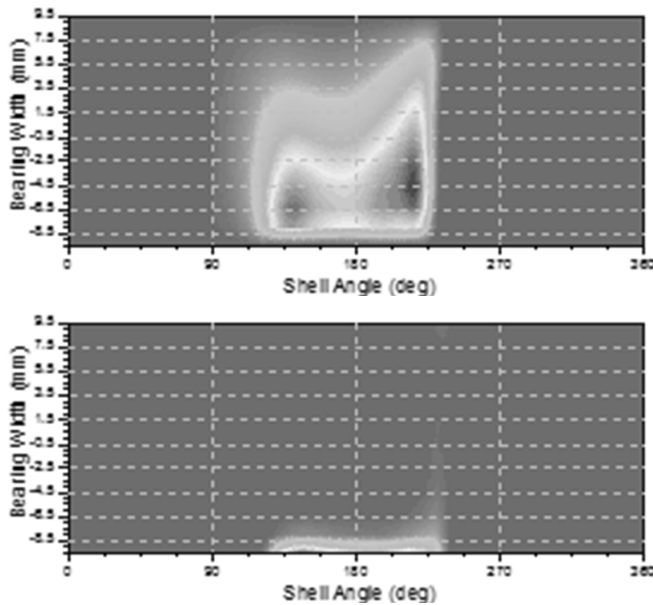
Fig. 4. Average hydrodynamic pressure and average rough contact pressure cloud atlas of 3# main bearing: top–average hydrodynamic pressure, bottom–average rough contact pressure

5. Optimal simulation

There are many affecting factors to the main bearing lubrication state, the fourth diesel engine main bearing is optimized from the four aspects of groove width, lub oil pressure, bearing clearance and roughness in this paper. The parameters of the optimal solution are shown in Table 2.

Table 2. Optimal solution

	Groove width (mm)	Lub oil pressure (MPa)	Bearing clearance (μm)	Roughness (μm)
Original scheme	19	0.5	25	0.8
Optimal scheme	19.8	0.4	28.8	1

Figure 5 is the optimized 3# main bearing journal center locus and average rough contact pressure cloud atlas, which indicates that since the inertia force and the gas force cancel each other out, the whole main bearing showed relatively smooth trajectory, good operation and lubrication, and there is no centripetal movement trend. This optimal scheme, on the basis of increasing the minimum oil film thickness, reduces the average friction power consumption, the maximum oil film pressure and the peak contact pressure, improving the friction performance of main bearing to a certain extent.
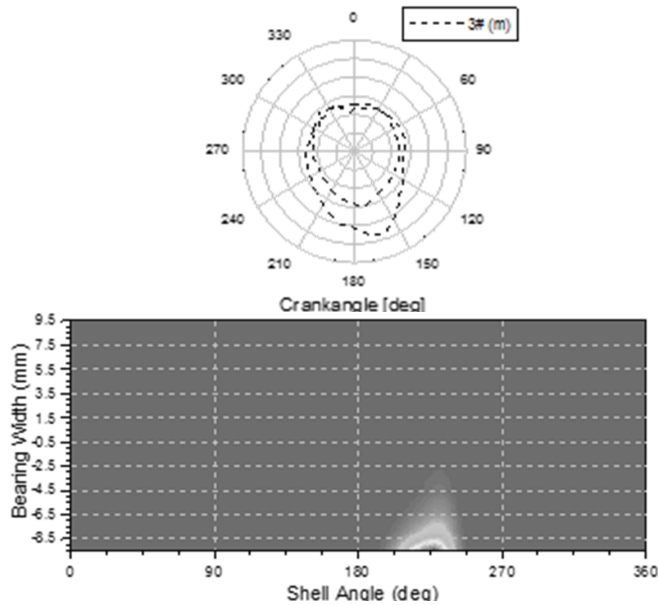
Fig. 5. Optimized 3# main bearing journal center locus and average rough contact pressure cloud atlas

6. Conclusion

Based on the average flow model, Greenwood/Tripp asperity contact theory, thermoelastic hydrodynamic lubrication theory, finite element method (FEM), multibody dynamics method, and the influence factors of the diesel engine crankshaft main bearing journal and bearing bush surface roughness, the crankshaft and bear-

ing seat deformation and thermal effect, we come to the conclusion as follows:

Selecting the third main bearing to analyze the influence factors, which have the worst lubrication situation. By means of enlarging the groove width, reducing the pressure of lubricating oil, increasing the bearing clearance and increasing roughness to ensure that the diesel engine main bearing minimal oil film thickness is as large as possible, the maximum oil film pressure as small as possible, to achieve good lubrication.

References

[1] H. ALLMAIER, C. PRIESTNER, F. M. REICH, H. H. PRIEBSCH, F. NOVOTNY-FARKAS: *Predicting friction reliably and accurately in journal bearings—extending the EHD simulation model to TEHD.* Tribology International *58* (2013), 20–28.

[2] J. RAISIN, N. FILLOT, D. DUREISSEIX, P. VERGNE, V. LACOUR: *Characteristic times in transient thermal elastohydrodynamic line contacts.* Tribology International *82* Part: B (2015), 472–483.

[3] A. MUMINOVIC, N. REPCIC, M. COLIC: *Thermo elasto hydrodynamic lubrication model of mixed friction.* Procedia Engineering *69* (2014), 49–56.

[4] B. HUANG, L. WANG, J. GUO: *Performance comparison of circular, two-lobe and elliptical journal bearings based on TEHD analysis.* Industrial Lubrication and Tribology *66* (2014), No. 2, 184–193.

[5] H. ALLMAIER, D. E. SANDER, F. M. REICH: *Simulating friction power losses in automotive journal bearings.* Procedia Engineering *68* (2013), 49–55.

Research on prediction model of viscosity-temperature of lubricating oil[1]

Gao Yongwei[2,3], Gaofeng[2], Li Yan[2]

Abstract. When the lubricating oils are used, the viscosity of the fluid will change because of the influence of the temperature. In order to obtain the bearing performance of dynamic pressure bearing, it is necessary to accurately predict the viscosity of the lubricating oil at a specific temperature. In this paper, a model for viscosity prediction of lubricating oil is proposed. After fitting the experimental data of temperature and viscosity of eight kinds of lubricating oil, it is found that the model is not affected by low viscosity factors in high temperature region, it can be used to accurately predict the viscosity of a specific temperature. It provides a theoretical basis for the study of bearing pressure characteristics of dynamic bearing.

Key words. Lubricating oil, viscosity-temperature correlation, curve fitting, viscosity measurement.

1. Introduction

The viscosity of dynamic and static pressure bearings is mainly affected by temperature, pressure, molecular weight and other factors, wherein, temperature has the most significant impact.Research on viscosity-temperature correlation of lubricating oil has a history of over 100 years. In 1886, Reynolds fit experimental data to get a simple viscosity-temperature index equation [1]. In 1928, Walther put forward a double logarithm viscosity-temperature model [2] to predict kinematic viscosity of other temperature points by testing viscosity of two temperature points only. In 1936, Geniesse and Delbridge introduced constant values to improve the double logarithm viscosity-temperature model [3] to raise upper bound of temperature range to 260 °C. In 1966, Roelands proposed a viscosity-temperature equation of two specific constant values [4] whose temperature range, whereas, was narrow and later presented a viscosity-temperature-pressure correlation by taking pressure impact

---

[2]School of Mechanical and Precision Instrument Engineering, Xi'an University of Technology, Xi'an, Shanxi, 710048, China

[3]School of Mechanical Engineering, North China University of Water Resources and Electric Power, Zhengzhou, Henan, 450045, China

into account. In 1967, Wright modified the double logarithm viscosity-temperature correlation [5] by further expanding temperature range of hydrocarbon lubricating oils and lowering their applicable kinematic viscosity to 0.21 cst. In 1974, Manning simplified Wright formula and utilized polynomial fitting of experimental data to further expand the formula's applicable temperature range and applicable kinematic viscosity range. In 2006, Christopher took the lead in introducing Bessel function to viscosity-temperature correlation to get better fitting precision.

The above viscosity-temperature correlation studies mostly made logarithm operation and linear fitting of experimental data to get viscosity-temperature characteristic correlation but failed to take experimental data processing of lubricating oils of low viscosity in high temperature regions into account and thoroughly eliminate exponential trend, as a result of which, the fitting precision failed to achieve the best. Therefore, a viscosity-temperature characteristic prediction model is proposed, which has simple operation and high fitting precision, not restricted by area and applicable to accurate prediction of kinematic viscosity of common lubricating oils.

2. Principle of viscosity test

According to principle of rotary viscosity measurement, cylinder immersed in lubricating oil may change rev due to impact of viscous moment of fluid, thus operation is made on torque and rev of cylinder measured to draw dynamic viscosity on the calculating basis of Newton's law of friction

$$f = \mu A \frac{\mathrm{d}v}{\mathrm{d}r}\,, \tag{1}$$

where f refers to the tangential force, μ refers to the dynamic viscosity, A denotes the contact area and $\mathrm{d}v/\mathrm{d}r$ denotes the shear rate. In equation (1) $f = M/r$, $A = 2\pi rh$, $\mathrm{d}v/\mathrm{d}r = r\frac{\mathrm{d}\omega}{\mathrm{d}r} = \gamma$. The above relations are substituted to equation (1) to draw the following:

$$\frac{M}{2\pi h r^2} = \mu r \frac{\mathrm{d}\omega}{\mathrm{d}r}\,. \tag{2}$$

After separation of variables and integration we obtain

$$\mu = \frac{M}{4\pi h \omega} \left(\frac{1}{r_1^2} - \frac{1}{r_2^2} \right)\,. \tag{3}$$

According to (3), the value of dynamic viscosity can be drawn by measurement of rev and moment. Figure 1 shows the schematic diagram of principle of viscosity measurement.
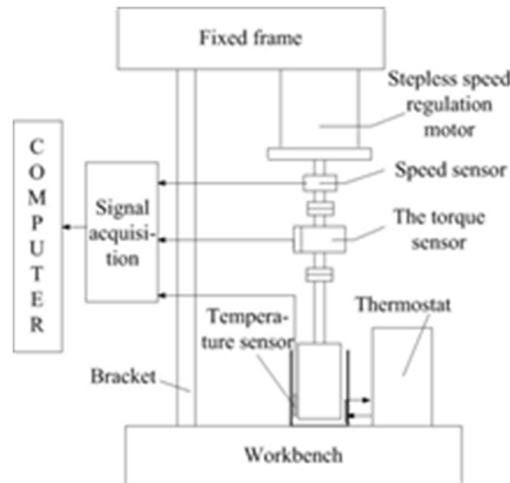
Fig. 1. Schematic diagram of viscosity measurement

3. Viscosity test

DV-II+(LV) rotary viscometer made by American company Brookfield is selected in the viscosity test and experiment, which is mainly composed by main engine, rotor component, temperature probe, support and so on. DV-II viscometer has range of dynamic viscosity measurement of 1–6×10^6 MPa s and measurement precision of $\pm1.0\,\%$. Its range of temperature measurement is $-100°$–$149\,°$C and precision is $\pm1°$C. Tested oil products include Mobil ISOVG10, ISOVG22, ISOVG32 and ISOVG46 and Germany's LUKAS HLP10, HLP 22 and HLP32 lubricating oil products. The test result of the equipment is dynamic viscosity, which must be converted to kinematic viscosity. The experimental data of converted kinematic viscosity are as shown in Fig. 2.
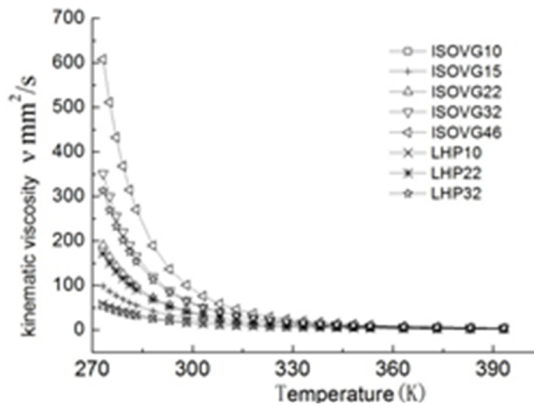
Fig. 2. Diagram of measured data of viscosity of lubricating oil

4. Viscosity-temperature characteristic of lubricating oil

4.1. Classical viscosity-temperature correlation

The classical viscosity-temperature correlations of lubricating oil [6–11] are mostly based on exponential operations and their transformed fitting functions [12]. The classical correlations are applied to fitting analysis on the experimental data.

4.1.1. Reynolds viscosity-temperature correlation. Put

$$\mu = \mu_0 \exp(\alpha T). \tag{4}$$

Logarithm is taken at both sides to draw

$$\ln \mu = \ln \mu_0 + \alpha T.$$

The following equation is set to be a fitting equation:

$$y = f(T) = A - BT \tag{5}$$

Single logarithm operation is made on viscosity data of ISOVG10 lubricating oil drawn in the experiment and linear fitting is made on absolute temperature T in the fitting equation of $y = A - BT$ to draw the following fitting coefficients: $A = 11.47$, $B = 0.02859$ and the following evaluation indexes of fitting precision: SSE (sum of squares of error of corresponding point of fitting data and original data: the lower, the better): 0.9266, R-square (coefficient of determination: the more approximate to 1 it is, the better data fitting the model will have): 0.9639. The fitting curve is as shown in the following Fig. 3.
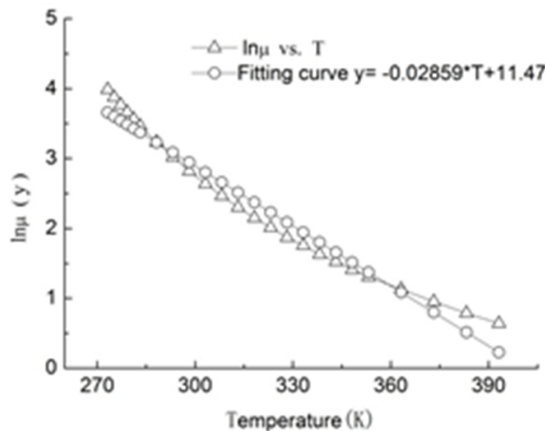
Fig. 3. Comparison of Reynolds viscosity temperature equation with experimental data

Figure 3 shows that Reynolds viscosity-temperature correlation fails to eliminate exponential characteristic and has not high fitting precision, thus prediction of

viscosity in specific temperature by this correlation may exhibit a high error.

4.1.2. Manning viscosity-temperature correlation. Manning simplified Wright's correlation is as follows:

$$\log(\log(Z)) = A - B\log(T),\tag{6}$$

where $Z = v + 0.7 + \exp(-1.47 - 1.84 - 0.51v^2)$, v referring to kinematic viscosity. According to Manning formula, linear fitting is made on experimental data of kinematic viscosity and temperature of ISOVG10 lubricating oil to draw the fitting equation of $y = A - BT$, where $A = 23.24$, $B = 3.895$. The fitting precision is as follows: SSE: 8.884e–4, R-square: 0.9999. The fitting curve is as shown in Fig. 5.
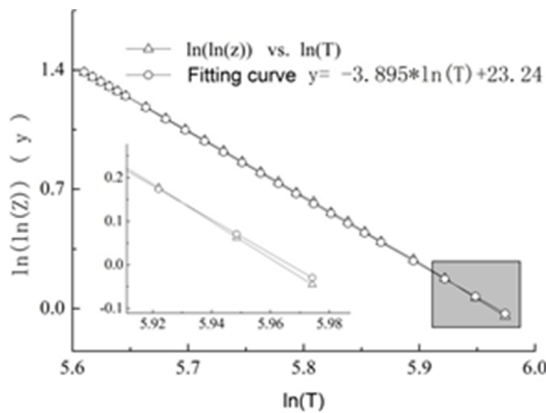
Fig. 4. Comparison of Manning viscosity temperature equation with experimental data

4.1.3. Christopher viscosity-temperature equation. Christopher followed the double logarithm form in classical viscosity-temperature correlations, whose correlation is as follows:

$$\ln(\ln(Z')) = A - B\ln(T),\tag{7}$$

where $Z' = v + 0.7 + \exp^v K_0(v + 1.244067)$, $K_0(x)$ referring to zero-order modified Bessel function of the second kind and the expression of $K_0(x)$ is

$$K_0(x) = \int_0^\infty \frac{\cos(xt)\,\mathrm{d}t}{\sqrt{t^2 + 1}}.\tag{8}$$

According to Christopher formula, linear fitting is made on experimental data of kinematic viscosity and temperature of ISOVG10 lubricating oil to draw the fitting equation $y = A - BT$, where $A = 22.37$ and $B = 3.742$, the fitting precision is as follows: SSE: 3.652e–4, R-square: 0.9999. The fitting curve is as shown in Fig. 5.

Figure 5 shows that Christopher formula further improves fitting precision but the fitting curve still presents an exponential trend and parameter R-square fails to achieve the optimal value 1.
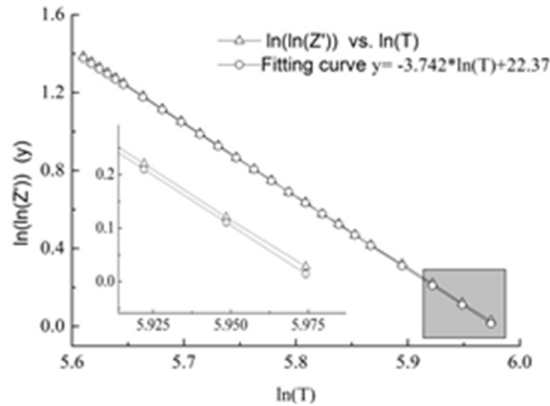
Fig. 5. Comparison of Manning viscosity temperature equation with experimental data

4.1.4. Establishment of prediction model of viscosity-temperature correlation Classical viscosity-temperature correlations of lubricating oil are mostly concerned with double logarithm operation of kinematic viscosity correlation or polynomial. So far, the optimal viscosity-temperature correlation—Christopher formula—still fails to eliminate the exponential trend.

According to Figs. 3–5, data at the lower right corner of curve are not well fit, failing to thoroughly eliminate exponential trend. Therefore, it is proposed that experimental data are modified by shape of curve of zero-order modified Bessel function of the second kind, double logarithm operations are made after the modification, and fitting is made with experimental data of temperature of single logarithm operation in the following fitting equation

$$\ln(\ln(Z'')) = A - B\ln(T),\tag{9}$$

where $Z'' = v + 0.7 + 3 * K_0(v + 2.106412)$. The form of $K_0(x)$ is as shown in equation (8). The function is applied to fitting of experimental data of kinematic viscosity and temperature of ISOVG10 lubricating oil to get fitting coefficients of $A = 22.98$, $B = 3.848$, and fitting precision of SSE: 9.706e–5, R-square: 1. The fitting curve is as shown in the following Fig. 6.

Figure 6 shows that the model has high fitting precision of viscosity-temperature correlation of ISOVG10 lubricating oil and effectively modifies the problem of not high fitting precision of low viscosity in the above classical viscosity-temperature equations, which is suitable for prediction of viscosity-temperature correlation in high temperature regions due to broader temperature range. The complete form of the proposed prediction model of viscosity-temperature correlation of lubricating oil is

$$\ln(\ln(v + 0.7 + 3 * K_0(v + 2.106412))) = A - B * \ln(T).$$

The model is used to fit measured temperature and viscosity data of lubricating oil products including Mobil ISOVG10, ISOVG22, ISOVG32 and ISOVG46 and
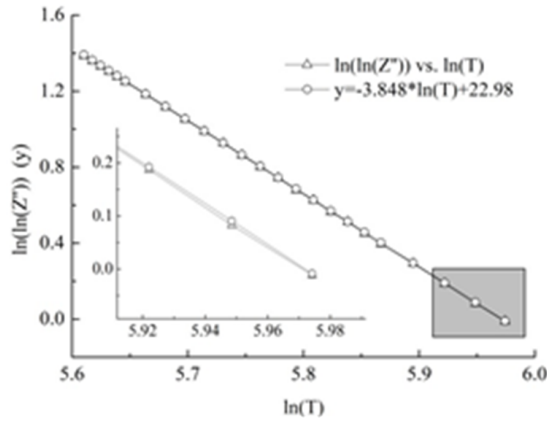
Fig. 6. Comparison of viscosity-temperature prediction model with experimental data

Germany's LUCAS HLP10, HLP22 and HLP32 in the experiment. The drawn fitting coefficients and precision are as shown in Table 1.

Table 1. Coefficient and accuracy of common lubricating oils fitting by viscosity-temperature prediction model

Name	A	B	SSE	R-square
ISOVG10	22.98	3.848	9.706e–5	1
ISOVG15	22.65	3.765	1.482e–4	1
ISOVG22	23.14	3.892	2.544e–4	1
ISOVG32	23.20	3.821	5.345e–5	1
ISOVG46	22.95	3.760	3.456e–5	1
HLP10	23.76	3.985	2.590e–5	1
HLP22	22.31	3.684	8.015e–5	1
HLP32	22.39	3.679	7.981e–5	1

According to Table 1, the model which is commonly applicable to prediction of viscosity-temperature correlation of lubricating oil has high fitting precision and broad range of application.

5. Conclusion

1. Linear fitting is made on measured viscosity and temperature data by classical viscosity-temperature characteristic correlations. It is found that Reynolds viscosity-temperature correlation has not high fitting precision and small temperature range; Manning and Christopher double logarithm viscosity-temperature correlations give rise some deviation in processing of lubricating oil of low viscosity in high temperature regions and fail to achieve the optimal fitting precision in spite of some precision.

2. A prediction model of viscosity-temperature correlation of lubricating oil is put forward, which is a fully processed model by shape of zero-order modified Bessel function of the second kind to have more precise prediction of viscosity-temperature correlation and undergo no impact of low viscosity factors of high temperature regions, whose range of application is broader and fitting precision is higher.

References

[1] O. REYNOLDS: *On the theory of lubrication and its application to Mr. Beauchamp Tower's experiments, including an experimental determination of the viscosity of olive oil.* Philosophical Transactions of the Royal Society, London *177* (1886), 157–234.

[2] C. WALTHER: *Die Temperaturabhängigkeit der viskosität I.* Journal Erdöl und Teer *4* (1928), 510–511.

[3] J. C. GENIESSE, T. G. DELBRIDGE: *Variation of viscosity with temperature.* Proceedings Second Mid-Year Meeting. American Petroleum Institute, Division of. Refining (1932), 56–58.

[4] C. J. A. ROELANDS: *Correlational aspects of the viscosity-temperature-pressure relationship of lubricating oils.* Delft University of Technology, Netherlands (1966).

[5] R. E. MANNING: *Computational aids for kinematic viscosity conversions from 100 to 210 F to 40 and 100° C.* Journal of Testing and Evaluation *2* (1974), No. 6, 522–528.

[6] K. R. RAJAGOPAL, G. SACCOMANDI, L. VERGORI: *Couette flow with frictional heating in a fluid with temperature and pressure dependent viscosity.* International Journal of Heat and Mass Transfer *54* (2011), No. 4, 783–789.

[7] C. MCCABE, S. CUI, P. T. CUMMINGS: *Characterizing the viscosity–temperature dependence of lubricants by molecular simulation.* Fluid Phase Equilibria *183–184* (2001), 363–370.

[8] A. HUSSAIN, S. BISWAS, K. ATHRE: *A new viscosity-temperature relationship for liquid lubricants.* Wear *156* (1992), No. 1, 1–18.

[9] A. A. SOARES, J. M. FEREIRA, L. CARAMELO, J. ANACLETO, R. P. CHHABRA: *Effect of temperature-dependent viscosity on forced convection heat transfer from a cylinder in cross flow of power-law fluids.* International Journal of Heat and Mass Transfer *53* (2010), Nos. 21–22, 4726–4740.

[10] V. Y. LOSKUTOV, N. N. YADREVSKAYA, N. V. YUDINA, N. V. USHEVA: *Study of viscosity-temperture properties of oil and gas-condensate mixtures in critical temperature ranges of phase transitions.* Procedia Chemistry *10* (2014), 343–348.

[11] S. BAIR: *The pressure and temperature dependence of volume and viscosity of four diesel fuels.* Fuel *135* (2014), 112–119.

[12] C. J. SEETON: *A novel Q-learning algorithm with function approximation for constrained Markov decision processes.* Tribology Letters *22* (2006), No. 1, 67–78.

Study of the linear induction motor with bimetallic secondary element

Fedor N. Sarapulov[1], Ivan A. Smolyanov[1, 2],
Fedor E. Tarasov[1]

Abstract. The electromechanical and thermal characteristics of the linear induction motor used in the mining industry are studied in the article. The detailed equivalent circuits method verification was implemented using comparison of the motor characteristics calculation results obtained by this method and by the finite element method in 2-D and 3-D arrangements. The characteristics computed by applying of the detailed equivalent circuits and the finite element method show the high convergence. In addition the detailed equivalent circuits method specifies the lower requirements to the computational performance.

Key words. Linear induction motor, detailed magnetic equivalent circuit, finite element method, electromechanical features, numerical calculation, magnetic field, thermal processes..

1. Introduction

The linear induction motor (LIM) is not a new type of the electric machine. The first construction types were designed more than 150 years ago [1, 2]. The rapid study of this electric machine type accrued to the 20th century [3]. Nowadays many scientists study the linear electric drives. The LIM structures diversity for various engineering applications makes it impossible to construct the comprehensive theory of the linear electric machines as it was made in the field of the circular machines and thereby it confirms the study relevance of the characteristics of the various types linear induction motors by means of the numerical methods.

The application field of linear electric drives widens year by year. Because of the large scale of their use it is difficult to specify certain linear drive application field as they can be used in the transport systems [4, 5], metallurgy [6, 7], machine building [8] and in bioengineering as well as in the residential use [1]. There are many studies of various types of the linear electric motors of different purpose on the ground of

---

[1]Ural Federal University named after First President of Russia B. N. Yeltsin, Mira street 19, 620002 Yekaterinburg, Russia

[2]Corresponding author; e-mail: `i.a.smolianov@urfu.ru`

which we can make a conclusion about the ambiguous of performance evaluation of certain type of engine.

A wide range of linear motors types and structures brings about plenty of approaches to calculation of their characteristics. As of today, the commonest approach is the finite element method. The variety of the commercial and free programs with the embedded graphic universal interface (GUI) and the opportunity of the object details and results accuracy increase are among the advantages of the method. They require the higher computational resources than other mathematical methods when solving three-dimensional problems particularly. We can become familiar with the results of the application of the method in the works [9–11]. The next numerical method of popularity is an equivalent circuits' method described in a number of works [12–14]. This type of mathematical model does not give a high accuracy for the linear machines calculation and requires the usage of correction factors. The equivalent circuits are often used in the optimization problems for selection of the optimal structure [13, 15]. The planar equivalent circuit is a kind of detailed equivalent circuits [16]. They are usually used for round or specific electrical motors design. The analytic expression mathematical models are applied seldom [7, 17]. Generally the analytic expressions have the high accuracy and low requirements to the computing capacity. The disadvantage of this method is its applicability to the constrained type of the structures.

The linear induction motor (LIM) used in the mining industry is considered in this article. The overburden operations stimulation and the open pit mining cause the open pit depth enhancement and the increased gaseousness of the environment. The constrained lifting angle of usual transport makes the usage of transporter equipment with the linear electrical drive urgent. The electromechanical characteristics and the thermal operating conditions calculated by means of magnetic and thermal detailed equivalent circuits are considered. The verification of this method is performed by comparison of characteristics obtained with the results calculated by means of finite element method in 2-D and 3-D.

2. Formulation of the problem

Mineral resources are transported from the open pit in carriages chained with each other. The bimetallic secondary element (SE) is mounted on the bottom of a carriage. The car couplings are placed on the tracks above the inductors (primary element). The inductor is powered only when SE passes over the inductor. It is a short-time duty. The primary element operates under the limit conditions that cause heavy overheating of its winding. The inductor is placed in technical oil in order to avoid emergency conditions [18–20]. The main geometrical dimensions are indicated in Table 1 [18].

The inductor is powered by the AC power supply with frequency of 50 Hz. The phase current in the winding is equal to 380 A. The primary element winding is connected as it is shown in Fig. 2. Two coils of the same phase can be placed in one groove with exception of 6 grooves located in the ends (semifilled). Synchronous velocity is 13.2 m/sec.
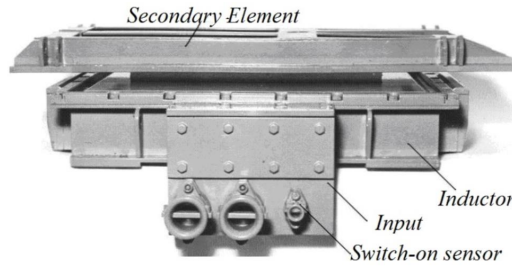
Fig. 1. General view of the linear induction motor

Table 1. Main geometrical dimensions

Groove width	12 mm	Air gap	12 mm
Tooth width	10 mm	Depth of conductive (Cu) SE	3 mm
Groove height	64 mm	Depth of SE steel plate	8 mm
Yoke height	108 mm	Number of grooves	36
Inductor's width	500 mm	SE width	700 mm
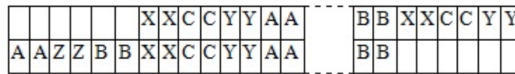
Fig. 2. Winding phase distribution in grooves

3. Mathematical formulation of the problem

The present section of the paper comprises the mathematical description and the assumptions for the considered models. The advantages and disadvantages of the models as well as the possibilities for their modernization for the mathematical analysis results accuracy improvement are analyzed in brief.

The significant problems arise during the calculation of the electromechanical characteristics in the region of the velocities close to the synchronous velocity. The linear induction machine is the nonsymmetric electromechanical device with the thickness and the transverse edge effects. The three-dimensional model allows for consideration of the all edge effects occurring in the machine with the maximum accuracy, but at the same time the present model requires the high computational performance. The three-dimensional electromagnetic problem solving at the synchronous velocities essentially reduces the convergence and the results accuracy. The currents spreading in the secondary element should be considered in the two-dimensional electromagnetic problems. In the present paper the transverse edge effect is suggested to be considered in the two-dimensional models with the use of the Bolton coefficient. The calculation and the application of the present coefficient for the linear electromechanical power converters analysis are described in detail in [21–23].

3.1. Detailed magnetic equivalent circuit

When dividing the considered electrical machine into the layers by height and sections by length, the mathematical model of the linear induction motor can be presented as a collection of the electrical and magnetic circuits. The fragment of the detailed equivalent circuit is presented in Fig. 3, where the magnetic resistances are as follows: R_a is the magnetic resistance of the yoke section in the active region, R_{ak} is the magnetic resistance of the yoke section in the edge region, R_n and R_t are the is the magnetic resistances of the magnetic flux normal and tangential components respectively, R_{ase} is the magnetic resistance of the SE core section. The phases currents are designated as J_a, J_b, J_c, while the induced currents are designated as J_s. The equation system (1) can be constructed in the matrix form [19, 20] for the present system

$$\boldsymbol{Z}^M \boldsymbol{\Phi} = \boldsymbol{I}^c + \boldsymbol{I}^s, \tag{1}$$

where $\boldsymbol{Z}^M$ is the magnetic impedance matrix, $\boldsymbol{\Phi}$ is the vector of magnetic fluxes in the inductor yoke sections, $\boldsymbol{I}^c$ is the column vector of the currents in the calculation domain layers, $\boldsymbol{I}^s = \boldsymbol{K}_I \boldsymbol{I}_\Phi$ is the column vector of the stator currents, $\boldsymbol{K}_I$ is the matrix of linear transformation of the phase currents into slot currents and $\boldsymbol{I}_\Phi$ is the column-vector of the phase currents.

The accuracy of the induced currents calculation depends on the structure of the matrix of the numerical differentiation over coordinates. The present problem is too wide and is beyond the scope of the present paper. The mathematical justification of the present phenomenon can be found in reference [24].

The currents vector of the SE strips is written as follows:

$$\boldsymbol{I}^c = \frac{\varepsilon^{\text{trans}} + \varepsilon^{\text{move}}}{\boldsymbol{R}}, \tag{2}$$

where $\varepsilon^{\text{trans}} = -\frac{\partial \boldsymbol{\Phi}}{\partial t}$ is the transformation EMF, $\varepsilon^{\text{move}} = v\boldsymbol{D}\boldsymbol{\Phi}$ is the EMF due to movement, $\boldsymbol{v}$ is the velocity and $\boldsymbol{D}$ is the matrix of the numerical differentiation over coordinates.

When solving the equations system (1) with respect to the magnetic flux, the integral values (of the power, force, magnetic induction on particular sections) can be found. The forces are defined as follows:

$$F_{xn} = \frac{1}{2} Re\left(B_{nxn} \overset{*}{I}_{cxn} \right), \tag{3}$$

$$F_{xxn} = \frac{1}{2} Re\left(B_{nx+1n} \overset{*}{I}_{cxxn} \right), \tag{4}$$

$$F_{txn} = \frac{1}{2} Re\left[B_{mxn} \left(\overset{*}{I}_{cxn} + \overset{*}{I}_{cxxn} \right) \right]. \tag{5}$$

Here, F_{xn} is the thrust of the top half layer, F_{xxn} is the thrust of the low half layer, F_{txn} is the levitation force, B_{mxn} is the tangential magnetic flux density, B_{nxn} and

$B_{\mathrm{nx+1n}}$ are the normal magnetic flux density of the low and top layers, respectively, $\overset{*}{I}_{\mathrm{cxn}}$ and $\overset{*}{I}_{\mathrm{cxn}} + \overset{*}{I}_{\mathrm{cxxn}}$ are the induced conjugate currents to the low and top layers.
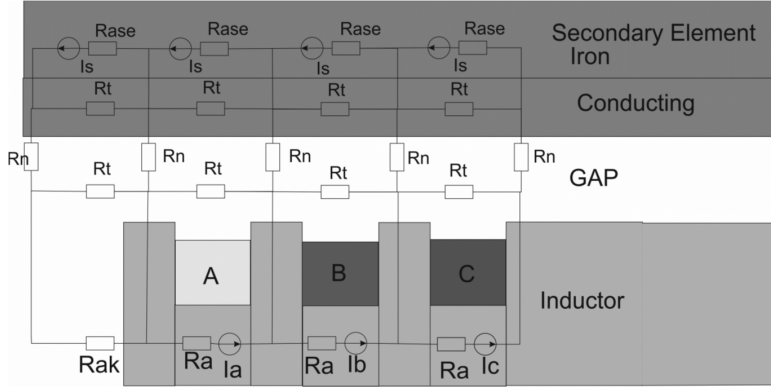
Fig. 3. Fragment of detailed equivalent circuit

3.2. Detailed thermal equivalent circuits

The calculation of the LIM thermal processes does not require the high detail level, as compared to the DMEC. Therefore the LIM is often divided into from 1 to 10 sections along the length with the thermal masses separation at each section [22, 25, 26]. In the present paper the LIM is divided into 4 sections by the length (Fig. 3). Each section has 4 thermal masses: CML is the end winding copper mass, CMP is the slot winding copper mass, CS is the steel-core mass, C2 is the SE section mass. The differential equation (6) is written for each thermal mass. Let us introduce the example of the heat balance differential equations system building without consideration of the thermal radiation (7) for the detailed thermal equivalent scheme, presented in Fig. 4.

$$\frac{\mathrm{d}T_i}{\mathrm{d}t} = A \cdot T_{i-1} - B \cdot T_i + C \cdot T_{i+1} + D + q'_{\mathrm{v}i}. \qquad (6)$$

Coefficients of the system of equations are

$$A = \frac{a}{t_{\mathrm{z}}^2} + \frac{\upsilon}{t_{\mathrm{z}}}, \ B = \frac{2a}{t_{\mathrm{z}}^2} + \frac{a}{c_{\mathrm{p}}d\Delta} + \frac{\upsilon}{t_{\mathrm{z}}}, \ C = \frac{a}{t_{\mathrm{z}}^2}, \ D = \frac{\alpha}{c_{\mathrm{p}}d\Delta}T_{\mathrm{c}},$$

where $a = \lambda/(c_{\mathrm{p}}d)$ is the heat diffusivity of the SE's strip, q_{v} is the specific heat dissipation power, c_{p} is the specific heat capacitance of the strip material, d is the density of the strip material, υ is the velocity of the strip; T_i is the average temperature of the ith section whose height equals to t_{z}, thickness equals to Δ and length equals to L_t.

$$\frac{\mathrm{d}T_i^{k,N}}{\mathrm{d}t} =$$
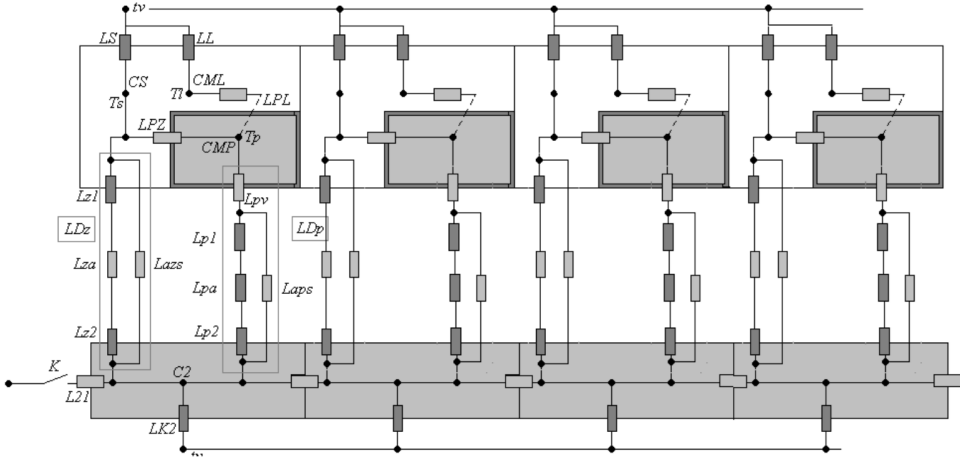
Fig. 4. Detailed thermal equivalent circuit

$$
=\begin{cases}
\begin{rcases}
A_1 T_{\mathrm{c}} - BT_1^k + CT_2^k + D + 0 \\
... \\
AT_{i-2}^k - BT_{i-1}^k + K_{\mathrm{cv}}CT_i^k + (1-K_{\mathrm{cv}})CT_{\mathrm{c}} + D + 0
\end{rcases} \rightarrow \text{Edge zone,} \\[2ex]
\begin{rcases}
\left[\frac{(\mathrm{LDp}+\mathrm{LDz})\cdot T_1^N}{C2} - \left(K_{\mathrm{cv}}A + C\right)T_i^N \right] + \\[2ex]
+ \frac{\mathrm{LDz}\cdot T_4^N + \mathrm{LDp}\cdot T_3^N}{C2} + K_{\mathrm{cv}}AT_{i-1}^K + C\cdot T_1^{N+1} + \frac{T_{\mathrm{c}}}{C2} + \frac{\mathrm{PR}}{C2}
\end{rcases} \text{Region of SE,} \\[2ex]
\frac{-(\mathrm{LPL}+\mathrm{LL})\cdot T_2^N + \mathrm{LPL}\cdot T_3^N + \mathrm{PL} + \mathrm{LL}\cdot T_{\mathrm{c}}}{\mathrm{CML}} \Big\} \rightarrow \text{Frontal part of winding,} \\[2ex]
\frac{-(\mathrm{LPL}+\mathrm{LPZ}+\mathrm{LDp})\cdot T_3^N + \mathrm{LPL}\cdot T_2^N + \mathrm{LPZ}\cdot T_4^N + \mathrm{LDz}\cdot T_2^N + \mathrm{PP}}{\mathrm{CMP}} \Big\} \rightarrow \text{Groves,} \\[2ex]
\frac{-(\mathrm{LPZ}+\mathrm{LS}+\mathrm{LDz})T_4^N + \mathrm{LS}\cdot T_{\mathrm{c}} + \mathrm{LPZ}\cdot T_3^N + \mathrm{LDz}\cdot T_1^N + \mathrm{PS}}{\mathrm{CS}} \Big\} \rightarrow \text{Core zone,} \\[2ex]
\begin{rcases}
(1-Kcv)A\cdot T_{\mathrm{c}} + K_{\mathrm{cv}}\cdot A\cdot T_{i+1}^k - B\cdot T_{i+5}^k + C\cdot T_{i+6}^k + D + 0 \\[1ex]
A\cdot T_{i+7}^k - B\cdot T_{i+8}^k + C\cdot T_{i+9}^k + D + 0
\end{rcases} \rightarrow \text{Edge zone,}
\end{cases}
$$

$$(7)$$

where T_1^N, T_2^N, T_3^N, T_4^N are the N-section temperatures of the SE active zone, end and slot windings, the inductor core correspondingly. Symbol T_{c} is the environment temperature, T_i^k is the k-edge region temperature, the thermal conductions between the different LIM parts are designated as follows: LDp is the thermal conduction between the SE and the slot winding parts, LDz is the same quantity between the SE and the inductor teeth, LPL is the thermal conduction between the slot and the end winding parts, LPZ is the thermal conduction between the winding and the core, and LK is the SE heat release into the air.

The power losses in the mentioned inductor winding end parts (PL), the slot parts (PP), the core steel (PS) and the SE section (PR) are defined as in (8) (the losses in steel can be neglected) [22]:

$$
\begin{aligned}
\text{PL} &= \underbrace{\frac{1}{2} R_{\mathrm{f}} \sum_{i=a,b,c} \left| I_i^{\mathrm{f}} \right|^2}_{\text{Losses in the inductor } (\mathrm{P_{ind}})} \cdot \frac{L_1}{L_1 + B_i} \\
\text{PP} &= P_{\mathrm{ind}} \cdot \frac{B_i}{L_1 + B_i} \\
\text{PR} &= \underbrace{\mathrm{Re} \left(\frac{1}{2} \sum_{i=a,b,c} U_i^{\mathrm{f}} \cdot I_i^{\mathrm{f}} \right)}_{\text{Active power input } (\mathrm{P_2})} - \underbrace{F_{\mathrm{t}} \cdot v}_{\substack{\text{Mechanical} \\ \text{power } (\mathrm{P_2})}} - P_{\mathrm{ind}}
\end{aligned}
\tag{8}
$$

where L_1 is the winding end length, B_i is the inductor core width, I_i^{f} is the phase current, U_i^{f} is the winding phase voltage, R_{f} is the winding active resistance, F_t is the traction force, and v is the SE velocity.

3.3. Finite elements method

The electcromagnetic quasistatic problem, being solved in the two-dimensional or three-dimensional statement, is described by the equations (9). The three-dimensional problem was solved only for the half of the modeling area, as is shown in Fig. 5, due to the symmetry of the physical phenomena occurring along the LIM width.

The basic equations are written as follows:

$$
\begin{aligned}
\boldsymbol{J} &= \sigma \left(\boldsymbol{E} + \boldsymbol{v} \times \boldsymbol{B} \right) + \mathrm{j}\omega \boldsymbol{D} + \boldsymbol{J}_{\mathrm{e}}, \\
\nabla \times \boldsymbol{H} &= \boldsymbol{J} \\
\boldsymbol{B} &= \nabla \times \boldsymbol{A}, \\
\boldsymbol{E} &= -\mathrm{j}\omega \boldsymbol{A}.
\end{aligned}
\tag{9}
$$

where $\boldsymbol{J}$ is the current density, $\boldsymbol{E}$ is the electric field strength, $\boldsymbol{B}$ is the magnetic flux density, $\boldsymbol{D}$ is electric flux density, and $\boldsymbol{A}$ denotes the magnetic vector potential.

The thermal processes are described with the use of the differential equation (10), where Q_{e} is the thermal energy source, which consists of the electric losses Q_{rh} and magnetic losses Q_{mi} in the LIM design elements (the both losses can be neglected).

$$
\rho C_{\mathrm{p}} \frac{\partial T}{\partial t} + \rho C_{\mathrm{p}} \cdot u \cdot \nabla T = \nabla (k \nabla T) + Q_{\mathrm{e}},
\tag{10}
$$

where ρ is the density, C_{p} is the specific heat capacity, u is the velocity, and T is the temperature. Quantity $Q_{\mathrm{e}} = Q_{\mathrm{rh}} + Q_{\mathrm{ml}}$ is the heat generation, $Q_{\mathrm{rh}} = \frac{1}{2} Re \left(\boldsymbol{J} \cdot \boldsymbol{E}^* \right)$ are the electric losses, $Q_{\mathrm{ml}} = \frac{1}{2} Re \left(\mathrm{j}\omega \boldsymbol{B} \cdot \boldsymbol{H}^* \right)$ are the magnetic losses.

The velocity for the SE in the equation (10) is specified according to the LIM operation mode. The oil velocity calculation was performed with the use of the Laminar Flow module, described by the equations (11). The electromagnetic forces
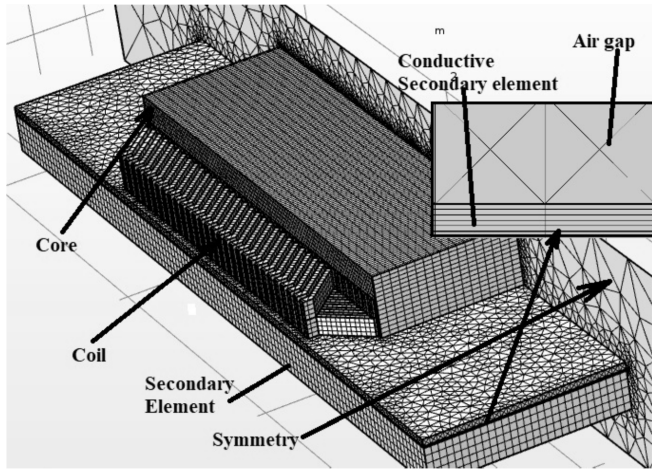
Fig. 5. The mesh for the LIM three-dimensional model

(12) in the equation (11) can be neglected.

$$\rho\frac{\partial \boldsymbol{u}}{\partial t} + \rho\left(\boldsymbol{u} \cdot \nabla\right)\boldsymbol{u} = \nabla\left[-p\boldsymbol{I} + \mu\left(\nabla\boldsymbol{u} + (\nabla\boldsymbol{u})^{\mathrm{T}}\right)\right] + \boldsymbol{F},$$

$$\rho\nabla \cdot (\boldsymbol{u}) = 0.$$

(11)

where p is the specific pressure, μ is the dynamic viscosity, and $\boldsymbol{I}$ is the unit matrix. The force may be expressed as

$$F = \frac{1}{2}Re\left(\boldsymbol{J} \times \boldsymbol{B}^*\right).$$

(12)

4. Performance calculation

The results of simulation based on the finite elements method were obtained in the Comsol Multiphysics software package, and the DMEC were implemented in the Matlab software package.

4.1. Electromechanical characteristics

The methods verification was performed by means of comparison of the mechanical characteristics (Fig. 6), calculated by the finite elements method in the two-dimensional arrangement (the FEM 2D curve), the DMEC method with the use of the high order numerical derivation (DMEC high order) and the DMEC method based on the first order polynomials. It can be seen from the Fig. 6 that in case of the slip ratios close to unit, the detail level as well as the order slightly influence the error. According to the formula (3) the error occurs in case of the synchronous velocities, as far as the currents calculation (2) essentially depends on the applied nu-

merical calculation method. The tooth-groove granularity is sufficient for obtaining the accurate results in case of the high order DMEC. The present approach permits to reduce the system matrix dimension without compromising the results accuracy.
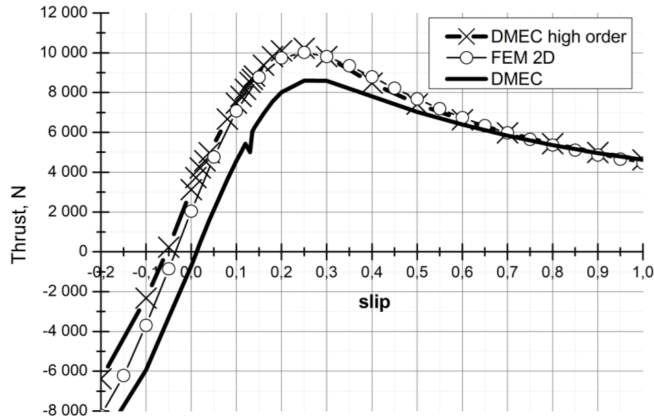
Fig. 6. Mechanical characteristic

The slip dependence of the power factor and efficiency is one of the crucial features of the motor. Therefore, it is appropriate to consider the results convergence on the basis of the present characteristics. As it was mentioned above, in case of the velocities values close to the idle run the calculation results obtained by the different methods were practically the same. The significant divergence is observed at the nominal conditions (in this case the slip ratio is approximately 0.1–0.2). As it is seen from Fig. 7, bottom part, the maximum error is observed at the curve calculated with the use of the DMEC with the first order polynomials. The divergence of the efficiency curves, calculated by the finite element methods and the high order DMEC, is caused by neglect of the winding end losses, which constitute the significant part of the power supplied to the inductor in case of the large currents, in the FEM. The divergence of the obtained power factor in Fig. 7, top part, is caused by the particularity of the inductor currents presentation and the simplification of the primary element (both the inductor and the core) shape.

The motor design is such that the efficiency (Fig. 7, bottom part) and the power factor (Fig. 7, top part) possess the maximum values in case of the nominal conditions. The longitudinal effect reduction is achieved by the increase of the secondary element torque from each inductor side by 20 %. The present effect can be observed in the Fig. 8. The inductor location is shown in the Fig. 8 by the rectangle drawn by the heavy line. The current density component, which induces the tractive effort, is a sequence higher than the current component, which closes the circuit. Therefore the traction forces predominate in the SE active zone, which is shown in the Fig. 8.

The three-dimensional model allows for the most adequate consideration of the design features in case of the high-quality mesh construction, but in this case the calculation time is increased while the results convergence at the synchronous velocities is improved. Comparison of the calculated forces at the velocities close to
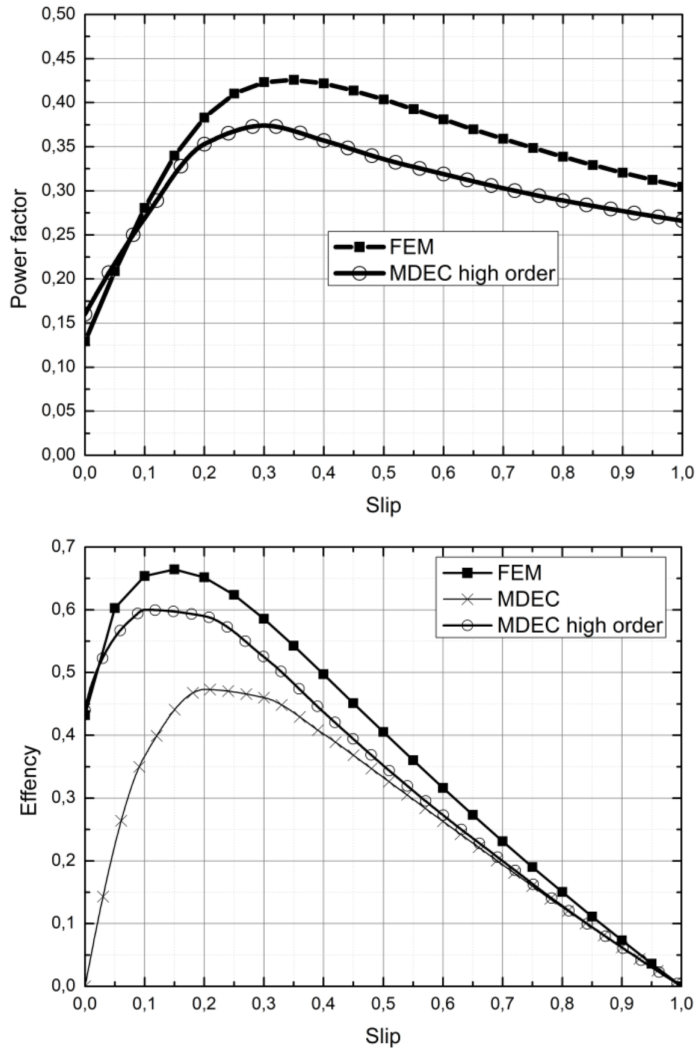
Fig. 7. Top–slip dependence of the power factor, bottom–efficiency

the idle run is presented in Table 1. The three-dimensional problem calculation time for the present slip ratio is presented in the brackets in the "FEM 3D" column. The implication is that the calculation time is increased with the slip ratio increase. For the three-dimensional electromagnetic problem solving at the close synchronous velocities the additional boundary conditions, which significantly influence the obtained results accuracy, should be introduced. Therefore the results obtained only at the velocities close to the idle run are compared in the paper. On the basis of the present results it can be concluded that in case of the adequate detail level the calculation results in the two-dimensional statement can be obtained with the adequate accuracy.
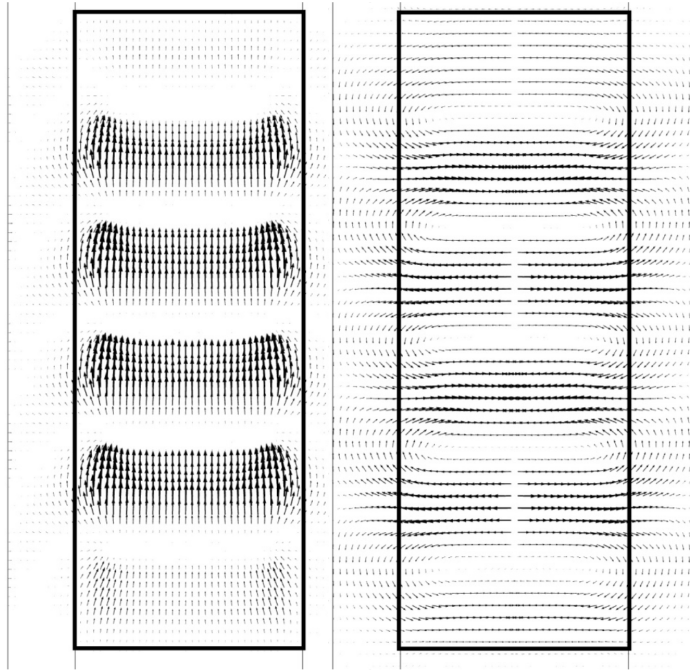
Fig. 8. Left–direction of traction forces, right–current in the electrically
conductive SE

Table 1. Comparison of the traction forces for the different slip ratios

Slip	FEM 2D	FEM 3D	DMEC high order	DMEC
1.00	4 600.4 N	4 459.0 N (4.5 hours)	4 550 N	4 550 N
0.95	4 654.1 N	4 500.2 N (5 hours)	4 655 N	4 655 N
0.90	4 868.3 N	4 792.3 N (8 hours)	4 964 N	4 964 N
0.80	5 366.7 N	5 307.1 N (15 hours)	5 366 N	5 439 N

4.2. Calculation of the LIM thermal modes

The calculation of the mining transport thermal modes is necessary for assurance of the transport failure-free operation. Therefore during the LIM design it is necessary to build the accurate verified model which allows for the quick calculation of the temperatures field in the required points. The temperatures of the inductor slot and end windings, as well as the SE and the inductor core are analyzed in the present section. The primary element operates when the SE passes over it (the SE length is taken equal to the conveyor train length). It is assumed that the electric insulation of the winding is able to withstand the temperature up to 220 °C.

The good convergence was achieved for the temperatures of the different LEM elements calculated with the use of the different models (Fig. 9). The inductor

winding temperatures divergence can be explained by the fact that in the FEM the whole power is generated in the winding active zones while in the detailed thermal equivalent circuits the thermal losses are distributed between the active and the end part of each section. Therefore the calculated temperature of the winding will be lower in case of the end parts consideration in the FEM. The slight divergence of the SE temperatures is caused by the correction of the SE width with respect to the inductor width in the FEM.
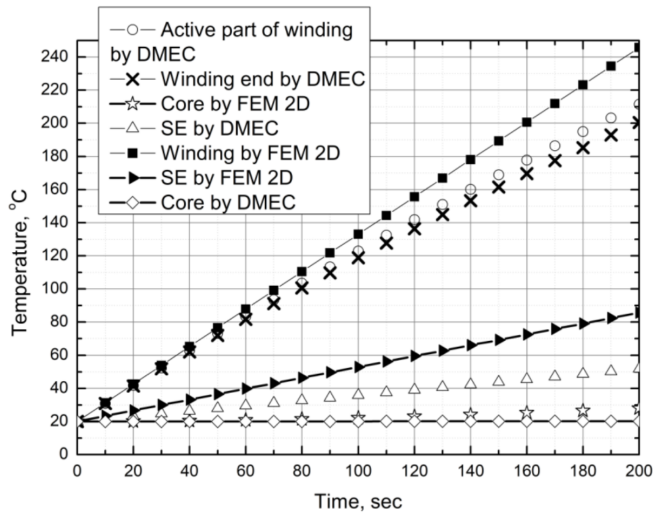
Fig. 9. Temperatures of the different LIM design elements

As compared to the all inductor parts its winding warms most of all. Therefore let us consider the heating of the present design element separately in Fig. 10. The temperatures of the end and active parts at the time instants 25 seconds, 125 seconds and 250 seconds are marked by the points in the present figure. The maximum operation time of the inductor is 250 seconds. In the given time period the carriage will manage to travel over distance of more than 6 meters, and will move beyond the inductor operating area. Therefore in case of compliance with the nominal conditions of the inductor operation the winding will not fail to function.

The secondary element warms up when the carriage passes over the powered inductor operated under the short-time operation conditions. The temperatures of the secondary elements parts Se1...Se4 are presented in Fig. 11.

5. Conclusion

The convergence of the results obtained by the detailed magnetic equivalent circuits (with the use of the high order polynomials) and the finite elements methods is rather good. The three-dimensional magnetic problems solving requires the high calculation capacities, which is not appropriate in some applications. It can be concluded that the effective application of the numerical derivation over coordinate
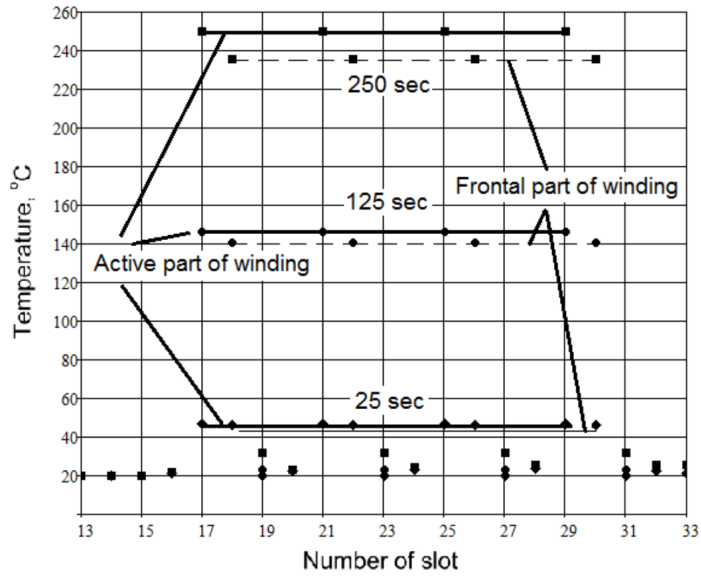
Fig. 10. Inductor winding parts temperature in the different time intervals
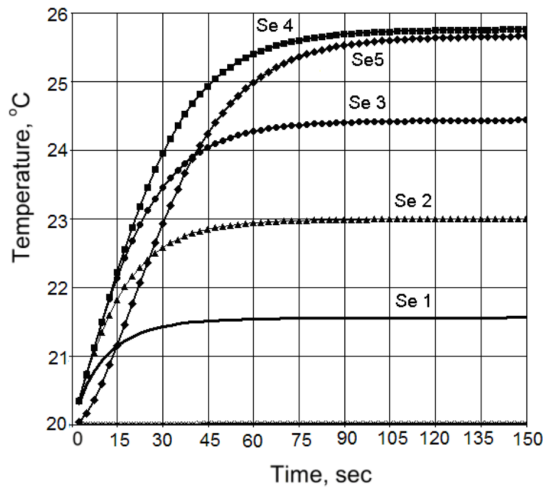
Fig. 11. Time dependences of the SE sections under the first (Se 1), the second (Se 2), the third (Se 3), the fourth (Se 4) quarters of the inductor and beyond its end (Se 5)

allows for significant computational performance saving. The significant time saving caused by the application of the DMEC method instead of the FEM in the two-dimensional statement can be observed only in the optimization problems or the enumeration of the parameters values during solving.

The motor operation at the 0.1–0.3 slip ratios ensures the maximum efficiency and the power factor. The increase of the secondary element torque from each

inductor side by 20 % allows for the decrease of the transverse edge effect influence, which facilitates the elimination of the adverse transverse forces in the active zone.

The thermal modes of the traction linear induction motor were calculated with the use of the detailed thermal equivalent circuits as well as the FEM. The slight divergence of the results, obtained by the different methods is explained by the different assumptions accepted in the mentioned above methods (for instance, during the consideration of the inductor winding ends influence and the transverse edge effect influence). The thermal equivalent circuit formation with the dividing into separate 4 parts by the LIM length maintains the high accuracy of the results. Therefore it should be mentioned that the LIM warming analysis on the basis of the detailed magnetic equivalent circuits' method does not require the high detail level of the model. It allows for the significant saving of the computational performance during the time-dependent calculation of the thermal characteristics.

References

[1] J. F. GIERAS: *Linear induction drives.* Oxford University Press, New York, USA (1994).

[2] E. R. LAITHWAITE: *Induction machines for special purposes.* George Newnes Ltd. (1966).

[3] R. HELLINGER, P. MNICH: *Linear motor-powered transportation: History, present status, and future outlook.* Proceedings of the IEEE *97* (2009), No. 11, 1892–1900.

[4] L. S. MATTOS, E. RODRIGUEZ, F. COSTA, G. G. SOTELO, R. DE ANDRADE, R M. STEPHAN: *MagLev-Cobra operational tests.* IEEE Transactions on Applied Superconductivity *26* (2016), No. 3, Article Sequence No. 3600704.

[5] F. SARAPULOV, V. FRIZEN, I. SMOLYANOV, E. SHMAKOV: *Dynamic study of thermal characteristics of linear induction motors.* International Conference on Electrical Machines, Drives and Power Systems (ELMA), 1–3 June 2017, Sofia, Bulgaria, IProceedings IEEE (2017), 414–419.

[6] E. L. SHVYDKIY, I. A. SMOLYANOV, F. SARAPULOV, K. E. BOLOTIN: *Calculation methods of tubular linear induction motor.* IEEE Russia Section Young Researchers in Electrical and Electronic Engineering Conference (ElConRus), 1-3 February 2017, St. Petersburg, Russian Federation, Proceedings IEEE (2017) 1579–1580.

[7] J. F. GIERAS, Z. GIENTKOWSKI, J. MEWS, P. SPLAWSKI: *Analytical calculation of electrodynamic levitation forces in a special-purpose linear induction motor.* IEEE International Electric Machines & Drives Conference (IEMDC), 15–18 May 2011, Niagara Falls, ON, Canada, IEEE Journals & Magazines, IEEE Transactions on Industry Applications *48* (2012), No. 1, 106–116.

[8] J. F. GIERAS: *Linear electric motors in machining processes.* International Conference on Electrical Machines and Systems (ICEMS), 26–29 October 2013, Busan, Korea (South), Journal of International Conference *2* (2013), No. 4, 380–389.

[9] Q. LU, Y. LI, Y. YE, Z. Q. ZHU: *Investigation of forces in linear induction motor under different slip frequency for low-speed Maglev application.* IEEE Transactions on Energy Conversion *28* (2013), No. 1, 145–153.

[10] D. LI, Y. WEN, W. LI, J. FANG, J. CAO, X. ZHANG, G. LV: *Numerical calculation of primary slot leakage inductance of a single-sided HTS linear induction motor used for linear metro.* Cryogenics *82*, (2017), 38–47.

[11] J. F. GIERAS, Z. J. PIECH, B. Z. TOMCZUK: *Linear synchronous motors: Transportation and automation systems.* CRC Press, New York, USA (2012).

[12] W. XU, G. G. SUN, G. WEN, Z. W. WU, P. K. CHU: *Equivalent circuit derivation and performance analysis of a single-sided linear induction motor based on the winding*

function theory. IEEE Transactions on Vehicular Technology *61* (2012), No. 4, 1515–1525.

[13] A. SHIRI, A. SHOULAIE: *Design optimization and analysis of single-sided linear induction motor, considering all phenomena.* IEEE Transactions on Energy Conversion *27* (2012), No. 2, 516–525.

[14] W. XU, J. G. ZHU, Y. ZHANG, Y. LI, Y. WANG, Y.z,GUA: *An improved equivalent circuit model of a single-sided linear induction motor.* IEEE Transaction on Vehicular Technology *59* (2010), No. 5, 2277–2289.

[15] A. H. ISFAHANI, B. M. EBRAHIMI, H. LESANI: *Design Optimization of a low-speed single sided linear induction motor for improved efficiency and power factor.* IEEE Transactions on Magnetics *44* (2008), No. 2, 266–272.

[16] V. OSTOVIC: *Dynamics of saturated electric machines.* Springer-Verlag New York, USA (1989).

[17] X. DAI, J. CAO, Y. LONG, Q. LIANG, J. MO, S. WANG: *Analytical modeling of an eddy-current adjustable-speed coupling system with a three-segment Halbach magnet array.* Electric Power Components and Systems *43* (2015), No. 17, 1891–1901.

[18] P. I. ZAKHARCHENKO, S. V. KARAS, F. N. SARAPULOV: *The features of the conveyor train linear drive structure and operation modes; The explosion-proof electrical equipment.* Collection of research papers of the Ukraine Research Institute of the explosion-proof electrical equipment the under the general editorship of the member of the Ukraine National Academy of Sciences Pivnyak G.G. Donetsk, "Yugo-Vostok" Ltd. (2007), 331–343. In Russian.

[19] V. S. IVANENKO, S. V. KARAS: *The heat of the double-side linear induction motor: News of Higher Educational Institutions.* Mining Journal (1987), No. 11, 109–114. In Russian.

[20] V. S. IVANENKO, S. V. KARAS, A. N. BURKOVSKII: *Selection of the cooling method, thermal calculation and experimental verification of the low-speed linear induction motor: The explosion-proof electrical equipment.* Collection of research papers of the All-union Research Institute of the explosion-proof electrical equipment. Donetsk: All-union Research Institute of the explosion-proof electrical equipment, 1985, 96–102. In Russian.

[21] F. E. TARASOV, S. BYCHKOV, S. L. NAZAROV, V. FRIZEN: *Induction MHD-pump with flat coils.* Acta Technica CSAV *60* (2015), No. 1, 71–79.

[22] F. N. SARAPULOV, S. F. SARAPULOV, P. SHIMCHAK: *Mathematical model of linear induction machines based on equivalent circuit.* UGTU-UPI, Ekaterinbur (in Russia), (2005).

[23] I. A. SMOLYANOV, E. L. SHVIDKIY, F. N. SARAPULOV, S. F. SARAPULOV: *Research electromechanical characteristics of magnetohydrodynamic pump.* IEEE Conference of Russian Young Researchers in Electrical and Electronic Engineering (EIConRus), 1–3 February 2017, St. Petersburg, Russian Federation, Proceedings IEEE (2017) 1590–1593.

[24] V. DMITRIEVKII, V. V. GOMAN, F. N. SARAPULOV, V. PRAKHT, S. F. SARAPULOV: *Choice of a numerical differentiation formula in detailed equivalent circuits models of linear induction motors.* International Symposium on Power Electronics, Electrical Drives, Automation and Motion (SPEEDAM), 22–24 June 2016, Anacapri, Italy, Proceedings IEEE (2016), 458–463.

[25] F. N. SARAPULOV, S. F. SARAPULOV, V. E. FRIZEN: *Use of detailed equivalent circuit method for investigation of electromagnetic, thermal and hydrodynamic processes in induction electric engineering units.* Acta Technica CSAV *60* (2015), No. 2, 131–153.

[26] F. N. SARAPULOV, V. V. GOMAN: *Development of mathematical models of thermal processes in linear induction motors.* Russian Electrical Engineering *80* (2009), No. 8, 431–435.

Application of voltage compensation in variable frequency speed control system[1]

Gaozhong Zhu[2]

Abstract. In variable frequency speed control systems, a problem occurs that the asynchronous motor exhibits insufficient torque at low frequency starting. One possible solution of this problem consists in using control strategy based on constant ration between the voltage and frequency. The paper presents a method to improve the load carrying capacity based on voltage compensation measures. According to the combination of motor equivalent circuit and low-frequency vector, the formula of voltage compensation at different frequencies is deduced. The simulation model of variable frequency speed control system is established. The effect of the voltage compensation and voltage compensation of torque of the motor at different loads are analyzed. The experiment proves that the voltage compensation has achieved a good compensation effect in the frequency conversion speed regulation system, and illustrates the importance of voltage compensation when the frequency conversion starts.

Key words. Voltage compensation, torque, variable frequency speed regulation system, constant voltage frequency ratio.

1. Introduction

People have paid more and more attention to the AC speed regulation system [1–5]. The traditional frequency conversion speed control system is aimed at reducing the current impact of motor starting while in real life applications, especially some heavy load starting machines are often used. According to the constant voltage and frequency control ideas [6–7], when the starting frequency is low, the starting voltage is reduced, while the starting torque is proportional to the square of the starting voltage. In this way, the starting voltage will inevitably lead to the reduction of starting torque. When the starting torque of the heavy load starting machine is greater than the torque of the load, the starting process of the motor

---

[2]School of Mathematics and Physics, Wei Nan Normal University, Wei Nan, 714099, China

can be accelerated. But the traditional variable frequency speed regulation starts with the way of step-down and thyristor voltage regulation soft start, which cannot meet the requirement of heavy load starting, so it is very difficult for motor to start with heavy load. Therefore, voltage compensation is one of the important means to improve the low speed performance of the motor speed control system. In terms of voltage compensation, many domestic and foreign scholars have done a lot of work. References [8–9] propose a direct compensation for duty cycle, but the realization process is more complicated. References [10] and [11], respectively, compensate the reference voltage under synchronous rotating dq coordinate system and $\alpha\beta$ stationary coordinate system. The realization process is relatively simple. A new output voltage compensation method based on error observer is proposed, but its dynamic performance is not good [12].

As can be seen from the above text, it is clear that the motor starting method puts forward new requirements. It must work with small starting current and low frequency, while requiring high starting torque and load adaptability in order to increase the starting torque and reduce the starting current. This paper presents a new starting method based on measures leading to voltage compensation that reduces the voltage drop on the stator winding impedance and increases the starting torque of the motor. In view of the above situation, the simulation model of variable frequency speed control is established and the voltage compensation effect under different conditions is analyzed. The experiment proves that the voltage compensation exhibits a good compensation effect in the variable frequency speed control system.

2. Constant pressure and frequency control strategy

The T-type steady-state equivalent circuit of induction motor is shown in Fig. 1.
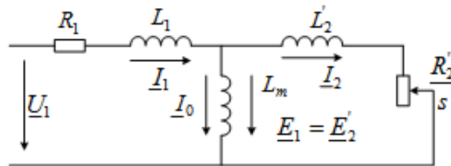
Fig. 1. Steady-state equivalent circuit of asynchronous motor

In Fig. 1, R_1 and R_2' represent the resistance of each phase of the stator and rotor of each phase, equivalent to the stator side, respectively, L_1 and L_2' represent that the inductances of the stator and rotor recalculated on the stator, $\underline{U}_1$ represent the stator phase voltage, $\underline{E}_1$ and $\underline{E}_2$ represent the electromotive force induced on the stator leakage inductance and rotor leakage inductance, respectively, and L_{m} represents the equivalent inductance corresponding to the air gap. This holds for each phase winding of the stator [13].

It is known that the control strategy formula working with constant voltage-frequency ratio is

$$E_1/f_1 = C_1\Phi_{\mathrm{m}} = C\,,\tag{1}$$

where $C_1 = 4.44 N_1 K_1$, Φ_m represents the magnetic flux in the air gap of the motor, N_1 represents the series winding number of the stator per phase and K_1 denotes the coefficient of the corresponding fundamental wave.

The relationship between the voltage of each phase of the stator and induced electromotive force in the steady state is

$$\underline{U}_1 = \underline{E}_1 + \underline{I}_1 \underline{Z}_1 \, ,$$

where

$$\underline{E}_1 = \mathrm{j} 2\pi f_1 L_\mathrm{m} \underline{I}_\mathrm{m}, \ \underline{Z}_1 = R_1 + \mathrm{j} 2\pi f_1 L_1 \, . \tag{2}$$

When the stator frequency f_1 is high, the effective value of $\underline{E}_1$ is also high, and the impedance of the stator winding can be ignored. It is considered that the effective value of the stator phase voltage is $\underline{U}_1 \approx E_1$. In this project, $\underline{E}_1$ is replaced by $\underline{U}_1$ so as to obtain a constant ratio of voltage and frequency. The constant voltage ratio control equations is

$$U_1 / f_1 = C_1 \Phi_\mathrm{m} = C \tag{3}$$

The control characteristic curve is shown in Fig. 2, line I
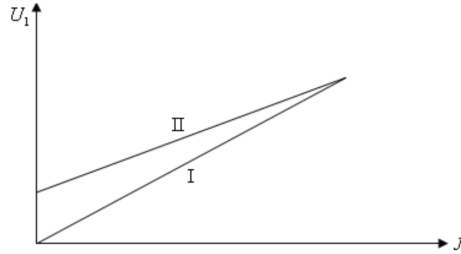
Fig. 2. Voltage compensation curve

The precondition of the constant voltage-frequency ratio control mode is to ignore the voltage drop on the stator impedance. However, when the frequency f_1 is low, the effective value of the electromotive force of the stator $\underline{E}_1$ becomes also small small (see (2)). But only the term $R_1 \underline{I}_1$ does not decrease. Compared with $\underline{E}_1$, the proportion of $R_1 \underline{I}_1$ increases and the equation $\underline{U}_1 \approx \underline{E}_1$ is not set up. In other words, the stator resistance voltage drop cannot be neglected any more when the frequency is lower. In order to make $E_1 / f_1 = C$, a control mode can also be applied at low frequencies. The voltage compensation measures is often used in the actual project. According to the magnitude of the load current, the effective value of the stator phase voltage is picked up properly to compensate the influence of the stator voltage drop. The voltage compensation characteristic curve is shown in Fig. 2, line II.

When the frequency f_1 is low, the control principle of $U_1 / f_1 = C$ will fail if the voltage compensation is not performed, and the asynchronous motor will inevitably work in the weak magnetic working state. The maximum torque of the asynchronous motor will inevitably decrease seriously. As a result, the overload capacity of the motor is reduced. After voltage compensation of $R_1 \underline{I}_1$, it can keep the air gap flux

constant when the motor works at low frequency, thus ensuring the stable operation of the control mode $U_1/f_1 = C$.

3. Voltage compensation principle

According to the basic principle of constant voltage to frequency ratio control strategy, when the motor is powered on frequency of $50\,\mathrm{Hz}$, the influence of the voltage drop on the stator winding resistance component cannot be neglected. If the applied voltage does not consider this factor for compensation, the flux will be significantly reduced, and cannot keep the maximum frequency torque value. If the voltage compensation is too high, the motor is in the state of magnetic saturation, the stator current rises rapidly, but the starting torque of the motor increases very little. The motor generates serious heat and the motor may be burnt out for a long time. Therefore, it is very important to accurately calculate the magnitude of the voltage compensation value below the power frequency to ensure that the motor runs under a constant flux. The voltage compensation value, when the motor starts under constant flux, is called the voltage full compensation. According to [13], more accurate for voltage full compensation method is an analytical method, so this paper uses analytic calculation method for finding the voltage compensation.

Because most of the asynchronous motors work in the state of rotor short circuit, the basic relations of voltages and currents of asynchronous motor (when the rotor is short circuited) follow from Fig. 1. These relationships are

$$
\left.
\begin{aligned}
\underline{U}_1 &= -\underline{E}_1 + \underline{I}_1(R_1 + \mathrm{j}X_1) \\[2mm]
\underline{E}_1 &= -\underline{I}_0(R_\mathrm{m} + \mathrm{j}X_m) \\[2mm]
\underline{E}_1 &= \underline{E}_2' \\[2mm]
\underline{E}_2' &= -\underline{I}_2(R_2' + \mathrm{j}X_2') \\[2mm]
\underline{I}_1 + \underline{I}_2' &= \underline{I}_0
\end{aligned}
\right\}
\tag{4}
$$

Combining the equivalent model of the induction motor in Fig. 1 and basic relations between the voltages and currents, the time phasor diagram of the motor under the working frequency is shown in Fig. 3.

In Fig. 3, X_1 represent the stator leakage inductance, X_2' represent the rotor leakage inductance recalculated on the stator, φ_2 represents the rotor power factor angle, and $Z_2 = \sqrt{R_2'^2 + X_2'^2}$.

According to the phasor diagram in Fig. 3 and steady-state equivalent circuit diagram of the induction motor in Fig. 1 one can obtain

$$
\underline{U}_1^2 = \left[-\underline{E}_1 + \underline{I}_2 \frac{R_2'/s}{\underline{Z}_2} R_1 + \left(\underline{I}_0 + \underline{I}_2 \frac{X_2'}{\underline{Z}_2}\right) X_1\right]^2 +
$$
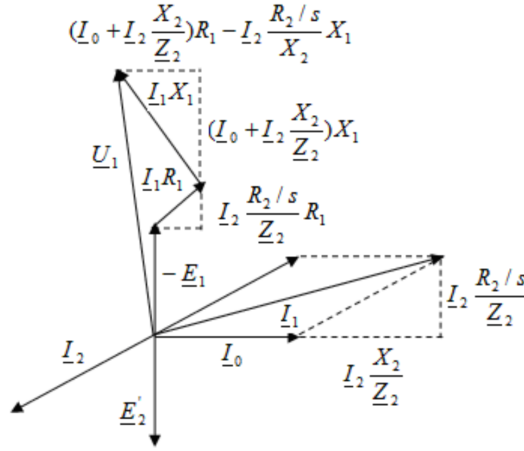
Fig. 3. Full phasor diagram of the induction motor

$$+ \left[\underline{I}_2 \frac{R_2'/s}{\underline{Z}_2} X_1 - \left(\underline{I}_0 + \underline{I}_2 \frac{X_2'}{\underline{Z}_2} \right) R_1 \right]^2 . \tag{5}$$

In (5), $\underline{E}_1 = I_2 \underline{Z}_2 = \underline{I}_0 X_{\mathrm{m}}$ and $\underline{I}_0 = \underline{I}_2 \frac{\underline{Z}_2}{X_{\mathrm{m}}}$. Taking equation $Z_2 = \sqrt{R_2'^2 + X_2'^2}$ into (5), we get

$$\underline{U}_1^2 = \underline{I}_2^2 \left[\alpha \left(\frac{R_2'}{s} \right)^2 + \beta \left(\frac{R_2'}{s} \right) + \gamma \right] . \tag{6}$$

In (6) there holds

$$\alpha = \left(1 + \frac{X_{\mathrm{s}}}{X_{\mathrm{m}}} \right)^2 + \left(\frac{R_{\mathrm{s}}}{X_{\mathrm{m}}} \right)^2 , \ \beta = 2R_{\mathrm{s}} ,$$

$$\gamma = \left(1 + \frac{X_{\mathrm{r}}}{X_{\mathrm{m}}} \right)^2 R_{\mathrm{s}}^2 + \left[\left(1 + \frac{X_{\mathrm{r}}}{X_{\mathrm{m}}} \right) X_{\mathrm{s}} + X_{\mathrm{r}} \right]^2 .$$

Putting equation (6) into the motor's torque expression, we get

$$T_{\mathrm{e}} = \frac{I_2' R_2/s}{\frac{\omega_1}{n_{\mathrm{p}}} g} = \frac{3 n_{\mathrm{p}} U_1^2}{\omega_1 g} \frac{1}{\alpha \left(\frac{R_2}{s} \right) + \gamma \left(\frac{s}{R_2} \right) + \beta} . \tag{7}$$

When the motor runs at low frequency, the stator side pressure drop is more reflected in the motor time phasor map, the proportion of $\underline{I}_1 R_1$ is larger, and the proportion of $\underline{I}_1 X_1$ decreases. Its phasor diagram is shown in Fig. 4.

The comparison between Figs. 3 and 4 shows that when the motor runs at low frequency, the stator voltage is in the first quadrant, but the calculation principle of its voltage is the same as that of the power frequency. The stator side voltage and torque formula of the motor are the same as for the power frequency, which is

not given here. When the motor parameters are known, the value of the voltage full compensation of the motor at different frequencies can be calculated accurately according to the formula (7).

$$(\underline{I}_0 + \underline{I}_2 \frac{X_2}{\underline{Z}_2})R_1 - \underline{I}_2 \frac{R_2/s}{X_2} X_1$$

$$(\underline{I}_0 + \underline{I}_2 \frac{X_2}{\underline{Z}_2})X_1$$

$$\underline{I}_1 X_1$$

$$\underline{U}_1$$

$$\underline{I}_2 \frac{R_2/s}{\underline{Z}_2} R_1$$

$$\underline{I}_1 R_1$$

$$-\underline{E}_1$$

$$\underline{I}_1$$

$$\underline{I}_0$$

$$\underline{I}_2$$

$$\underline{I}_2 \frac{X_2}{\underline{Z}_2}$$

$$\underline{E}_2'$$
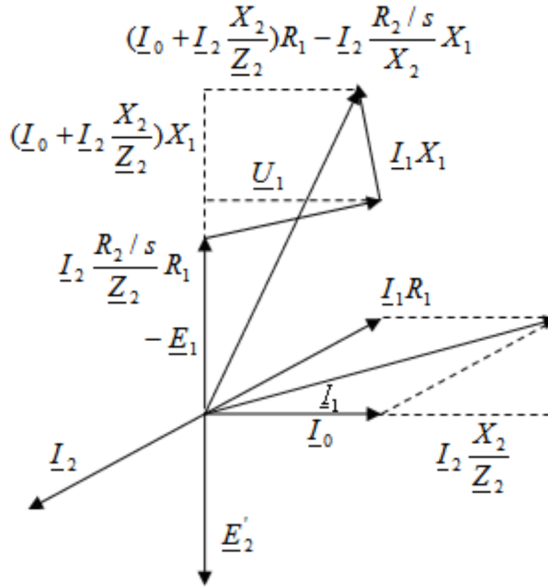
Fig. 4. Phasor chart of asynchronous motor for power frequency

4. Simulation analysis

According to the principle of variable frequency speed regulation system of voltage compensation, the system simulation experiment is carried out in this paper, The simulation model of AC speed control system is established. In the simulation experiment, the JLJ132-2.5/4 torque motor is used as the asynchronous motor. The parameters of the motor are as follows: the rated voltage of stator is 380 V, the rated current is 6.3 A, the rated rotor voltage is 110 V and current is 18.3 A, the rated speed is 1450 rpm and maximum output torque (at locked rotor) is 25 Nm.

4.1. Voltage compensation of motor in heavy load

In order to verify the feasibility and importance of the voltage compensation in the AC speed control system under the same frequency division, the simulation research is carried out in two cases without voltage compensation and voltage compensation, respectively. The load resistance of the motor is overloaded.

Figures 5a, 5b, and 5c show the frequency spectrum, speed, and torque without voltage compensation, respectively. In the absence of voltage compensation, the output spectrum of the output voltage can be seen from the output waveform shown

in Fig. 5a. In this case, the content of harmonics in the output voltage is large, the starting torque of the motor is not large and the instability factors of starting torque are obvious. From the torque waveform of Fig. 5c, it can be seen that the maximum starting torque 5 N m, which is obviously lower than the theoretically calculated starting torque of the voltage under the constant voltage frequency control strategy, so that the load capacity of the motor obviously decreased. When the motor starts on a large and heavy duty machine such as a crane or mine hoist, the starting torque at this time cannot meet the starting requirements.

Therefore, it is necessary to ensure the voltage compensation to improve the motor starting torque and increase the carrying capacity.

Figures 6a, 6b and 6c show similar waveforms for full voltage compensation of the 50/3Hz frequency, respectively. In the case of full voltage compensation, it can be seen from the output waveform in Fig. 6a that the harmonic content of the output voltage is small and the waveform symmetry is good. As can be seen from the starting torque waveform of the motor, its maximum value is now 11 N.m. The output torque waveform is basically consistent with the maximum torque of the compensated theory after the voltage compensation, so that the magnetic flux of the motor is kept constant.

4.2. Voltage compensation effect of motor at different loads

Under different loads, the starting torque of the motor is different by different starting modes, and the motor torque ripple after the stable operation is also different. In order to verify the reliability and stability of the voltage compensation method under different loads, this paper gives shows the time evolution of the output torque and speed under different loads with three frequency divisions. The load in Fig. 7 is 5 N m, the load of Fig. 8 is 4 N m, and the load of Fig. 9 is 3 N m.

Figures 7, 8 and 9 show the waveform of the speed and torque output at different loads for the 50/3 Hz frequency. With the increase of electric current in the steady state of the motor, the speed of the motor under steady state decreases, and the starting torque of the motor is constant. It can be seen from the speed-torque characteristics of the 50/3 Hz frequency under different loads, that the constant flux operation of the motor at low frequency is guaranteed. At the same time, the landing of the simultaneous rotational speed of the load phase is a constant value. From the output speed diagram and the torque waveform in Figs. 7–9, the speed of the landing is kept constant, and the voltage of the motor is considered to reach the effect of full compensation.

5. Experimental verification

In order to verify the effect of frequency conversion heavy load starting voltage compensation, a set of loading heavy load experiment system is designed in this paper. The design of the experimental loading system is shown in Fig. 10. Taking the JLJ132-2.5/4 torque motor as an example, the parameters of the experimental motor are the same as those mentioned above. Choose different voltage compensation
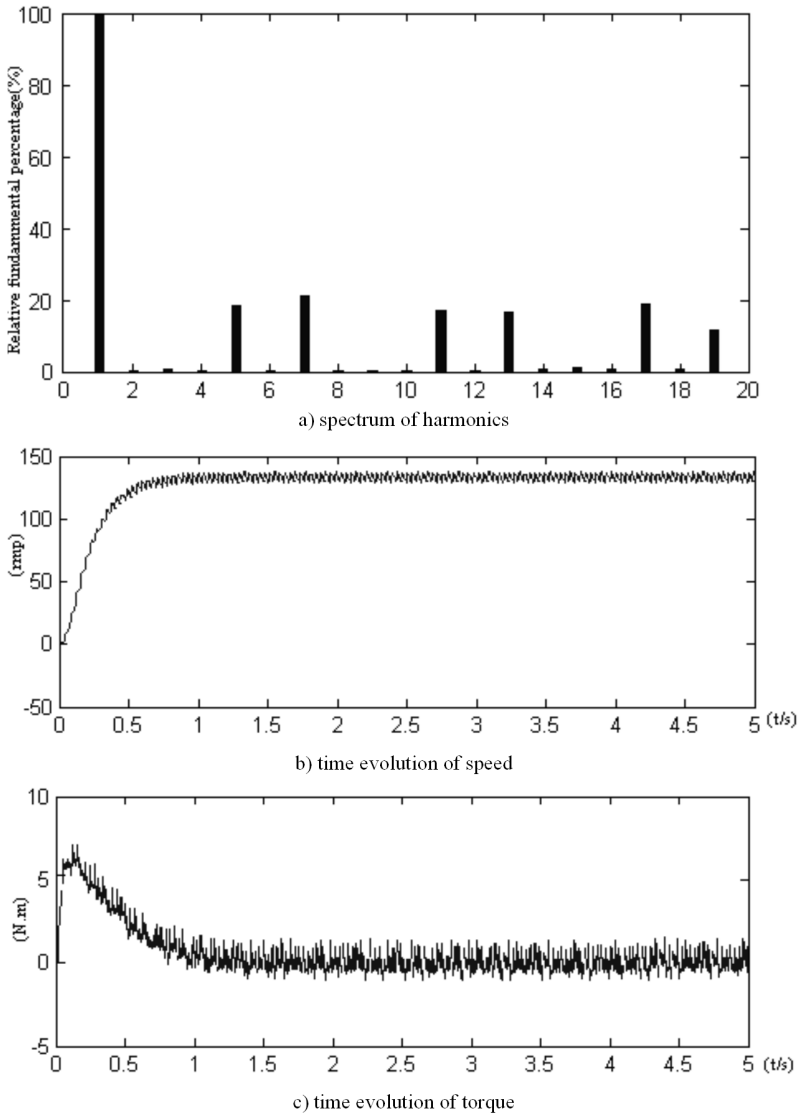
Fig. 5. Output voltage spectrum, time evolution of speed and time evolution of
torque for 50/3 Hz without voltage compensation

values and different frequencies for different control objects to reduce the energy
consumption during startup. Verify the effect of voltage full compensation. In the
calculation of voltage compensation, the magnitude of the effective value of the
stator voltage is difficult to be measured directly because the output of the inverter
is a series of voltage fragments. For the 5th harmonic, the reverse rotation magnetic
field is generated, but for the seventh harmonics, the positive-order rotating magnetic
field is generated. Therefore, the influence of their motor torque can offset part of
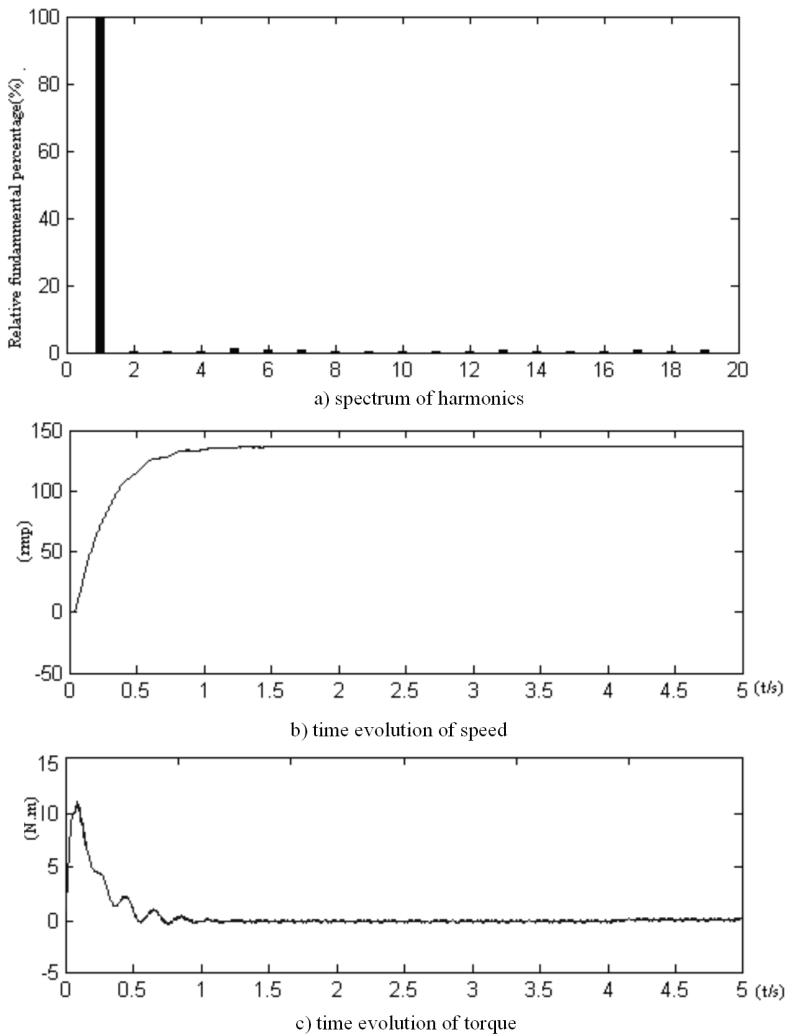
Fig. 6. Output voltage spectrum, time evolution of speed and time evolution of
torque for $50/3$ Hz without voltage compensation

each other [13]. In this experiment, the effective value of the voltage base wave is
used to approximate the effective value of the voltage in the experiment. The results
of voltage compensation experiment are shown in Table 1.

It can be seen from Table 1 that under the condition of low frequency operation,
the theoretical calculation of stator side voltage and corresponding speed of motor are
similar to the measured ones. Therefore, it is considered that the compensation has
reached the effect of $E_s/f_s = C$, so that the motor has a large torque at low frequency
operation. Further proof from the experimental viewpoint of voltage compensation
in the frequency control system has achieved good compensation effect.
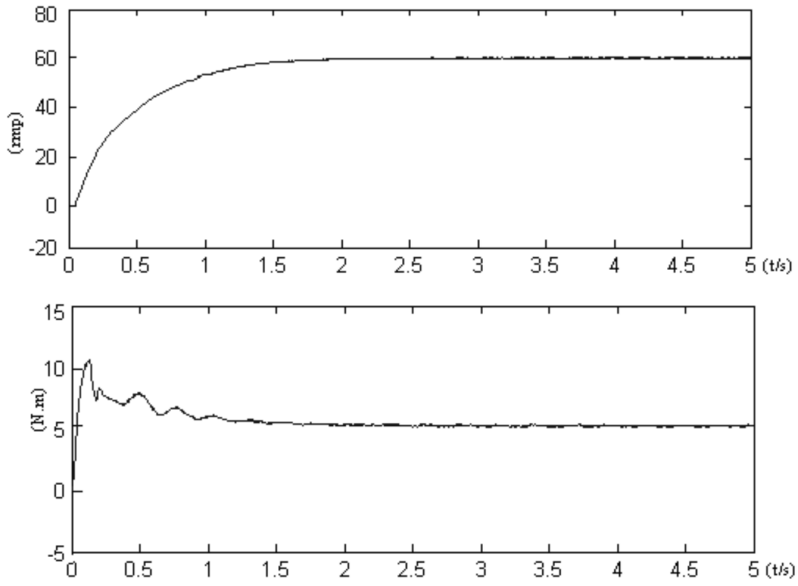
Fig. 7. Time evolution of speed (top) and time evolution of torque (bottom) for
$50/3$ Hz without voltage compensation for load $5\,\mathrm{N\,m}$
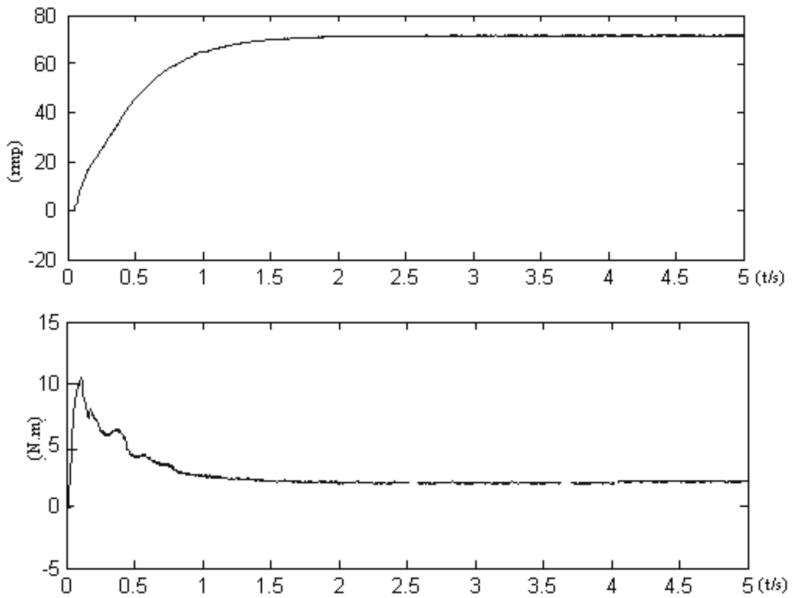
Fig. 8. Time evolution of speed (top) and time evolution of torque (bottom) for
$50/3$ Hz without voltage compensation for load $4\,\mathrm{N\,m}$
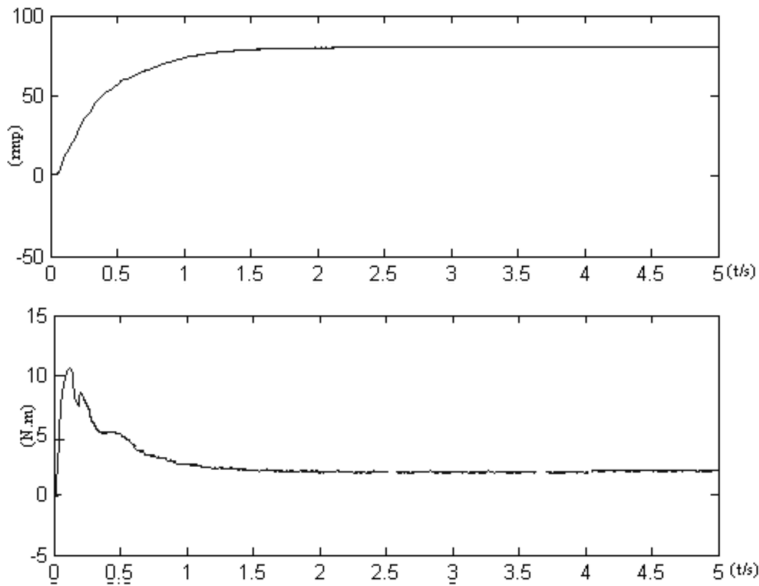
Fig. 9. Time evolution of speed (top) and time evolution of torque (bottom) for
50/3 Hz without voltage compensation for load 3 N m
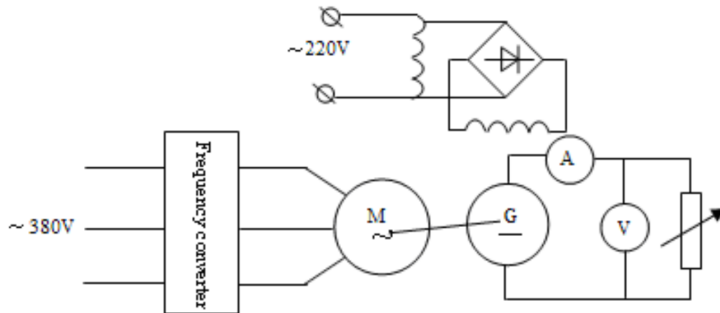
Fig. 10. Starting voltage test for AC frequency control system overload

6. Conclusion

In the variable frequency speed regulation system, aiming at the problem that induction motor adopts constant voltage to frequency ratio control strategy and low starting torque at starting, the method of voltage compensation is adopted in this paper. According to the steady state equivalent circuit of asynchronous motor and low frequency vector induction motor, a formula is derived to calculate the voltage compensation. A simulation model of variable frequency speed regulation system is established, and the effect of voltage compensation and the effects of voltage compensation on torque and speed of motor at different loads are analyzed. The experiment proves that the voltage compensation has achieved good compensation effect in the variable frequency speed control system, and illustrates the importance

of voltage compensation when the frequency conversion starts.

Table 1. Voltage compensation data

Load (N m)	Dividing fre-quency	Theoretical voltage (V)	Actual volt-age (V)	Current (A)	Theoretical speed (rpm)	Measured speed (rpm)	Synchronous speed (rpm)
3	11	31.4	32	2.7	76	73	136
	9	35.7	36.9	2.7	106	103	166
	7	42.4	43.1	2.8	144	142	214
	5	54.1	56.4	2.7	240	238	300
	3	81.6	79.8	2.6	440	438	500
4	11	31.4	32	3.0	71	68	136
	9	35.7	38.	3.1	101	99	166
	7	42.4	43	3.0	139	135	214
	5	54.1	56.3	3.0	235	233	300
	3	81.6	79.5	2.9	435	433	500
5	11	31.4	32	3.3	66	64	136
	9	35.7	38	3.2	96	93	166
	7	42.4	42.9	3.4	144	144	214
	5	54.1	56.1	3.3	230	229	300
	3	81.6	78.9	3.2	430	426	500

References

[1] CH. KLUMPNER, P. NIELSEN, I. BOLDEA, F. BLAABJERG: *New matrix converter-motor (MCM) for industry applications*. IEEE Transactions on Industrial Electronics *49* (2002), No. 2, 325–335.

[2] R. VARGAS, U. AMMANN, B. HUDOFFSKY, J. RODRIGUEZ, P. WHEELER: *Predictive torque control of an induction machine fed by a matrix converter with reactive input power control*. IEEE Transactions on Power Electronics *25* (2010), No. 6, 1426–1438.

[3] T. F. PODLESAK, D. C. KATSIS, P. W. WHEELER, J. C. CLARE, L. EMPRINGHAM, M. BLAND: *A 150-kVA vector-controlled matrix converter induction motor drive*. IEEE Transactions on Industry Applications *41* (2005), No. 3, 841–847

[4] P. W. WHEELER, J. C. CLARE, M. APAP, K. J. BRADLEY: *Harmonic loss due to operation of induction machines from matrix converters*. IEEE Transactions on Industrial Electronics *55* (2008), No. 2, 809–816.

[5] M. ATEN, G. TOWERS, C. WHITLEY, P. W. WHEELER, J. C. CLARE, K. BRADLEY: *Reliability comparison of matrix and other converter topologies*. IEEE Transactions on Aerospace and Electronic Systems *42* (2006), No. 3, 867–875.

[6] J. KLÍMA: *Analytical closed-form solution of a space-vector modulated VSI feeding an*

induction motor drive. IEEE Transactions on Energy Conversion *17* (2002), No. 2, 191–196.

[7] Y. S. Lai: *Machine modeling and universal controller for vector-controlled induction motor drives.* IEEE Transactions on Energy Conversion *18* (2003), No. 1, 23–32.

[8] Y. Zhang, J. Zhu: *Direct torque control of permanent magnet synchronous motor with reduced torque ripple and commutation frequency.* IEEE Transactions on Power Electronics *26* (2011), No. 1, 235–248.

[9] Y. Wang, Z. Lu, H. Wen, Y. Wang: *Dead-time compensation based on the improved space vector modulation strategy for matrix converter.* PESC Record - IEEE Annual Power Electronics Specialists Conference, 12–17 June 2005, Recife, Brazil, 27–30.

[10] K. B. Lee, F. Blaabjerg: *A nonlinearity compensation method for a matrix converter drive.* IEEE Power Electronics Letters, *3* (2005), No. 1, 19–23.

[11] A. Arias, L. Empringham, G. M. Asher, P. W. Wheeler, M. Bland, M. Apap, M. Sumner, J. C. Clare: *Elimination of waveform distortions in matrix converters using a new dual compensation method.* IEEE Transactions on Industrial Electronics *54* (2007), No. 4, 2079–2087.

[12] K. B. Lee, F. Blaabjerg: *An improved DTC-SVM method for sensorless matrix converter drives using an overmodulation strategy and a simple nonlinearity compensation.* IEEE Transactions on Industrial Electronics *54* (2007), No. 6, 3155–3166.

[13] J. M. Stephenson, A. Hughes, J. Mann: *Torque ripple minimisation in a switched reluctance motor by optimum harmonic current injection.* IEE Proceedings - Electric Power Applications *148* (2001), No. 4, 322–328.

Mathematical model for investigation of welding forces at contacts bounce in the process of a medium voltage vacuum contactor switching on

Y. I. Bajda[1], M. A. Leliuk[1]

Abstract. A mathematical model for determining the possible welding forces of contacts at their bounce during the switching of process taking into account internal and surface heat sources and latent heat of phase transitions based on the Leibenson method is presented. The influence of the shape of the current and the phase of voltage switching on the value of the welding force is shown. Calculations have been carried out that make it possible to determine the dynamics of the motion of the regions of phase transitions, their maximum values the time of solidification of the contact material. The correctness of the calculation method is proved.

Key words. Key words: vacuum contactor, contact bounce, welding force, Stefan problem.

1. Problem definition

In medium voltage networks for switching and load control (electric motors, capacitors and transformers) vacuum contactors have become most widespread. This is due to the simplicity of their design and control, high speed and unpretentiousness in operation (the drives do not require maintenance under normal climatic conditions), environmental safety, high fire and explosion resistance. The areas of application of contactors include: high-voltage reactive power compensation installations; switching circuits of electric motors in heavy operation modes (mining, oil and gas, metallurgy) [1]. The world monopoly for the manufacture of contactors is held by Germany (ABB, Siemens), France (Schneider Electric), Korea (Hyundai, LG, LS), Japan (Mitsubishi Electric).

Vacuum contactors consist of three poles with vacuum interrupters, a control system, a drive mechanism and a mechanical system [1, 2]. The main operational

---

[1]National Technical University "Kharkiv Polytechnic Institute", Kyrpychova Str. 2, 61002 Kharkiv, Ukraine

parameters of vacuum contactors depend on the switching characteristics of vacuum interrupters which are given in the technical specification [3, 4]. Table 1 presents the technical specification of the TJC 1-7.2 / 450-4 / 5A vacuum interrupters by the Shaanxi Baoguang Vacuum Electric Device Co., Ltd. [5].

As the experience of leading Companies shows, the increase in switching characteristics of vacuum interrupters is due to the development of new compositions of contact materials of the main contacts and their geometry providing radial or axial movement of the arc during the opening of the contacts [6, 7]. And one of the reasons that reduces the service life of the electrical contacts of the vacuum interrupters is their bounce when switching on, which leads not only to the increased wear of the contacts due to the appearance of electric arc, but also to their welding, which can lead to an accident in the electrical circuit [3, 4].

The reason for the bounce of the contacts is the excessive kinetic energy of the moving masses and the elastic properties of the contact system. Therefore, when developing new or improving the existing design of any of the driving elements of vacuum contactors, it is necessary to take into account the possibility of bouncing contacts and know the possible value of their welding force, since the reliability of the contactor's operation is that when the contactor is switched off, the force of the drive mechanism is enough to break the welded contacts.

2. Analysis of investigations and publications

Manufacturers of vacuum interrupters put forward stringent requirements for the duration and number of contact bounces during the operation of switching on. These requirements are met through the design of the drive mechanism and the mechanical system in accordance with Table 1: the average closing and opening speed of the main contacts, the duration of the bounces during the closing, the distance between the contacts in the "off" position. This applies to contactors with forced electromechanical and microprocessor control. And the use of a microprocessor control system expands the functionality of the contactor and allows to adjust the speed of closing the contacts of the vacuum interrupter and, accordingly, to reduce the contacts bounce. Thus, in [8] it is proposed to use a control system with a pulsed supply of an electromagnet which makes it possible to reduce the kinetic energy of the movable contact by controlling the coil current. In [9, 10] the connection between the phase of the voltage switching on and the contact closure speed is considered, the optimum phase angle of the voltage switching on is found at which the number of contact bounces is minimal. In [11] the pressure of the metal vapor generated by the arc during contact bounces which can be comparable or even greater than the force of the contact spring is taken into account.

The result of the contact bounces during the closure (at the final stage) can be welding of the contacts and as a consequence - not opening the contacts during the switching off operation. This can lead to emergency operation throughout the network, so when calculating the mechanical system, it is necessary to establish a relationship between the characteristics of the drive mechanism and the characteristics of the return and contact springs taking into account the possible value of the

welding force of the contacts.

Table 1. Technical specification of TJC 1-7.2/450-4/5 A vacuum interrupters

Voltage ratings at rated contact stroke		
Parameter	Unit	Data
Rated frequency	Hz	50/60
Rated voltage	kV	7.2
Rated short-time power-frequency withstand voltage (1 min)	kV	32
Rated lightning impulse withstand voltage	kV	60
Current ratings		
Rated current	A	450
Circuit resistance at lowest rated contact force	μΩ	≤ 50
Rated short-time withstand current	kA	8
Rated duration of short-circuit	s	1
Rated making current	kA	4.5
Rated breaking current	kA	3.6
Limit breaking current (rated characteristics to be given on request)	kA	4.5
Mechanical data		
Weight of movable parts	kg	0.2
Closing force due to bellow and atmosphere	N	60±20
Force required to hold contacts open at full stroke	N	90±20
Mechanical requirements		
Clearance between open contacts	mm	4±0.5
Average opening speed (average of first 75 % of contact gap)	m/s	0.7±0.1
Average closing speed (average of last 30 % of contact gap)	m/s	0.25±0.05
Rated added external contact final force	N	90±10
Contact bouncing duration at closing operation	ms	≤2
Closing and opening non-simultaneity of three-phase contacts	ms	≤2
Life		
Storage life	years	20
Mechanical endurance	times	300000
Contacts limit erosion	mm	2

The difficulty in calculating the force of contacts welding at their bounce is that the bounce of the contacts and its parameters (the total vibration time, the start time of the first and subsequent bounces, if any, the duration of the bounces) are determined not only by the material of the contacts and the speed of their strikes each other but also by the design of the drive mechanism, in particular contact and counter-acting springs. In turn, the welding force is determined both by the parameters of the contact bounce and by the thermophysical parameters of the material, taking into account the change in its phase state [12–15]. The need to develop a mathematical model of welding lies in the fact that existing models are

extremely problematic in use, it is often necessary to do the work from the beginning to the end, from the development of the software and ending with calculations. In addition, due to the individuality of the design, the available models do not always correspond to the objects under consideration.

The following can be attributed to the shortcomings of the available models: as in [12, 15, 16], the heating of contacts by internal heat sources is not taken into account. Such heating is considered in [13, 15], but with the current flowing through closed contacts. The process of heating the contact surface at their bounce is described in more detail in [15, 16], however, [15] does not take into account the time variation of arc power, and [16] does not consider internal heat sources.

3. Goal of the paper

Development of a mathematical model for calculating the welding forces of contacts at switching on, taking into account the effect of surface and volumetric heat sources, the latent heat of phase transitions in the nonstationary mode, depending on:
– bounce parameters of contacts,
– the values of the load power factor and the initial phase of the network voltage,
– thermophysical parameters of contact materials.

4. Developed mathematical model

The vibration parameters are determined by the mechanical properties of the system, and the thermal effect of the arc on the contact by the parameters of the electrical network. It is possible that the welding force will be greater at a smaller amplitude value of the switched-on current which depends on the power factor of the electrical circuit and on the phase of switching on (see Fig. 1).

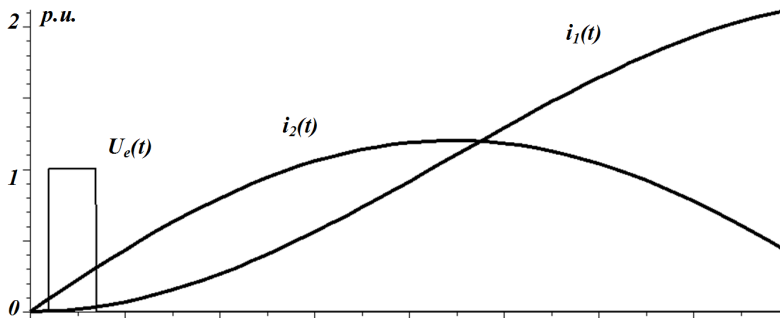Fig. 1. Arc voltage and the circuit current as a function of the phase of the switched-on voltage in relative units, where $U_e(t)$ is the short arc voltage, $i_1(t)$ is the shape of the current at the zero phase of the switching on and $i_2(t)$ is the shape of the current at the phase of the switching on of 90 electrical degrees

The relations for dissipated power during the burning time of the short arc for

the currents shown in Fig. 1 are

$$K = \frac{\int_{t_0}^{t_d} U_e(t) i_2(t)\,\mathrm{d}t}{\int_{t_0}^{t_d} U_e(t) i_1(t)\,\mathrm{d}t} \approx 12\,. \tag{1}$$

Calculation assumptions adopted in the development of the model are the following: during the burning of the short arc, the thermal power inputted into the contact is determined by the current and the equivalent near-electrode voltage drop; the anode arc with one reference spot is considered; the thermal power of the arc is inputted into the zone with the evaporation temperature of the contact material [15, 16]; the thermophysical parameters do not depend on temperature but are taken as averaged for each of the calculated regions (see Fig. 2).
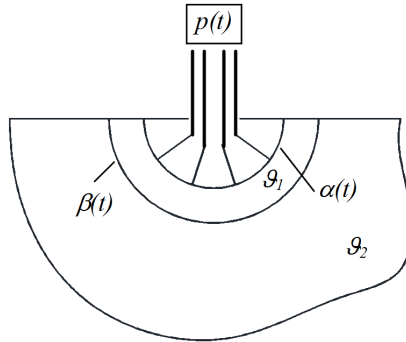
Fig. 2. Graphical representation of the computational model, where $p(t)$ is the specific power of the arc, inputted into contact, $\alpha(t)$ is the moving boundary of the evaporation front, $\beta(t)$ is the moving boundary of the melting front, ϑ_1 is the temperature in the melt area and ϑ_2 is the temperature in the solid phase

Mathematical formulation of the problem in a spherical coordinate system reads

$$\begin{cases} c\gamma_1 \cdot \frac{\partial \vartheta_1}{\partial t} = \lambda_1 \cdot \left(\frac{\partial^2 \vartheta_1}{\partial r^2} + \frac{2}{r} \cdot \frac{\partial \vartheta_1}{\partial r} \right) + \frac{\rho_1 \cdot i^2(t)}{4\cdot\pi^2 r^4}, \ \alpha(t) \leq r \leq \beta(t), \\[2mm] c\gamma_2 \cdot \frac{\partial \vartheta_2}{\partial t} = \lambda_2 \cdot \left(\frac{\partial^2 \vartheta_2}{\partial r^2} + \frac{2}{r} \cdot \frac{\partial \vartheta_2}{\partial r} \right) + \frac{\rho_2 \cdot i^2(t)}{4\cdot\pi^2 r^4}, \ \beta(t) \leq r \leq \infty, \end{cases} \tag{2}$$

$$\begin{cases} \vartheta_1(\alpha(t)) = \vartheta_k, \ \vartheta_1(\beta(t)) = \vartheta_p, \\[2mm] \vartheta_2(\beta(t)) = \vartheta_p, \ \vartheta_2(\infty) = \vartheta_0, \end{cases}$$

where $c\gamma_i$ and λ_i are, respectively, the averaged values of the volumetric heat capacity and thermal conductivity for each of the regions, ϑ_i are the design temperatures, $i(t)$ is the current, ρ_i are the resistivities averaged over the regions, $\alpha(t)$ is the moving boundary of the evaporation front of the material, $\beta(t)$ is the moving boundary of the melting front of the material, ϑ_k is the boiling point of the material, ϑ_p is the melting point of the material, ϑ_0 is the initial contacts' temperature.

Such problems are related to Stefan problems [14]. To analyze the problem, it is desirable to have an analytical solution of the problem (2) but in the presented (taking into account the latent heat of phase transitions) there is no analytical solution of the problem due to non-linearity, and, in addition, the law of movement of the boundaries of phase transitions is unknown. For the same reasons, it is difficult to obtain a numerical solution which is even more difficult to be analyzed. An approximate Leibenson method is used to obtain an analytical solution of the problem. The method consists in replacing the real law of temperature change with a function that satisfies the quasi-static temperature distribution and boundary conditions. The condition for applicability of the method is

$$a^2 > v \cdot L \,, \tag{3}$$

where a^2 is the thermal diffusivity, v is the velocity of the phase front movement and L is the characteristic size of the problem.

The technique assumes that the dynamic temperature distribution over the shape is analogous to the static distribution, and the undefined constants are a function of unknown laws of movement of the boundaries of phase transitions.

The solution of the system (2) under the indicated conditions can be written in the form (the complete solution is not given in view of its cumbersome nature):

$$\vartheta_1 = f_1\left(i(t), r, \alpha(t), \beta(t), D_i\right),$$
$$\vartheta_2 = f_2\left(i(t), r, \alpha(t), \beta(t), D_i\right), \tag{4}$$

where f_1 and f_2 are known functions, D_i are known constants, such as thermal conductivity, boiling point, melting point of the material, etc., r is the current value of the radius, and $\alpha(t)$ and $\beta(t)$ are the radii of moving boundaries of phase transitions.

To determine the unknown values of $\alpha(t)$ and $\beta(t)$ in (4), it is necessary to use the heat flux balance condition on the moving boundaries of the boiling and melting fronts. As a result, a system of two nonlinear ordinary differential equations with corresponding initial conditions with respect to the unknown laws of movement of the boundaries of the fronts of evaporation and melting is obtained:

$$\begin{cases} Q_{is} \cdot \gamma_1 \cdot \dfrac{d\alpha(t)}{dt} = \dfrac{U_e(t) \cdot i(t)}{2 \cdot \pi \cdot \alpha(t)^2} + \lambda_1 \cdot \dfrac{\partial \vartheta_1(i(t), \alpha(t), \beta(t))}{\partial r}, \\[2mm] Q_p \cdot \gamma_2 \cdot \dfrac{d\beta(t)}{dt} = -\lambda_1 \cdot \dfrac{\partial \vartheta_1(i(t), \alpha(t), \beta(t))}{\partial r} + \lambda_2 \cdot \dfrac{\partial \vartheta_2(i(t), \alpha(t), \beta(t))}{\partial r}, \\[2mm] \alpha(0) = \alpha_0, \ \beta(0) = \beta_0, \\[2mm] \beta(t) > \alpha(t), \end{cases} \tag{5}$$

where $U_e(t)$ is the equivalent near-electrode voltage drop during the combustion of the short arc, Q_{is} is the latent heat of vaporization, γ is the average density of the material by regions and Q_p is the latent heat of melting.

In the system of equations (5) the voltage on the arc is a function of time, and the current value is determined from the solution of the electric circuit equation

$$\begin{cases} L_e \cdot \dfrac{\mathrm{d}i(t)}{\mathrm{d}t} + r_e \cdot i(t) = U_m \cdot \sin(\omega \cdot t + \psi), \\[2mm] i(0) = 0, \end{cases} \tag{6}$$

where L_e is the inductance of the circuit, r_e is the active resistance and ψ is the initial voltage phase.

From the equation and the initial condition (6) it follows that the maximum value and the shape of the current are determined by the power factor and the initial phase of the voltage

$$r_e = z \cdot \cos(\varphi), \ \ L_e = \frac{z \cdot \sin(\varphi)}{\omega} \ . \tag{7}$$

5. An example of calculations: welding force of copper contacts

The initial data for the calculation is the time dependence of the contact bounce obtained experimentally as well as the parameters of the electrical circuit: the amplitude of the network voltage and its initial phase, the resistance value of the circuit (current amplitude definition), power factor. For contactors with the application category AC-3 and AC-4, the power factor at the rated operating current greater than 100 A equals 0.35 [17].

Figure 3 shows an example of the shape of the circuit current with the following parameters: $\psi = 0.05 \cdot \pi$, $\cos\varphi = 0.35$ and $I_n = 400$ A.
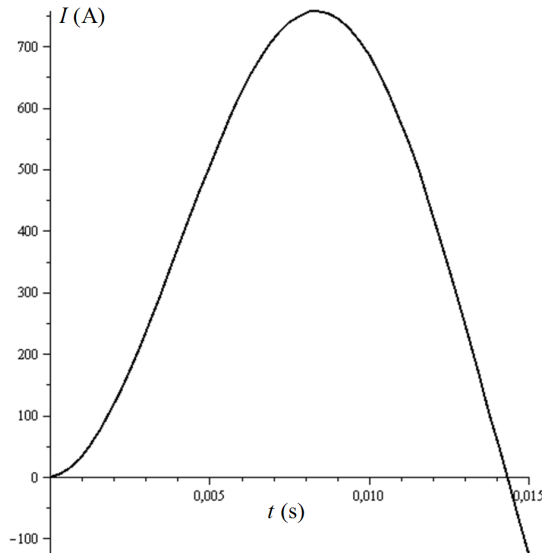
Fig. 3. Shape and value of the calculated circuit current at $\psi = 0.05 \cdot \pi$

For convenience of calculation, the origin of the current count coincides with the beginning of the first rebound of the contact $i(t_n + t)$. Figure 4 shows the function of the voltage on the contacts at their bounces obtained experimentally.
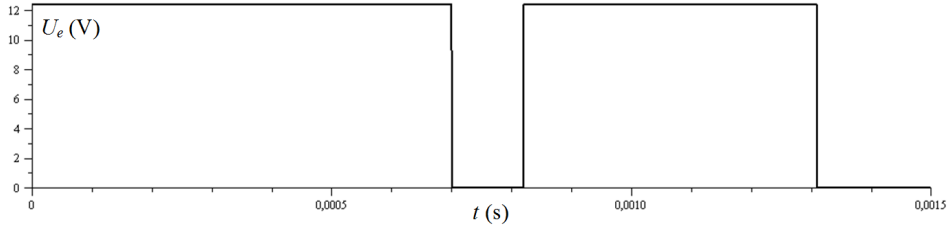
Fig. 4. Voltage of the short arc on the contacts at their bounces (the beginning of time coincides with the beginning of the first contact rebound)

The result of the system (5), (6) solution is presented in Fig. 5.
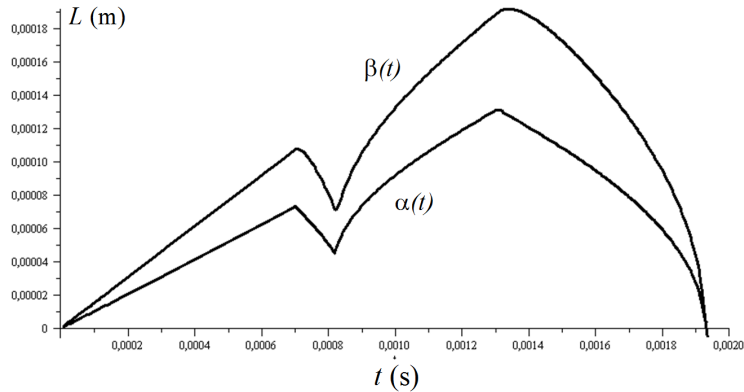
Fig. 5. The law of movement of the boundaries of phase transitions at the initial phase of the switching on $\psi = 0.05 \cdot \pi$, where $\alpha(t)$ is the moving boundary of the evaporation front and $\beta(t)$ is the moving boundary of the melting front

As it can be seen from Fig. 5, during the pause between rebounds, the contact material does not solidify. In addition, the second (smaller in duration) rebound significantly increases the area of the molten material which is due to the increase in current in the circuit and stored earlier (at the first rebound) energy. The maximum value of the melting radius is $\beta_{\max} = 1.89 \cdot 10^{-4}$ m. Having adopted the tensile strength at tension for copper of $2.5 \cdot 10^8$ N/m^2, we obtain the possible welding force F_s as

$$F_s = \pi \cdot \beta_{\max}^2 \cdot \sigma_B = 28.22 \text{ N}, \tag{8}$$

where $\beta_{\max}$ is the maximum value of the melting radius and σ_B is the tensile strength at tension for copper.

Figure 6 shows the circuit current in the case of the initial phase of the switching off of $\psi = 0.5 \cdot \pi$.

The graph of movement of the phase transition boundaries is presented in Fig. 7.
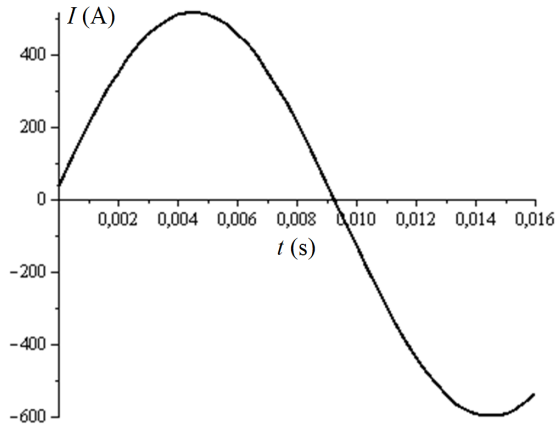
Fig. 6. Shape and value of the calculated circuit current at $\psi = 0.5 \cdot \pi$
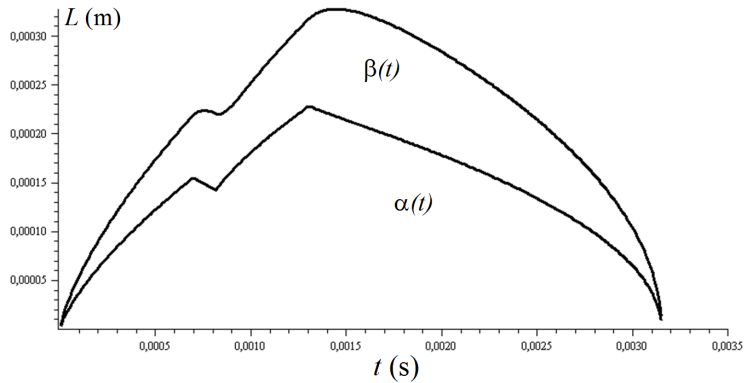
Fig. 7. The law of movement of the boundaries of phase transitions at the initial phase of the switching on $\psi = 0.5 \cdot \pi$, where $\alpha(t)$ is the moving boundary of the evaporation front and $\beta(t)$ is the moving boundary of the melting front

The possible value of the welding force in this case $F_s = 84\,\mathrm{N}$. The ratio of welding forces for the presented initial phases of switching on is

$$\frac{F_{\psi=0.5\cdot\pi}}{F_{\psi=0.05\cdot\pi}} \approx 3\,. \tag{9}$$

Consequently, the effect of the initial phase of the switching on on the welding force is significant.

Finally, the fulfillment of the condition (3) which determines the limits of applicability of the Leibenson method is verified. As the characteristic size, the maximum value of the melting front at the initial phase of the switching on is selected $\psi = 0.5\cdot\pi$

$$1.18 \cdot 10^{-4} > 0.232 \cdot 3.26 \cdot 10^{-4} = 7.56 \cdot 10^{-5}\,\frac{\mathrm{m}^2}{\mathrm{s}}\,. \tag{10}$$

Since condition (3) is satisfied for the maximum possible value of the melting front, it is also satisfied for all other smaller values, that is, the solution of the problem by the Leibenson method is correct.

6. Conclusion

1. The mathematical model of contacts welding at their bounce which is based on the Leibenson method, taking into account the effect of surface and internal heat sources, latent heat of phase transitions, thermophysical parameters of the material, the value and shape of the switched on current, the initial phase of switching on the voltage of the power source is developed.

2. The developed model allows to calculate the dynamics of movement of the boundaries of phase transitions determining their maximum values, the possible welding force and the cooling time of the contacts' materials.

3. The influence of the shape of the current and the initial phase of the voltage on the value of the welding force of the contacts is shown.

4. It is proved that the use of Leibenson method for solving the problem is correct.

5. The results of calculating the welding force of the contacts make it possible to determine the value of the force of the return spring which is necessary for the operation of switching off the contactor in the case of contacts welding. This value will be taken into account in the design of the electromagnet, namely, in determining the force of pressing the armature to the core of the electromagnet to fix the contactor in the on position.

References

[1] M. A. LELIUK: *Structure and kinematic schemes of medium voltage vacuum contactors.* Journal of the Kharkiv Polytechnic Institute. *Problems of improvement of electrical machines and apparatus.* Theory and Practice (in Ukrainian) (2016), No. 32, 29–31.

[2] C. T. CHI: *A high performance AC permanent magnet contactor.* Journal WSEAS Transactions on Electronics 5 (2008), Nos. 7–9, 313–3222.

[3] P. G. SLADE: *The vacuum interrupter: Theory, design, and application.* Publisher: CRC Press, Taylor & Francis Group (2007).

[4] E. P. A. VAN LANEN: *The current interruption process in vacuum analysis of the currents and voltages of current-zero measurements.* Doctoral Thesis, Delft University of Technology, Faculty Electrical Engineering, Mathematics and Computer Science (2008), paper 147.

[5] HTTP://WWW.ECVV.COM/PRODUCT/2145016.HTML

[6] H. FINK, D. GENTSCH, M. HEIMBACH: *New vacuum interrupters for contactors and switches.* ABB review (1999), No. 3, 32–36.

[7] P. G. SLADE: *Advances in material development for high power, vacuum interrupter contacts.* IEEE Transactions on Components, Packaging, and Manufacturing Technology: Part A 17 (1994), No. 1, 96–106.

[8] T. S. DAVIES, H. NOURI, F. BRITTON: *Towards the control of contact bounce.* IEEE

Transactions on Components, Packaging, and Manufacturing Technology: Part A *19* (1996), No. 3, 353–359.

[9] C. Y. HUNG: *Contact-bounce control and remote monitoring interface implementation of a PM contactor*. Journal WSEAS Transactions on Systems and Control *6* (2011), No. 5, 157–171.

[10] C. T. CHI: *An approach to the reduction of contact bounce for AC contactor*. International Journal of Innovative Computing, Information and Control (IJICIC) *5*, (2009), No. 10(A), 3031–3044.

[11] S. N. KHARIN, H. NOURI, T. DAVIES: *Effect of metallic vapour pressure on the vibration of electrical contacts in vacuum*. Materials Science Forum *440–441* (2003), 505–512.

[12] N. V. KOROLEV: *Welding of electrical contacts at switching on high currents*. Doctoral thesis, Kharkiv (in Russian) (1984).

[13] N. E. LYSOV: *Welding of closed single-point and planar contacts*. Electrical Engineering (in Russian) (1964), 25–28.

[14] A. N. TIKHONOV, A. A. SAMARSKII: *Equations of mathematical physics*. Nauka, Moscow (in Russian) (1972), Publisher: Dover Publications, Series: Dover Books on Physics (2011).

[15] E. I. KIM, V. T. OMELCHENKO, S. N. KHARIN: *Mathematical models of thermal processes in electrical contacts*. Akademya nauk Kazakh SSR, Alma-Ata (in Russian) (1977).

[16] E. I. BAJDA: *Theoretical calculation of the welding forces of contacts at their closing on emergency overcurrents*. Electrical Engineering & Electromechanics (in Russian) (2012), No. 3, 11–13.

[17] IEC 62271-106:2011: *High-voltage switchgear and controlgear - Part 106: Alternating current contactors, contactor-based controllers and motor-starters*. IEC Webstore International Electrotechnical Commission, TC 17/SC 17A (2011).

A study on effect of spark timing on the emission characteristics from the lean-burn natural gas engine

Ma Zhichao[1], Du Jinyin[1], Xu Yanming[1], Wang Xin[1], Li Feifei[1]

Abstract. In the present paper, the spark ignition lean-burn natural gas engine established by Toyota 8A engine is introduced. The effect of spark timing on emission characteristics from the lean-burn natural gas engine is investigated experimentally. The test results have demonstrated that spark timing and revolution can commonly affect the emissions from the lean-burn natural gas engine. With the increase of the spark timing, the NO_x emission is increased as well while the engine-out THC emissions is decreased. The engine-out CO emissions has something to do with the revolution, for example, spark timing is increased with a slow-speed engine, while the CO emission is reduced gradually and vice versa.

Key words. Spark timing, lean-burn, natural gas engine, emissions.

1. Introduction

With the rapid development of world economy and increase of population, the energy consumption and greenhouse gases and various harmful substances become more and more severe. Survival environment of human being are facing dire challenges. Under such circumstance, it is necessary to make rational use of mineral resources and develop clean fuel to ensure sustainable development. In the perspective of energy safety, the energy consumption structure should be adjusted to get rid of petroleum dependencies and making natural gas as alternative fuel for internal combustion engine is a rational choice [1], [2]. The harmful emissions from natural gas engine are less than the traditional one. The major component of natural gas is methane (CH_4) which becomes CO_2 and water after combustion and produces $1/2$ of greenhouse gases of coal, $2/3$ of petroleum and consequently reduces the environmental pollution [3]. In addition, octane number of natural gas is approximate 130 which indicate good anti-detonating quality and the compression ratio is 12

[1]Department of Marine Engineering, Tianjin Maritime College, Tianjin, 300350, China

when taking the natural gas as the engine fuel, therefore, natural gas engine can improve thermal efficiency. Lean-burn technology is more popular as it can reduce the NO_x emissions [4]. In this paper, the spark ignition lean-burn natural gas engine is established by Toyota 8A engine. The objective of this study is to extend our understanding related to the effect of spark timing on emission characteristics from this lean-burn natural gas engine.

2. Experimental apparatus

The tested engine is refitted by a Toyota 8A-FE gasoline engine. Toyota 8A-FE engine, which is an electronic control gasoline engine, has 4 cylinders, 16 valves. The parameters are given in the Table 1.

Table 1. Main parameters of Toyota 8A-FE engine

Cylinder	Vertical, four-stroke, water-cooled, in-line	Cylinder number	Four
Valve	Four valves/cylinder, double overhead camshafts	Bore diameter×stroke (mm)	78.7×69
Fuel supply	Closed-loop multi-point electric fuel injection	Displacement L (mm)	1.342
Working sequences	1-3-4-2	Compression ratio	9.3

The entire test set-up contains three main parts: natural gas supply system, ignition system and electronic control system.

In Fig. 1, system layout on natural gas engine is shown. The natural gases flow out from high-pressure receiver through the manual-operated valve and total control valve to the filter which remove the impurities, then the gas flow to the check valve and flow meter, subsequently, the gas pressure are reduced to a required value through the 1st-stage and 2nd-stage reducing valves finally to the air rails. To supply mixture gas to the engine, in accordance with the engine speed and load, the natural gas is injected to the inlet port and further into the cylinder together with fresh air by the electronic control unit, which adjusts the injection timings and injection pulse width, the relative air fuel ratio (λ) of air-natural gas mixture could be altered under different engine operation conditions.

The electronic control system for the natural gas engine is composed of two parts, i.e. the electronic control unit (lower computer, ECU) and PC monitoring system (upper monitor). The electronic control unit comprises of electronic control injection system and high-energy ignition system. Injection pulse width and injection timing can be controlled by electronic control injection system according to the engine speed
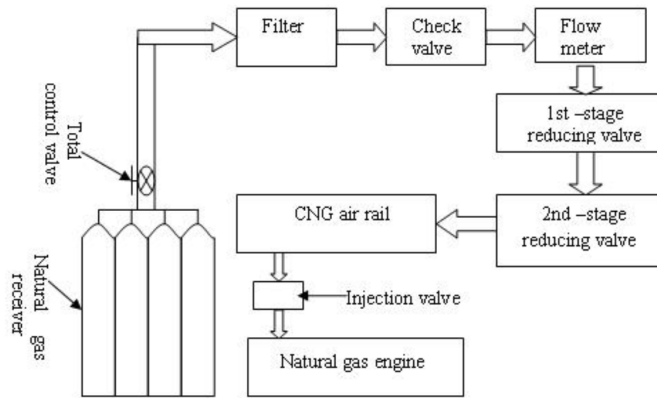
Fig. 1. Layout of natural gas supply system

and load while the ignition energy and timing are controlled by high-energy ignition system. PC monitoring system is a debugging platform which sends the controlled parameters to the ECU to achieve human-machine data exchange. The electronic control unit is a linkage between PC monitoring system and engine while monitoring system is a platform on online display and parameter setting.

3. Experimental research

Figure 2 shows the curves on NO_x emission varies with spark timings at different revolution and different throttle opening.
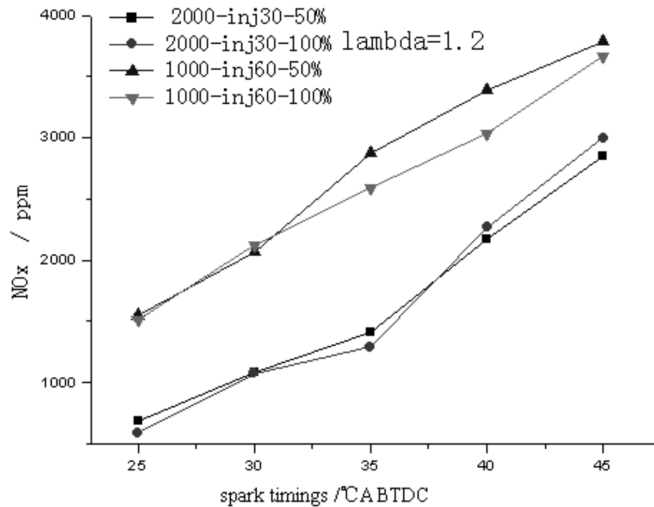
Fig. 2. NO_x emission versus spark timings

It can be seen that increased spark timing can result in increased NO_x emission

as the ignition takes place before TDC at an earlier ignition timings (as shown in Fig. 3.
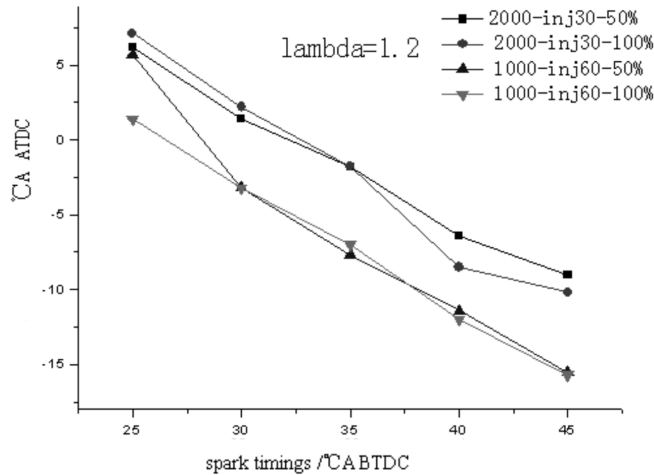
Fig. 3. Ignition timing versus spark timings

At this moment, the piston travels upwards and compresses the pressure and temperature to a high point. At the moment of ignition, the cylinder pressure and temperature are higher, maximum combustible pressure value is near the small cylinder volume. The higher combustible temperature caused by maximum combustion pressure and oxygen in the cylinder can result in NO_x emission. When the spark timing is reduced, the later ignition and the slower combustion lead to drop in maximum temperature and pressure which turn to reduction in NO_x emission. In addition, at the same spark timing, NO_x emission produced at 1000 rpm is more than that of 2000 rpm. The advanced ignition and shorter combustion durations due to low speed cause a higher combustible temperature (as shown in Fig. 4), therefore, NO_x emission is higher at a lower speed than that a higher speed. At the same revolution, injection timing has little effect on the NO_x emission since it does not much affect the ignition timing and combustion durations (as shown in Figs. 3 and 4) and cylinder combustion temperature is almost constant.

In Fig. 5, the curves on the engine-out THC emissions at 1000 rpm and 2000 rpm, $\lambda = 1.2$ variation with spark timings are shown. It can be seen from the figure that with the increase of spark timing the engine-out THC emissions is reduced. The main reason is that great spark timing makes the ignition take place before TDC at an earlier moment (as shown in Fig. 3) and short combustion durations (as shown in Fig. 4) produce a high temperature and pressure which reduces the engine-out THC emissions. Besides, throttle opening has effect on the engine-out THC emissions as well. When throttle is fully opened, air inflow and cylinder temperature rise so that it can improve combustion. In consequence, at wide open throttle, the engine-out THC emissions remain constant with the variation of spark timings. However, the latter spark timing, which makes the ignition take place after TDC (as shown in figure 3) and have a longer combustion durations (as shown in Fig. 4) finally lead to

high engine-out THC emissions.
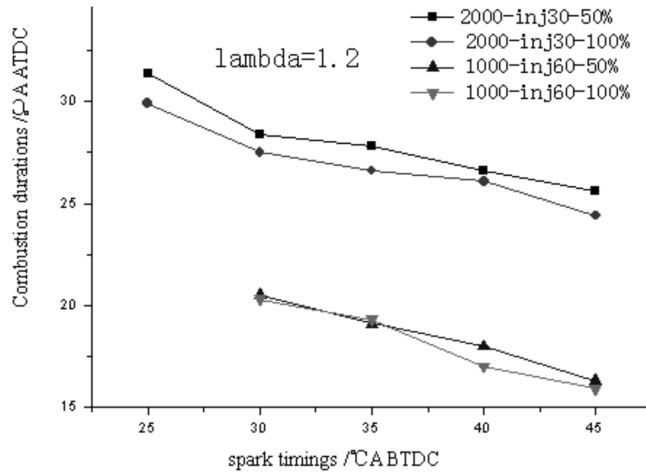
Fig. 4. Ignition timing versus spark timings
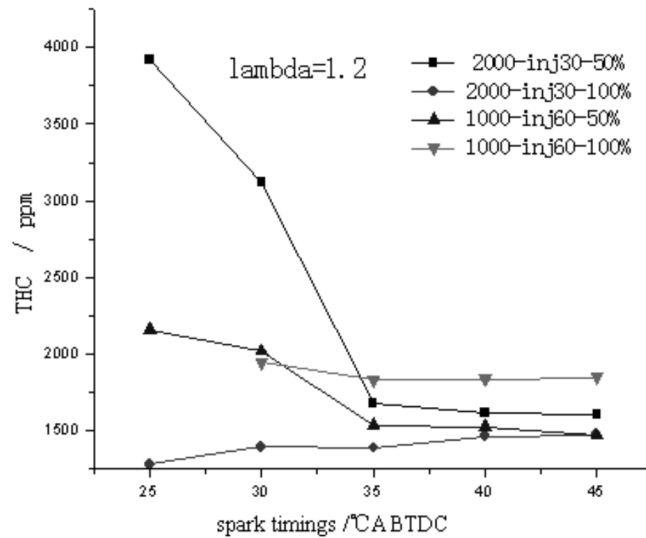
Fig. 5. Engine-out THC emissions versus spark timings

Figure 6 shows that when $\lambda = 1.2$, for different throttle opening and revolution, the engine-out CO emissions vary with the different spark timings. It can be seen that when the spark timing is increased at a high speed, the engine-out CO emissions increase as well and vice versa. At a low speed, the spark timing is increased and ignition is advanced gradually (as shown in Fig. 3) and combustion durations becomes shorter (as shown in Fig. 4) that brings about a high combustion temperature and pressure, good combustion and reduced CO emissions. At a high speed, ignition is

retarded to $7°$ and main combustion period increased to $10°$. A drop in maximum combustion temperature is the reason of increased CO emissions. In conclusion, the CO emissions is reduced with the variation of increased spark timings at a low speed, while it increased at a high speed.
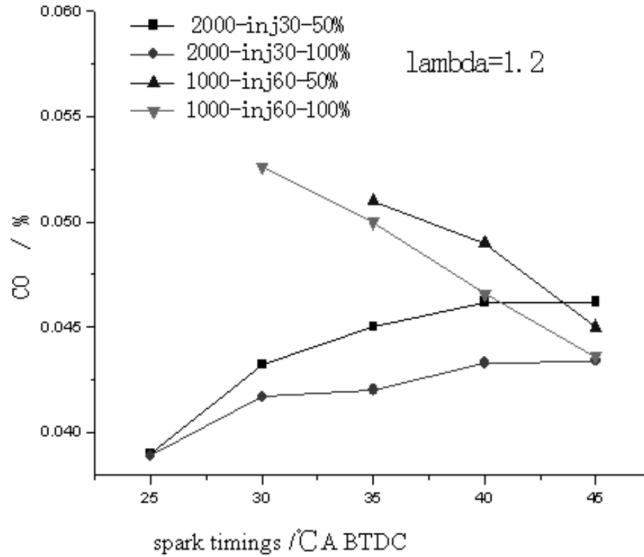
Fig. 6. Engine-out CO versus spark timings

4. Conclusion

Experiment apparatus and research of lean-burn natural gas engine and the effect of spark timing on emission characteristics from this engine are introduced respectively in details. It indicates that the spark timing and revolution can commonly affect the emissions characteristics from lean-burn natural gas engine. With the increase of spark timing, the NO_x emission is increased as well while the engine-out THC emissions is decreased. The engine-out CO emissions is related to the revolution, with the increase of spark timing, The engine-out CO emissions is reduced gradually at a low speed, while that is increased gradually at a high speed.

References

[1] H. M. CHO, B. Q. HE: *Spark ignition natural gas engine-A review*. Energy Conversion and Management (Elsevier) *48* (2007), 608–618.
[2] M. U. ASLAM, H. H. MASJUKI, M. A. KALAM, H. ABDESSELAM, T. M. I. MAHLIA, M. A. AMALINA: *An experimental investigation of CNG as an alternative fuel for a retrofitted gasoline vehicle*. Fuel *85* (2006), Nos. 5–6, 717–724.
[3] S. SHIGA, S. OZONE, H. T. C. MACHACON, H. KARASAWA, H. NAKAMURA, T. UEDA, N. JINGU, Z. HUANG, M. TSUE, M. KONO: *A study of the combustion and emission*

characteristics of compressed-natural-gas direct-injection stratified combustion using a rapid-compression-machine. Combustion and Flame *129* (2002), Nos. 1–2, 1–10.

[4] R. Tilagone, G. Monnier, A. Satre, Y. Lendresse, J. Personnaz, D. Cullerier, F. Turin: *Development of a lean-burn natural gas-powered vehicle based on a direct-injection diesel engine.* CEC/SAE Spring Fuels & Lubricants Meeting & Exposition, 21 June 2000, Paris, France, Technical Papers 2000-01-1950 (2000).

[5] Z. C. Ma: *Study on combustion and emission characteristics of a spark ignition natural gas engine.* Master's thesis, Tianjin University, Tianjin (2007).

Design of a wind turbine model for clean energy: Case study—Khorasan Razavi regional electricity company

Ashkan Mohammadzadeh[1], Aleme Keikha[2,3]

Abstract. Using wind as a clean and free source of generating electrical energy has been increasingly developed so that wind generated electricity by 2015 equals 5.5 % of total electrical energy produced in the world, and by 2020, 10 % of the total global electricity would be obtain from wind. Thus, the purpose of the present research is to study effective organizational strategies on investment for wind energy utilization in Khorasan Razavi Regional Electricity Company. This is an applied study in term of purpose and a descriptive survey in term of data collection and processing. Research statistical population included 200 managers, employees, consultants, and experts affiliated to strategic planning at Khorasan Razavi Regional Electrical Company headquarter in 2016. 127 samples were randomly selected through simple random sampling method. Research data were collected through using a questionnaire the reliability of which was measured 0.796 through using Chronbach's alpha test. Research results indicate that the organizational strategy influences investment on utilizing wind energy in Khorasan Razavi regional electricity company. Further, of 9 identified strategies, environmental assessment strategy in strategic planning process and change management in strategic planning process showed no significant effect on planning wind energy utilization in Khorasan Razavi regional electricity company.

Key words. Wind turbine, organizational strategy, investment in wind energy, regional electricity, Khorasan Razavi.

1. Introduction

Power plays a critical role in formulating economic development plans including economic development, welfare and improved life conditions, increased income, and national economic growth factors, which are largely influenced by power effects. Nowadays, wind is used for several functions. Wind turbines construction focuses on windmills, water pumping wind turbine, agricultural wells power supply, fish

---

[1]Master of executive management, Khorasan Razavi, Mashhad, Iran
[2]Faculty member, University of Zabol, Zabol, Iran
[3]Corresponding author

farming, improving the environment, as well as electricity generation for industrial and household. National development infrastructures and economic development rely upon infrastructure projects. In developing countries, infrastructures are mostly delayed due to huge capitalization; and hence, are the first items removed at the time of debt and budget deficiency comparing public current costs. In 2015, about 50 GW of wind energy potential has been operated, which raised global wind energy potential up to 30 % to 480 GW. This level of increased power capacity was larger than other renewable technologies in the year. During 2015, 80 nations have added their capacity and at least 85 nations have reported an increase by more than 10 MW; 22 nations of which have passed 1 GW and 87 % of total global capacity has been attributed to the top 10 nations. Leading countries in the area of new installations included China, U. S. A, India, Germany, and U. K followed by Canada. The UE has 23 % of the global market and 41 % of global total capacity [1, 2].

To use extant wind sources for power generation in Iran, it requires reliable information of wind potential in understudied region for wind power plant construction. Iran, regarding windy areas, provides a proper foundation for developed utilization of wind turbines. According to wind Atlas and based on the data of 60 stations at different national regions, the sites' nominal capacity is about 60 000 MW. Relying upon the predictions, the amount of national economic recoverable wind energy is estimated up to 18 000 MW demonstrating considerable national potential in the area of wind power plant construction, and cost-effective investment in wind energy industry. Lahmeyer Group has cooperated in running wind potentiometric project in Iran and estimated recoverable wind potential about 100 000 MW.

Regarding advantages of wind power plant construction, it is necessary to mention that launching the power plants may obviate wind turbine demands; moreover, it also replies some part of national and international power supply demand and is easily converted to electrical energy. Variation in energy sources, sustained energy system, high maneuver in utilization from a watts to several MW, no need for water, and no environmental pollution, high efficiency, as well as wind energy in most central, desert, and mountainous areas are other advantages of power plants [3, 4].

2. Proposed method

The dynamic analysis of conventional electrical machines is performed using dynamic analytical equation for each phase winding. The basic scheme is depicted in Fig. 1.

The terminal voltage of the TFG can be determined differentiating the flux linkage of the stator windings, as shown in equation (1). This equation is a general form of stator voltage for alternating current generators [5]. The flux linkage is computed as function of rotor position and armature currents by 3D static finite element analysis [5]. The form of equation (1) must be expanded to implement the look-up table data. Finally, the current differential term of the equation is isolated and implemented in Matlab/Simulink.
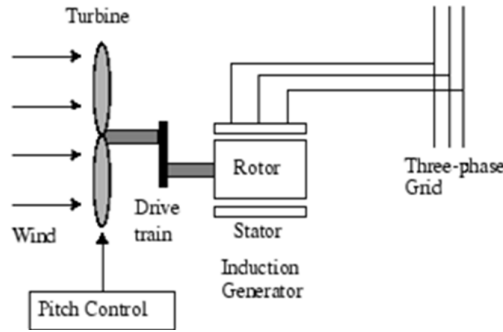
Fig. 1. Wind turbine modeling

$$v(t) = -Ri(t) + \frac{\mathrm{d}\lambda(i,\theta)}{\mathrm{d}t}, \tag{1}$$

$$\frac{\mathrm{d}i}{\mathrm{d}t} = \left(v(t) + Ri(t) - \frac{\mathrm{d}\lambda(i,\theta)}{\mathrm{d}\theta}\omega_{\mathrm{m}}\right) \frac{\mathrm{d}i}{\mathrm{d}\lambda(i,\theta)}. \tag{2}$$

Here, $v(t)$ is the terminal voltage, R is the phase resistance, $i(t)$ is the phase current, t is time, θ is the rotor angular position of the electric system and ω_m is the angular velocity of the rotor.

The aerodynamic torque developed by the rotor blades is calculated in this subsystem using the theory given in [4]. The kinetic energy E [J] of air mass m [kg] moving at a speed v_{wind} [m/s] is

$$E = \frac{1}{2}mv_{\mathrm{wind}}^2. \tag{3}$$

If the air density is ρ [kg/m^3], mass flow through an area A is given as

$$\dot{m} = \rho A v_{\mathrm{wind}}. \tag{4}$$

Thus, the equation for the power (in W) through a cross-sectional area A normal to the direction of wind is

$$P_{\mathrm{wind}} = \frac{1}{2}\rho A v_{\mathrm{wind}}^3. \tag{5}$$

In the case of a wind turbine, the area A is the area swept by the rotor blades. Only a part of this power may be captured due to the non-ideal nature of the rotor, hence the need for the coefficient C_{p}. The result is shown in (6)

$$P_{\mathrm{rotor}} = \frac{1}{2}\rho\pi R_{\mathrm{rotor}}^2 v_{\mathrm{wind}}^3 \tag{6}$$

and the aerodynamic torque Γ_{rotor} can then be calculated as

$$\Gamma_{\text{rotor}} = \frac{P_{\text{rotor}}}{\omega_{\text{rotor}}} = \frac{\frac{1}{2}\rho\pi R_{\text{rotor}}^2 v_{\text{wind}}^3}{\omega_{\text{rotor}}} \ . \tag{7}$$

The model of turbine blade for this research is shown in Fig. 2 based on Ansys software. This model is used to evaluate the energy based on power equations.

3. Results

The most fundamental measure of a wind turbine's performance is given by its power curve. The wind turbine model developed in the previous section is tested by running the simulation at wind speeds from 1 to 20 m/s, with increments of 1 m/s between runs. As expected, the power output peaks at rated wind speed and then falls due to stalling.

Research data normality was determined through using Kolmogorov--Smirnov test and the results are presented in Table 1.

Table 1. Results of Kolmogorov—Smirnov test

Significance level	Kolmogorov–Smirnov test	Variable
0.198	1.075	Team participation
0.165	1.116	Organizational commitment
0.169	1.112	Environmental assessment
0.103	1.217	Senior management participation
0.099	1.226	Education status
0.064	1.313	Cultural aspects
0.107	1.210	Change management
0.14	1.030	Strategic alignment
0.053	1.346	Technology development

According to Table 1, data normality reveals that regarding test statistic value and significance level that is larger than 0.05, it is concluded that data are normally distributed; further, the researcher is allowed to use parametric parameters. Thus, according to the test results, the researcher used one-sample t-test to reply research hypotheses stating that identified organizational strategies influence wind energy investment. The results are shown in Table 2.

Regarding that mean senior management participation obtained 12.47, which is larger than mean variable; in addition, as significance level $\sigma = 0.000$ is less than 0.05, it may be stated that senior management participation in human resource planning process is larger than medium. As a result, it can be expressed that senior management participation influences human resource strategic planning process for wind energy investment at confidence level 95 %.

According to the questionnaire, mean team participation obtained 12.42, which is larger than the variable mean; further, as significance level is $\sigma = 0.000$, which is
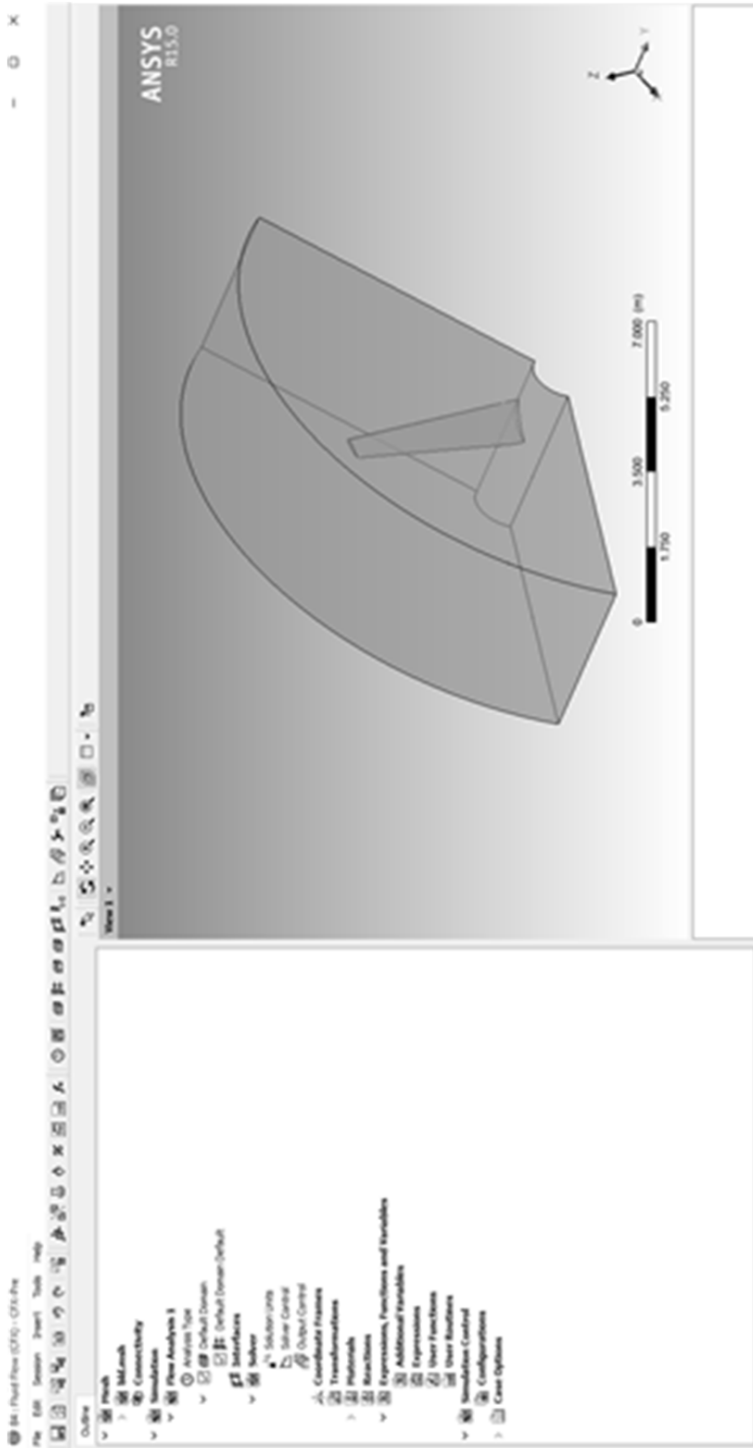
Fig. 2. Wind blade model
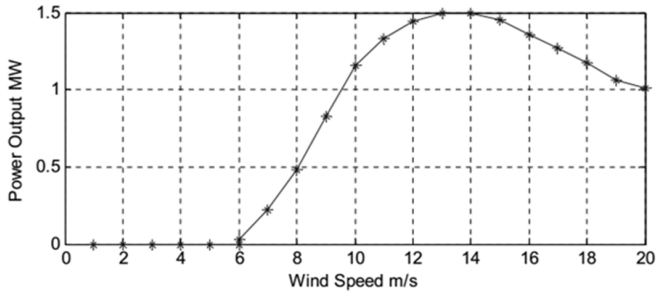
Fig. 3. Power curve for model

smaller than significance level of 0.05; hence, it can be stated that team participation in human resource strategic planning process is larger than medium. As a result, team participation influences human resource strategic planning process for wind energy investment at confidence level 95 %.

Table 2. One-sample t-test results of research hypothesis

Research variable	t-statistic	Significance level	High boundary	Low boundary
Management participation	3.425	0.000	2.259	0.758
Team participation	4.309	0.000	3.354	1.287
Organizational commitment	2.208	0.002	2.379	0.819
Environmental assessment	0.875	0.076	2.257	0.917
Education status	3.209	0.000	2.597	0.928
Cultural factors	4.597	0.003	2.397	0.518
Change management	0.658	0.095	1.297	0.587
Strategic alignment	3.928	0.002	2.394	0.952
Technology development	3.496	0.000	2.824	0.849

   Mean organizational commitment obtained 11.97, which is larger than the variable mean. Also, as significance level equals $\sigma = 0.002$, which is less than 0.05, it can be stated that organizational commitment in human resource strategic planning process is larger than the medium. Thus, it is expressed that organizational commitment influences human resource strategic planning process for wind energy investment at 95 %.

   Mean environmental assessment obtained 11.24, which is almost equal to the variable mean. Moreover, since $\sigma = 0.076$ is larger than significance level 0.05, it can be stated that environmental evaluation in human resource strategic planning process equals the mid-level. Thus, environmental assessment has no effect on human

resource strategic planning process for wind energy investment at confidence level 95 %.

According to the table, mean cultural factors attained 11.93, which is larger than the variable intermediate. In addition, as $\sigma = 0.003$ is less than 0.05, it may be expressed that cultural aspects are larger than the intermediate in human resource strategic planning process. As a result, cultural aspects influence human resource strategic planning process for wind energy investment at 95 %.

Mean change management was measured 14.95 that almost equals the variable mean. According to significance level $\sigma = 0.095$, which is larger than 0.05, it may be declared that change management in human resource strategic planning process equals the median. Therefore, change management has no effect on human resource strategic planning process for wind energy investment at 95 %.

According to the table, mean strategic alignment was obtained 7.6 that is larger than the mean variable. Regarding $\sigma = 0.002$, which is smaller than 0.05, it can be stated that strategic alignment is larger than the mean in human resource strategic planning process. Thus, strategic alignment shows an effect on human resource strategic planning process for wind energy investment at 95 %.

As observed in the table, mean technology development was obtained 16.59, which is larger than the mean variable. According to $\sigma = 0.000$ that is less than significance level of 0.05, it implies that technology development is larger than the mean in human resource strategic planning process. As a result, technology development is effective for wind energy investment in human resource strategic planning process at 95 %.

4. Conclusion

The present research investigated the relationship between nine major organizational factors with strategic planning achievement in Iran grid management for wind energy usage. Finally, the effects of five factors of senior management participation in strategic planning process, senior management knowledge awareness and strategic planning significance, staff team participation in strategic planning process, change management, and proper environmental evaluation in strategic planning process were maintained. Comparing research results with corresponding studies demonstrates consistent results. Factors of staff team participation, management awareness, management participation, change management, and environmental assessment, which have been referred as effective factors of achieving strategic planning in earlier studies, are also true about Khorasan Razavi regional electricity company. However, as earlier mentioned in the literature and research hypotheses, three factors of organizational commitment to strategic planning process and organizational commitment, staff acceptance, and proper databases were confirmed by testing research hypotheses. Now, Khorasan Razavi Regional Electricity Company is one of the national regions consumes more power than it generates due to too many large polluted industrial estates requiring increased electrical energy generation. Thus, it seems necessary that organizational managers and planners to plan for using wind energy, which is highly advantageous as it holds the fastest growth resource com-

paring other energy sources for power supply. As a result, it must be interested; and further, organizational strategies and infrastructures must be revised for better utilization of the renewable energies.

References

[1] Y. NOOROLLAHI, S. M. ALIASHRAF, M. ZAMANI: *Wind energy potentiometric in west Area Company using GIS.* Iranian Journal of energy *14* (2011), No. 1, 1–22.

[2] HOOSHMAND, MAHMOOD, HOSSEINI, S. H: *Economic assessment of power supply using wind energy by private sector in Iran.* Journal of monetary and financial economy *21* (2014), No. 87, 8–106.

[3] L. E. BENITEZ, P. C. BENITEZ, G. C. VAN KOOTEN: *The economics of wind power with energy storage.* Energy Economics *30* (2008), No. 4, 1973–1989.

[4] Y. A. HAMOUDA: *Wind energy in Egypt: Economic feasibility for Cairo.* Renewable and Sustainable Energy Reviews *16* (2012), No. 5, 3312–3319.

[5] S. HIMPLER, R. MADLENER: *Repowering of wind turbines: Economics and optimal timing.* Institute for Future Energy Consumer Needs and Behavior an der RWTH Aachen University, FCN Working Paper *19* (2011).

Design of air pressure detection system based on sectionalized linear fitting[1]

Duan Huimin[2,3], Gao Xianhe[2], Zhou Zehua[2]

Abstract. An improved air pressure detection system is proposed to solve the problem in balancing linearity and operational speed of a regular air pressure detection system. Our system utilizes an Atmega16 microcontroller as the controller, and a high-precision pressure sensor 10N1600A-T and 24-bit AD chip HX711 to detect the air pressure, to perform analog digital conversion and to process the data using an improved sectionalized linear fitting method. Detection results can be displayed through the LED nixietube, and can be output as a 0 to 5 V analog signal, an RS485 remote mode, or a relay switch signal to meet different control needs. Our testing proves that the system can accurately detect the pressure variation of 0 to 1600 kPa and the sectionalized terminal-based linear fitting method can improve the system linearity and ensure the operational speed, so that the subsequent control system can quickly and accurately respond to the pressure variation.

Key words. Air pressure, detection, linear fitting, analog digital conversion.

1. Introduction

The complexity of the industrial environment and the intelligence need of the instrumentation encourage the intelligent and precise control of industrial equipment. Air pressure detection system is an integral part of industrial field applications, which play a crucial role on accurately detecting and quickly displaying the air pressure signal, and making intelligent adjustment to the control device according to the variation of air pressure [1, 2].

It is a general problem for the current air pressure detection equipment to achieve both linearity and operational speed. Those instruments which are used only for providing air pressure rather than being directly used for subsequent control system perform well in linearity, but not in the detection speed. While for those instruments which the test results are used to control the subsequent device adjustment, the

---

operational speed is faster, but the linearity is insufficient. To solve this problem, our system uses a high precision detection and conversion chip and a sectionalized linear data fitting method [3–5]. As the algorithm is simple, both the linearity and the speed of the system are improved, ensuring the subsequent control system to quickly and precisely respond to the air pressure variation.

2. System hardware design

2.1. System block diagram and working principle

Our air pressure detection device is composed of power supply, single chip microcomputer minimum system, digital display, RS485 interface, DAC7571 analog output, relay output, HX711 sensor detection, EEPROM power-down storage and abnormal alarm module (see Fig. 1).
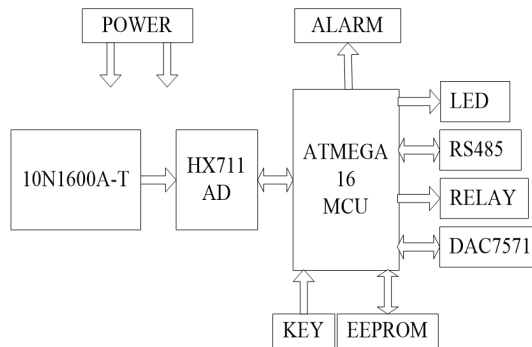
Fig. 1. Diagram of air pressure detection system

The air pressure is first detected by a pressure sensor (10N1600A-T) [6], and then converted into digital signal by a 24-bit AD chip (HX711), which is sent to the Atmega16 microcontroller to complete the data processing [7, 8]. The controller can control the LED nixietube display [9], the relay output, analog voltage DAC7571 output, digital RS485 output and abnormal alarm. The system can set the start threshold, delay start time and threshold, overshoot start threshold and exception alarm range through the keys. EEPROM is used to protect the power-down storage data. MODBUS communication protocol is used to perform remote communication via RS485, which can ensure compatibility of the system with other devices [10]. An improved sectionalized linear fitting is used to process the data for increasing linearity.

2.2. Air pressure detection module

This module is composed of high-precision pressure sensor 10N1600A-T and 24-bit high-precision AD chip HX711, as shown in Fig. 2. 10N1600A-T pressure sensor can detect air pressure with a range of 0 to 1600 kPa, with a good repeatability and

stability. The full scale output voltage of 10N1600A-T is 100 mV. HX711 converts the analog voltage signal of 10N1600A-T into digital signal. The maximum input voltage of A channel is ±20 mV when the gain is 128. The maximum input voltage of B channel is ±40 mV when the gain is 64. A channel is chosen to use in the design. To ensure HX711 channel A to have an allowed input range, the output voltage of 10N1600A-T must be divided. HX711 and Atmega16 communicate through I^{2}C bus [11].
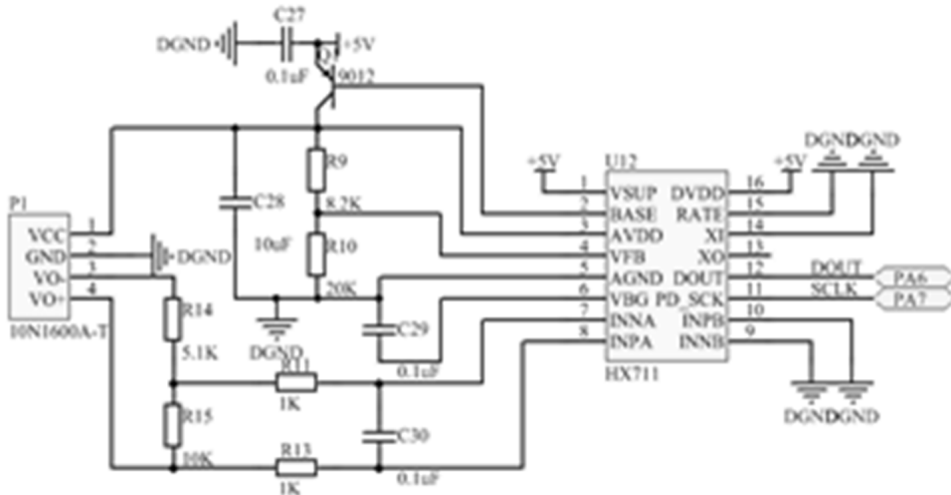
Fig. 2. Schematic diagram of air pressure detection circuit

3. 0-5 V analog signal generating module

Our air pressure detection system has an analog signal generating module. As shown in Fig. 3, a DAC7571 chip is used to generate a 0 to 5 V continuous output, making it a standard interface for industrial control equipment. To ensure system safety, ADUM1201 is used between DAC7571 and Atmega16 for electrical isolation. They communicate through I2C bus [11].
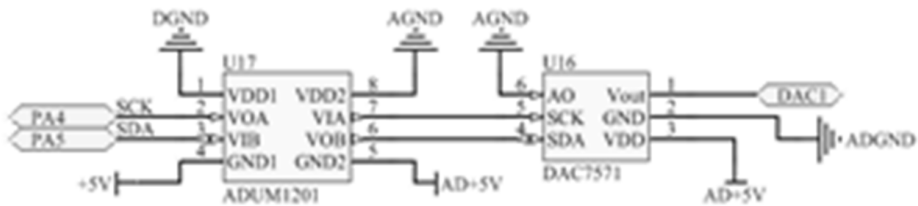
Fig. 3. Schematic diagram of the 0 5 V analog signal generating circuit

4. Software design

4.1. Main program flowchart

According to the principles described in subsection 2.1, the main program is composed of subprograms such as pressure detection, sectionalized linear fitting, LED nixietube display, abnormal alarm, DAC7571 analog signal output, RS485 communication, key scanning and EEPROM. The main program flowchart is shown in Fig. 4.
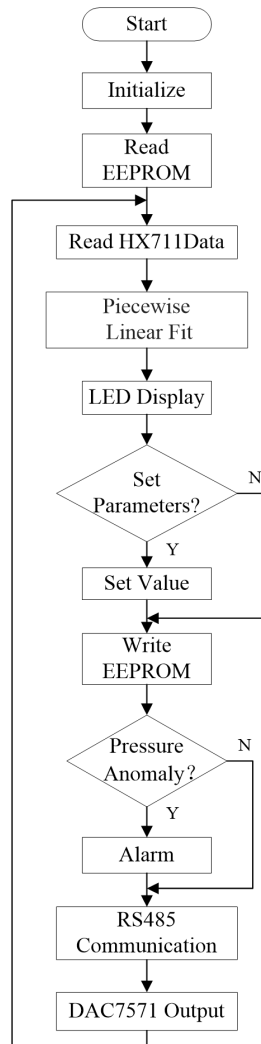
Fig. 4. Main program flowchart

4.2. Improved linear fitting algorithm

4.2.1. Linear fitting Linearity is an important indicator of the static characteristics of a sensor. It is also known as nonlinear error, which is used to represent the difference between the output-input calibration curve and the fitted line for sensor [12].

This value is usually interpreted as a relative error:

$$\xi_{\mathrm{L}} = \pm \frac{\Delta L_{\max}}{y_{\mathrm{FS}}} \times 100\,\%\,, \tag{1}$$

where ξ_{L} is the linearity, for which a small value represents a better linearity, $\Delta L_{\max}$ is the maximum difference between the average calibration curve and the fitted straight line, and y_{FS} is the theoretical full-scale output.

As shown in equation (1), the fitted line is the basis for obtaining the corresponding linearity. If the fitted line is selected in a different way, the calculated $\Delta L_{\max}$ and linearity value will be also different. The methods of linear fitting include the best straight line method, terminal-based method,mean point method and least square method etc.

4.2.2. Terminal-based line method Terminal-based line method uses both ends of the calibrate curve of the sensor as the fitted straight line. The linearity obtained accordingly is the so-called terminal-based linearity [13]. The linear regression equation of terminal-based method is

$$y = kx + b\,, \tag{2}$$

where y is the output, x is the input, k is the slope of the line and b is the Y-interception.

As shown in Figure 5, ① and ② are the actual measured output curves of a pressure sensor, ③ is the linearly fitted line obtained from terminal-based method. Equation (2) can be now rewritten as

$$y = \frac{\overline{y}_{\mathrm{FS}} - \overline{y}_0}{x_{\mathrm{s}}} x + \overline{y}_0\,, \tag{3}$$

where x is the measured pressure of sensor, x_{s} is the full-scale value, y is the output of pressure sensor, $\overline{y}_0$ is the average output of the zero point, and $\overline{y}_{\mathrm{FS}}$ is the average output of the full-scale point.

Compared to the least square method, the terminal-based line method is simpler and faster, but it generally has a poor precision. In this design, we proposed an improved method, which first divide the curve into multiple sections and then use the terminal-based line method for each section [14]. As an example, the input within the detection range is divided into L sections, for which L fitted linear regression equations can be obtained, as well as the measured output after fitting.

By using the sectionalized linear fitting based on terminal-based line method,

linearity is improved and the operational speed is also ensured, making it for the subsequent control system to respond to the changed pressure data quickly and precisely. The improved method is shown in Fig. 6.
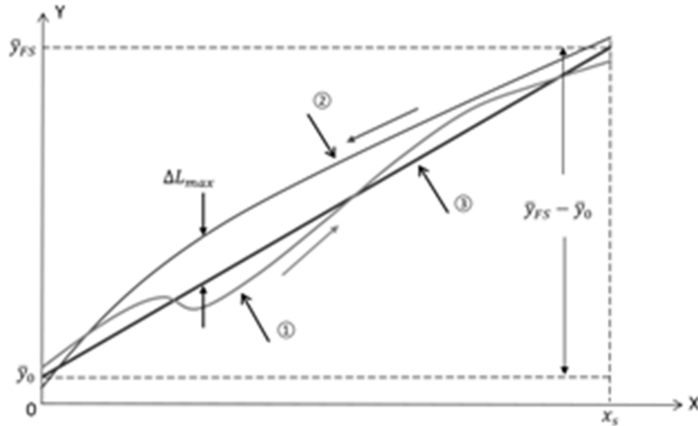
Fig. 5. Terminal-based line method schematic diagram
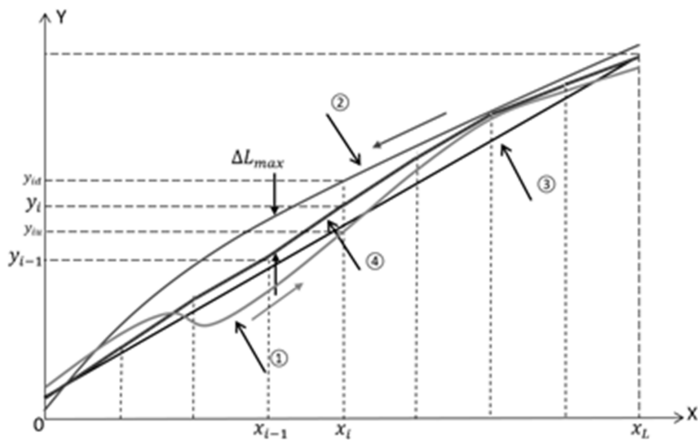
Fig. 6. Sectionalized linear fitting schematic diagram based on terminal-based line method

For section i, assuming that the input of sensor 10N1600A-T is x_i, the actual measured output of the AD chip HX711 in the upstroke and downstroke is y_{iu} and y_{id}, respectively, for which the averaged value is assigned as the fitted output y_i:

$$y_i = (y_{iu} + y_{id})/2. \tag{4}$$

Similarly, y_{i-1} can be obtained for input of x_{i-1}. The fitted linear regression equation of section i can be calculated by using $x_{i-1}, x_i, y_{i-1}, y_i$, and equation

$$y = k_i x + b_i. \tag{5}$$

By comparing the $\Delta L_{\max}$ in Figs. 5 and 6, one can see that, with an L-sectionalized linear fitting, the linearity ξ_{L} is reduced as the $\Delta L_{\max}$ is decreased, proving that our improved algorithm improves the linearity of the system within the detection range.

4.2.3. Improved 8-sectionized linear fitting On basis of the hardware system working principle mentioned above, 10N1600A-T converts the detected air pressure into the analog voltage output, which is then transformed into digital signal by HX711 and processed by Atmega16. 10N1600A-T has a detection range of 0 to 1600 kPa and a full-scale output of 0 to 100 mV. HX711 has an accuracy of 24 bit, for which the maximum capacity is 2^{24}, or 16777216. Therefore, with a 1 kPa pressure variation, the changes of the corresponding AD value is about $16777216/1600{=}10485.76{\approx}10486$.

In order to achieve a better linear characteristic, a 8-section linear fitting is used in our system. As it is the most direct AD value data processing in the Atmega16 microcontroller, so in the realization of fitting, we take the AD value as independent variables x and dependent variables y. Therefore, the AD value range 0 to 16777216 of HX711 is divided into 8 equal sections, or the sensor's detection range is divided into 8 equal sections. By doing this, we can both achieve the desired results and save the operation time. The relevant values of each section are shown in Table 1.

Table 1. Sensor input and AD chip output value comparison

$i = 0 - 7$	Standard pressure (kPa)	Theoretical AD value x_i	Actual detection AD value y_{iu} in upstroke	Actual detection AD value y_{id} in downstroke
0	0.00	0	6294	11548
1	200.00	2097152	2105541	2116026
2	400.00	4194304	4227858	4248830
3	600.00	6291456	6228541	6436159
4	800.00	8388608	8346665	8531214
5	1000.00	10485760	10475274	10611589
6	1200.00	12582912	12633244	12696158
7	1400.00	14680064	14856225	14724104
8	1600.00	16777216	16827548	16743662

When the system is calibrated, the standard air pressure is increased from 0 kPa to 1600 kPa in a step of 200 kPa; the actual measured results of the system are shown as the "actual detection AD value y_{iu} in upstroke" column in Table 1. When the standard pressure is decreased from 1600 kPa to 0 kPa in a step of 200 kPa, the actual measured results of the system are shown as "actual detection AD value y_{id} in downstroke" column in Table 1. By using a sectionalized linear fitting based on terminal-based line method, the linear regression equation of each section can be

calculated and stored.

For example for the second section, the input is x_2 and x_3, respectively, and the values y_2 and y_3 can be obtained from ratios y_{2u}/y_{2d} and y_{3d}/y_{3d} (Equation (3)), respectively, and the linear regression equation of the second section is then obtained as

$$y = 0.9985x + 50332 \,. \tag{6}$$

$y = 0.9985x + 50332$

If the actual detected AD value corresponding to the current air pressure is 4598732, the Atmega16 first calculates that this input value is in the second section, then the above section linear regression equation (6) is used for the fitting, or uses x of 4598732 in (6), so that

$$y = 0.9985 * 4598732 + 50332 = 4642166 \,.$$

The fitted output of measured pressure corresponding to the AD value of 4598732 is about 442.701 kPa.

The subprogram flowchart of a 8-sectionalized linear fitting based on terminal-based line method is shown in Fig. 7.
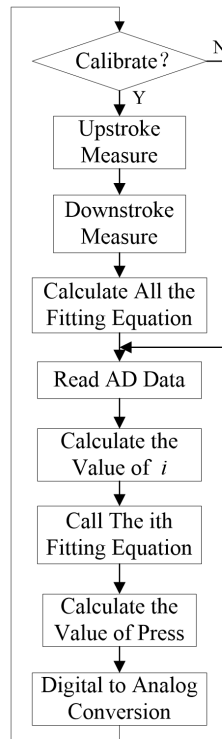
Fig. 7. 8-sectionalized fitting flowchart

5. Conclusion

Our proposed air pressure detection system, which uses an improved 8-sectionalized terminal based linear fitting method, can detect and display the air pressure and output analog and digital signal. The fitted results obtained from a standard terminal based and an improved 8-sectionalized terminal based method are listed in the Table 2 and Table 3, respectively. The final output results from our detection system are listed in Table 4.

As shown in Table 2, $\Delta L_{\max} = 168708$ can be obtained from the data shown in the "Upstroke ΔL" and "Downstroke ΔL" columns, the corresponding ξ_{L} being

$$\xi_{\mathrm{L}} = \pm\frac{\Delta L_{\max}}{\Delta_{\mathrm{FS}}} \times 100\,\% = \frac{-168708}{16777216} \times 100\,\% = 1.006\,\%. \qquad (7)$$

As shown in Table 3, $\Delta L_{\max} = 123209$ can be obtained from the data shown in the "Upstroke ΔL" and "Downstroke ΔL" columns, the corresponding ξ_{L} being

$$\xi_{\mathrm{L}} = \pm\frac{\Delta L_{\max}}{\Delta_{\mathrm{FS}}} \times 100\,\% = \frac{-123209}{16777216} \times 100\,\% = -0.734\,\%, \qquad (8)$$

which is decreased compared to the xi_{L} value obtained from a standard method with sectionalized, indicating that the linearity of the system is improved.

As shown in Table 4, the relative error of our air pressure detection system is below 1.5 % for the entire detection range, and below 1 % for most detection range, qualifying our system as a level 1.5 according to the industrial instrumentation accuracy standards.

Our system is designed to solve the balancing problem of the linearity and operational speed of a regular air pressure detection system. Detection results can be displayed through the LED nixietube, and output as a 0 to 5 V analog signal, an RS485 remote mode, or a relay switch signal to meet different control needs. Our testing proves that the system can accurately detect the pressure variation of 0 to 1600 kPa, the sectionalized terminal-based linear fitting method can improve the system linearity and ensure the operational speed, so that the subsequent control system can quickly and accurately respond to the pressure variation.

Standard pressure (kPa)	Theoretical AD value	Actual detection AD value in upstroke	Actual detection AD value in downstroke	Linear regression equation parameters k	Linear regression equation parameters b	Fitted AD value	ΔL in upstroke	$\Delta L/\Delta_{FS}$ in upstroke	ΔL in downstroke	$\Delta L/\Delta_{FS}$ in downstroke
0	0	6294	11548	0.9999	8921	8921	2627	0.016 %	-2627	-0.016 %
100	1048576	1050149	1053819			1057392	7243	0.043 %	3573	0.021 %
200	2097152	2105541	2116026			2105863	323	0.002 %	-10163	-0.061 %
300	3145728	3164602	3180331			3154334	-10268	-0.061 %	-25997	-0.155 %
400	4194304	4227858	4248830			4202806	-25053	-0.149 %	-46024	-0.274 %
500	5242880	5248123	5342495			5251277	3154	0.019 %	-91218	-0.544 %
600	6291456	6228541	6436159			6299748	71206	0.424 %	-136412	-0.813 %
700	7340032	7303332	7508853			7348219	44887	0.268 %	-160634	-0.957 %
800	8388608	8346665	8531214			8396690	50025	0.298 %	-134524	-0.802 %
900	9437184	9408872	9569305			9445161	36289	0.216 %	-124143	-0.740 %
1000	10485760	10475274	10611589			10493632	18358	0.109 %	-117957	-0.703 %
1100	11534336	11557405	11661214			11542104	-15301	-0.091 %	-119110	-0.710 %
1200	12582912	12633244	12696158			12590575	-42669	-0.254 %	-105583	-0.629 %
1300	13631488	13740540	13713277			13639046	-101494	-0.605 %	-74231	-0.442 %
1400	14680064	14856225	14724104			14687517	-168708	-1.006 %	-36587	-0.218 %
1500	15728640	15838740	15744369			15735988	-102752	-0.612 %	-8381	-0.050 %
1600	16777216	16827548	16743662			16784459	-43088	-0.257 %	40798	0.243 %

Table 2. The data with a standard linear fitting

Table 3. The data with 8 sections linear fitting

Standard pressure (kPa)	Theoretical AD value	Actual detection AD value in upstroke	Actual detection AD value in downstroke	i	k_i	b_i	Fitted AD value	ΔL in upstroke	$\Delta L/\Delta_{\mathrm{FS}}$ in upstroke	ΔL in downstroke	$\Delta L/\Delta_{\mathrm{FS}}$ in downstroke
0	0	6294	11548	0	1.0022	8921	8921	2627	0.016 %	−2627	−0.016 %
100	1048576	1050149	1053819	0	1.0022	8921	1059804	9655	0.058 %	5985	0.036 %
200	2097152	2105541	2116026	1	1.0145	−16777	2110784	5243	0.031 %	−5243	−0.031 %
300	3145728	3164602	3180331	1	1.0145	−16777	3174564	9962	0.059 %	−5767	−0.034 %
400	4194304	4227858	4248830	2	0.9985	50332	4238345	10486	0.063 %	−10485	−0.062 %
500	5242880	5248123	5342495	2	0.9985	50332	5285348	37225	0.222 %	−57147	−0.341 %
600	6291456	6228541	6436159	3	1.0045	12582	6332350	103808	0.619 %	−103810	−0.619 %
700	7340032	7303332	7508853	3	1.0045	12582	7385644	82312	0.491 %	−123209	−0.734 %
800	8388608	8346665	8531214	4	1.0035	20971	8438939	92274	0.550 %	−92275	−0.550 %
900	9437184	9408872	9569305	4	1.0035	20971	9491185	82313	0.491 %	−78119	−0.466 %
1000	10485760	10475274	10611589	5	1.0115	−62915	10543431	68157	0.406 %	−68158	−0.406 %
1100	11534336	11557405	11661214	5	1.0115	−62915	11604066	46661	0.278 %	−57148	−0.341 %
1200	12582912	12633244	12696158	6	1.0135	−88080	12664701	31458	0.188 %	−31457	−0.187 %
1300	13631488	13740540	13713277	6	1.0135	−88080	13727433	−13107	−0.078 %	14156	0.084 %
1400	14680064	14856225	14724104	7	0.9515	822083	14790164	−66061	−0.394 %	66060	0.394 %
1500	15728640	15838740	15744369	7	0.9515	822083	15787884	−50857	−0.303 %	43515	0.259 %
1600	16777216	16827548	16743662	7	0.9515	822083	16785604	−41944	−0.250 %	41942	0.250 %

Table 4. Air pressure test data

Standard pressure (kPa)	Actual detection pressure	Relative error
0	0.000	0.00 %
100	101.068	1.07 %
200	201.295	0.65 %
300	302.743	0.91 %
400	404.191	1.05 %
500	504.038	0.81 %
600	603.886	0.65 %
700	704.334	0.62 %
800	804.782	0.60 %
900	905.129	0.57 %
1000	1005.477	0.55 %
1100	1106.625	0.60 %
1200	1207.772	0.65 %
1300	1309.120	0.70 %
1400	1410.468	0.75 %
1500	1505.615	0.37 %
1600	1600.763	0.05 %

References

[1] S. XIONG, C. HU, J. ZHU: *Research of differential pressure style leakage detect method based on cubage compensation.* Industrial Instrumentation & Automation (2009), No. 5, 46–49.

[2] W. SUN, R. YAN, L. SUN, D. MENG, Z. LI, H. GUO, W. LI: *Study of the space station on-orbit leak detection based on the differential pressure gas sensor.* International Conference on Green Computing and Communications and Internet of Things and Cyber, Physical and Social Computing, 20–23 August 2013, Beijing, China, IEEE Conferences (2013),1718–1721.

[3] J. CHEN, J. XIAO: *An efficient query processing algorithm based on time slice model fitting in wireless sensor networks.* Computer Measurement & Control *22* (2014), No. 1, 142–144, 154.

[4] W. ZHOU, J. BAO, L. DING: *Nonlinear correction of sensor calibration.* Journal of Test and Measurement Technology *27* (2013), No. 4, 358–361.

[5] F. R. MILLER, J. W. NEILL: *Lack of fit tests for linear regression models with many predictor variables using minimal weighted maximal matchings.* Journal of Multivariate Analysis *150* (2016), 14–26.

[6] B. CUI, W. BI: *Design of air-leakage test instrument based on precision pressure transducer.* Metrology & Measurement Technology *34* (2014), No. 4, 26–29.

[7] X. SHI, S. LI: *Embedded PLC based on AVR microcontroller.* Instrument Technique and Sensor (2017), No. 6, 54–63.

[8] R. LIU, S. QI, X. WU: *Design of the intelligent air pressure sensor with low power consumption for marine meteorological observation.* Process Automation Instrumentation *37* (2016), No. 1, 96–99.

[9] Y. Zhu: *Design of digital barometer controlled by single chip microcomputer*. Modern Electronics Technique *38* (2015), No. 16, 100–102, 105.

[10] X. Meng, X. Li: *Serial communication system design between touch screen and MCU based on MODBUS protocol*. Journal of Chongqing University of Technology (Natural Science) *28*(2014), No. 9, p. 87–91.

[11] J. Zhang, W. Ru, L. Zhao, Y. Hu: *Design and implementation of I^2C bus test system*. Instrument Technique and Sensor *12* (2016), 118–120.

[12] J. Chang, Y. Shi, R. Chang: *Detection and conversion (The third edition)*. Beijing: China Machine Press (2009), No. 1, 45–49.

[13] Y. Yu, J. Chang, J. Cheng: *The principle and engineering application of sensor (The fourth edition)*. Xian: Xidian University Press (2014), No. 5, 150–161.

[14] E. Amaldi, S. Coniglio, L. Taccari: *Discrete optimization methods to fit piecewise affine models to data points*. Computers & Operations Research *75* (2016), 214–230.

An oil-sealed optical fiber Fabry–Perot sensor for enhancing temperature sensitivity[1]

Kaiwei Jiang[2,5], Jinyu Gu[3,5], Jinrong Li[3], Mengxing Huang[4], Guanjun Wang[2,6], Yutian Pan[2,6]

Abstract. For enhancing the sensitivity of conventional silica-based fiber temperature sensor effectively, an oil-seal fiber sensing technology was proposed here. Firstly, the pressure-assisted arc discharge technology was utilized here to fabricate a silica microbubble based fiber-tip Fabry–Perot (FP) sensor with a thin-film end surface. Then, the microbubble was coated with Cr and Au film before immersed with silicone oil in an enclosed tank. As the thin film of diagram was very sensitive to the out pressure variation, when changing the outer temperature, the corresponding oil pressure will be varied simultaneously. So the position of thin film and the FP interference spectrum will be moved at the same time. So, the merit of high pressure sensitivity was converted to the advantage of temperature sensitivity in this way. Experiment results founded that a six times of sensitivity enhancement was feasible, which shows its potential application in high sensitive temperature measurement.

Key words. Optical fiber sensor, silica diaphragm, Fabry–Perot interference, oil-seal technology, temperature measurement, end coating.

[2]College of Mechatronic Engineering, North University of China, Taiyuan, China, 030051
[3]College of Information and Telecommunication Engineering, North University of China, Taiyuan, China, 030051
[4]College of Information Science & Technology, Hainan University, Haikou, China, 570228
[5]E-mails of joint first authors: Jiangkaiwei@nuc.edu.cn, jinyugu@email.nuc.edu.cn
[6]E-mails of the corresponding authors: wangguanjun@163.com, panyutian@nuc.edu.cn

1. Introduction

Optical fiber sensing technology, especially the optical fiber Fabry–Perot (FP) sensing technology, has received extensive attention in the past ten years due to its own unique advantages [1, 2]. Optical fiber FP sensor technology has the advantages of low cost, high sensitivity and miniaturization and has shown good performance in experiments [3–6]. It has been widely used in physical measurements such as temperature, pressure, refractive index and deformation. In recent years, there have been a variety of optical fiber temperature sensor based on FP interference mechanism. One of the methods is to etch the end of the fiber with a chemical such as hydrofluoric acid. As the germanium-doped core corrodes faster than the pure silica cladding, a concave hole structure appears on the end face of the optical fiber after being corroded for a certain period of time. The optical fiber FP interference can be achieved by fusing the two concave optical fibers or welding the concave optical fibers with the film, and is used for temperature detection.

Although this structure has a higher sensing temperature and a larger range, the etching process causes the optical fiber cavity to have a certain degree of roughness and affect the overall performance [7]. The other is a temperature sensor based on an air cavity or a dielectric cavity, such as a soldered portion of a photonic crystal fiber and a single-mode optical fiber, or a space-temperature-sensitive material is filled in the end space, temperature sensing is performed by utilizing the change of the refractive index to cause the change of the optical cavity length. However, due to the existence of light loss, the measurement accuracy needs to be improved [8, 9]. The conventional FP sensors based on the FP cavity are less sensitive to temperature. For example, Xuefeng Li et al. proposed different thermal expansion coefficients of gold, nickel, quartz and metal plated on the ends of single-mode fiber, respectively, resulting in the change of FP cavity length with a sensitivity higher than $14 \, \text{pm}/°\text{C}$ [10]. Guilin Zhang et al. proposed inserting the fiber end into a polymer-filled capillary glass tube to form an air microcavity FP sensor with a temperature sensitivity of $5.2 \, \text{nm}/°\text{C}$ [11].

Tiegen Liu et al. proposed the optical fiber FP temperature sensor based on the pressure change caused by the thermal expansion of the sealed air. The sensor consists of a miniature FP cavity and an air cavity, separated by a thin silicon diaphragm. The thermal expansion of the seal air in the air chamber will cause the pressure difference between the two chambers to change, resulting in the deformation of the silicon membrane and finally the change of the FP chamber length. Correspondingly, the temperature sensitivity is $6.07 \, \text{nm}/°\text{C}$ [12].

The Li team and the Villatoro team proposed to weld together a conventional single-mode fiber and a length of hollow or solid photonic crystal fiber to form a microbubble-based FP cavity temperature sensor with temperature sensitivities of $1.35 \, \text{pm}/°\text{C}$ and $0.95 \, \text{pm}/°\text{C}$ [13, 14]. Xiaogang Jiang et al. proposed the arc discharge of multimode fiber after corrosion. The temperature sensitivity of the microbubble fiber is $2 \, \text{pm}/°\text{C}$ [15]. These types of fiber optic temperature sensors have some disadvantages. Some of them produce some complex large errors, while others are detrimental to experimental detection due to the complexity of demodulation.

In order to effectively enhance the sensitivity of optical fiber FP temperature sensor, a fiber-optic microbubble structure FP pressure sensor based on expansion assisted discharge method is designed here. The thickness, uniformity and symmetry of the microbubble membrane layer are effectively controlled by using the weak discharge and the slow release pressure method. The wall thickness of the microbubble finally fabricated is about $2\,\mu m$. Next, a metal chromium film and a gold film are sequentially plated on the end faces of the microbubbles, and then the coated sensor is packaged in a metal cylinder with an oil seal structure. In this case, the change of the external temperature causes the pressure in the cylindrical cavity to increase, which leads to the variation of the cavity length of the micro-bubble end film layer and the optical fiber FP spectrum. This change translates the properties of highly sensitive pressure sensing of microbubbles into the advantage of highly sensitive temperature sensing.

Here, The sensitivity of the micro bubble structure to the temperature is much higher than the sensitivity of the micro bubble packaged in a hermetically sealed metal cylinder with air. More than 6 times the sensitivity enhancement can be achieved in this paper. This result has important value for the development of similar optical fiber microbubble structure with high sensitivity temperature sensor.

2. Preparation and working principle

The parameters of the silica glass tube used in the experiment are $125\,\mu m$ in diameter, $75\,\mu m$ in inner diameter. A single mode optical fiber with a core diameter of $8\,\mu m$ and a cladding diameter of $125\,\mu m$ is used here. The method is to fused with the single-mode optical fiber and the glass tube flattened with the end face by commercial fusion splitter. The other end of the glass tube is connected to the first pressure pump, used to fill the glass tube with pressure. A hollow microbubble is then formed at the end of the single mode fiber by arc discharge. The thinner the film layer, the greater the amount of deformation when subjected to pressure. It is necessary to choose the appropriate discharge parameters. The discharge time is set to about $300\,ms$ and the discharge intensity is set to about -5 bit. The discharge was repeated until the end wall thickness of the microbubble structure reached about $2\,\mu m$, as shown in Fig. 1.

Magnetron sputtering is a physical vapor deposition phenomenon, which belongs to the category of glow discharge. The end surface of the first microbubble coated with a layer of Cr to increase the adhesion of the Au film, and finally plated with Au. The optical fiber sensor and the film substrate must be cleaned before coating. The cleaning method is to dry quickly after being fully filled with water and soaked in ethanol and the purpose of cleaning is to remove dirt and chemical fouling. In the process of coating, selection of the appropriate power and coating time have great influence on the film forming rate and film quality. Thus, it is necessary to choose the substrate and film materials. The microbubble end coating helps to reduce the degree of influence of the external factors and improve the reflectivity.
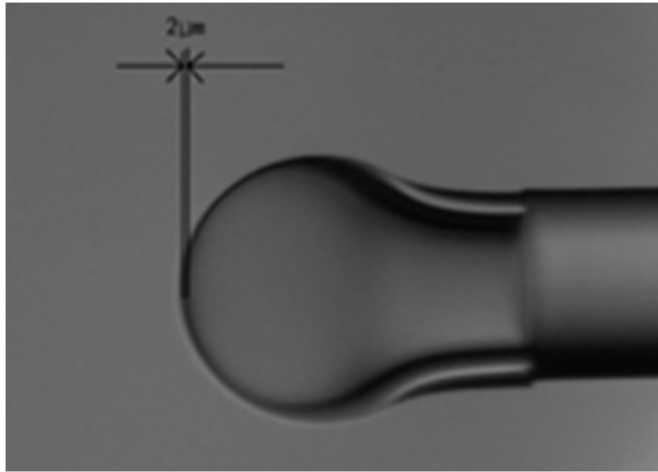
Fig. 1. Microbubble under 20× magnification

2.1. Principle of operation

The light emitted by the light source is incident perpendicularly to the end face of the optical fiber through the optical fiber, a part of the light is reflected at the end of the optical fiber, and the other part of the light is transmitted to the end face of the optical fiber microbubble and then coupled back to the optical fiber so that the two reflected light could interfere. Changes in the external temperature will cause the surface deformation of the micro-bubble, eventually leading to change of FP cavity length. As shown in Fig. 2.
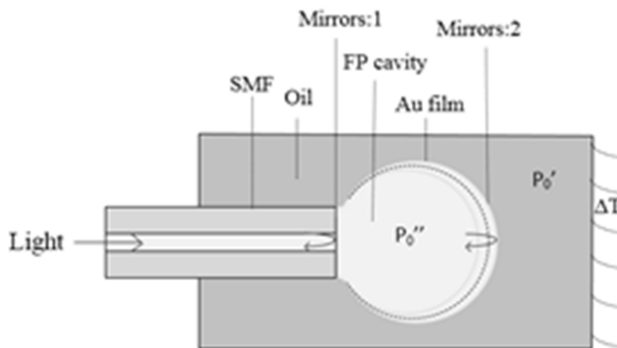
Fig. 2. Schematic diagram of sensor

An optical fiber FP temperature sensor is coated on the end face of an optical fiber microbubble (the coating is designed to reduce the interference of experimental results with the external refractive index) and placed in a sealed, oil-filled metal cylinder. According to the principle of closed ideal gas thermal expansion $PV =$

nRT, we can see that when the volume V is constant, the change of the external temperature causes the change of the inside pressure of the cylinder. At this time, the external surface of the microbubbles will be subjected to certain pressure and the microbubble film will be driven to move, which will make the FP cavity length and the reflected FP spectrum varied correspondingly.

Here, T is the temperature, n is the amount of sealed gas, and R is a constant. According to the small deflection theory of circular diaphragm with clamped edges, we have

$$L = \frac{P(a^2 - r^2)^2}{64D} \tag{1}$$

Here, L is the change of the cavity length of the micro bubble, P is the pressure difference between the cylinder and the micro bubble chamber, that is $P = P' - P''$, r is the radius distance to the diaphragm center, a is the radius, $D = Et^3/(12(1 - \mu^3))$, E, μ, t are the Young modulus, Poisson's ratio and temperature, respectively. Therefore, the relationship between the pressure and temperature can be expressed as

$$P = P' - P'' = \frac{T}{T_0} \left[\frac{P_0' V_0'}{V_0' + \Delta V} - \frac{P_0'' V_0''}{V_0' - \Delta V} \right], \tag{2}$$

where T is the change of the temperature, T_0 is the initial temperature, P_0', V_0', P_0'', V_0'' are pressure and volume of cylinder and the microbubble cavity at a temperature of T_0, respectively, and ΔV is the volume change. When the formula (2) is brought into formula (1), the result is as follows

$$L = \frac{(P_0' - P_0'')a^4 T}{64DT_0} = \frac{3(1 - \mu^3)Ta^4}{16ET_0 t^3} \left[\frac{P_0' V_0'}{V_0' + \Delta V} - \frac{P_0'' V_0''}{V_0' - \Delta V} \right]. \tag{3}$$

The cavity length becomes shorter when the temperature T is increased by the formula (3). So the sensitivity of the temperature sensor is

$$S(a, t, P_0) = \frac{\partial L}{\partial T} = \frac{3(1 - \mu^3)a^4}{16ET_0 t^3} \left[\frac{P_0' V_0'}{V_0' + \Delta V} - \frac{P_0'' V_0''}{V_0' - \Delta V} \right]. \tag{4}$$

From formula (4), we get the factors that affect the temperature sensitivity are the thickness of the micro bubble and the appropriate radius.

3. Experimental analysis

After the metal coating process, the micro-bubble structure is connected to an optical fiber demodulator and a computer, and the sensor head is put into the water in the incubator. The temperature of the thermostat is adjusted to change the temperature while the change of the reflection spectrum is displayed on the computer interface, as shown in Fig. 3.

In this configuration, the fabricated sensor is placed in a hollow, central cylinder (central hollow for oil loading), the port is sealed with PDMS glue, and the other end is tightened to seal the structure. When the outside temperature changes, the
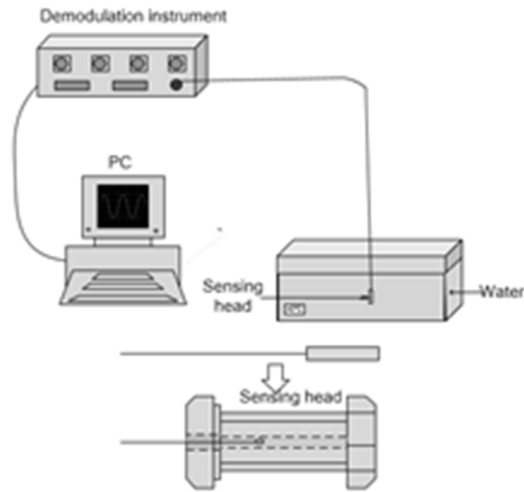
Fig. 3. Flowchart of experiment

internal temperature changes through the metal heat conduction. According to the thermal expansion and contraction principle, when the temperature rises, the FP cavity length of the sensor changes, so that the reflection spectrum changes too. The packaged sensors are placed in an incubator and the temperature is adjusted to $30\,°C$, $40\,°C$, $50\,°C$, $60\,°C$, $70\,°C$, $80\,°C$ and $90\,°C$, respectively. The experimental system is shown in Fig. 4.
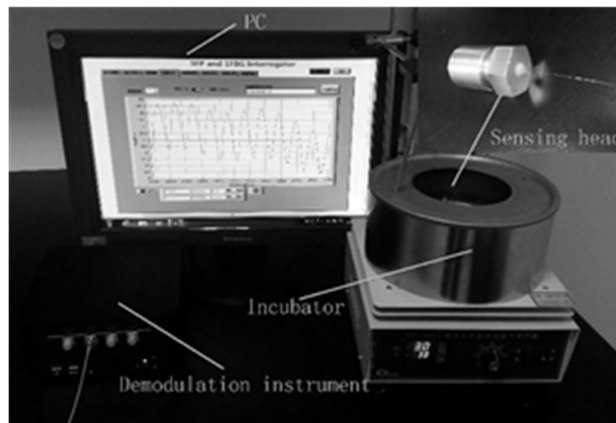
Fig. 4. Experimental system diagram

As can be seen from Fig. 5, top part, the reflection spectrum shifts to the right as the temperature increases. Fig. 5, bottom part shows the relation between temperature and wavelength. We know that when the temperature rises, the heated fibrous material will expand in the SiO_2 material, whereas the cooled material shrinks. This is because the state of objects in motion varies with temperature. As the temper-

ature increases, the vibration amplitude of the particles increases and the object expands. However, as the temperature decreases, the vibration amplitude of the particles decreases and the object contracts.
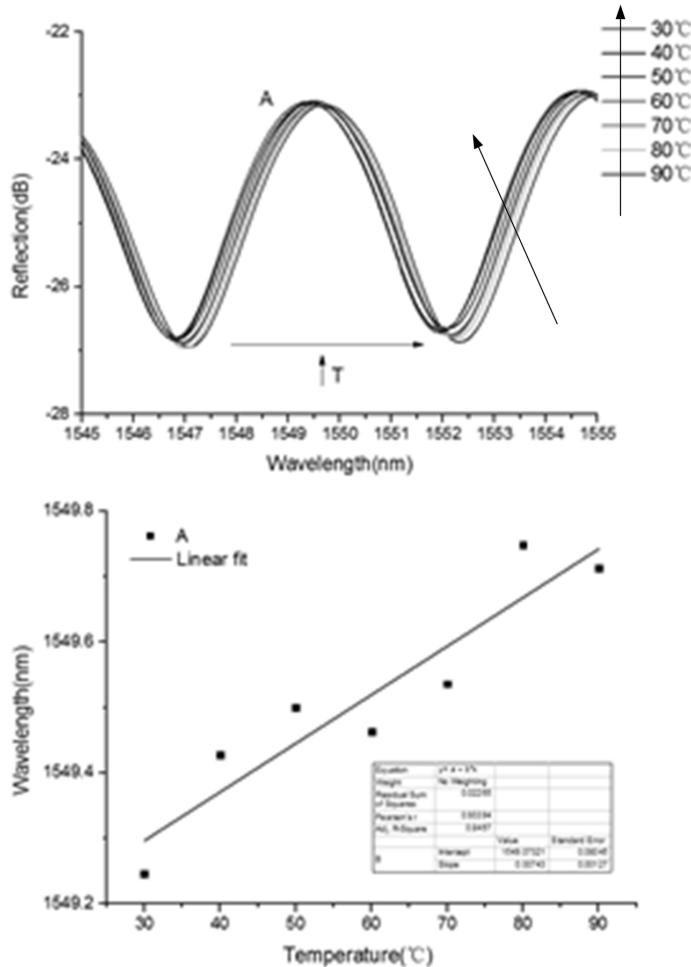
Fig. 5. Top–reflection spectrum of without oil-filled sensor, bottom–relation between temperature and wavelength

The microbubble is encapsulated in a cylinder filled with two methyl silicone oil and is completely sealed to measure the reflection spectrum as shown in Fig. 6, top part. Figure 6, bottom part shows the relationship between temperature and wavelength, that is, the sensitivity after this oil-filled method. It can be seen that when the temperature rises from $30\,^\circ$C to $90\,^\circ$C, the reflection spectrum moves to the right and the wavelength shift is significantly higher than that of the oil-free filling situation. When the temperature rise and thermal expansion of silicone squeeze on the micro-bubble, the micro-bubble structure will be deformed. In other words, changes

in the length of the microbubble extrusion chamber eventually lead to changes of the reflectance spectrum.
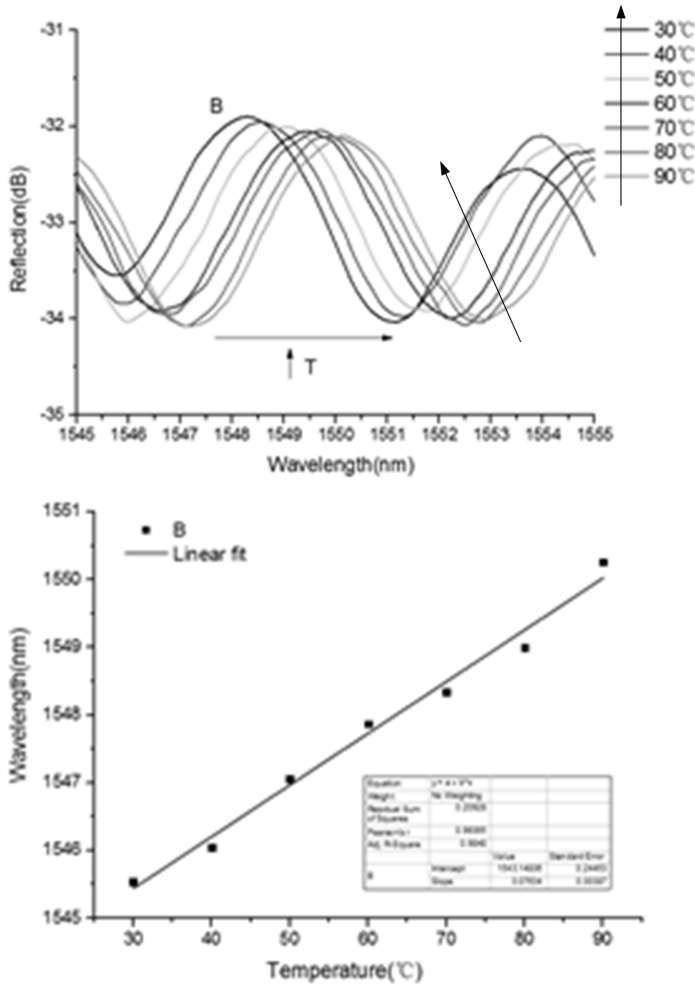
Fig. 6. Top–reflection spectrum of oil-filled sensor, bottom–relation between temperature and wavelength

Based on the above experiment, we analyzed the experimental sensitivity, as shown in Fig. 7. We can see the relationship between temperature and wavelength, that is the temperature sensitivity of oil-filled and unfilled structure. Because at the same temperature, the thermal expansion coefficient of silicone oil is much higher than the air. The sensitivity is linear and the sensitivity of the oil-filled structure was 76 pm/°C and the sensitivity of the unfilled structure was about 7 pm/°C. The temperature sensitivity of oil-filled is without oil-filled temperature sensitivity of 10 times.

It can be seen from Fig. 8 that at the same temperature, the reflection spectra
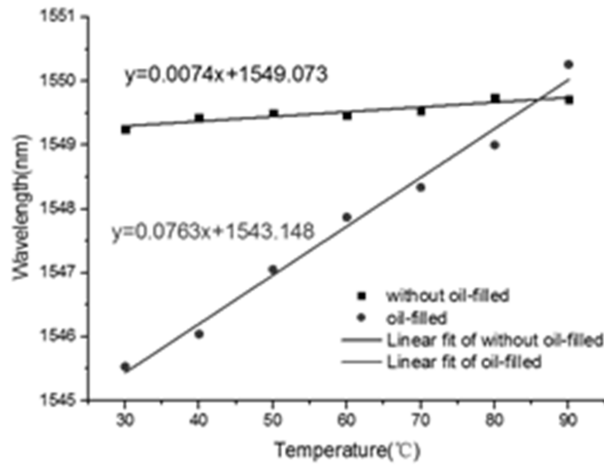
Fig. 7. Comparison of the temperature sensitivity

of the oil-filled sensor during heating and cooling are almost the same, and the variation of wavelength fluctuation is negligible. The fluctuations of the wavelength may be due to the limitation of the temperature control equipment. Therefore, the fabricated FP temperature sensors based on microbubble structure has good repeatability and reliability. In addition, we also can find that the sensor is with good linear relationship and the linearity is 98.66 %.
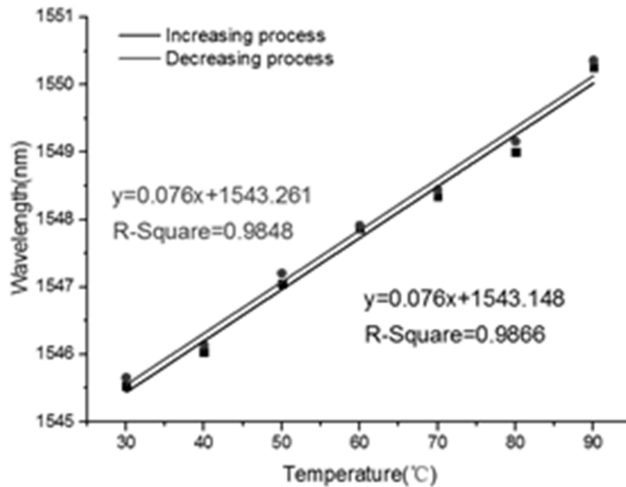
Fig. 8. The responding of oil-filled sensor interference peak in the heating process and cooling process

4. Conclusion

In this paper, a low-cost, innovative oil-seal method to enhance the temperature sensitivity of the sensor is proposed. Meanwhile, a silica microbubble with ultrathin film of about 2 micron scale is fabricated and then fused with single mode fiber by a commercial fusion splicer. After plating Cr and Au films, the microbubble FP sensor is encapsulated in a cylindrical cavity completely sealed with silicone oil. The experimental results show that the temperature sensitivity of the sensor before sealing is $6 \, \text{pm}/°$ with the temperature raises from $30 \, °\text{C}$ to $90 \, °$. The temperature sensitivity of the sensor increases to $36 \, \text{pm}/°\text{C}$ after sealing, resulting in more than 6 times the sensor temperature sensitivity enhancement. The content of this paper is a good reference for the development of new FP sensors based on microbubble structure. In addition, the production cost of this sensor is very low.

References

[1] J. WANG, B. DONG, E. LALLY, J. GONG, M. HAN, A. WANG: *Multiplexed high temperature sensing with sapphire fiber air gap-based extrinsic Fabry–Perot interferometers.* Optics Letters *35* (2010), No. 5, 619–621.

[2] T. ZHU, D. WU, M. LIU, D. W. DUAN: *In-line fiber optic interferometric sensors in single-mode fibers.* Sensors (Basel) *12* (2012), No. 8, 10430–10449.

[3] Y. BAI, Y. QI, Y. DONG, S. JIAN: *Highly sensitive temperature and pressure sensor based on Fabry-Perot interference.* IEEE Photonics Technology Letters *28* (2016), No. 21, 2471–2474.

[4] S. LIU, Y. WANG, C. LIAO, G. WANG, Z. LI, Q. WANG, J. ZHOU, K. YANG, X. ZHONG, J. ZHAO, J. TANG: *High-sensitivity strain sensor based on in-fiber improved Fabry–Perot interferometer.* Optics Letters *39* (2014), No. 7, 2121–2124.

[5] C. LIAO, S. LIU, L. XU, C. WANG, Y. WANG, Z. LI, Q. WANG, D. N. WANG: *Submicron silica diaphragm-based fiber-tip Fabry–Perot interferometer for pressure measurement.* Optics Letters *39* (2014), No. 10, 2827–2830.

[6] Q. RONG, H. SUN, X. QIAO: *A miniature fiber-optic temperature sensor based on a Fabry–Perot interferometer.* Journal of Optics *14* (2012), No. 4, p. 059501.

[7] S. PEVEC, D. DONLAGIC: *Miniature all-fiber Fabry–Perot sensor for simultaneous measurement of pressure and temperature.* Applied Optics *51* (2012), No. 19, 4536–4541.

[8] W. H. TSAI, C. J. LIN: *A novel structure for the intrinsic Fabry-Perot fiber-optic temperature sensor.* Journal of Lightwave Technology *19* (2001), No. 5, 682–686.

[9] T. WANG, M. WANG, H. NI: *Micro-Fabry-Perot interferometer with high contrast based on an in-fiber ellipsoidal cavity.* IEEE Photonics Technology Letters *24* (2012), No. 11, 948–950.

[10] X. LI, S. LIN, J. LIANG, Y. ZHANG, H. OIGAWA, T. UEDA: *Fiber-optic temperature sensor based on difference of thermal expansion coefficient between fused silica and metallic materials.* IEEE Photonics Journal *4* (2012), No. 1, 155–162.

[11] G. ZHANG, M. YANG, M. WANG: *Large temperature sensitivity of fiber-optic extrinsic Fabry–Perot interferometer based on polymer-filled glass capillary.* Optical Fiber Technology *19* (2013), No. 6, Part A, 618–622.

[12] T. LIU, J. YIN, J. JIANG: *Differential-pressure-based fiber-optic temperature sensor using Fabry-Perot interferometry.* Optics Letters *40* (2015), No. 6, 1049–1052.

[13] E. LI, G. D. PENG, X. DING: *High spatial resolution fiber-optic Fizeau interferomrtic strain sensor based on an in-fiber spherical microcavity.* Applied Physics Letters *92* (2008), No. 10, 101117–101119.

[14] J. VILLATORO, V. FINAZZI, G. COVIELLO, V. PRUNERI: *Photonic-crystal-fiber-enabled micro-Fabry–Perot interferometer.* Optics Letters *34* (2009), No. 16, 2441–2443.

[15] X. JIANG, D. CHEN: *Low-cost fiber-tip Fabry-Perot interferometer and its application for transverse load sensing.* Progress In Electromagnetics Research Letters *48* (2014), 103–108.

Cross-effect of temperature and stress measurement in optical fiber sensor based on time offset[1]

Lujun Cui[2,4], Yanlong Cao[3], Honghong Guo[2], Shirui Guo[2]

Abstract. Structure multi-parameter optical fiber measurement, such as stress, displacement, corrosion and temperature, is of the utmost importance for structural health monitoring. We propose and demonstrate an optical fiber sensing system based on time offset for simultaneous temperature and stress measurements. Uncoupling method of temperature and stress has still a technical problem in the new optical fiber sensing measurement. In this study, we discuss the cross-influence between the stress and temperature measurements, The principle of the cross-effect is investigated and then validated by the theoretical simulation experiments. Furthermore, heating tests and tensile tests are also conducted in laboratory. The experimental results show that the optical fiber sensor based on time offset exhibits a good linear performance with 98 % linear coefficient. The experiments also demonstrated that, if the stress or temperature is not too large, for the free optical fiber measurement, the cross-effect can be neglected. For the different optical path length, the temperature sensitivity varies greatly for the optical fiber sensor based on time offset, and in the stress measurement experiments, the output intensity values increase obviously along with the temperature changes, so that the stress changes caused by the ambient temperature in optical fiber should be compensated in practical measurements.

Key words. Optical fiber sensor, temperature measurement, stress measurement, time offset, cross-effect.

[2]The University Key Subject Opening Laboratory of Henan Province, School of Mechanical & Electronic Engineering, Zhongyuan University of Technology, Henan, 450007, China

[3]Zhejiang University, Hanzhou, 310058, China

[4]Corresponding author; e-mail: `cuilujun@126.com`

1. Introduction

Optical fiber sensor has been regarded as one of the most promising monitoring system because of their electromagnetic interference immunity, high durability, and absolute measurement, which have been successfully used in many engineering fields such as civil, aerospace and hydraulic engineering [1, 2, 3]. And many optical fiber sensors have been developed, e.g., FBG-based displacement sensor or pressure sensor, LPFG-based corrosion sensor or twist sensor, Brillouin stress/temperature sensor [4]. However, most of the optical fiber sensors, like that FBG (or FBG-based sensor) and Brillouin optical fiber sensor are simultaneously sensitive to stress and temperature makes the measurement fall into trouble. And there is one important limitation for the application of optical fiber sensors which is the cross-sensitivity of all the measurements. This problem has been investigated by many researchers and many discriminating techniques have been reported to solve the problems of the stress-temperature coupling in the optical fiber sensing system. Numerous studies on uncoupling methods have been conducted since 1990s [5, 6, 7]. One absolute temperature compensation method was introduced to solve the temperature-stress cross sensitivity problem, which is regarded as one of the most effective methods. The temperature-compensation sensor and the stress sensor use the same coated materials, and this method need not know the temperature sensing coefficient of the stain sensor [8]. And several methods to increase the measurement sensitivity and range of the optical fiber interferometric sensors which are based on wavelength technique have been reported. Farahi presented an interferometric technique which allows simultaneous measurement of stress and temperature applied to a sensing fiber [5]. J. J. Tian demonstrated a optical fiber sensor which is implemented by a cascaded-cavity Fabr-Perot (FP) fiber interferometer for simultaneous temperature and stress measurements. The temperature-stress cross-talk was compensated by solving a sensitivity-coefficient matrix equation for the two cavities [9]. Zhou et al. constructed a cascaded-cavity Fabry-Perot fiber interferometer sensor by splicing a specific hollow annular core fiber with a standard single-mode fiber. Their sensor can simultaneously measure the temperature and stress with cross-sensitivity compensation [9, 10, 11].

However, the above methods of stress-temperature cross sensitivity compensation are prone to failure for the optical fiber sensing system based on time offset, and, therefore, simultaneous temperature and stress measurement by a simple fabrication technique that avoids cross-sensitivity is demanded. This paper reports the experiments for simultaneous discriminated measurement of stress and temperature using optical fiber sensing system based on time offset. The principle of the simultaneous temperature and stress measurement method is investigated and then validated by the theoretical simulation experiments in laboratory. The discrimination of stress and temperature has some actual using value for the optical fiber sensing system based on time offset. Furthermore, this could lead to realizing the distributed optical fiber stress and temperature measurement simultaneously. The article is divided into four sections: the sensing mechanism of the optical fiber sensor based on time offset is introduced, and the sensing principle and the influence factors of sensing

system sensitivity are analyzed in Section 2. Section 3 describes the fabrication of the optical fiber stress/temperature sensor based on time offset. Then a serials of experiments with cross-sensitivity consideration were carried out, and the corresponding experiment results were obtained and analyzed, the characteristics of the optical fiber sensor was discussed results were in this section. Finally, concluding remarks and further research are given in Section 4.

2. Theory

In our experiment, a commercial communication single-mode fiber was used for detecting the ambient temperature and stress around the optical fiber. For an optical pulse in the specific length L, the propagation time t of optical pulse in the optical fiber could be expressed by equation (1), where the parameter c is the vacuum speed of light, and parameter n is the refractive index of optical fiber.

$$t = nL/c. \tag{1}$$

For the outside temperature changes ΔT or stress changes $\Delta \varepsilon$ around the single optical fiber, the total time offset change is sum of Δt_T and Δt_ε, which were caused by the changes of stress and temperature, so we have

$$\Delta t = \Delta t_T + \Delta t_\varepsilon \tag{2}$$

where

$$\Delta t_T = \frac{1}{c} \times \left[\left(\frac{\partial n}{\partial T} \right) L + n \left(\frac{\partial L}{\partial T} \right) \right] \, dT = \frac{1}{c} \times P_T^0 \Delta T$$

and

$$\Delta t_\varepsilon = \frac{1}{c} \times \left[\left(\frac{\partial n}{\partial \varepsilon} \right) L + n \left(\frac{\partial L}{\partial \varepsilon} \right) \right] \, d\varepsilon = \frac{1}{c} \times P_\varepsilon^0 \Delta \varepsilon \,.$$

In order to consider the cross sensitivity of stress and temperature, it is possible to use the Taylor expansion to find their response when the temperature and stress change were applied the optical fiber simultaneously:

$$\Delta t \times c = \left[\frac{\partial n}{\partial T} L + n \frac{\partial L}{\partial T} \right] \Delta T + \left[\frac{\partial n}{\partial \varepsilon} L + n \frac{\partial L}{\partial \varepsilon} \right] \Delta \varepsilon +$$

$$+ \left[\frac{\partial^2 n}{\partial T^2} L + n \frac{\partial^2 L}{\partial T^2} \right] (\Delta T)^2 + \left[\frac{\partial^2 n}{\partial \varepsilon^2} L + n \frac{\partial^2 L}{\partial \varepsilon^2} \right] (\Delta \varepsilon)^2 +$$

$$+ \left[\frac{\partial L}{\partial \varepsilon} \frac{\partial n}{\partial T} + \frac{\partial^2 n}{\partial L} \partial \varepsilon L + \frac{\partial L}{\partial T} \frac{\partial n}{\partial \varepsilon} + n \frac{\partial^2 L}{\partial T \partial \varepsilon} \right] \Delta T \Delta \cdots \,. \tag{3}$$

In this work, we do not consider higher order variations in (3), so the equation

(3) can be simplified as

$$\Delta t = \frac{1}{c} \times \left(P_T^0 \Delta T + \times P_\varepsilon^0 \Delta\varepsilon + P_{T\varepsilon}\Delta T \Delta\varepsilon + P_{\varepsilon T}\Delta\varepsilon\Delta T \right), \qquad (4)$$

where

$$P_{T\varepsilon} = P_{\varepsilon T} = \frac{\partial L}{\partial \varepsilon}\frac{\partial n}{\partial T} + \frac{\partial^2 n}{\partial T \partial \varepsilon}L + \frac{\partial n}{\partial \varepsilon}\frac{\partial L}{\partial T} + n\frac{\partial^2 L}{\partial T \partial \varepsilon}, \qquad (5)$$

$P_{T\varepsilon}$ and $P_{\varepsilon T}$ being the cross sensitivity coefficients of stress and temperature. As the number of cross sensitivity coefficient $P_{\varepsilon T}$ is very small, if the changes of temperature ΔT or stress $\Delta\varepsilon$ are not too large, it is unnecessary to consider the high order item, for the free optical fiber, so the cross sensitivity coefficient can be neglected. However, if the length of the monitoring fiber is too large, the cross coefficient is needed to be considered as the item is proportional to fiber length L.

So, the equation (2) can be written in the following form:

$$\Delta t = \Delta t_T + \Delta t_\varepsilon = \frac{1}{c} \times \left(P_T^0 \Delta T + P_\varepsilon^0 \Delta\varepsilon + P_{T\varepsilon}\Delta T \Delta\varepsilon \right). \qquad (6)$$

For the optical fiber refractive index n, it was regularly considered as a constant, actually, the parameter n not only was the function of the wavelength λ, but also changes along with the temperature and stress. If the parameters C_T, C_ε and α_{f} denote the coefficient of optical fiber refractive index for temperature, refractive index for stress, and thermal expansion, respectively, these parameters are defined as

$$C_T = \frac{1}{n} \times \frac{\partial n}{\partial T}, \quad C_\varepsilon = \frac{1}{n} \times \frac{\partial n}{\partial \varepsilon}, \quad \alpha_{\mathrm{f}} = \frac{\partial \varepsilon}{\partial T} \qquad (7)$$

and the partial derivative $\frac{\partial L}{\partial T}$ in the equation (5) is expressed as $\frac{\partial L}{\partial T} = \frac{\partial L}{\partial \varepsilon} \times \frac{\partial \varepsilon}{\partial T} = \alpha_{\mathrm{f}} \times L$, then

$$P_T^0 = \left[\left(\frac{\partial n}{\partial T}\right) L + n\left(\frac{\partial L}{\partial T}\right) \right] = nL(C_T + \alpha_{\mathrm{f}}), \qquad (8)$$

$$P_\varepsilon^0 = \left[\left(\frac{\partial n}{\partial \varepsilon}\right) L + n\left(\frac{\partial L}{\partial \varepsilon}\right) \right] = nL(C_\varepsilon + 1). \qquad (9)$$

Then we can obtain

$$\Delta t = \frac{1}{c} \times \left[nL(C_T + \alpha_{\mathrm{f}})\Delta T + \times nL(C_\varepsilon + 1)\Delta\varepsilon + 2P_{T\varepsilon}\Delta T \Delta\varepsilon \right] \qquad (10)$$

and the parameter $P_{T\varepsilon}$ is calculated by

$$P_{T\varepsilon} = P_{\varepsilon T} = nL(C_T + n \times C_T \times C_\varepsilon + C_\varepsilon \times \alpha_{\mathrm{f}} + L \times \alpha_{\mathrm{f}}). \qquad (11)$$

The term $P_{\varepsilon T}\Delta\varepsilon\Delta T$ in equation (10) is the cross effect term, and it can be seen that the cross effect is a function of sensing length L. Equation (11) indicated that, if the stress or temperature is not too large, for the free optical fiber the cross effect term can be neglected. Figure 1 shows the dependence of the cross coefficient $P_{\varepsilon T}$ of optical fiber sensor system on the optical fiber length L and temperature T.
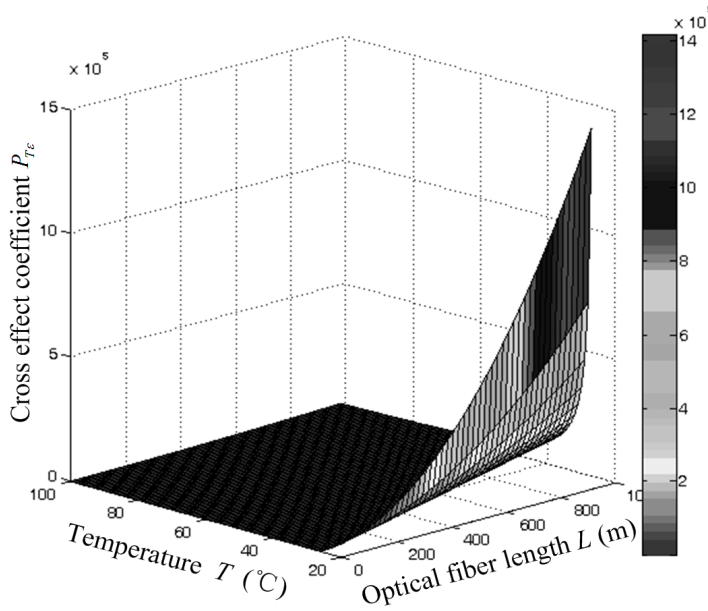
Fig. 1. Cross coefficient $P_{\varepsilon T}$ of optical fiber sensor system vs the optical fiber
length L and the temperature T

Meanwhile, the cross efficient $P_{\varepsilon T}$ can be determined from the equation (11).
Figure 1 shows that the cross effect of in optical fiber during the temperature and
stress measurement could be affected more seriously along with elongation of the
optical fiber length L. So, if the optical fiber length L of the monitoring fiber is too
long, the cross effect term is needed to be considered as the item is proportional to
the length L of the optical fiber. Figure 1 indicates that if the temperature T and
optical fiber length L are very small, the cross effect can be neglected, however, if
the length of the monitoring fiber is too large, the cross effect coefficient $P_{\varepsilon T}$ needs
to be compensated. At the same time, the cross effect coefficient $P_{\varepsilon T}$ can also be
neglected in case of high ambient temperature.

3. Experiment and discussion

The experimental configuration of the optical fiber sensing system based on time
offset is shown in Fig. 2. In order to demonstrate the cross effect of optical fiber sens-
ing system in real temperature and stress measurements, temperature and stress
experiments were first carried out by using 1 m-long single-mode optical fiber as
sensing path segment to detect temperature and stress, respectively. In figure 2,
the 0.5 m-long single-mode optical fiber was enclosed in an commercial thermostat
(MAX-TH80). To control the temperature and humidity around optical fiber sens-
ing path, the thermostat was provided with $\pm 0.1\,^{\circ}\mathrm{C}$ temperature control accuracy.
And another 0.5 m-long single-mode optical fiber was fixed into the digital stress

gauge (JC-4C), and it provided $\pm 20000\,\mu\varepsilon$ stress detection range with $20\mu\varepsilon$ detection resolution. The configuration enabled us to apply heat and axial stress to the sensing optical fiber synchronously.

Fig. 2. Experiment setup of single optical fiber stress or temperature sensing system

The performance of optical fiber sensor was tested with the experiment set-up in Fig. 2, which was made up of several parts: a tunable repetition rate ul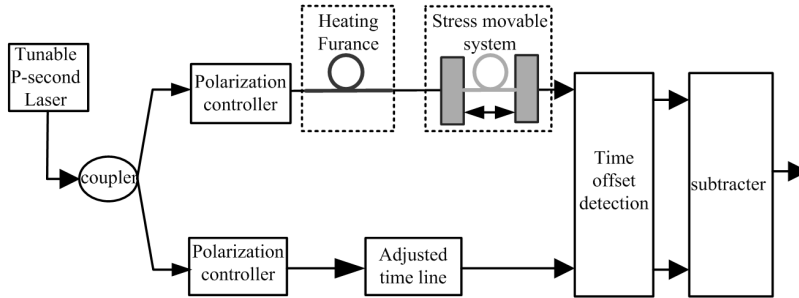tra-fast optical clocks actively mode-locked fiber laser, a mechanical adjustable time delay line in reference optical path, time offset correlation detection and subtracter. The average laser pulse output power and pulse repetition could be adjusted to $20\,\text{mW}$ and $10\,\text{GHz}$, respectively. The time offset correlation detection unit, which was composted by a KDP frequency-doubling crystal and photodiodes, could generate the second-harmonic signal and photoelectric signal.

A succession of optical pulse from the ultra-fast optical clocks actively mode-locked fiber laser with fixed pulse repetition rate was divided into two optical path pulse serials by $50/50$ optical coupler shown in Fig. 2. The polarization controller could split the laser pulse into beams and polarize them in different polarization planes. By adjusting the mechanical time delay-line after the polarization controller, time intervals of a few seconds between the two polarized lasers pulsed in the reference optical path, compared to the optical pulse in sensing path, could be achieved. The optical pulse series in two paths are recombined in two respective polarization planes by the polarization beam splitter (PBS). After that, the two optical pulses are separated into optical pulse pairs of respective polarization plane into reference path and sensing path, then, two optical pulse correlation signals will be obtained by using the time offset correlation detection, after the process of photoelectric conversion and subtraction, the final electric signal output intensity is obtained.

To determine the cross effect, a succession of detecting experiments were carried out using different length L for the optical sensing path, a fixed 1 m-long single-mode optical fiber was arranged in reference optical path, and the sensing optical fiber path using different optical length L was heated at $2\,^\circ\text{C}$ intervals in Fig. 2, and for each intervals, the output values of sensing system were recorded by computer. Figure 3 indicates the correlation value of time offset in sensing system against the temperature changes around the fiber.

Figure 3 shows that the optical fiber sensing system based on time offset exhibits
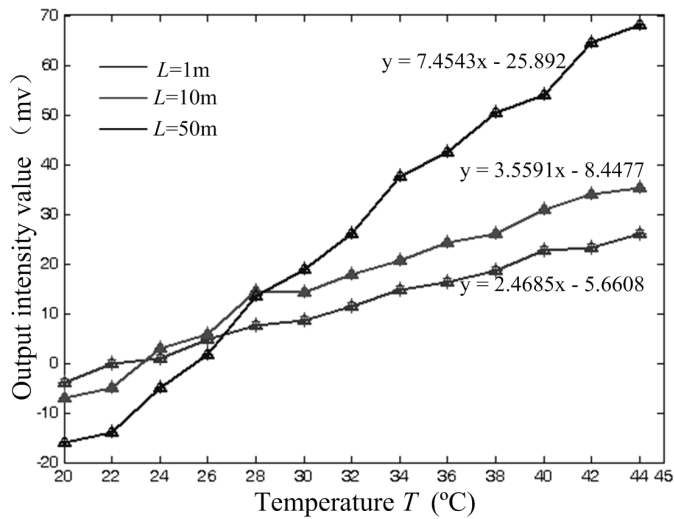
Fig. 3. Output intensity values vs. temperature T for different optical length

different sensitivity for different lengths L in reference optical fiber path. Compared with other two 1 m and 10 m optical paths lengths, the sensitivity of the sensing system which possesses the 50 m optical length is higher, and on the contrary, the measurement range is shorter, therefore we know that the temperature sensitivity and measurement range were contradictory and related to the length of monitoring fiber in the optical fiber sensing system. In real measurement, it is noted that much higher sensitivity or large detective range can be obtained by optimizing optical fiber sensing path length L.

At the same time, at room temperature the sensing optical fiber for optical path $L = 1$ m was prolonged by 500 με intervals in Fig. 2, and for each interval, the output values of sensing system were recorded by computer. Figure 4 indicates the correlation value of time offset in sensing system against the stress changes around the optical fiber.

During the stress measurement of the optical fiber sensing system using the fixed optical length, the experiments indicated that compared with the temperature of 298 K and 308 K, the output intensity value of the sensing system is larger in the temperature of 318 K, however under the different circumstance temperature the sensitivity of the sensor is almost same, meanwhile, aimed to the same stress in optical fiber, the sensing output intensity value increase obviously with the temperature increasing, so it is concluded that in stress measurement of the optical fiber sensing system, the stress change caused by the temperature effect around the optical fiber should be modified. As shown in Fig. 4, by fitting the experimental data, the relationship between the electrical signals output intensity of the optical fiber sensor and detective stress in electronic stress meter was shown to be linear with coefficient of 98 %.
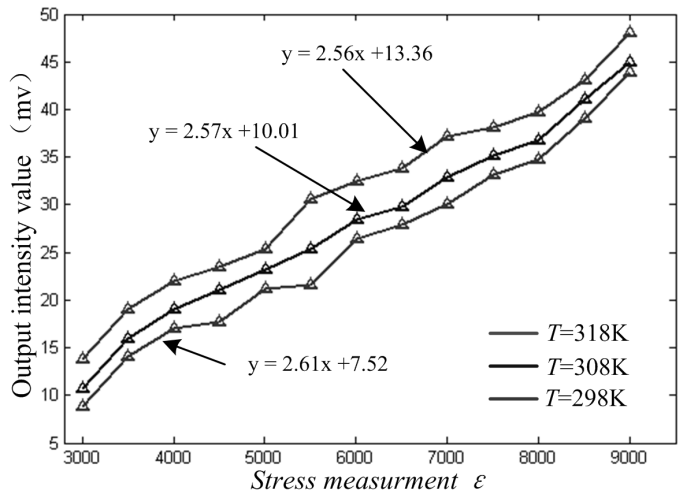
Fig. 4. Output intensity values vs. stress ε for fixed optical length

4. Conclusion

In the paper, we demonstrated an optical fiber temperature and stress sensor based on time offset, the fundamental sensing principle and characteristic are explained. As the optical fiber sensor based on time offset is sensitive to temperature and stress simultaneously, the cross effect between temperature and stress is discussed in theory, and a series of temperature and stress testing experiment were conducted, the experiment results indicated that the optical fiber testing system exhibited good linear performance, the linear coefficient could reach 98 %. During the temperature measurement experiments, for different optical path length, the sensitivity varies greatly in the optical fiber sensor based on time offset. In the stress measurement experiments, the output intensity values increase obviously along with the temperature, so the stress changes caused by the ambient temperature in optical fiber should be compensated in practical measurements. Although optical fiber temperature sensor based on time offset is proposed, there are still some areas needing further improvement, we need to improve and find a compensation method for the thermal effect in the optical fiber sensing system.

References

[1] X. Lu, M. A. Soto, L. Thévenaz: *Temperature-strain discrimination in distributed optical fiber sensing using phase-sensitive optical time-domain reflectometry*. Optics Express *25* (2017), No. 14, 16059–16071.

[2] M. Sun, B. Xu, X. Dong, Y. Li: *Optical fiber strain and temperature sensor based on an in-line Mach–Zehnder interferometer using thin-core fiber*. Optics Communications *285* (2012), No. 18, 3721–3725.

[3] H. Sun, S. Yang, X. Zhang, L. Yuan, Z. Yang, M. Hu: *Simultaneous measure-*

ment of temperature and strain or temperature and curvature based on an optical fiber Mach—Zehnder interferometer. Optics Communications *340* (2015), 39–45.

[4] J. He, Z. Zhou, J. Ou: *Simultaneous measurement of strain and temperature using a hybrid local and distributed optical fiber sensing system.* Measurement *47* (2014), 698–706.

[5] F. Farahi, D. J. Webb, J. D. C. Jones, D. A. Jackson: *Simultaneous measurement of temperature and strain: Cross-sensitivity considerations.* Journal of Lightwave Technology *8* (1990), No. 2, 138–142.

[6] J. Jung, H. Nam, J. H. Lee, N. Park, B. Lee: *Simultaneous measurement of strain and temperature by use of a single-fiber Bragg grating and an erbium-doped fiber amplifier.* Applied Optics *38* (1999), No. 13, 2749–2751.

[7] B. O. Guan, H. Y. Tam, X. M. Tao, X. Y. Dong: *Simultaneous strain and temperature measurement using a superstructure fiber Bragg grating.* IEEE Photonics Technology Letters *12* (2000), No. 6, 675–677.

[8] Z. Zhou, J. P. He, K. Yan, J. P. Ou: *Fiber-reinforced polymer-packaged optical fiber sensors based on Brillouin optical time-domain analysis.* Optical Engineering *47* (2008), No. 1, p. 014401.

[9] J. Tian, Y. Jiao, S. Ji, X. Dong, Y. Yao: *Cascaded-cavity Fabry–Perot interferometer for simultaneous measurement of temperature and strain with cross-sensitivity compensation.* Optics Communications *412* (2018), 121–126.

[10] A. Zhou, B. Qin, Z. Zhu: *Hybrid structured fiber-optic Fabry–Perot interferometer for simultaneous measurement of strain and temperature.* Optics Letters *39* (2014), No. 18, 5267–5270.

[11] X. Zhang, W. Peng, L. Y. Shao, W. Pan, L. Yan: *Strain and temperature discrimination by using temperature-independent FPI and FBG.* Sensors and Actuators A: Physical *272* (2018), 134–138.

Simulation of sensor intelligent video analysis system based on embedded system[1]

Qiuping Ni[2], Yuanxiang Tang[3, 4]

Abstract. In recent years, embedded intelligent video analysis system that is based on embedded system has been widely applied to security industry and every aspect of social life. Establishing the mapping correlation between images and event description can overcome defects of the traditional video surveillance technique. Besides, its system hardware is a visual measuring sensor system that takes imaging sensors as the leading, and VxWorks operating system which is equipped with S3C2440 processor is used in the embedded monitoring system to realize precise concurrent control and two-channel and dual-mode high-speed serial communication. Moreover, it solves problems that relate to real-time and concurrent control of multiple function modules, synchronization and mutex among modules, monitoring and management of system deadlock, etc. It can precisely generate all external signal characteristics of real equipment, accurately joint with test equipment, and achieve full analog simulation. The simulative training of the system shows its significant advantages and good applicability and also provides a new direction for the development of intelligent video analysis system.

Key words. Embedded system, imaging sensors, intelligent video analysis, simulation.

1. Introduction

With the development of economy, the advancement of society and the improvement of people's living standard, various security issues have been paid more attentions; as a result, video surveillance technology has been extensively applied in more fields to ensure personal and property security [1]. To solve the shortcomings

---

[2]School of Economy and Management, Yibin University, Yibin, Sichuan, 644007, China

[3]School of Computer and Information Engineering, Yibin University, Yibin, Sichuan, 644007, China

[4]Corresponding author

of video surveillance videos such as low search efficiency, difficult analysis and time consumption, people tend to find out a more intelligent method which can rapidly read, check and analyze a large number of videos to improve the analysis level and work efficiency. Intelligent video system emerged at the right moment.

The intelligent security monitoring system can automatically analyze monitoring pictures and made relevant judgment through computer and can issue warnings when there are abnormalities, which gets rid of manual intervention [2, 3]. Compared to the traditional video monitoring system, the intelligent video analysis system has advantages of low consumption, high stability, real time and high reliability [4]. Zhang et al. [5] proposed a intelligent home security system. Based on intelligent video analysis system, a historical pattern based foreground segmentation method which was suitable for indoor scenario analysis and an exact cutting based region of interest (ROI) generation method and scene-structure modeling method was also proposed. Moreover a concurrence relation graph of visual words was established for reliable behavioral analysis. Caterina et al. [6] proposed a Digital Signal Processor (DSP) based embedded intelligent monitoring and tracking sensor and used Pan/Tilt/Zoom (PTZ) camera to track targets and keep them in the center of the visual field. The system ran in real-time, and it was implemented on the fixed-point single core DSP DM6437 Evaluation Module. The adaptive template matching tracking algorithm employed a robust Sum of Weighted Absolute Differences (SWAD) to maintain high accuracy under noise and partial occlusion when conventional SAD failed. With the development of computer technologies, the optimization of hardware equipment and the diversification of application requirements, the current embedded intelligent video analysis technology has not been able to satisfy the market demands. This study proposed a design scheme for a sensor based embedded intelligent video analysis system based on analog simulation training system, the visual measurement system of image sensor and video capture technology and introduced its composition structure and operation principles.

2. Overall architecture of system

2.1. System demand analysis

The designed embedded intelligent video analysis system is mainly used for monitoring of indoor environment. Hence it should be able to collect, compress and transmit video data of monitored environment in real time, transmit through communication protocol network, display monitored environment and store the video, and automatically detect moving objects in monitored environment and made analysis on their behaviors.

2.2. Design of overall architecture of system based on demand analysis

Intelligent video analysis technique originates from the researches of computer vision and computer pattern recognition [7, 8]. Based on the mapping relation

between images and descriptions of incidents, it can distinguish and recognize key objectives or behaviors in complicated video pictures to solve various practical application problems [9]. Sensor based embedded video analysis system was composed of video surveillance server, embedded monitoring system and network user terminal. VxWorkds operation system which is installed with S3C2440 processor was used in the embedded monitoring system. The signals captured by the visual measurement sensor were transmitted to the server terminal after being processed by image sensor system.

3. Design of system hardware

The sensor based embedded intelligent video analysis system was designed, and the core was the design of sensors. The system took an embedded digital sigma processor (DSP) BF525C (600 Hz). The hardware structure of the intelligent image sensor is shown in Fig. 1. Storage was composed of a main storage and an auxiliary storage; the main storage is DDR2SDRAM (2 GB) and the auxiliary storage was SLC Nand Flash (1 GB). Peripheral equipment included power module, serial communication port, USB2.0 port, CCD sensor camera, CCD video input port, video frequency input port, Ethernet network port and light-emitting diode (LED). The power module was mainly responsible for supply power for DSP and core main board. Serial port was mainly used for connecting with PC for debugging of system hardware. USB port was responsible for program writing of large data volume. JTAG port was used for chip internal test. Ethernet interface was used for data communication. LED was responsible for indicating system state.
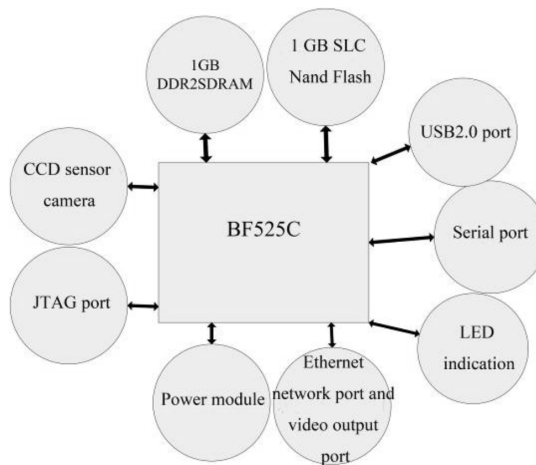

Fig. 1. Structure of the hardware system

Imaging sensor is an important component of digital camera, called photosensitive element. It was responsible for transforming optical images into electronic signals; therefore, it was an important component of the video monitoring system. This study connected the imaging sensor with the optical projector to collect videos. The

usage of imaging sensors required the additional drive circuit and digitized analog to digital (A/D) switching circuit. This study adopted the three-line imaging sensor of the charge coupled device (CCD) series produced by SONY Company, which was characterized by good quality, high integration level and low power consumption.

The imaging sensor was connected with the working circuit. The clock module included RESET, XVCLK1 (clock) and PCLK (pixel clock). When the sensor started, digital images transmitted images through the pixel clock and reference signals. The register module was equipped with serial camera control bus (SCCB) for operations like reading and writing. Collected videos were sent to CPU for processing, analysis and computation. The digital interface voltage of the operating circuit of the imaging sensor was 1.8 V direct current.

4. Experiment on the detection of the boxing training aid

In the embedded development environment, software mainly included Bootloader [10], Linux core, root file system, application program, etc. The real-time requirements are as follows. The system is required to generate multiple line signals and control the parallel temporal structure. It should be able to query in real time and rapidly interrupt response in the condition of high-speed serial communication. Different lines should be synchronous but not reject each other. Different tasks and interruption response time should be strictly controlled. The embedded system based intelligent video analysis system could satisfy all the aforementioned requirements.

4.1. Operating system

The embedded system based intelligent video analysis system had high requirements on the amplitude, duration, pulse width and frequency of signals. Due to the high concurrency of the tasks, the deadline requirement for each task was also strict. Therefore, signals and communication ports should be controlled independently. Vx-Works real-time multi-task operating system was adopted to fulfill related operations as it could satisfy the above requirements.

4.2. Transplantation of system boot loader

System boot program is a segment of program which operates before operating system core and can initialize hardware equipment, adjust hardware and software environment and load kernel image.

But system root program is unable to guide all systems in different platforms. Therefore, the code should be portable. Multiple platforms can be guided through transplantation.

U-boot, also known as Universal Bootloader [11], supports multiple system boots, such as Linux, VxWorks, etc. [12]. It is transplanted according to its execution process and the hardware platform of target board (Micro 2440 board). The source code structure of U-boot is shown in Table 1.

Table 1. Water quality grades and content standards

Catalogue	Content
Include	Header file
Drivers	The driving program of peripheral chip
Common	Versatility code with no connection with the framework of processor
Board	File related to development board
CPU	File related to processor
Net	Related to networking protocol
FS	Related to document system

4.3. Design and test of each module

The intelligent analysis module had functions of snapshot, picture recording, video data transmission and motion dynamics detection. It collected video data through image sensors, then processed the frames of the video data, and finally performed basic processing for video data transmission.

4.3.1. Snapshot module. Snapshot occupied an important position in intelligent video analysis. The monitor would screenshot some pictures and store them in JPEG format when capturing video pictures or compress the pictures in YUV and BMP format using open source image compression library libjpeg.

The first step of snapshot was establishing descriptors for picture file and cut out a frame of image. If the format of video source was MJPEG, then temporary memory was applied for. The framework image was copied to temporary memory and written into image file. If the format of video source was MJPEG, then Libjpeg library compressed the screenshot directly as JPEG format.

4.3.2. Video module. Picture recording was designed based on the video capture module. It referred to writing the video streaming collected by video threads into video documents whose format had been specified.

Video module also needed to compress video. Video is usually compressed into MJPEG format. The compressed video had small internal storage, which was convenient for storage and transmission.

The first step was to set up video film. Then a frame in the compressed MJPEG video file was acquired. The video file was stored as AVI format. The acquired frame was written into the file one by one. Finally the file was closed.

4.3.3. Transmission module. Video data transmission was mainly fulfilled relying on the communication between network server and client. The communication of client was realized by online browser. Therefore, it was necessary to establish network server based on HTTP protocol to respond the connection request released by client. The data interaction between them is shown in Fig. 2.
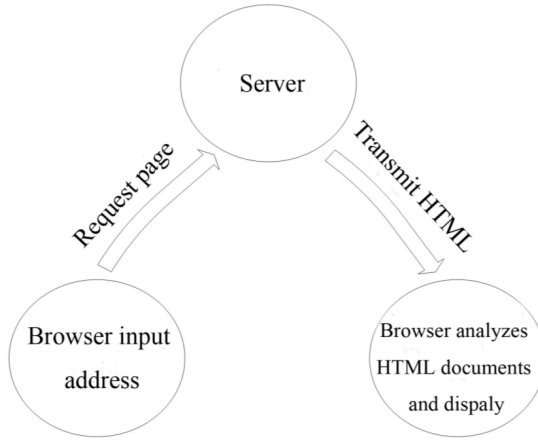
Fig. 2. Process of data interaction

4.3.4. Motion detection module. The motion detection module is the key link in intelligent video analysis [13], which can detect moving objects in monitoring pictures as well as classify and understand the movements. It can also extract changed areas from the collected background images. The detection method is usually selected according to different needs. The common motion detection algorithms include inter-frame difference method, background difference method, optical flow method and background difference based on statistic models [14, 15].

Based on background differencing, the motion of objects was detected using Gaussian Mixture Model.

Background differencing refers to extracting different parts as the moving targets by comparing the image in the current frame with the constructed background model. The formula is as follows:

$$P_n(x, y) = |f_n(x, y) - f_{n+1}(x, y)| \tag{1}$$

$$Q_n(x, y) = \begin{cases} 1 & P_n(x, y) \geq T \\ 0 & P_n(x, y) < T \end{cases} \tag{2}$$

where (x, y) refers to the position of a pixel point, $f_n(x, y)$ and $f_{(n+1)}(x, y)$ stands for the pixel points whose coordinates in two successive frames are both x, y, T stands for a threshold, and $Q_n(x, y)$ stands for the pixel point whose coordinates are (x, y) in binary image.

If $P_n(x, y)$ is larger than T, then the output result is 1, suggesting the point (x, y) is the moving target; otherwise, the output result is 0, indicating the point (x, y) is background.

The first step of motion detection was to acquire one frame of image from the cached image at fixed time interval. Then the background of the video was processed by modeling. One frame was collected after delay. Then the calculation of

background differencing was performed on the two frames using the above formulas. Whether intelligent alarm should be executed was determined based on the percentage of foreground points and the size of threshold.

4.3.5. Alarm module. Alarm module was based on the above modules. Alarm module should be connected with access controller, buzzer alarm and electronic fence.

The follow of system alarm was as follows. Firstly the camera collected video signals in the monitored environment. Then the motion detection module determined whether the moving objects in the environment had abnormal behaviors; if it had, then abnormality alarm information was sent to the service management port. The emergency degree was determined according to the preset alarm rules.

If it satisfied the alarm conditions, alarm information was sent to security personnel and meanwhile the buzzer alarm alarmed according to the preset alarm disposal scheme. The system could even be connected to the access controller; the access controller closed when the system alarmed.

5. Experiment and analysis

From the aspect of function realization, this study used the imaging sensor to collect video information and transmit it through the PC104 bus. Users can visit video images obtained by the intelligent video analysis system online. The system was tested to verify the feasibility and effectiveness of the system design. The monitoring video images collected by the imaging sensor were analyzed by the capturing packet software Charles. The obtained testing data are shown in Table 2.

Table 2. Data of performance test

Test time (s)	27
Number of transmitted frames	603
Image size	33254305 B
Frame image	52 kB
Image transmission speed	27.66 frames/s
Image pixels	640×480
Pixel transmission speed	1362337 pixels/s
Bit rate of transmission	3.58 Mbps

The sensitivity of the intelligent video analysis system in detecting moving objects was tested. The experiment was carried out in an interior corridor with stable illustration and single background. The person in the picture was monitored, and the result is shown in Fig. 3.

This study realized functions of the embedded sensor intelligent video analysis system, including the video collection of imaging sensor, accurate transmission and high-pixel display. This study used three-line imaging sensors, thus the pixels of

Fig. 3. The monitoring results of the moving objects using intelligent video
analysis system

video data reached up to 640×480, indicating the embedded video analysis system
operated steadily and the image quality was good. There were averagely 27.66 frames
of images that could be transmitted every second, indicating the transmission was
fast and users could clearly see the video pictures. Figure 3 shows, that the back-
ground differencing and Gaussian model methods could effectively detect moving
objects; alarm signals could be released rapidly when there was abnormality.

6. Conclusion

The embedded system based intelligent video analysis system applied embedded
computer and real-time operating system to accomplish the construction of hard-
ware system as well as the base development of software system, which realized the
parallel and real-time control of multiple functional modules, solved the problem
of synchronization and mutual exclusion between the modules and deadlock detec-
tion issue, and achieved the generation of multi-path time–varying signals and the
high-speed serial dual-channel double-mode communication. This study proposed
and designed a novel embedded intelligent video analysis system which was featured
by stable operation, clear pictures and high transmission speed and could monitor

moving objects. But the system remains to be further improved due to the presence of many problems.

References

[1] G. Yang, X. Tan, Y. R. Zhang: *An intelligent video surveillance system for android smart phone.* Advanced Materials Research *850–851* (2014), 884-888.

[2] Z. Y. Wang, L. Chen: *Design of mobile phone video surveillance system for home security based on embedded system.* Chinese Control and Decision Conference (2015 CCDC), 23–25 May 2015, Qingdao, China, IEEE Conferences (2015), 5856–5859.

[3] B. Cui, J. Cui, Y. Duan: *Intelligent security video surveillance system based on DaVinci technology.* International Conference on Measuring Technology and Mechatronics Automation (ICMTMA), 16–17 Januar 2013, Hong Kong, China, IEEE Conferences (2013), 655–658.

[4] M. Komorkiewicz: *Real-time detection of movement in prohibited direction for video surveillance system.* Image Processing & Communications *17* (2012), No. 4, 251–264.

[5] J. Zhang, Y. Shan, K. Huang: *ISEE Smart Home (ISH): Smart video analysis for home security.* Neurocomputing *149* Part B, (2015), 752–766.

[6] G. Di Caterina, I. Hunter, J. J. Soraghan: *DSP embedded smart surveillance sensor with robust SWAD-based tracker.* International Conference on Advanced Concepts for Intelligent Vision Systems (ACIVS), 4–7 September 2012, Brno, Česká Repulika, Springer Nature (LNCS), *7517* (2012), 48–58.

[7] H. Liu, S. Chen, N. Kubota: *Intelligent video systems and analytics: A survey.* IEEE Transactions on Industrial Informatics *9* (2012), No. 3, 251–264.

[8] G. Garibotto: *Video surveillance and biometric technology applications.* International Conference on Advanced Video and Signal Based Surveillance, 2–4 September 2009, Genova, Italy, IEEE Conferences (2009), 288.

[9] M. Campos, T. Martins, M. Ferreira, C. Santos: *Detection of defects in automotive metal components through computer vision.* International Symposium on Industrial Electronics (ISIE), 30 June–2 July 2008, Cambridge, UK, IEEE Conferences (2008), 860–865.

[10] P. Li, J. Liao, C. Hu, Y. Yin, M. Q. H. Meng: *Design of medical remote monitoring system base on embedded Linux.* International Conference on Information and Automation (ICIA), 6–8 June 2011, Shenzhen, China, IEEE Conferences (2011), 590–594.

[11] S. Yang, W. Shao, H. Song, W. Xu: *Compass: A data center bootloader for software defined infrastructure.* International Conference on Networking and Services (ICNS), 24–29 May 2015, Rome, Italy, IARIA (2015), 98–103.

[12] P. Sagar, N. Naveen, A. Joseph, K. H. Abdul Nazer, M. Likhin: *Implementation of CMNN based industrial controller using VxWorks RTOS Ported to MPC8260.* International Conference on Advances in Computing and Communications, 29–31 August 2013, Cochin, India, IEEE Conferences (2013), 239–242.

[13] S. C. Huang: *An advanced motion detection algorithm with video quality analysis for video surveillance systems.* IEEE Transactions on Circuits and Systems for Video Technology *21* (2011), No. 1, 1–14.

[14] J. H. Duncan, T. C. Chou: *Temporal edges: The detection of motion and the computation of optical flow.* International Conference on Computer Vision, 5–8 December 1988, Tampa, FL, USA, IEEE Conferences (1988), 374–382.

[15] Y. Luo, T. D. Wu, J. N. Hwang: *Object-based analysis and interpretation of human motion in sports video sequences by dynamic bayesian networks.* Computer Vision and Image Understanding *92* (2003), Nos. 2–3, 196–216.

Soccer player detection and tracking based on image processing[1]

Somayeh Lotfi[2,4], Baharak Shakeri Aski[2,3],
Safoora Zakeri[2]

Abstract. Recent advances in soccer player detection and tracking have led to many new methods specifically designed for player tracking. Most of the attention, however, has been given to soccer video objects such as ball and players' detection and tracking. Though there is a number of existing literature to soccer player detection and tracking problems, we try to provide a higher detailed picture for a complete review. Within the broad survey and complex system, we p Table suggest the classification to describe modern soccer player detection and tracking. In addition, tables are utilized in the content to provide an overall view of soccer player detection and tracking methodologies.

Key words. Sports analytics, soccer player detection, soccer player tracking, blob based method, feature based method, occlusion detection.

1. Introduction

Nowadays, we could find much applications for video analysis in sports, such as statistics collection and video archiving, pattern analysis and motion replay. Because of development of new recording and processing devices, and the growing need for the media industry to extract meaningful information and analysis games, sports video analysis has attracted so attention. [1–3]. Sports video analysis consists of extraction of the spatiotemporal data with the corresponding athlete as well as a higher level abstraction of the events. In ball games, annotating video indexing becomes a more difficult task which requires the position of the ball as well as the position of the players [4, 5].

---

[1]This paper is extracted from research projects for Islamic Azad University, Bandar Abbas branch, Iran.

[2]Department of Computer Engineering, Bandar Abbas Branch, Islamic Azad University, Bandar Abbas, Iran

[3]Department of Computer Engineering, Ramsar Branch, Islamic Azad University, Ramsar, Iran

[4]Corresponding author; e-mail: `s.lotfi@iauba.ac.ir`

2. Methodology

We have implemented a vision system which automatically detects the ball in an acquired soccer video sequence. The proposed system is composed of three main blocks: in the first one, a background subtraction technique is combined with a circle detection approach to extract ball candidate regions. Then a feature extraction scheme is used to represent image patterns, and finally data classification is performed by using a supervised learning scheme. Figure 1 schematizes the proposed approach.
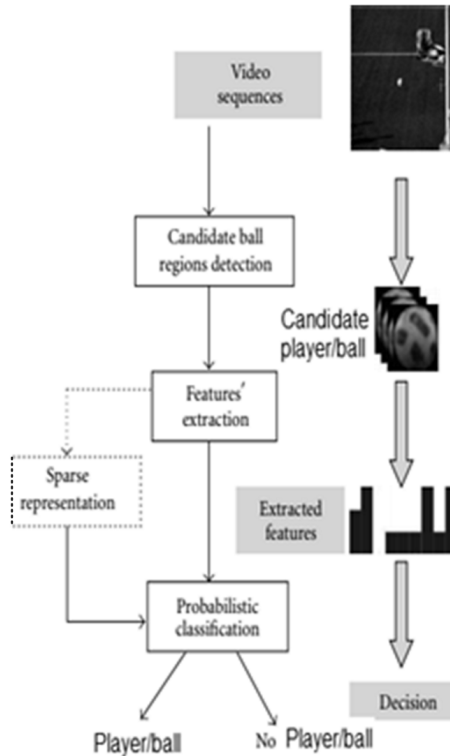
Fig. 1. Graphical overview of the proposed approach

The scale space of an image is defined as a function $L(x, y, \sigma)$, that is produced from the convolution of a variable-scale Gaussian function, $G(x, y, \sigma)$, with an input image, $I(x, y)$, that is

$$L(x, y, \sigma) = G(x, y, \sigma) * I(x, y), \tag{1}$$

where $*$ is the convolution operator and $G(x, y, \sigma)$ is defined as

$$G(x, y, \sigma) = \frac{1}{2\pi\sigma^2} e^{-\frac{x^2+y^2}{2\sigma^2}}, \tag{2}$$

The key points are detected using scale-space extreme in the difference of Gaussian (DoG) function D in convolution with the image $I(x, y)$:

$$D(x, y, \sigma) = [G(x, y, k\sigma) - [G(x, y, \sigma)] * I(x, y) = L(x, y, k\sigma) - L(x, y, \sigma), \quad (3)$$

where k is the multiplicative constant factor which separates two nearby scales. In order to detect the local maxima and minima of $D(x, y, \sigma)$, each sample point is compared to its eight neighbors in the current image and to its nine neighbors in the scales above and below. It is selected only if it is larger than all of these neighbors or smaller than all of them. Once a keypoint candidate has been found by comparing a pixel to its neighbors, the next step is to perform a detailed fit to the nearby data for location, scale, and ratio of principal curvatures. This information allows points to be rejected if they have low contrast or are poorly localized along an edge. A 3D quadratic function is fitted to the local sample points. The approach starts with the Taylor expansion (up to the quadratic terms) with sample point at the origin

$$D(X) = D + \frac{\partial D^{\mathrm{T}}}{\partial X} X + 0.5 X^{\mathrm{T}} \frac{\partial^2 D^{\mathrm{T}}}{\partial X^2} X, \quad (4)$$

where D and its derivatives are evaluated at the sample point $X = (x, y, \sigma)$. The location of the extremum is obtained taking the derivative with respect to X and setting it to 0, giving

$$\widehat{X} = -\frac{\partial^2 D^{-1}}{\partial X^2} \frac{\partial D}{\partial X}. \quad (5)$$

That is, a 3×3 linear system easily solvable. The function value at the extremum

$$D(\widehat{X}) = D + 0.5 \frac{\partial D^{\mathrm{T}}}{\partial X} \widehat{X} \quad (6)$$

is useful for rejecting unstable extrema with a low contrast. A this point, the algorithm rejects also keypoints with poorly defined peaks, that is, those points having, in the difference of Gaussian function, a large principal curvature across the edge but a small one in the perpendicular direction. By assigning a consistent orientation, based on local image properties, the keypoint descriptor can be represented relative to this orientation and therefore achieve invariance to image rotation.

3. Results

3.1. Player detection

The rule G>R>B, where G, R, B are the Green, Red and Blue components in the RGB space, respectively, is held for the majority of ground pixels. In our proposed method, we apply this feature to extract the ground at first and construct a binary image where the non-ground pixels detected according to this rule are marked using

equation

$$\text{Ground}(x, y) = \begin{cases} 0, & g(x,y) \geq r(x,y) \geq b(x,y), \\ 1, & \text{otherwise}. \end{cases} \tag{7}$$

Figure 2 shows these problems. As is shown in this figure, varying number of players in each frame, motion blur, and occlusion of players are the main problems of the soccer analysis. Also, our focus is fixed point implementation which is depicted in Fig. 3

Fig. 2. Challenge in player detection and tracking

(a)   (b)
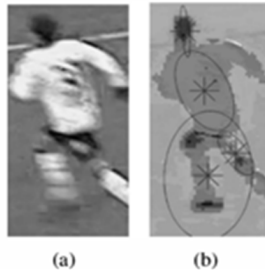
Fig. 3. Sample image of (a) player, (b) 16×4×4 uniform quantized players

As a result, we apply Sobel gradient algorithm to the RGB image to detect the sharp changes to preserve the ball [5]. In Sobel gradient algorithm, the derivative of the intensity values across the image is calculated and the change is found where the derivatives reach their maxima. The gradient is a vector and the components are measured in the x and y direction. The components are found using equations

$$\Delta x = \frac{f(x + \mathrm{d}x, y) - f(x, y)}{\mathrm{d}x}, \tag{8}$$

$$\Delta y = \frac{f(x, y + \mathrm{d}y) - f(x, y)}{\mathrm{d}y}, \tag{9}$$

$$M = \sqrt{(\Delta x)^2 + (\Delta y)^2}, \quad \theta = \tan^{-1}\left[\frac{\Delta y}{\Delta x}\right]. \tag{10}$$

Fig. 4. Blobs by removing unreasonable parts

Since the entire image is usually classified and blobbed, many blobs are formed that do not represent objects. These are discarded through a frequently complex system of rules and checks for the likelihood of the blob representing a valid object. Sets of blobs are then checked for mutual consistency. As shown in Fig. 4 the blobs are identified by removing unreasonable parts.

4. Ball detection and tracking

In Fig. 5, the ball and the lines on the ground were discarded. However, Sobel method retains the ball and the lines. Figure 6 is an example of this.

Fig. 5. Ground elimination result

Then the image containing the non-ground pixels (Fig. 5) and the Sobel gradient image (Fig. 6) are added, which yields an image with the players, ball, lines, goal post, spectators and scoreboard. Finally, the image is converted to the binary image and ground is eliminated from the resultant image shown in Fig. 5. Dilation and erosion methods are applied to connect the disjoint lines.

Fig. 6. Sobel gradient image

5. Conclusion

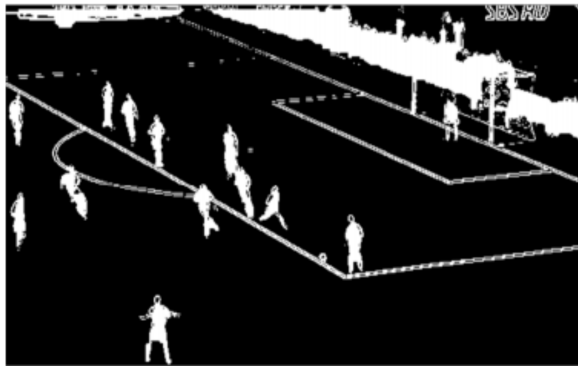We have presented a summary of detection methodologies, procedures, and technologies for a soccer game. We indicate that there are two major methodologies for player detection techniques: feature based classification approaches and blob-based methods relying on background subtraction. Furthermore, heuristic-based methods have the merit of no prior information of athletes but do not operate well in real-time applications as a result of the high computational complexity. Moreover, we divide each of these groups to extra particular clusters. Eventually, we present a short summary for any of these techniques. The results show the capability and robustness of detecting player, ball and track lines.

References

[1] N. BABAGUCHI, Y. KAWAI, T. KITAHASHI: *Event based indexing of broadcasted sports video by intermodal collaboration.* IEEE Transactions on Multimedia *4* (2002), No. 1, 68–75.

[2] L. BALLAN, G. M. CORTELAZZO: *Marker-less motion capture of skinned models in a four camera set-up using optical flow and silhouettes.* International Symposium on 3D Data Processing, Visualization and Transmission, 18–20 June 2008, Atlanta, GA, USA, Proceedings of 3DPVT (2008), paper 37.

[3] L. Y. DUAN, M. XU, T. S. CHUA, Q. TIAN, C. S. XU: *A mid-level representation framework for semantic sports video analysis.* ACM International Conference on Multimedia, 2–8 November 2003, Berkeley, CA, USA, Proceedings of Multimedia (2003), 33–44.

[4] H. SABIRIN, H. SANKOH, S. NAITO: *Automatic soccer player tracking in single camera with robust occlusion handling using attribute matching.* IEICE Transactions on Information and Systems *E98.D* (2015), No. 8, 1580–1588.

[5] R. A. SHARMA, V. GANDHI, V. CHARI, C. V. JAWAHAR: *Automatic analysis of broadcast football videos using contextual priors.* Signal, Image and Video Processing *11* (2017), No. 1, 171–178.

Research on topology control and channel allocation of wireless mesh network based on ALPOCA algorithm

Lanhui Huang[1]

Abstract. As modern network technology and Internet technology develops at a high speed, wireless Mesh network technology has been gradually applied to people's lives with its vast coverage area and good coverage efficiency. At the same time, its shortcomings are gradually exposed, especially its low wireless channel resource utilization rate. In view of this, this paper establishes a connected tree topology based on the original network topology and applies the ALPOCA algorithm for simulation analysis, which improves the utilization of channel resources and makes the channel allocation more reasonable. The application of this algorithm promotes the further development of wireless Mesh network.

Key words. ALPOCA algorithm, wireless Mesh network, topology control, channel allocation
.

1. Introduction

Normally, there is one and only one node within a wireless Mesh network required to be connected to a network connection such as a DSL Internet modem, which then wirelessly shares its Internet connection with other nodes nearby. At present, how to improve the capacity of wireless Mesh network has become a hot topic of global concern. Pathak et al. [1] applied efficient and convenient algorithms to improve network throughput and delay the attenuation of network life. Akyildiz et al. [2] established a framework that allows nodes to work on multiple channels simultaneously and configures multiple interfaces for each node. Wu et al. [3] summarized the current situation and predicament of partial intersecting channels and predicted the direction of the next step. Kodialam et al. [4] put forward a partially intersecting channel allocation algorithm used in traffic-aware scenes and multicast scenes, resulting in a significant increase in network throughput. Srinivasan et al. [5] first proposed to receive data from a channel on another channel and verified that

---

[1]School of Computer Science and Technology, Baoji University of Arts and Science, Baoji, 721016, Shaanxi, China; e-mail: hlhbjwl@sohu.com

the improved channel resource space division multiplexing can utilize partial intersecting channels, which is more reliable. Haghighizadeh et al. [6] also presented a detailed analysis of the model established in the case of intersecting channels. The results show that the results are consistent with the theoretical analysis and prove the usability of some intersecting channels. In order to study the wireless Mesh network topology control and the rational allocation of channel resources, this paper establishes a network model and carries on the simulation analysis based on the ALPOCA algorithm, analyzes the interference effectively, uses the channel resources efficiently and increases the network throughput.

2. Introduction to wireless mesh network

The wireless Mesh network includes Mesh routers and Mesh clients. The former constitute the backbone network while the latter are peer nodes which can be directly connected to form multi-hop mobile ad hoc networks.

Wireless Mesh network has the following characteristics:

- Using fewer wires means that the cost of building a network is lower.

- The more nodes installed, the faster the wireless network.

- Dependent on the WiFi standard (802.11a, b and g) which has been applied to almost all wireless networks.

- Convenient in places where Ethernet wall connections are inadequate - such as outdoor concert venues, warehouses or outdoor transport facilities.

Mesh network is "self-configuring" [7] and "self-repairing" [8] in the sense that it can seek the rapidest and most trustworthy path to send data even if the node is blocked or loses signal.

According to the different functions of nodes, the wireless Mesh network can be divided into the infrastructure Mesh network, the client Mesh network and the hybrid Mesh network. The infrastructure Mesh network router nodes constitute the Mesh backbone network through the interconnection, the client nodes communicate with each other through the router node. The client wireless mesh network architecture is shown in Fig. 1. In the network, each client node uses the peer-to-peer mode to communicate. All Mesh clients have self-organizing and self-configuring networking capabilities. Compared with other multi-hop networks, the client wireless mesh network has very flexible networking characteristics.

Hybrid Mesh network is the integration of the infrastructure Mesh network and the client Mesh network [9], whose underlying client nodes have two kinds of communication methods, i.e., access to the network through the router node or peer-to-peer communication. The flexible communication method of the client can avoid the congestion problem of the router to a certain extent. As a result, hybrid Mesh networks have greater network connectivity and higher network reliability.
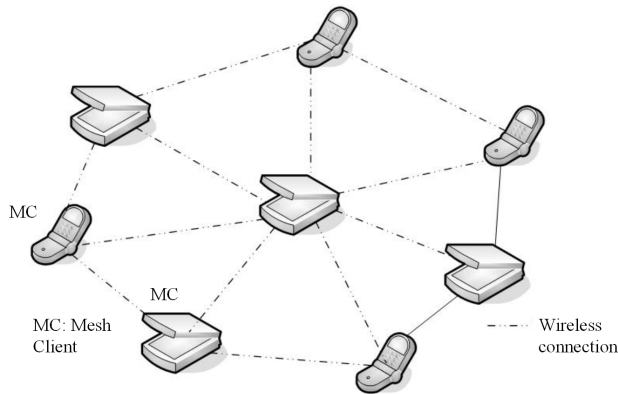
Fig. 1. Client Mesh network

3. Introduction to ALPOCA algorithm

At present, the tree topology is widely used in channel aggregation algorithm for traffic aggregation scenarios. For example, there are centralized channel allocation algorithm C-HYA (Centralized Hyacinth) and POCAM algorithm, mainly for the tree topology [10], but these algorithms have the following problems: first, the interference measure is inaccurate. Second, these algorithms are mainly for the scenes where topology is given, without considering the guarantee of connectivity in scenes without topology given. Third, the impact of traffic on channel allocation is not fully taken into account in these algorithms. In view of these problems, the author analyzes the bandwidth loss caused by different channel allocation in the network by ALPOCA algorithm, constructs the connected topology, and allocates the channels based on bandwidth loss and traffic characteristics to optimize the overall network capacity. Figure 2 shows the flow of the partially intersecting channel assignment algorithm ALPOCA for the traffic aggregation scenario.

3.1. Topology establishment

Before the implementation of the channel allocation algorithm, this paper establishes a wireless Mesh network architecture as the carrier of the channel allocation algorithm through the topology establishment process [11]. This paper pre-fixed network topological structures and links and the channel allocation algorithm was proposed to construct the connected topology first (see Fig. 3).

4. Algorithm simulation and result analysis

4.1. Simulation environment establishment

The simulation test of topology control and channel allocation algorithm is carried out in this part. In order to deploy the ALPOCA-based wireless Mesh network simu-
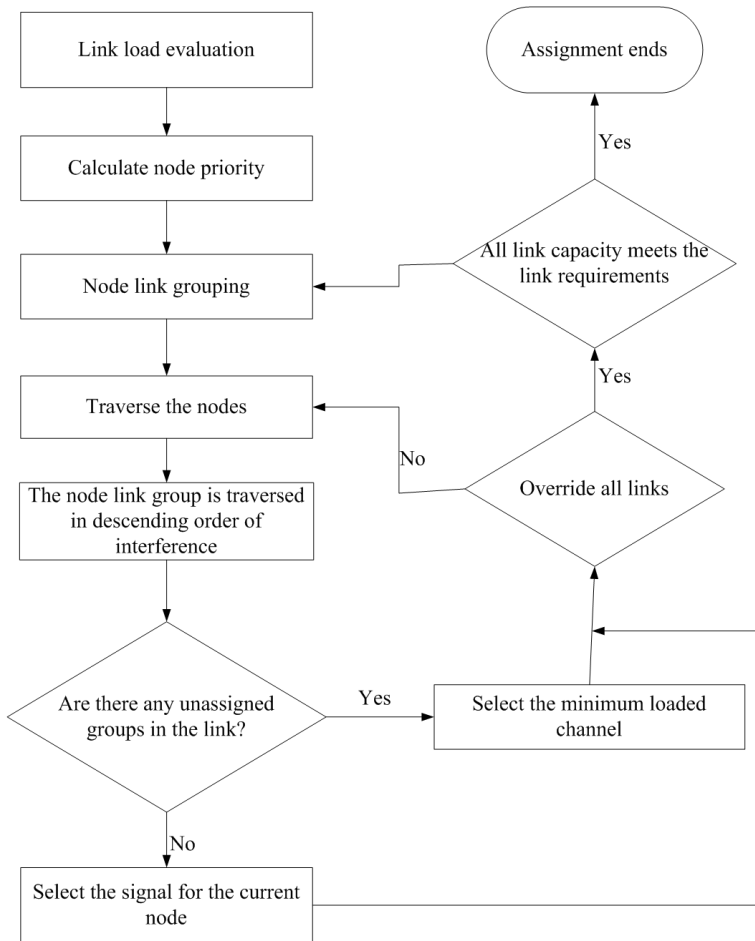
Fig. 2. ALPOCA algorithm flow chart

lation scene more vividly, we use the network scene generator designed by MATLAB to complete the deployment of the simulation scene. By configuring the parameters such as scene size, number of nodes, node location, node type of wireless propagation model, a simulation scenario that meets the expectations of the experimenter can be constructed.

4.2. Simulation platform workflow

This paper chooses NS3, a discrete event network simulator, as a simulation platform. NS3 is free software and is publicly available for research, development and use under the GNU GPLv2 license [12]. The project aims to create an open simulation environment for computer network research, which is widely used in the research community, meeting the simulation needs of modern network researches.
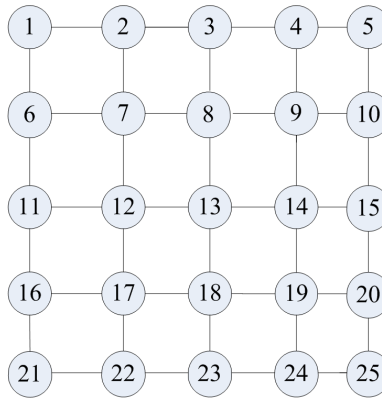
Fig. 3. Network topology diagram

The procedure of a simulation establishment covers the following steps.

- Topology definition: to simplify the construction of the infrastructure and determine its relationship, NS3 has a container and helper systems that can be used for this process.

- Model development: the model is added to the simulation system for node and link configuration; the model is set to its default value by the property system.

- Execution: simulation of infrastructure generation event and recording of data requested by the user.

- Analysis: apply tools for statistical analysis of these data to obtain conclusion.

- Graphic visualization: draw the raw or processed data collected during the simulation using tools such as Gnuplot, matplotlib, or XGRAPH.

We suppose that every node has two interfaces, namely, a fixed interface and a switchable interface [13]. The former adjusts the duration of a packet on the specified channel and is mainly used for receiving the packet. The latter can be frequently switched between the remaining non-fixed channels.

Interference between channels of two links connecting to a single node is crucial in multi-channel allocation. Since the distance between the two links is 0, the two links connected to the same node seriously interfere with each other. For the initial stage of channel allocation, the network traffic load information is unknown. Thus, the degree of overlap between channels is considered to be the only factor interfering measurement [14].

4.3. Simulation results and analysis

Because network performance is affected by traffic convergence, the increase in send rate allows the throughput to reach a saturation stable value after rising. The

simulation results show that ALPOCA throughput is roughly stable at 64 kbps and
CLTE throughput is roughly stable at 52 kbps. Besides, ALPOCA throughput in-
creased by 20.3 % compared with CLTE, see Fig. 4.
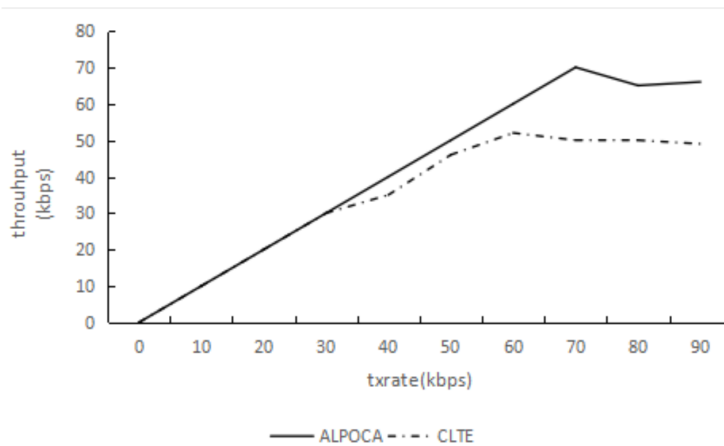
Fig. 4. Throughput comparison

At the beginning, the delay of these two algorithms grows slowly. When the
sending rate exceeds a certain value, the ALPOCA latency was reduced by about
21.0 % relative to CLTE. Compared to the CLTE algorithm using only orthogonal
channels (see Fig. 5), the partial intersecting channel allocation algorithm based on
traffic aggregation scenarios ALPOCA (Aggregate Load based Partially Overlapped
Channel Assignment) can effectively optimize throughput and latency.
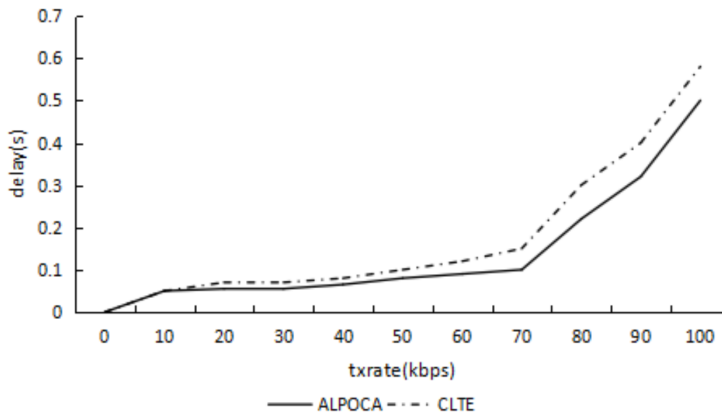
Fig. 5. Delay comparison

In this paper, the performance of ALPOCA algorithm and CLTE algorithm is
analyzed and compared, and the influence of different number of nodes and number
of gateways on the performance of wireless Mesh network is analyzed. It is found
that the ALPOCA optimization algorithm proposed in this paper has better network

performance than the CLTE algorithm which only considers the network's largest collision load. Nevertheless, whether the throughput performance of the algorithm is improved is to be further studied and improved.

5. Conclusion

Based on the ALPOCA algorithm, this paper studies the topology control and channel assignment as well as interference of wireless Mesh networks [15]. As the algorithm combines traffic conditions, it is superior to other algorithms in performance. ALPOCA performs noninterference channel assignment in units of link sets consisting of multiple links from the same parent node in the multicast tree. When there are multiple channels that meet the interference-free constraints, channels are assigned to the link set by maximizing the parent node channel spacing. After the uninterrupted channel assignment is complete, the ALPOCA assigns channels to the rest links in the multicast tree with the aim of reducing network interference [16]. ALPOCA can solve the hidden channel problem, while avoiding the impact of random distribution channels on the network performance.

Because of the limitation of time and conditions, the proposed algorithm is still in the theoretical research and simulation stage. In future studies, the algorithm will be applied to the Mesh network test bench according to the actual situation to actually verify its improvement to network performance.

References

[1] P. H. PATHAK, R. DUTTA: *A survey of network design problems and joint design approaches in wireless mesh networks.* IEEE Communications Surveys & Tutorials *13* (2011), No. 3, 396–428.

[2] I. F. AKYILDIZ, X. WANG, W. WANG: *Wireless mesh networks: A survey.* Computer Networks *47* (2005), No. 4, 445–487.

[3] D. WU, S. H. YANG, L. BAO, C. H. LIU: *Joint multi-radio multi-channel assignment, scheduling, and routing in wireless mesh networks.* Wireless Networks *20* (2014), No. 1, 11–24.

[4] M. KODIALAM, T. NANDAGOPAL: *Characterizing the capacity region in multi-radio multi-channel wireless mesh networks.* International conference on Mobile computing and networking MobiCom'05, 28 August–2 September 2005, Cologne, Germany, Proceedings ACM New York (2005), 73–87.

[5] R. SRINIVASAN, D. M. BLOUGH: *Throughput optimization in MIMO mesh networks.* International workshop on Wireless network testbeds, experimental evaluation and characterization WiNTECH'11, 19–19 September 2011, Las Vegas, NV, USA, Proceedings ACM New York (2011), 101–102.

[6] N. HAGHIGHIZADEH, A. MOHAMMADI: *Characterization of wireless mesh backhaul networks with MIMO systems.* International Symposium on Telecommunications, 27–28 August 2008, Tehran, Iran, Proceedings IEEE Conferences (2008), 388–392.

[7] J. BEN-OTHMAN, L. MOKDAD, M. O. CHEIKH: *On improving the performance of IEEE 802.11s based wireless mesh networks using directional antenna.* Local Computer Network Conference LCN, 10–14 October 2010, Denver, CO, USA, Proceedings IEEE Conferences (2010), 785–790.

[8] M. PAN, H. YUE, P. LI, Y. FANG: *Throughput maximization of cooperative wireless*

mesh networks using directional antennas. International Conference on Communications in China (ICCC), 15–17 August 2012, Beijing, China, Proceedings IEEE Conferences (2012), 709–714.

[9] A. MISHRA, V. SHRIVASTAVA, S. BANERJEE, W. ARBAUGH: *Partially overlapped channels not considered harmful.* International conference on Measurement and modeling of computer systems, 26–30 June 2006, Saint Malo, France, ACM SIGMETRICS - Performance Evaluation Review *34* (2006), No. 1, 63–74.

[10] B. JAUMARD, A. VORUGANTI, M. KADDOUR: *Assigning and scheduling partially overlapping channels in wireless mesh networks.* International Conference on Wireless and Mobile Computing, Networking and Communications (WiMob), 7–9 October 2013, Lyon, France, Proceedings IEEE Conferences (2013), 394–401.

[11] M. JAHANSHAHI, M. DEHGHAN, M. R. MEYBODI: *A mathematical formulation for joint channel assignment and multicast routing in multi-channel multi-radio wireless mesh networks.* Journal of Network and Computer Applications *34* (2011), No. 6, 1869–1882.

[12] X. LIU, J. LUO: *Joint channel assignment and link scheduling for wireless mesh networks: Revisiting the partially overlapped channels.* Annual IEEE International Symposium on Personal, Indoor and Mobile Radio Communications, 26–30 September 2010, Instanbul, Turkey, Proceedings IEEE Conferences (2010), 2063-2068.

[13] G. ZENG, B. WANG, Y. DING, L. XIAO, M. MUTKA: *Efficient multicast algorithms for multichannel wireless mesh networks.* IEEE Transactions on Parallel and Distributed Systems *21* (2010), No. 1, 86–99.

[14] A. RANIWALA, K. GOPALAN, T. C. CHIUEH: *Centralized channel assignment and routing algorithms for multi-channel wireless mesh networks.* ACM SIGMOBILE Mobile Computing and Communications Review *8* (2004), No. 2, 50–65.

[15] G. BIANCHI: *Performance analysis of the IEEE 802.11 distributed coordination function.* IEEE Journal on Selected Areas in Communications *18* (2000), No. 3, 535–547.

[16] P. CHATZIMISIOS, V. VITSAS, A. C. BOUCOUVALAS: *Throughput and delay analysis of IEEE 802.11 protocol.* IEEE International Workshop on System-on-Chip for Real-Time Applications, 30–31 October 2002, Liverpool, UK, Proceedings IEEE Conferences (2002), 168–174.

Cloud computing resource scheduling method based on improved particle swarm optimization and ant colony algorithm

Pan Li[1]

Abstract. In the cloud computing environment, the number of users is huge, and the total number of tasks submitted by users is very large. The key to cloud computing research is how to schedule these massive tasks and make them efficiently and reasonably. In view of the characteristics of cloud computing environment, the particle swarm optimization (PSO) and ant colony optimization are improved, and based on both, we proposed a task scheduling algorithm. The algorithm uses the improved particle swarm optimization algorithm to perform the previous iteration. After the iteration is completed, a certain number of fine particles are selected to generate the initial pheromone of the ant colony algorithm. The ant colony algorithm uses the initial pheromone generated to perform the post-iteration, and the final task scheduling result is obtained. The stimulation results show that this algorithm is superior to PSO and ant colony algorithm, and the total completion time and cost of the task are significantly reduced, which is an efficient scheduling algorithm.

Key words. Cloud computing, resource scheduling, particle swarm optimization, ant colony algorithm, integration.

1. Introduction

Cloud computing is a commercial realization of the integration of network technologies and traditional computer such as distributed computing, virtualization, network storage and the like. In order to enable the system to process service requests quickly, generate service instances and return service data, how to schedule tasks efficiently and reasonably in the cloud and realize the global optimization system have become the focus and difficulties of cloud computing research [1]. Under cloud environment, task scheduling is a NP complete problem [2]. Heuristic intelligent algorithm is generally considered as an optimal algorithm to solve the

---

[1]Personnel Division, Zhengzhou Institute of Technology, Zhengzhou, Henan, 450044, China

NP complete problem. The search process is more complex, but has better performance. Compared with the traditional algorithm, it has incomparable superiority. At present, there is more mature resource scheduling algorithms based on Genetic Algorithm (GA) [3], Ant Colony Optimization (ACO) [4] and Particle Swarm Optimization (PSO) [5] Strategy, etc. Huang [6] proposed a cloud computing task scheduling strategy based on genetic algorithm to reduce the maximum task completion time. Gao [7] proposed a cloud computing task scheduling algorithm based on ant colony algorithm, which takes into account the performance attributes of the computing node and the task response capability of the node under load pressure. Shao [8] proposed a cloud computing resource scheduling strategy based on improved Particle Swarm Optimization (PSO) algorithm for cloud computing service cluster resource scheduling and load balancing. Ge [9] used genetic algorithm scheduling cloud computing tasks, and achieved relatively better experimental results. This paper proposes a cloud computing resource scheduling method based on improved particle swarm optimization algorithm and ant colony algorithm to speed up the convergence and shorten the task execution time, so that it can effectively improve the efficiency of task scheduling.

2. Description of cloud computing resource scheduling problem

Cloud computing task scheduling problem can be described as: in the cloud environment, n independent tasks are assigned to m resource node execution ($m < n$). Here, the task set is expressed as $T = \{t_1, t_2, ..., t_n\}$, the resource node set is expressed as $VM = \{vm_1, vm_2, \cdots, vm_m\}$, $t_j (j = 1, 2, ..., n)$ represents the jth task, and $vm_i, \ (i = 1, 2, ..., m)$ represents the ith resource. Each task can only be executed on one resource. The assignment relation between task set $T = \{t_1, t_2, ..., t_n\}$ and resource node set $VM = \{vm_1, vm_2, \cdots, vm_m\}$ can be represented by a matrix X as

$$X = \begin{pmatrix} x_{11} & x_{12} & ... & x_{1n} \\ x_{21} & x_{22} & ... & x_{2n} \\ ... & ... & & ... \\ x_{m1} & x_{m2} & & x_{mn} \end{pmatrix}, \tag{1}$$

where, x_{ij} represents the assignment between task t_j and resource vm_i, $x_{ij} \in [0, 1]$, $\sum_{i=1}^{m} x_{ij} = 1$, $i \in \{1, 2, ..., m\}$, $j \in \{1, 2, ..., n\}$, if task t_j is executed on resource vm_i, $x_{ij} = 1$, otherwise $x_{ij} = 0$. ETC_{ij} is the expected execution time of task t_j in resource vm_i. Corresponding to the distribution of tasks and resources matrix X, we can form the matrix ETC as

$$\text{ETC} = \begin{pmatrix} \text{ETC}_{11} & \text{ETC}_{12} & ... & \text{ETC}_{1n} \\ \text{ETC}_{21} & \text{ETC}_{22} & ... & \text{ETC}_{2n} \\ ... & ... & & ... \\ \text{ETC}_{m1} & \text{ETC}_{m2} & & \text{ETC}_{mn} \end{pmatrix}. \tag{2}$$

Further, b_j is the start time of task t_j, $CT_{ij}, \ (i \in \{1, 2, \cdot, m\}, \ j \in \{1, 2, \cdot, n\})$ is the

expected completion time of t_j in resource vm_i, $CT_{ij} = b_j + \text{ETC}_{ij}$. The maximum value of CT_{ij} is the total task completion time. Finally, $C_{\max} = \max(CT_{ij})$ is the adaptation of the schedule.

3. The design of cloud computing task scheduling

3.1. Particle Swarm Optimization

According to the basic process of the realization of the particle swarm optimization algorithm, the algorithm's overall improvement ideas are mainly concentrated on the following several points: according to the fitness of the particles to choose good particles, eliminate the poorly adapted of the particles; the inertia factor η, individual learning factor α and group learning factor β are adjusted reasonably; the particle swarm optimization algorithm is optimized by a penalty function.

3.1.1. Filter of the particles The fitness function of particle in this particle swarm is defined as

$$\text{fit}(i) = \frac{1}{\min\{T(i)\}} + \frac{1}{\min\{C(i)\}}, \tag{3}$$

where i represents the $i-th$ resource in the cloud environment resource, $T(i)$ represents the time overhead of the task on the resource i, and $C(i)$ represents the cost of the task on the resource i.

The constraint function is defined as

$$\text{constraint}(i) = \sum_{j=1}^{h} \max(0, g_j(x)) + \sum_{p=1}^{r} |h_p(x)|, \tag{4}$$

$$\text{s.t.} \quad \begin{cases} g_j(x) \geq 0, \ j = 1, 2 \ldots h, \\ h_p(x) = 0, \ p = 1, 2 \ldots r. \end{cases}$$

The constraint function $\text{constraint}(i)$ contains the constraints of the problem used, which is composed of all the constraints, $g_j(x) \geq 0$ is the inequality constraint, and $h_p(x)$ is the equality constraint. The value of the constraint function reflects the degree of the particle distance boundary and the larger the value of the constraint function is, the more particles should be eliminated.

Considering the fitness value of the particle and the constraint value of the particle, the strategy of selecting particles is as follows:

1. According to the objective function, the initial fitness of all the particles in the particle swarm is calculated, and the fitness value of all the particles is sorted.

2. The constraint function is formulated to calculate the constraint value of all the particles in particle swarm.

3. According to the actual situation of particle elimination, the particle elimination is carried out, and the elimination of the undesirable particles is completed

by combining the values of the functions fit(i) and the values of the constraint(i) results. The specific process is to set the particles whose initial fitness value is sorted as the first $\varepsilon\%(\varepsilon > 0)$ to be eliminated, that is, if the initial fitness value of the ith particle is ranked before $\varepsilon\%$, the particle is eliminated, otherwise, the next round of screening is performed. The rest of the particles are sorted again by the value of for screening: set a value δ ($\delta > 0$) representing the maximum violation of the constraints of the limit value. If $\delta <$ constraint(j), then the particle j is eliminated.

3.1.2. Parameter adjustment Particle swarm parameters have a huge impact on the performance of PSO. The influence of inertia factor η on the performance of the algorithm is very direct. The smaller the value η, the better the convergence of the algorithm. The larger the value is, the better is the local optimality. The individual learning factor α_1 affects the optimal search of particles. The group learning factor β_1 affects the optimal search of groups. To make the algorithm converge quickly and efficiently, the parameters η, α_1, β_1 need to be effectively and dynamically adjusted. In this paper, three parameters are dynamically adjusted to adjust the current value and incremental value respectively.

The adjustment formula for the inertia factor reads

$$\eta = \eta + \frac{2\eta_{\mathrm{best}} - (\eta_{\min} + \eta_{\max})}{2(\eta_{\max} - \eta_{\min})} \, , \tag{5}$$

where $\eta_{\max}$ and $\eta_{\min}$ are the maximum and minimum values of η, respectively, η_{best} is the measure of the current η best performance and $\frac{2\eta_{\mathrm{best}} - (\eta_{\min} + \eta_{\max})}{2(\eta_{\max} - \eta_{\min})}$ is the inertia increment.

The adjustment formula for individual learning factor α_1 reads

$$\alpha_1 = \alpha_1 + \frac{\varphi}{N} \, , \tag{6}$$

where φ/N is an increment of individual learning factor, which is related to the group size N. The larger the particle swarm size is, the more the individuals are related to each other, the more knowledge they learn, and the more difficult they are. Symbol φ denotes the constant coefficient of individual learning increment, and its value is small.

The adjustment formula for individual learning factor β_1 reads

$$beta_1 = \beta_1 + \frac{\psi}{N} \, , \tag{7}$$

where ψ/N is the group learning factor increment, which is related to the group size N. The larger the particle swarm size is, the more complicated the individual relationship in the group is and the more difficult it is to learn. Symbol ψ denotes the constant coefficient of group learning increment, and its value is small.

3.1.3. Optimization processing The general form of optimization problem with constraints can be expressed as

$$\min f(x), \tag{8}$$

$$\text{s.t.} \quad \begin{cases} g_j(x) \geq 0, j = 1, 2 \ldots, q, \\ \\ h_p(x) = 0, p = 1, 2 \ldots, m, \end{cases}$$

The general form of conversion into unconstrained conditions:

$$F(x, c) = f(x) + c \left(\sum_{j=1}^{q} (\max(0, g_j(x)))^2 + \sum_{p=1}^{m} (h_p(x))^2 \right), \tag{9}$$

where c is the penalty factor, which is given a very large value; $g_j(x) >\geq 0$ is the set of inequality constraints, and $h_p(x) = 0$ is the set of equality constraints.

3.2. Ant Colony Algorithm

3.2.1. Pheromone initialization The initial value of pheromone is set as

$$\tau_{\mathrm{s}} = \tau_{\mathrm{c}} + \tau_{\mathrm{g}}, \tag{10}$$

where τ_{c} is a given pheromone constant and τ_{g} is a pheromone value converted from the scheduling result of the previous particle swarm optimization algorithm. The specific method is to select the top $10\,\%$ individuals with the best fitness value in the group when the PSO algorithm is terminated as the optimal solution set. At the beginning, set τ_{g} to 0, and for each solution in the optimal solution set τ_{g} adds a constant k.

3.2.2. Path selection The probability of the kth ant moving from resource node i to resource node j at time t is set as

$$p_{ij}^{k}(t) = \left(\begin{array}{c} \frac{[\tau_{ij}(t)]^{\alpha_2}[\eta_{ij}(t)]^{\beta_2}}{\sum_{s \in \text{allowed}_k}[\tau_{is}(t)]^{\alpha_2}[\eta_{is}(t)]^{\beta_2}}, \ j \in \text{allowed}_k, \\ \\ 0 \ \ else. \end{array} \right), \tag{11}$$

where $\text{allowed}_k = C - \text{tabu}_k$ represents the resource node allowed by ant k at time $t + 1$, tabu_k represents the tabu list, and saves the resource that ant k has searched for, η_{ij} represents the heuristic information, τ_{ij} represents the amount of residual information, α_2 and β_2 represent the relative importance of residual information and elicitation information, respectively to the ant colony optimization process.

The value of η_{ij} is

$$\eta_{ij} = \frac{1}{\text{ETC}_{ij}^{k}} = \frac{1}{\text{ETC}_{kj}}. \tag{12}$$

3.2.3. Update pheromones When ant k is transferred from one node i to another node j, the pheromone of the node changes. The timely update of pheromone helps to improve the accuracy of the ant colony algorithm. Equation (13) and (14) give the method of local updating pheromones:

$$\tau_{ij}(t+1) = (1-\rho)\tau_{ij}(t) + \sum_{k=1}^{\alpha_2} \Delta\tau_{ij}^k(t)\,, \tag{13}$$

$$\Delta\tau_{ij}^k(t) = \begin{cases} \frac{Q}{\text{ETC}_{ij}^k(t)} = \frac{Q}{\text{ETC}_{kj}}\,, \text{the } k\text{th ant chooses } x_{ij} \text{ between } t \text{ and } t+1\,, \\ 0 \ \ \text{else} \end{cases}$$
$$\tag{14}$$

Here, symbol ρ denotes a random number between 0 and 1 that represents pheromone volatility coefficient, $1-\rho$ is the pheromone residual coefficient, $\Delta\tau_{ij}^k$ is the number of pheromones that ant k leaves on the path in the current path transfer and Q is a constant.

When all the ants complete a loop, the pheromone should be globally updated with the following formula:

$$\tau_{ij}(t+n) = (1-\rho)\tau_{ij}(t) + \sum_{k=1}^{\alpha_2} \Delta\tau_{ij}^k(t)\,, \tag{15}$$

$$\Delta\tau_{ij}^k(t) = \begin{cases} \frac{Q}{\text{resourceTime}(j)}\,, \text{the } k\text{th ant chooses } x_{ij} \text{ in this cycle} \\ 0 \ \ \text{else}\,. \end{cases} \tag{16}$$

4. Simulation analysis

In this paper, we use CloudSim platform to simulate cloud environment, and compare the proposed algorithm with standard ACO algorithm and standard PSO algorithm. For the improved Particle Swarm Optimization algorithm, after many simulations, we find that the algorithm works best when the inertia coefficient, individual learning factor $\alpha_1 = 1.5$, group learning factor $\beta_1 = 2.5$. In this simulation, each algorithm runs 20 times repeatedly and the result is as follows.

5. Experimental results

Figures 1 and 2 show the task completion time of ACO algorithm, PSO algorithm and our algorithm when the node resource is 10 and the number of tasks is 50 and 500, respectively. It can be seen from the figures that the task scheduling algorithm proposed in this paper combines the fast convergence ability of PSO and the optimum ability of ACO.

When the node resource is 10 and the number of tasks is 50, 100, 150, 200, 250 and 300 respectively, the total task execution cost of the ACO algorithm, the PSO

algorithm and the algorithm in this paper is compared as shown in Fig. 3.

The algorithm proposed in this paper is lower than the other two algorithms in terms of completion time and cost, which shows that the algorithm has relatively good superiority and can further meet the resource scheduling requirements in cloud computing.
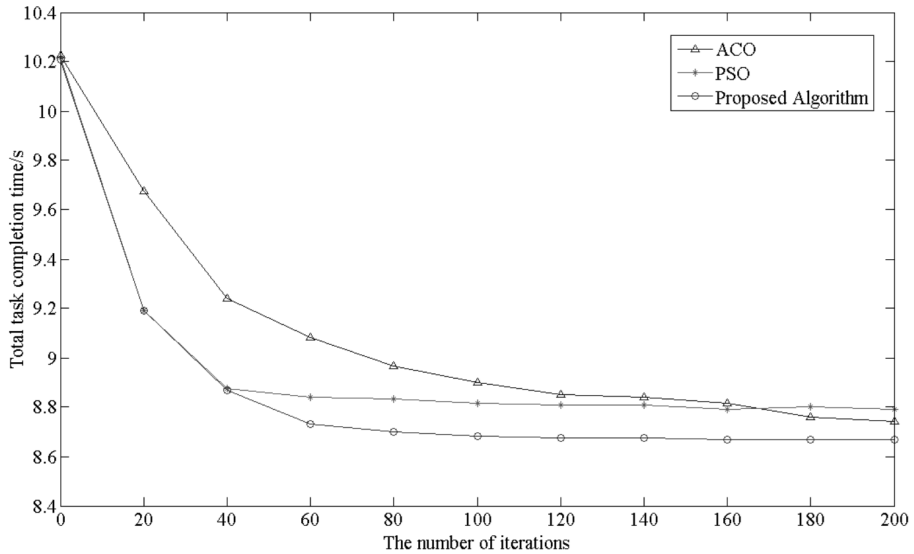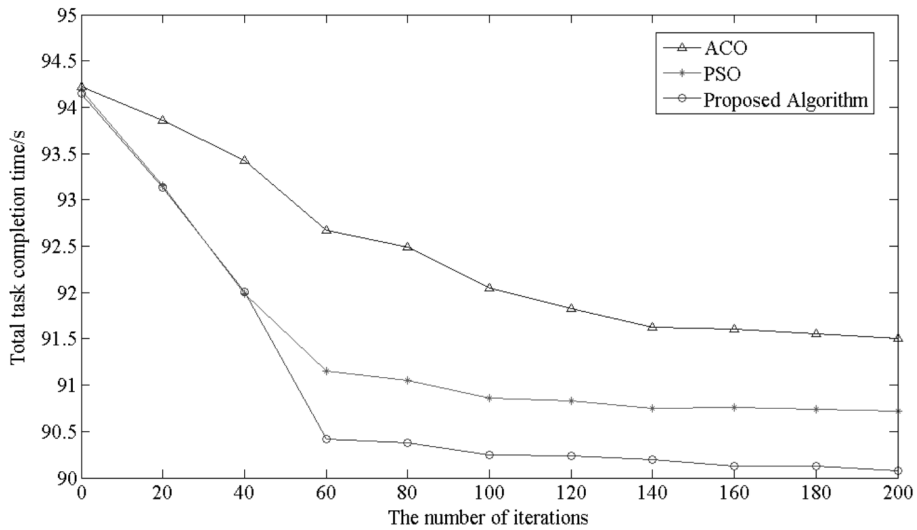

Fig. 1. Total completion time of 50 tasks

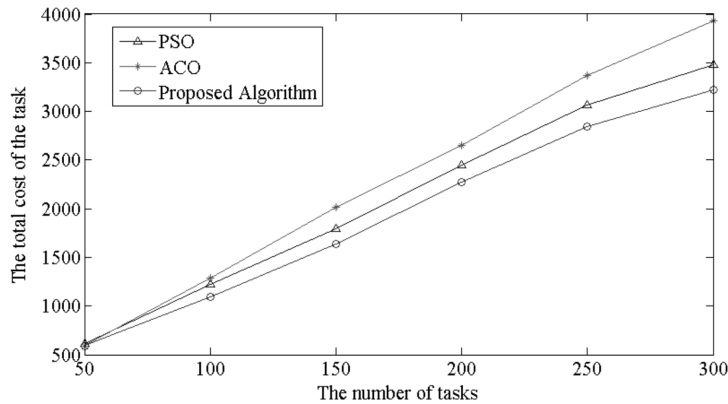Fig. 2. Total completion time of 500 tasks

Fig. 3. Cost of different tasks

6. Conclusion

In this paper, we proposed a cloud computing resource scheduling method based on improved particle swarm optimization and ant colony algorithm for cloud computing task scheduling problem. Firstly, we described a task scheduling problem of cloud computing, and then used the improved particle swarm optimization algorithm and ant colony algorithm to solve the cloud computing task scheduling problem. Finally, we tested the proposed method on Cloudsim platform. The simulation results show that the improved algorithm proposed in this paper can find a better scheduling solution for cloud computing tasks, accelerate the completion of cloud computing tasks and reduce costs, and it is an excellent algorithm for solving cloud computing task scheduling problems.

References

[1] J. Li, Q. Wang, C. Wang, N. Cao, K. Ren, W. Lou: *Fuzzy keyword search over encrypted data in cloud computing.* Proc. INFOCOM'10 Proceedings of Conference on Information Communications, 14–19 March 2010, San Diego, CA, USA, IEEE Press Piscataway, NJ, USA (2010), 441–445.

[2] F. Wang, M. Li, W. Daun: *Cloud computing task scheduling based on dynamically adaptive ant colony algorithm.* Journal of Computer Applications *33* (2013), No. 11, 3160–3162.

[3] S. Hartmann: *A competitive genetic algorithm for resource-constrained project scheduling.* John Wiley & Sons, Inc., Naval Research Logistics (NRL) *45* (1997), No. 7, 733–750.

[4] M. Kefayat, A. Lashkar Ara, S. A. Nabavi Niaki: *A hybrid of ant colony optimization and artificial bee colony algorithm for probabilistic optimal placement and sizing of distributed energy resources.* Energy Conversion and Management *92* (2015), No. 3, 733–750.

[5] Y. Zhang, S. Wang, G. Ji: *A comprehensive survey on particle swarm optimization algorithm and its applications.* Mathematical Problems in Engineering *2015* (2015), Article ID 931256.

[6] S. C. HUANG, M. K. JIAU, C. H. LIN: *A genetic-algorithm-based approach to solve carpool service problems in cloud computing.* IEEE Transactions on Intelligent Transportation Systems *16* (2015), No. 1, 352–364.

[7] R. GAO, J. WU: *Dynamic load balancing strategy for cloud computing with ant colony optimization.* Future Internet *7* (2015), No. 4, 465–483.

[8] Y. SHAO: *Virtual resource allocation based on improved particle swarm optimization in cloud computing environment.* International Journal of Grid and Distributed Computing *8* (2015), No. 3, 111–118.

[9] J. W. GE, Y. S. JUAN: *Research of cloud computing task scheduling algorithm based on improved genetic algorithm.* Applied Mechanics & Materials*347–350* (2013), No. 4, 2426–2429.

Research on improvement and application of big data mining algorithm for massive data

Yingmei Xu[1]

Abstract. Big data technology can excavate information and knowledge hidden in massive data, and provide basis for human social and economic activities, so as to improve operation efficiency in various fields and greatly improve the intensity of social and economic intensification. In this paper, the advantages and disadvantages of the traditional big data mining algorithms are analyzed, and an improved large data mining algorithm is proposed to solve these problems. The paper presents research on improvement and application of big data mining algorithm for massive data. Finally, the improved big data mining algorithm proposed in this paper is verified by experiments, and the experimental results show that the algorithm is effective.

Key words. Big data technology, data mining, decision tree, principal component analysis, distributed file system.

1. Introduction

In 21th century, the era of information explosion, the rapid development of computer technology, greatly facilitated the acquisition and storage of data, making many departments have a lot of data every day. Large data is usually from the source. Consolidation of data from different subjects or formats, such as survey data from different regions; financial data from different markets and so on. This modeling based on multiple data sets is very common. Understanding the heterogeneity and commonality of different sub-samples are two important targets of big data analysis, such as [1]. But its modeling is quite special. On one hand, because of the difference of data from different sources, the coefficient significance and estimation value of the same variable of different data sources may be different [2]. The traditional method is to simply merge all samples and set up a unified model, but this method is too general and neglects the heterogeneity of data. On the other hand, the models cannot be built separately because the correlation between the

---

[1]Department of Information Technology, Shangqiu Normal University, Shangqiu 476000, China

data sets is ignored.

Combination of decision tree is often also known as the random forest, it carried out in feature selection and build effective classifier is very useful [3]. A common dimension reduction method is to produce many big trees on the target attribute, and then according to the statistical results of each attribute to find the feature subset of the largest amount of information. For example, we are able to give a very large data sets generating very shallow level trees, each tree being only a small part of the training attribute. If the attribute often becomes the best splitting attribute, then it is likely to need to retain information characteristics. Statistical score of random forest data attribute will reveal to us compared with other properties, which the property is the best attribute prediction ability.

Big data analysis of the application and innovation in the financial field, such as relying on big data analysis to promote high-frequency trading, risk management, customer cross-behavior analysis. Internet financial structure and development model and development direction is it. According to the law of eight or two, 80 % of financial products will be standardized and popularized through Internet, mobile terminal and other technologies [4]. For example, credit card consumption records already contain information about the location of consumption; it can now be used by Internet finance. Financial industry is customer behavior analysis. Through big data the analysis of customer behavior can be realized. The realization of individualized and accurate customer service is helpful for enterprises to be more close to the innovative business model, to understand customer needs and to make advance judgments, so as to improve the management level and enhance the management efficiency.

2. Data analysis method based on big data

Big data is undoubtedly the most popular word of recent years. "Big data" was first proposed by the world's most famous consulting firm McKinsey, McKinsey view: big data is innovation. The next frontier of competition and productivity "can be used by big data to answer questions in areas that we have not been able to address before, and to gain knowledge and insights from them." Position trends and use these data to improve productivity and gain competitive advantage within the industry.

In general, the basic data analysis of time series data, which is in accordance with the storage time, has the data in the database. Time sequence prediction method can be used for short, medium and long term prediction. According to the analysis of the different data, and can be divided into: simple chronological average method, weighted average method sequence, moving average method, weighted moving average method, trend forecasting method, exponential smoothing method to predict seasonal trends, market life cycle prediction method. Due to a large number of time series is non-stationary, the characteristic parameters and data distribution change with time, therefore, only through a period of history data the training, establish the single neural network model, is unable to complete the modeling task accurately.

The main work of data preprocessing includes deleting empty records, deleting

abnormal record of call data (single call duration more than 10 hours), and clearing and marking part of the field value missing record. Through data cleaning and preprocessing, a total of 8916 valid users β are obtained, as is shown by equation (1).

$$\overset{\wedge}{\beta} = \arg \min_{\beta} \left\{ L\left(X, y, \beta\right) + P\left(\beta, \lambda\right) \right\}, \tag{1}$$

where X denotes multiple variables, λ is the research objective, and P stands for the interaction among different regions.

The integrative analysis method combines these two aspects and synthesizes the data of different regions through the objective function. Considering the heterogeneity and identity of the data from the statistical point of view, taking multiple variables as the research objective, the interaction between different regions is fully considered. At the same time, it is solving multiple models [5]. The integration analysis method originated in 1960s, the different sources, formats, characteristics of the data set together, compared with a single data set model, the integration of more original information. It can solve the instability of modeling caused by sample difference caused by region, time and other factors, and has significant advantages in model interpretation and prediction.

(1). To determine the evaluation index system is the basis of comprehensive evaluation. Attention should be paid to the comprehensiveness and systematization of the index system.

(2). Collect the data and measure the index value of different units of measurement with the same measure. The methods of relative treatment, functional treatment and standardized treatment can be used.

(3). Determine the weights of each index in order to ensure the scientific nature of the evaluation. According to the status of each index and the degree of impact on the overall, it is necessary to assign different weights to different indicators.

(4). The index is summarized, the comprehensive score is calculated, and the comprehensive evaluation is made accordingly.

While the acquisition end itself will have many databases, if you want to make an effective analysis of these mass data, you should import data from the front end into a centralized, large distributed database, or a distributed storage cluster, and you can do some simple cleaning and pre-processing on the import base. Some users will use Storm from Twitter to stream data to meet the real-time computing needs of some of the business. The features and challenges of importing and pre-processing are primarily the amount of data that is imported, and the import volume per second often reaches hundreds of megabytes, or even gigabits.

Principal component analysis (PCA) is a statistical process in which the original n-dimensional dataset is transformed into a new data set called principal component by orthogonal transformation. The first principal component has the largest square difference. Each subsequent component has the maximum variance under the condition of orthogonally with the aforementioned principal components. It is important to note that the principal component transformation is sensitive to the scale of orthogonal vectors. The data need to be normalized before the transformation [6]. The new principal component is not generated by the actual system, so the

interpretation of the data will be lost after the PCA transformation. If you say, the interpretation of the data is important for your analysis. Then PCA may not apply to you.

So what is big data? Big data, or huge amount of data, refers to the amount of data involved that is so large that it cannot be retrieved, managed, and processed within a reasonable amount of time through current mainstream software tools. Big data is a kind of business model and technology platform for the management and utilization of large-scale data, which is different from the traditional massive data. In addition to the geometric growth of data scale, it also includes the collection, classification, processing, analysis and presentation of all data types. So as to finally achieve the goal of excavating the potential huge value from is big data. There is no uniform definition of big data so far.

Clustering is similar to classification, but different from the purpose of classification, it is to divide a group of data into several categories according to the similarity and difference of data. However, the similarity between different categories of data is very small; cross-class data correlation is very low.

The mainstream market for big data comes from the early masses of pragmatism and the later days of conservatism. The two groups share $1/3$ share of the big data market. The common feature of the two groups is that they both have a good information technology foundation and a deep accumulation of big data. And understand the social and economic value of big data. The difference is that the former want to see mature solutions and successful applications, which are mostly financial and energy. Public services such as telecommunications, which require more secure big data security and a broad social application base, are mostly public administrations working on social issues such as the environment, energy and health.

Adopt Hadoop cluster disadvantage:

(1). With the design of single master, the design and implementation of the system greatly simplifies the design and implementation of the single master, which brings the problem of machine size limitation and single point failure.

(2). Programming is complex and the learning curve is too steep, making it difficult for many people to go deep [7].

$$
\begin{aligned}
V_j &= V_{j-1} \oplus W_{j-1} \\
&= V_{j-2} \oplus W_{j-2} \oplus W_{j-1} \\
&\quad \ldots \\
&= V_0 \oplus W_0 \oplus W_1 \oplus \ldots \oplus W_{j-2} \oplus W_{j-1} \,,
\end{aligned}
\tag{2}
$$

where V will greatly occupy the system resources, W denoting especially the I/O.

The main characteristic and challenge of this part of statistics and analysis is the large amount of data involved in the analysis, which will greatly occupy the system resources, especially the I/O. Mining is different from the previous statistical and analytical process. Data mining generally does not have any predefined topics, mainly on the existing data based on a variety of algorithms to calculate, so as to predict the effect of predict.

A typical algorithm for clustering K-means, for statistical learning for the clas-

sification of SVM and NaiveBayes, the main use of the tool is Hadoop Mahout [8]. The characteristics and challenges of the process is mainly used for mining algorithm is very complex, and involves the calculation of the amount of data and computing are large, commonly used data mining algorithms are based on a single thread.

High correlation filtering assumes that when two columns of data have similar trends, the information they contain also shows. This is the case. The machine learning model can be satisfied by using one of the similar columns. The similarity between the numerical columns is expressed by calculating the correlation coefficient. For noun column correlation coefficient can be expressed by calculating Pearson chi-square value. Only one column is reserved for two columns whose correlation coefficient is greater than a certain threshold. It is also important to note that correlation coefficient is sensitive to range. So we also need to normalize the data before computing, as is shown in equation (3).

$$p\left(\beta,\lambda,\gamma\right) = \lambda \sum_{j=1}^{p} \|\beta_j\|^{\gamma} = \lambda \sum_{j=1}^{p} \left(\left(\sum_{i=1}^{M} \left(\beta_j^{(i)} \right)^2 \right)^{\frac{1}{2}} \right)^{\gamma}. \tag{3}$$

For big data, p is the characteristics, while λ denotes general consideration that PB data is the starting point of big data. There are many data types. It can be traditional structured data with causality, such as relational database data. But more is the low value density of semi-structured and unstructured data, such as web logs, videos, pictures, geographical location information, etc. Big data contains a lot of value, but the value density is very low. It is often necessary to mine and analyze huge amounts of data in order to obtain useful information, thus generating value. For example, in the continuous monitoring process of video, the useful data is only 12 seconds.

As an advanced artificial intelligence technology, neural network is very suitable to deal with nonlinear problems due to its own self-processing, distributed storage and high fault tolerance, and it is very suitable to solve the problem of data mining.

The typical neural network models are divided into three categories: the first is the feed forward neural network model for classification prediction and pattern recognition, which is mainly represented by functional network and perception. The second one is a feedback neural network model for associative memory and optimization algorithms, represented by Hopfield's discrete model and continuous model, and the third is a self-organizing mapping method for clustering. Although neural networks have many models and algorithms, there are no uniform rules about which models and algorithms are used in data mining in specific fields. Moreover, it is difficult to understand the learning and decision-making process of the network.

3. An improved algorithm for big data mining

Classification and prediction are two methods of analyzing data that can be used to extract models that describe important data sets or predict future data trends. The classification method is used to predict the discrete categories of the

data objects, while the prediction is used to predict the continuous value of the data objects. Many classification and prediction methods have been proposed by researchers such as machine learning, expert system, statistics and neurobiology. Most of these algorithms are resident memory algorithms, usually assuming that the amount of data is small. Most of the initial data mining methods are based on these methods and memory based algorithms.

Internet finance is a concept developed on the basis of the Internet and big data, with the arrival of big data era. The accumulation of large amounts of data and the continuous improvement of data processing ability promote the development of the Internet financial industry. Internet finance is not a simple combination of the Internet and the financial industry, but the realization of security. Mobile and other network technology level, and it is by the user familiar with the acceptance.

Industry indicator data: telecom industry income, mobile phone penetration rate; Competition data, mainly with telecom companies and Unicom competition index data, such as the number of customers per company, the number of Internet users, mobile phone user penetration of ARPU, and so on; These competition data mainly come from the manual input of the regional managers of Xinjiang Mobile Branch; Business data, mainly refers to the Xinjiang Mobile Branch of the history of business data, such as personal customer mining data, call customer business data, voice business data, data flow business data [9]. Group customer business data; Network resource class data, refers to wireless resources and transmission network resources related to data; Comprehensive data, refers to human resources data, such as the number of employees; Market resource data, such as the number of channels; Financial data, such as operating income, sales expenses, labor costs, etc.

For this reason, people put forward a retraining method based on statistics and accuracy. When it is found that the existing model is no longer applicable to the current data, the model is retrained to obtain new weight parameters. The new model can also be used to analyze the computational advantages of parallel algorithms according to the size of the problem.

$$P_{\text{MCP}}(\theta, \lambda, \alpha) = \begin{cases} \lambda\theta - \frac{\theta^2}{2\alpha}, & \theta \leq \alpha\lambda \\ \frac{\alpha\lambda^2}{2}, & \theta > \alpha\lambda \end{cases} \quad P'_{\text{MCP}}(\theta, \lambda, \alpha) = \begin{cases} \lambda - \frac{\theta}{\alpha} & \theta \leq \alpha\lambda \\ 0, & \theta > \alpha\lambda. \end{cases} \quad (4)$$

Here, P_{MCP} is found that the existing model λ is no longer applicable to the current data and the model θ is retrained to obtain new weight parameters. Most of the simulation data are collected by software, which belongs to the data of fine time and space granularity. That is to say, the author can collect the location data of the user during the continuous period of the day. Reference [10] and others focus on the locations that often appear in the user location data.

In 2020, medical data will increase to 35ZB, which is 44 times the amount of data in 2009. In addition, in hospitals, each patient has not only the personalized diagnosis and treatment of syndrome differentiation, but also the diagnosis of diseases and their prognosis through various physical and chemical tests. Therefore, there X will be biochemical examination, biological information of various images or pathological

sections, and the data types are very complicated. This poses great challenges to the storage, as is shown in equation (5), where X represents the analysis and w denotes processing and transmission of data.

$$
\begin{bmatrix} X_{M-1}^{\mathrm{T}} & X_{M-2}^{\mathrm{T}} & \cdots X_1^{\mathrm{T}} \end{bmatrix}
\begin{bmatrix} w_{M-1} \\ w_{M-2} \\ \vdots \\ w_1 \end{bmatrix} = X_M^{\mathrm{T}} \; .
\tag{5}
$$

One of the characteristics of the penalty function is that the inter-group penalty function has the function of variable selection, and the second feature is that the function of variable selection can only be compressed within the group. The Ridge penalty functions (see [11]) are usually used in the group, which can not compress the coefficient to zero. These two characteristics are also the principle of realizing group selection without selection within the group [12]. The difference with single data set is that the group of integrated analysis is the same variable on different data sets. Multiple regression coefficients. Each group has only one explanatory variable, and the latter group is composed of multiple virtual variables or explanatory variable groups.

$$
R_{\mathrm{f}} = u_{\mathrm{f}} u_{\mathrm{f}}^{\mathrm{H}} =
\begin{bmatrix}
r(0) & r(1) & \cdots r(M-1) \\
r(1) & r(0) & \cdots r(M-2) \\
\vdots & \vdots & \vdots \\
r^*(M-1) & r^*(M-1) & r(0)
\end{bmatrix}
\tag{6}
$$

Here, R belongf to time series analysis, u_{f} is predicted according to the causality and r is the relationship of mutual influence among the indexes, where M belongs to the regression analysis. Statistical forecasting belonging to quantitative prediction is based on data analysis, in the prediction of qualitative analysis. Statistical forecasting methods can be divided into two categories: one is to predict the dependency relation according to the main index of time series variation with time, belong to time series analysis; the other is predicted according to the causal relationship of mutual influence among the indexes, which belongs to the regression analysis.

For enterprises, our country can handle large data enterprises not many, this is mainly because domestic enterprises are relatively weak in the fields of database, data warehouse and business intelligence. But as domestic enterprises in the forefront of big data industry, technical level can reach a higher level, such as Yonghong technology has core competitiveness in the fields of big data, distributed computing, data analysis and so on

4. Research on improvement and application of big data mining algorithm for massive data

At present, more and more Web data are in the form of data flow. Therefore, it is very important for Web data stream mining. These problems are still worth studying and solving.

Every unstructured data can be considered big data. This includes data on social networking sites, online financial transactions, corporate records, weather monitoring data, satellite data and other surveillance. Big data storage and management must use memory to store the collected data, set up the corresponding database, and manage and call. Semi-structured and unstructured big data management and processing technology. It mainly solves several key problems of big data, such as storage, representability, processability, reliability and efficient transmission.

$$P(\beta, \lambda) = \lambda \sum_{1 \leq j,k \leq p} a_{jk} \left(\frac{\|\beta_j\|_2}{\sqrt{M_j}} - \frac{\|\beta_k\|_2}{\sqrt{M_k}} \right)^2 \tag{7}$$

For a large amount of data accumulated in the financial industry, big data analysis can be just with the analysis function of the unique data mining valuable information, a new mode of development of the financial industry and the new business in order to adapt to the new needs of customers. And the precision of the personalized service is mainly to the customer as the center, through the improvement of customer service and in-depth customer analysis to meet the different needs of different customers. With the development of market economy, competition in the financial market is becoming increasingly fierce, consumers tend to be more diversified, more personalized, enterprises should change the traditional sales model, the use of computer technology and information technology, demand-oriented pricing respectively according to the different needs of the consumer and the price elasticity.

Different from the isomorphic data model, the significance of the explanatory variables in the heterogeneous data model is not necessarily the same, that is, for a given data model, it can not be completely equal, and the heterogeneous data model is more general. Isomorphic data models can be regarded as special cases of heterogeneous data models. There are usually two reasons for the inconsistency of variables in these models: one is the way the data sets are generated (or environmental factors). There was significant difference between the variables. Such as different regions, different data sets at different points in time; The second is to study the subdivision of the problem, just like the different subclass data of a disease. The variable selection of heterogeneous models should not only consider whether the explanatory variables are significant, but also consider in which models it is significant [13]. This involves double-tier selection.

With the rapid development of Internet and communication technology, data types are not only structured data, but also widely exist in social networks, the Internet of things, e-commerce and other network logs, audio, video. 85 % of the data belongs to unstructured data, which is often accompanied by social networks. New channels and technologies such as mobile computing and sensors are emerging and applied, but the existing data processing methods are only suitable for structured data, and can not unify a large amount of unstructured data with structured data. Integration makes it impossible to discover the value of the data, as is shown by Fig. 1.

In the basic information record of the batch data user, for the cost of the user calling, the flow cost generated by the user on the Internet, and the lack of the data
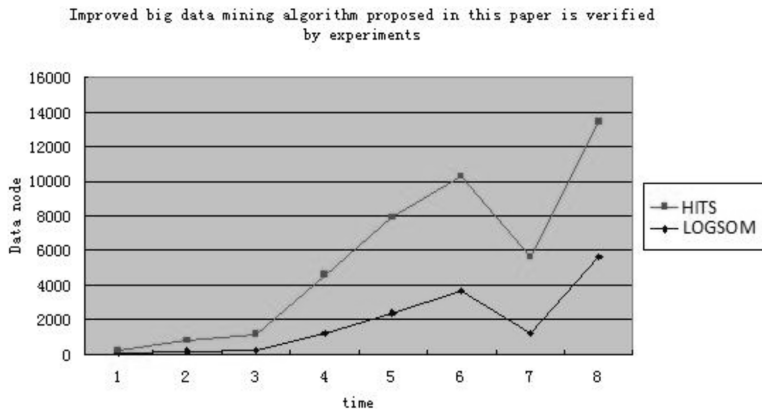
Fig. 1. Performance comparison chart of improved big data mining algorithm

of the value-added service cost. This is because the user does not incur additional costs in the sense of the corresponding field, and the unified assignment is 0. For the absence of mobile phone brand or operating system, we speculate that this is because the mobile phone used by the user does not belong to the mainstream brand or mainstream operating system. There is a lack of start time or end time in the user's call and Internet data record, so the part of the record is deleted. And the lack of latitude and longitude of the location information in the user call and online data is also cleared.

After big data's high efficiency analysis ability gathers enough information, it is necessary for relevant professionals and information technology experts to sum up and analyze the data in a targeted way. A high performance professional analytical technology architecture solution consisting of a large number of emerging technologies (such as Hadoop Map reduction, memory databases, etc.), which is interdisciplinary. Whether the cross-domain cooperation can be realized smoothly is an important problem in the practical application of big data technology.

5. Conclusion

The development of reliable distributed file system (DFS), energy efficiency optimization calculation into storage, storage, go to the big data storage redundancy and high efficiency and low cost of big data; breakthrough distributed non relational data management and processing technology of heterogeneous data, data fusion, data organization technology, modeling technology of big data; breakthrough big data index technology breakthrough; data backup, moving, copying technology; development of large data visualization technology.

Regression analysis is one of the most widely used statistical methods in practice. Regression analysis is a statistical method to describe the relationship between two or more variables. Regression analysis is widely used in practice, and the empirical formula between independent variable and dependent variable can be obtained by

regression analysis. Therefore, it is necessary to quantitatively analyze the correlation between variables, especially in the popular data mining technology. Regression analysis is also necessary. Empirical formula can be obtained by regression analysis of known training data, and the value of dependent variable can be predicted by using empirical formula in the case of known independent variables.

References

[1] A. MAEDCHE, S. STAAB: *Ontology learning for the Semantic Web.* IEEE Intelligent Systems *16* (2001), No. 2, 72–79.

[2] R. VESCOVO: *Pattern synthesis with null constraints for circular arrays of equally spaced isotropic elements.* IEE Proceedings - Microwaves, Antennas and Propagation *143* (1996), No. 2, 103–106.

[3] B. OTTERSTEN, M. VIBERG, P. STOICA, A. NEHORAI: *Exact and large sample ML techniques for parameter estimation and detection in array processing.* Radar Array Processing, Haykin, Litva, and Shepherd, eds., Springer–Verlag, Berlin, Category Telecomunications (1993), 99–151.

[4] F. ARES, S. R. RENGARAJAN, J. A. F. LENCE, A. TRASTOY, E. MORENO: *Synthesis of antenna patterns of circular arc arrays.* Electronics Letters *32* (1996), No. 20, 1845–1846.

[5] F. LI, H. LIU: *Statistical analysis of beam-space estimation for direction-of-arrivals.* IEEE Transactions on Signal Processing *42* (1994), No. 3, 604–610.

[6] P. COMON, G. H. GOLUB: *Tracking a few extreme singular values and vectors in signal processing.* Proceedings of the IEEE *78* (1990), No. 8, 1327–1343.

[7] C. T. LI, F. M. YANG, C. S. LEE: *Oblivious fragile watermarking scheme for image authentication.* IEEE International Conference on Acoustics, Speech, and Signal Processing (ICASSP), 13–17 May 2002, Orlando, FL, USA, *4* (2002), 3445–3448.

[8] R. O. SCHMIDT: *Multiple emitter location and signal parameter estimation.* IEEE Transactions on Antennas and Propagation *AP–34* (1986), No. 3, 276–280.

[9] P. E. HYBERG: *Circular to linear array mapping using calibration data.* Eighth International Conference on HF Radio Systems and Techniques, 10–13 July 2000, Guildford, UK, Conferece Publication (2000), 71–75.

[10] A. FORMICA: *Ontology-based concept similarity in Formal Concept Analysis.* Information Sciences, *176* (2006), No. 18, 2624–2641.

[11] J. Y. NIE: *A general logical approach to inferential information retrieval.* Encyclopedia of Computer Science and Technology (2001), CRC Press, USA, 203–226.

[12] S. Y. KUNG, K. S. ARUN, D. V. B. RAO: *State-space and singular-value decomposition-based approximation methods for the harmonic retrieval problem.* Journal of the Optical Society of America *73* (1983), No. 12, 1799–1811.

[13] P. STOICA, K. C. SHARMAN: *Novel eigenanalysis method for direction estimation.* IEE Proceedings F - Radar and Signal Processing *137* (1990), No. 1, 19–26.

Well data constraints based time domain full-waveform inversion method[1]

Xiong Wei[2], Jiang Lei[2], Yang Lipu[2], Xu Zhiping[2], Xu Shunqiang[2]

Abstract. In this paper, the seismic wave imaging of reservoirs under complex tectonic conditions is discussed. In order to improve its reliability and accuracy, the correlation method of time domain full waveform is used. Finally, the full-waveform inversion error functional model under the condition of the well data constraint is established. Then the Marmousi model is used to test and analyze the relevant data and the effect of the whole waveform inversion. The inversion needs to include the constraints of the regularization to ensure the reliability of the inversion, seismic, logging and geology. The prior information provided in the inversion as regularized information provides a data basis for seismic inversion. The process of time-domain full-waveform inversion is studied in this paper, and the process of offset and tomography is similar.

Key words. Full waveform inversion, well data constraint, time domain, Marmousi model.

1. Introduction

There are many types of waveform inversion which can be classified according to different criteria. By comparing different waveform inversion methods, it can be concluded that Laplace domain waveform is suitable for the initial low-wavenumber velocity field problem, and if the quality of the low-wavenumber velocity field is not high enough, the wave inputs of time domain and Fourier domain will not be completed during the inversion. Laplace-Fourier domain waveform inversion belongs to the mixed domain waveform inversion, where one-step inversion can be achieved [1].

According to the target type, the waveform inversion can be divided into two categories: first-wave inversion and full-wave inversion. If the inversion is performed

---

[2]Geophyscial Exploraton Center, China Earthquake Administration, Zhengzhou, Henan, 450000, China

for the entire underground structure, we must use the full waveform inversion, but if the inversion is for the partial structure near the surface, we should choose the first arrival waveform inversion instead [2].

2. Method and principle

2.1. Basic principle

The current seismic survey is achieved through the iteration of the artificial source and observation system, and the ideal waveform inversion can be obtained through continuous iterating.

In acoustic wave equation, the density has little effect on the reflected wave, and for constant density, the 2D acoustic wave equation can be rewritten as:

$$\frac{1}{v}\frac{\partial^2 u}{\partial t^2} = \frac{\partial^2 u}{\partial x^2} + \frac{\partial^2 u}{\partial z^2} \tag{1}$$

Various setting parameters in the full waveform inversion are defined according to the above equation: u is the normal stress, v is the medium velocity, x_{s} is the shot position, and x_{r} is the detection position. The relationship with the velocity field will be explored by using this equation. The error of the full waveform inversion can be obtained by using the least squares function as

$$E(v) = \frac{1}{2}\sum_{x_{\mathrm{s}}}\sum_{x_{\mathrm{r}}}\sum_{t}(u_{\mathrm{mod}}(x_{\mathrm{s}}, x_{\mathrm{r}}, t, v) - u_{\mathrm{obs}}(x_{\mathrm{s}}, x_{\mathrm{r}}, t))^2 \,. \tag{2}$$

Here, u_{mod} denotes the forward shot parameters and u_{obs} stands for the measurements of the shot collection.

The waveform velocity update gradient $g(v)$ is defined as the derivative of the error function, and can be expressed as:

$$g(v) = \frac{\partial E(v)}{\partial v} \,. \tag{3}$$

Through theoretical derivation, the wave equation of special medium can be written as

$$\left(\frac{1}{v^2}\frac{\partial^2}{\partial t^2} - \nabla^2\right)\frac{\partial u_{\mathrm{mod}}}{\partial v} = \frac{2}{v^3}\frac{\partial^2 u_{\mathrm{mod}}(v)}{\partial t^2} \,, \tag{4}$$

where ∇^2 denotes the second half of the rewritten acoustic wave equation for constant-density wave.

Using the adjoint state combining with the local perturbation wavefield, we obtain

$$\left\langle u_{\mathrm{mod}} - u_{\mathrm{obs}}, \frac{\partial u_{\mathrm{mod}}}{\partial v}\right\rangle = \left\langle u_{\mathrm{mod}} - u_{\mathrm{obs}}, F\left[\frac{2}{v^3}\frac{\partial^2 u_{\mathrm{mod}}(v)}{\partial t^2}\right]\right\rangle =$$

$$= \frac{2}{v^3} \left\langle F^* \left[u_{\text{mod}} - u_{\text{obs}} \right], \frac{\partial^2 u_{\text{mod}}\left(v\right)}{\partial t^2} \right\rangle, \tag{5}$$

where F is the propagation operator

2.2. Initial velocity acquisition

The tomography, the migration, or the waveform inversion require that the initial model should be highly accurate, which can be known by studying the current inversion and velocity analysis methods. The full waveform inversion receives a priori constraints from the initial model, and it is useless without prior constraints even its mathematical theory is perfect. In other words, whether the full waveform inversion is successful links to the accuracy of the initial model. Therefore, an accurate initial model is crucial in the full waveform inversion. This paper starts with two full waveform inversion methods to get the initial velocity. The first is to obtain the root mean square of the velocity field in the time domain by prestack migration and superposition velocity analysis, and then convert the velocity field from the time domain to the depth domain by using the Dix formula. The initial velocity for FWI modeling was obtained through the prestack depth migration analysis and tomography. The second is to obtain a preliminary model using the Laplace domain full waveform inversion method, and then the model was inputted into the time domain full waveform inversion model.

2.3. Velocity update gradient calculation

Through the acoustic wave equation, the function error value of the time domain full waveform inversion can be obtained. That is, by substituting (5) into (3), we can obtain the corresponding derivative, i.e., the velocity update gradient value:

$$g\left(v\right) = \frac{2}{v^3} \sum_{x_{\text{s}}} \sum_{t} \frac{\partial^2 u_{\text{mod}}\left(v\right)}{\partial t^2} F^* \left[u_{\text{mod}} - u_{\text{obs}} \right]. \tag{6}$$

The geophysical significance in (6) is that the wave inversion velocity has the second derivative relationship with wave field, and the product is obtained by inverting the measured and observed data. In other words, the $\partial^2 u_{\text{mod}}/\partial t^2$ term presents the second derivative relationship between the propagating wave field and time. Therefore, the local minimum phenomenon will occur in the full-waveform inversion under the conditions of high frequency and high wave number. And if the difference between the actual velocity and the input velocity is significant, the convergence of the inversion process may not be achieved.

In this paper, the gradient value is calculated by formula (6). This is the typical SD method for calculating the velocity update gradient, which is often referred to as the steepest descent method. Because this method is simple and practical, it has the most advantage in various multi-position unconstrained methods. Moreover, the convex quadratic problem can strictly converge with SD method, so the calculation

results are also the most reliable and accurate. However, SD method has a certain "sawtooth effect", that is, this method can only calculate the direction of the fastest falling part, but not the direction of the fastest falling in the global. The sawtooth effect will also affect the direction of the waveform. Even small movement will have a great influence, and will cause the low convergence velocity. Therefore, the SD method is mostly used in the pre-examination of the calculation process or the prophase iteration. This problem can be improved through conjugate gradient method.

The conjugate gradient method is also referred as CG method, where the new direction is calculated based on the existing search direction and the negative gradient direction, that is, the conjugation is performed in various directions under the convex quadratic objective function. The full waveform inversion includes following main functions: guiding and correcting the current iteration gradient based on the previous iteration, correcting the direction, and overcoming the slow convergence problem due to the sawtooth effect in steepest descent.

The conjugate gradient method is the best choice for the time domain full waveform inversion. The conjugate gradient method can outperform the steepest descent method in convergence. Through this method, the present paper adopted Fletcher-Reeves (FR) to conduct the full waveform inversion. Here, the value of the correction factor β can be obtained using the following expression:

$$\beta^{(k)} = \frac{\left(g^{(k+1)}\right)^t g^{(k+1)}}{\left(g^{(k)}\right)^t g^{(k+1)}}\,, \tag{7}$$

where $g^{(k)}$ and $g^{(k+1)}$ represent the gradient of the kth and $(k+1)$th iteration.

2.4. Determination of velocity update step

Based on Taylor's expansion, the velocity update step can be expressed as

$$\alpha = \frac{(Fg)^{\mathrm{T}}(u_{\mathrm{mod}} - u_{\mathrm{obs}})}{(Fg)^{\mathrm{T}}(Fg)} \tag{8}$$

where T denotes the matrix transpose operation. The finite difference positive operator can be used as approximate value in the full waveform inversion.

In (8), it is necessary to solve the Frechet differential, but compared with the nonlinear positive problem, it is difficult to achieve the differential solution. The parabolic fitting method is used to solve the step length. The core of this method is to use the three error functions $((\alpha, E)(\alpha_0, E_0)(\alpha_1, E_1)(\alpha_2, E_2))$ of three steps to obtain the functional expression for the step and error functional. Then the optimal step α_{opt} and the minimum of corresponding error function can be achieved. So, the error function of the inversion iteration will be minimized in the term of least squares during the full waveform inversion, which means the process is optimal. The key point is that assuming that the initial step length is 0, the error functional will be E_0, Then a finite difference forward model is used to simulate the remaining two

steps and the error functional with the relationship of $E_1 < E_0$ and $E_1 < E_2$. Finally we will obtain three valid (α, E) and the $E - \alpha$ relationship curve, from which the optimal step length α_{opt} can be obtained to be the abscissa value of the curve vertex (see Fig. 1).
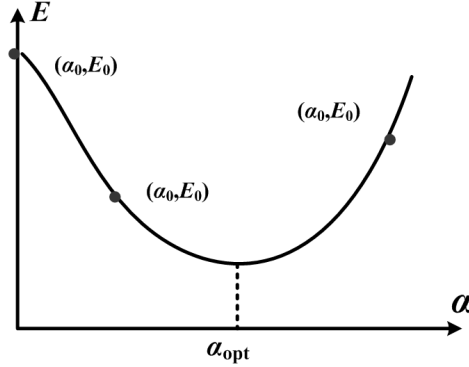

Fig. 1. Calculation velocity of the update step by function

In computing, the optimal step has to be found in a quick way, which can be calculated by the trial step and error functional

$$\alpha = \frac{\alpha_{\mathrm{try}}^2 \|g\|^2}{2\left(\alpha_{\mathrm{try}} \|g\|^2 + E(v) - E(v_{\mathrm{try}})\right)}, \tag{9}$$

where α is the iteration step length, g is the velocity update gradient, α_{try} is the trial step length, and v_{try} is the trial velocity.

It can be found that to obtain the optimal step length in the full waveform inversion, only one additional forward calculation is needed to obtain the inversion iteration update value when the parabolic fitting method is adopted. The overall thought is that: first, determine the trial step length, and require the iterative update velocity to be less than one percent of the background velocity; second, find the trial velocity based on the trial step length, and then obtain the error functional value by using the finite difference forward modeling. In (9), the optimal iteration step length can be obtained through the operation, and the waveform inversion velocity can be updated at the same time.

2.5. Well constraint error functional construction

In essence, seismic full-waveform inversion has typical non-linear ill characteristics:

(1) In the course of seismic exploration, due to imperfect observation methods, the data is completeness, the observation system is limited, the underground projection data acquisition is very difficult, leading to many uncertainties in the inversion;

(2) There are differences between the resolution of observation data for different

model spaces, that is, the uncertainty is different for each model space. If some components are over-determined, the convergence will be easy. If some components are underdetermined and difficult to be determined, the convergence problem will occur in the inversion process. And if some components are sporadic, and the inversion will be impossible based on current observation data. These natural defects and problems of full waveform inversion must be resolved through constraints in the inversion. And the full waveform inversion will be practical then. In seismic inversion, these problems are generally solved using normalization constraints.

Under the well constraint conditions, the error function of the full waveform inversion is evaluated as

$$E\left(v\right) = \frac{1}{2}\left\|u_{\mathrm{mod}} - u_{\mathrm{obs}}\right\|_2^2 + \gamma\left\|W \bullet \left(v - v_{\mathrm{well}}\right)\right\|_2^2 \tag{10}$$

where γ is the regularization factor, W is the regularization matrix, v is the velocity in the medium and v_{well} is the logging velocity.

The update gradient $g(v)$ is given as

$$g\left(v\right) = \frac{2}{v^3}\sum_{x_s}\sum_{t}\frac{\partial^2 u_{\mathrm{mod}}\left(v\right)}{\partial t^2},$$

$$F^*\left[u_{\mathrm{mod}} - u_{\mathrm{obs}}\right] + 2\gamma\sum_{n_{\mathrm{well}}}\left(v - v_{\mathrm{well}}\right). \tag{11}$$

3. Model trial

3.1. Model Marmousi model

The Marmousi model is a classical geophysical model that can perform time domain FWI algorithm testing [4]. To further increase the measurement velocity, the Marmousi model (see Fig. 2) needs to be improved. Set velocity grid value of $nx \times nz = 737 \times 350$, and sample at intervals of 8 m in the vertical and horizontal directions. The ground shot shock wave can be received through the observation system, with the number of 50 and the short interval of 88 m. The first shot is set at 880 m position, and then the shot value will be received through full well hole, and the wave will be measured at intervals of 8 m. The Ricker wavelet was used as the source with the frequency of 25 Hz. 4001 shots are recorded, and the sampling time is 2 s with the interval of 0.5 ms.

The Marmousi model is improved by increasing the constant velocity layer. Figures 2a and 2b show the real data model and the initial model. The initial model was iterated 240 times using the conjugate gradient method, and then the results of 4 iterations were selected and presented in Figs. 2(c)–(f). It can be found from the calculation results that at the 19th iteration, the structure of the model can be basically seen. At the 47th iteration, the structure at the depth of 1.5 km is visible. After the 150th iteration, the details of the construction of the entire model can be

restored. And at the 240th iteration, the geological structure and composition below 2000 m depth can be accurately and carefully presented. Through this iterative test, it can be found that, based on the premise of the accuracy of low-frequency information, the full waveform inversion of the initial model has a very good performance on high-frequency components.
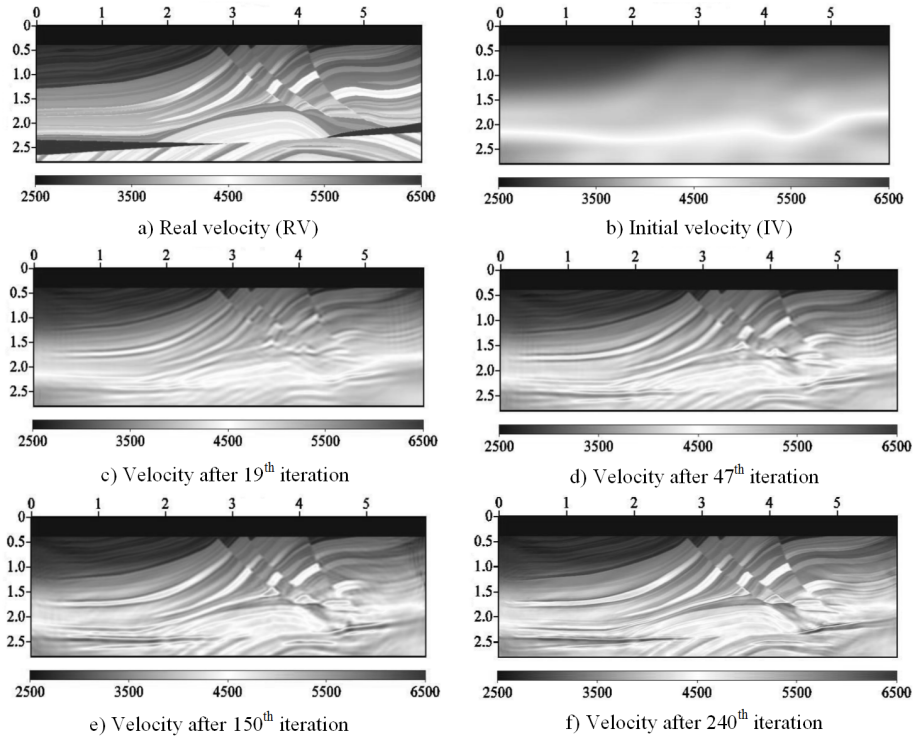

Fig. 2. Marmousi model (km)

Figure 3(a) shows comparison of the initial velocity, true velocity at 1.6 km depth and the curve after the iteration, while Fig. 3(b) and 3(c) are the inversion results at 3.2 km and 4.8 km, respectively. The results of these inversions were found to be satisfactory, except for some high-frequency components and partial areas deeper than two kilometers.

The possible reasons for the poor inversion performance in some regions are:

(1) In full-waveform inversion, the frequency is recovered gradually for low to high components, so that it is necessary to perform more iterations to converge for high-frequency components in the deep. In order to obtain a more ideal result, the iteration number should be over 500 or 1000, whereas our inversion only iterates 240 times due to the limitations of computational efficiency. (2) The velocity accuracy of the smoothing factor is not kept when the initial velocity of the high-frequency structure in the deep is calculated, and the accuracy of the low-frequency component is also greatly reduced because the velocity structures in different regions are very

different, which will affect the subsequent inversion and result in poor inversion results.

a) Distance = 1.6 km   b) Distance = 3.2 km   c) Distance = 4.8 km
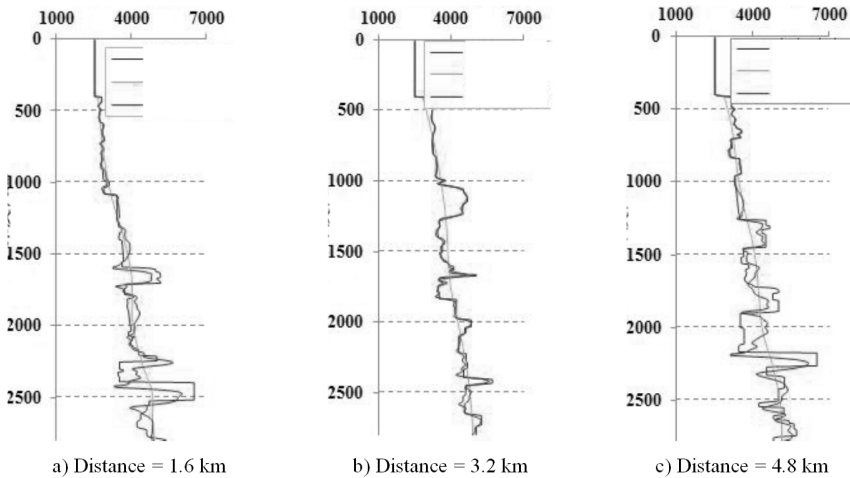
Fig. 3. Comparison of initial velocity, real velocity and 240 inversion velocity at different distances

Now, some of the factors that impact the inversion are briefly summarized as below: First, the recovery of the velocity is achieved gradually from the bottom to the top layers, from the low to the high frequency components during full waveform inversion, and therefore sufficient iteration number is needed to ensure the convergence of deep high-frequency components. Whereas considering the calculation efficiency, the maximum is 240 times in this work. The possibility of obtaining better inversion results can be greatly improved if the iteration number reaches 500 or even higher. Second, if smoothing operator is used in the acquisition of the initial velocity, the accuracy of velocity can hardly be guaranteed. And the distortion of the low-frequency components will occur due to the severe discrepancy between the smoothing operator and the surrounding velocity structure, which ultimately will directly or indirectly limit subsequent velocity inversion.

3.2. Well constraint inversion trial

The trial of well-constraint waveform inversion is performed by complex seismic geologic models. Due to the computational efficiency, the model was processed through resampling and depth truncation. The velocity grid size is 1041×566 in $nx \times nz$ and the grid sampling interval is 8 m for both vertical and horizontal directions. The observation is through ground shot and receiving. There are 56 shots spacing 80 m. The first shot is set at 600 m, It was received in full surface of the well with the detection space of 8 m. A 25 kHz Ricker wavelet was used as the source wavelet, and the shot data was collected at a sampling rate of 0.5 ms with the interval of 3 s. A uniform layer was used to plan the thin layers and keep them unchanged. Fig. 4a shows the real model velocity field, and Fig. 4b the smoothed velocity field after

tomographic inversion. The low frequency velocity component of the background shown in this figure has been well recovered. The basic structure can be seen vaguely. Such a velocity field is allowed to use as the initial velocity input according to the initial velocity conditions required for full waveform inversion. The velocity field shown in Fig. 4c is a well-constrained full-waveform inversion velocity field obtained after 40 iterations.

a) Real velocity field   b) Tomographic inversion velocity field

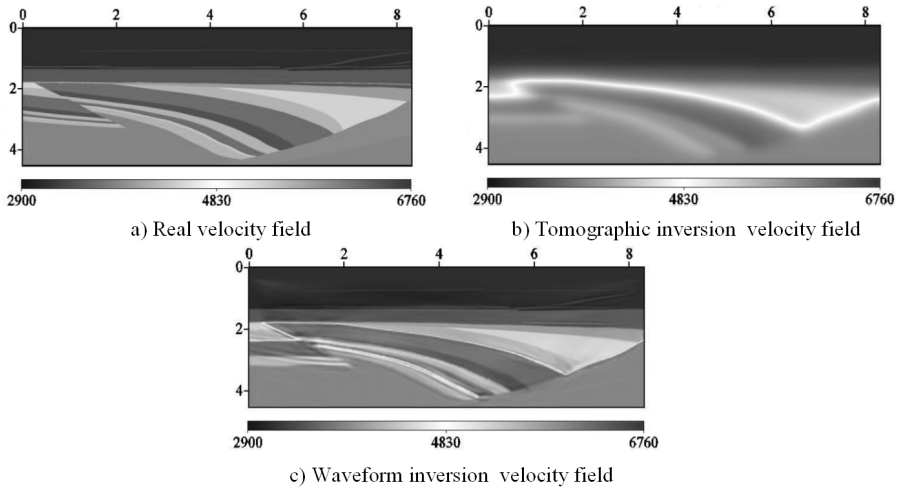c) Waveform inversion velocity field

Fig. 4. Constrained waveform inversion of seismic geologic model wells

As shown in the figure, the extremely thin layer is accurately presented in the shallow large layer. The thin layer in the middle thrust fracture section also recovered well. The right side clearly shows the profile and shape of the stratum pinch, but the thin layer in the left lower wall of the fault has not been effectively restored. The main reasons are that the lighting is insufficient because of the less coverage and the lighting of the upper plate is covered. This problem can be effectively solved by using bidirectional lighting analysis to optimize the observing system. Figures 5a and 5b present the comparison of true velocity, velocity smoothed by tomographic inversion, and inversion velocity with and without well constraints at distances of 3 km and 5.05 km, respectively. One can see that that the smooth travel time tomographic inversion velocity is more suitable for full waveform inversion. If the inversion does not have well constraints, there will be more uncertainties in the real velocity and inversion. Moreover, the inversion accuracy increases with increase of the distance to well, which verifies the validity and authenticity of the method.

4. Conclusion

Through the derivation and implement of the theory and method, as well as the trial calculation of actual data, the following knowledge and conclusions can be obtained:

(1) The success of full waveform inversion depends on the established initial

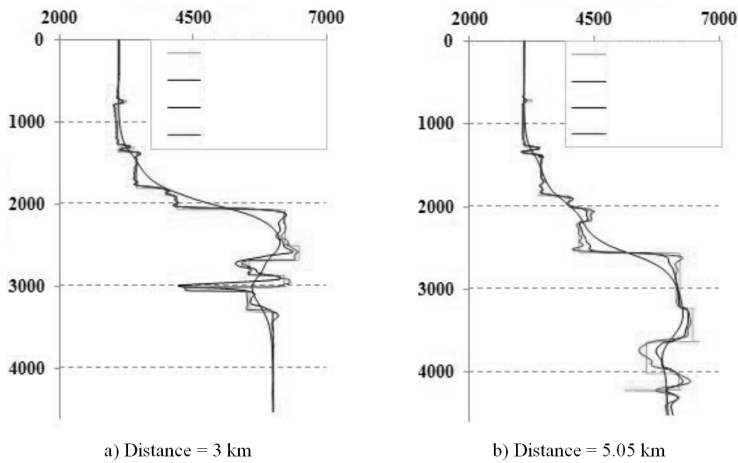a) Distance = 3 km   b) Distance = 5.05 km

Fig. 5. Different distance real tomographic inversion, no well constrained FWI
velocity and well constrained FWI velocity are compared

model. And the initial model is crucial to the success of the experiment, and one of
the key factors which determine the inversion effect.

(2) The upper structure can be recovered by the initial iteration, while the
low structure is continuously revised with the increasing of the iteration number.
Since the high-wavenumber component has a faster convergence rate than the low-
wavenumber component, an excessive convergence of the high-wavenumber compo-
nent at the velocity interface can occur.

(3) From the fundamental purpose, the ability to obtain a wavelet that is infinitely
close to the real source provides possibility for the successful full waveform reversion.
Based on this, the full waveform inversion can successfully retrieve the structure of
earthquake with high resolution.

References

[1] D. Vigh, E. W. Starr: *Comparisons for waveform inversion, time domain or fre-
quency domain?*. SEG Technical Program Expanded Abstracts, (2008), 1890–1894.
[2] E. Evans, M. Papouin, S. Abedi, M. Gauer, P. Smith, I. F. Jones: *Southern
North Sea preSDM imaging using hybrid gridded tomography*. SEG Technical Program
Expanded Abstracts (2005), 766–776.
[3] Y. Yueming, L. Zhenchun, H. Wengong, L. Qingmin: *Beamlet prestack depth mi-
gration and illumination: A test based on the Marmousi model*. Applied Geophysics *3*
(2006), No. 4, 203–209.
[4] A. Tarantola: *Inversion of seismic reflection data in the acoustic approximation*.
Geophysics *49* (1984), No. 8, 1259–1266.
[5] Y. Tang, S. Lee, A. Baumstein, D. Hinkley: *Tomographically enhanced full wave-
field inversion*. SEG Technical Program Expanded Abstracts, (2013), 1037–1041.